DGK Veröffentlichungen der DGK
Ausschuss Geodäsie der Bayerischen Akademie der Wissenschaften

Reihe C | Dissertationen | Heft Nr. 896

Qing Liu

Regional gravity field refinement for geoid height modeling based on the combination of data from various observation techniques

München 2023

Bayerische Akademie der Wissenschaften

ISSN 0065-5325 ISBN 978-3-7696-5308-3

Diese Arbeit ist gleichzeitig als E-Dissertation auf mediaTUM veröffentlicht:
https://mediatum.ub.tum.de/?id=1661723, München 2022

DGK Veröffentlichungen der DGK

Ausschuss Geodäsie der Bayerischen Akademie der Wissenschaften

Reihe C Dissertationen Heft Nr. 896

Regional gravity field refinement for geoid height modeling based on the combination of data from various observation techniques

Vollständiger Abdruck
der von der TUM School of Engineering and Design
der Technischen Universität München
zur Erlangung einer
Doktorin der Ingenieurwissenschaften (Dr.-Ing.)
genehmigten Dissertation

von

M. Sc. Qing Liu

München 2023

Bayerische Akademie der Wissenschaften

ISSN 0065-5325 ISBN 978-3-7696-5308-3

Diese Arbeit ist gleichzeitig als E-Dissertation auf mediaTUM veröffentlicht:
https://mediatum.ub.tum.de/?id=1661723, München 2022

Adresse der DGK:



Ausschuss Geodäsie der Bayerischen Akademie der Wissenschaften (DGK)

Alfons-Goppel-Straße 11 ● D – 80 539 München

Telefon +49 – 89 – 23 031 1113 ● Telefax +49 – 89 – 23 031 - 1283 / - 1100

e-mail post@dgk.badw.de ● http://www.dgk.badw.de

Prüfungskommission:

Vorsitz:	Prof. Dr.-Ing. Liqiu Meng
Prüfer*innen der Dissertation:	1. apl.Prof. Dr.-Ing. habil. Michael Schmidt
	2. Prof. Dr. techn. Roland Pail
	3. Prof. Dr.-Ing. Annette Eicker

Die Dissertation wurde am 23.06.2022 bei der Technischen Universität München eingereicht
und durch die TUM School of Engineering and Design am 04.10.2022 angenommen

---

© 2023 Bayerische Akademie der Wissenschaften, München

Alle Rechte vorbehalten. Ohne Genehmigung der Herausgeber ist es auch nicht gestattet,
die Veröffentlichung oder Teile daraus auf photomechanischem Wege (Photokopie, Mikrokopie) zu vervielfältigen

ISSN 0065-5325 ISBN 978-3-7696-5308-3

Abstract

In 2015, the International Association of Geodesy (IAG) introduced the International Height Reference System (IHRS) as the global standard for the determination of physical heights. At present, its realization relies on precise regional gravity field modeling, since high-resolution terrestrial, airborne, and shipborne gravity data are only available in specific regions. These data sets allow for a regional gravity field refinement through a combination with medium-resolution satellite altimetry data and low-resolution satellite gravimetry data. A proper combination of these heterogeneous data sets is the key to obtaining a high-resolution and high-precision regional gravity model. Consequently, this thesis aims at studying and developing different procedures for regional geoid modeling based on the combination of data from various observation techniques.

Spherical radial basis functions (SRBFs) are used for the representation of the gravity field and its functionals. Four properties in the SRBF setup influence the modeling accuracy, namely the bandwidth, the location, and the type of the SRBFs, as well as the extension of the data zone for reducing edge effects. These properties are discussed and specified in this work. Two groups of SRBFs are considered, namely the Shannon function, as well as the Blackman and the Cubic Polynomial (CuP) functions, both characterized by smoothing features. An SRBF with smoothing features serves further as a low-pass filter, e.g., for reducing the high-frequency noise in the gravity data.

For the determination of the unknown gravity field parameters, the data sets of the measured gravity functionals have to be combined. However, in case of a least-squares adjustment, the system is almost always ill-posed, and regularization is inevitable. As the conventional regularization methods cannot be applied if the relative weight factors of different observation groups are unknown, and the variance component estimation (VCE) might deliver unreliable regularization results, an extended approach is proposed in this work. It combines VCE for estimating the relative weights between the different data sets and the L-curve method for determining the regularization parameter.

The derived procedures and strategies are then applied for the regional (quasi-) geoid modeling in Colorado, USA. The computation is carried out in the frame of the "1 cm geoid experiment", which was initiated by the IAG in 2017 to test the possibility of reaching an accuracy of 1 cm in regional geoid modeling for the realization of the IHRS. Due to the high elevation and the rugged terrain of this study area, the modeling procedure is further adapted to consider the topographic effect. High-resolution terrestrial and airborne gravity measurements are combined along with a global gravity model (GGM) and topography models. It has to be stated that the final (quasi-) geoid model benefits from all types of data sets. The modeling results are validated using both the mean solution delivered by fourteen institutes worldwide with different modeling approaches and GNSS/leveling data. The comparison results show that the SRBF-based quasi-geoid model delivers one of the smallest standard deviations among all the participating groups w.r.t. the validation data, which proves the validity of the developed modeling procedures based on the SRBFs.

Different types of gravity measurements vary not only in their spatial resolution but also in their spectral sensitivity. It has been suspected that the single-level SRBF approach could be biased towards the high-resolution measurements and cannot extract the full information from measurements with medium to low resolution. To take into consideration the spectral sensitivities of different data types, a spectral combination based on SRBFs is implemented through the multi-resolution representation (MRR). The spectral domain is discretized into different resolution levels, and each type

of gravity observations is introduced to the estimation procedure at the level of its highest sensitivity. Furthermore, the resolution levels are connected by the pyramid algorithm, and its application based on sequential parameter estimation for regional gravity field modeling is realized in this thesis. The benefits of applying the MRR based on the pyramid algorithm are demonstrated by numerical investigations based on both simulated and real gravity measurements.

Kurzfassung

Im Jahr 2015 führte die "International Association of Geodesy" (IAG) das Internationale Höhenreferenzsystem (IHRS) als globalen Standard für die Bestimmung physikalischer Höhen ein. Dessen Realisierung basiert derzeit auf einer präzisen regionalen Schwerefeldmodellierung, falls in diesen Regionen hochaufgelöste terrestrische Messungen und/oder Daten der Flug- und Schiffsgravimetrie vorliegen. Diese Datensätze ermöglichen eine Verfeinerung des regionalen Schwerefeldes durch eine Kombination mit Satellitenaltimetriedaten mittlerer Auflösung und Satellitengravimetriedaten niedriger Auflösung. Voraussetzung für die Erstellung eines hochaufgelösten und hochpräzisen regionalen Schwerefeldmodells ist dabei eine geeignete Kombination dieser heterogenen Datensätze. Ziel dieser Arbeit ist es daher, verschiedene Verfahren zur regionalen Geoidmodellierung zu entwickeln und anzuwenden, die auf der Kombination von Daten verschiedener Beobachtungstechniken basieren.

Dabei werden für die Darstellung des Schwerefeldes und seiner Funktionale sphärische radiale Basisfunktionen (SRBFs) verwendet. Vier Eigenschaften des SRBF-Setups beeinflussen die Modellierungsgenauigkeit, nämlich die Bandbreite, der Ort und der Typ der SRBFs sowie die Ausdehnung der Datenzone. Letztere reduziert dabei die Randeffekte. Es werden zwei Gruppen von SRBFs betrachtet, nämlich die nicht glättende Shannon-Funktion sowie die Blackman- und die Cubic Polynomial (CuP)-Funktionen, die beide durch Glättungsmerkmale gekennzeichnet sind. SRBFs mit Glättungsmerkmalen dienen weiterhin als Tiefpassfilter, z.B. zur Reduzierung des hochfrequenten Rauschens in Schwerefelddaten.

Zur Bestimmung der unbekannten Schwerefeldparameter müssen die beobachteten Datensätze der Schwerefunktionale kombiniert werden. Im Falle einer Schätzung nach der Methode der kleinsten Quadrate ist das Normalgleichungssystem jedoch fast immer schlecht gestellt, sodass eine Regularisierung unumgänglich ist. Da die konventionellen Regularisierungsmethoden nicht angewandt werden können, wenn die relativen Gewichtungsfaktoren der verschiedenen Beobachtungsgruppen unbekannt sind und die Varianzkomponentenschätzung (VCE) möglicherweise unzuverlässige Regularisierungsergebnisse liefert, wird in dieser Arbeit ein erweiterter Ansatz vorgeschlagen, der die VCE zur Schätzung der relativen Gewichte zwischen den verschiedenen Datensätzen mit der Methode der L-Kurve zur Bestimmung der Regularisierungsparameter kombiniert.

Die abgeleiteten Verfahren und Strategien werden dann für die regionale (Quasi-)Geoidmodellierung in Colorado, USA, angewendet. Die Berechnung erfolgt im Rahmen des "1-cm-Geoid-Experiments", das 2017 von der IAG initiiert wurde, um die Möglichkeit zu testen, eine Genauigkeit von 1 cm bei der regionalen Geoid Modellierung für die Realisierung des IHRS zu erreichen. Aufgrund der großen Höhe und des zerklüfteten Geländes dieses Untersuchungsgebiets wird das Modellierungsverfahren weiter angepasst, um den topografischen Effekt zu berücksichtigen. Dabei werden die hochaufgelösten terrestrische Messungen und die Daten der Fluggravimetrie mit einem globalen Schwerfeldmodell (GGM) sowie Topographiemodellen kombiniert. Dabei lässt sich feststellen, dass das finale (Quasi-)Geoidmodell von allen Datensätzen profitiert. Anschließend wird dieses Ergebnis sowohl mit der mittleren Lösung aller übrigen 14 Einzellösungen, die mittels unterschiedlicher Modellierungsansätze berechnet wurden, als auch mit GNSS-/Levellingsdaten verglichen. Dabei zeigt sich, dass das SRBF-basierte (Quasi-)Geoidmodell mit die kleinsten Abweichungen unter allen teilnehmenden Gruppen gegenüber den Validierungsdaten aufweist, was die Qualität des entwickelten Ansatzes belegt.

Die Messungen der verwendeten verschiedenen Schwerefeldtechniken unterscheiden sich nicht nur in ihrer räumlichen Auflösung, sondern auch in ihrer spektralen Empfindlichkeit. Der einstufige

SRBF-Ansatz ist auf die hochaufgelösten, hochfrequenten Messungen ausgerichtet und nicht die gesamte Information aus Messungen mit mittlerer oder geringer Auflösung extrahieren kann. Daher wurde in dieser Arbeit die spektrale Kombination als Multi-Resolutions-Darstellung (Multi-Resolution-Representation, MRR) realisiert. Bei diesem Vorgang wird der Spektralbereich in verschiedene Auflösungsbereiche, die sogenannten Levels, unterteilt. Aufgrund der spektralen Auflösung wird jede verwendete Schwerefeldtechnik in das Schätzverfahren auf dem Level ihrer höchsten Empfindlichkeit eingeführt. Darüber hinaus werden die Levels mathematisch durch den sogenannten pyramidalen Algorithmus verbunden, der in dieser Arbeit durch eine sequentielle Parameterschätzung realisiert wird. Die Vorteile dieser Vorgehensweise werden durch numerische Untersuchungen mittels simulierter und realer Schwerefeldmessungen aufgezeigt und diskutiert.

Preface

This cumulative dissertation is based on the following three first-author papers:

P-I Liu, Q., Schmidt, M., Pail, R., and Willberg, M. (2020a). Determination of the regularization parameter to combine heterogeneous observations in regional gravity field modeling. *Remote Sensing*, 12(10), 1617. https://doi.org/10.3390/rs12101617

P-II Liu, Q., Schmidt, M., Sánchez, L., and Willberg, M. (2020b). Regional gravity field refinement for (quasi-) geoid determination based on spherical radial basis functions in Colorado. *Journal of Geodesy*, 94, 99. https://doi.org/10.1007/s00190-020-01431-2

P-III Liu, Q., Schmidt, M., and Sánchez, L. (2022). Combination of different observation types through a multi-resolution representation of the regional gravity field using the pyramid algorithm and parameter estimation. *Journal of Geodesy*, 96, 80. https://doi.org/10.1007/s00190-022-01670-5

These publications are cited within this dissertation using the letter P (for "publication") and a Roman number (for the chronological order).

The main body of this thesis starts with an introduction to the topic of regional gravity field modeling based on various types of observations. The fundamental theory and different gravity observation techniques are introduced. The applied modeling methods and procedures are explained, and the setting up of the estimation model is demonstrated. Numerical modeling results in different study areas are also discussed. In the end, conclusions and an outlook for future work are provided.

In the appendix, the three original publications are included along with a declaration of the author's contribution for each.

Besides the three first-author publications, the following two co-author publications supplement this dissertation:

CP-I Sánchez, L., Ågren, J., Huang, J., Wang, Y., Mäkinen, J., Pail, R., Barzaghi, R., Vergos, G., Ahlgren, K., and Liu, Q. (2021). Strategy for the realisation of the International height Reference System (IHRS). *Journal of Geodesy*, 95, 33. https://doi.org/10.1007/s00190-021-01481-0

CP-II Wang, Y., Sánchez, L., Ågren, J., Huang, J., Forsberg, R., Abd-Elmotaal, H., Barzaghi, R., Bašić, T., Carrion, D., Claessens, S., Erol, B., Erol, S., Filmer, M., Grigoriadis, V., Isik, M., Jiang, T., Koç, Ö., Li, X., Ahlgren, K., Krcmaric, J., Liu, Q., Matsuo, K., Natsiopoulos, D., Novák, P., Pail, R., Pitoňák, M., Schmidt, M., Varga, M., Vergos, G., Véronneau, M., Willberg, M., Zingerle, P. (2021). Colorado geoid computation experiment – Overview and Summary. *Journal of Geodesy*, 95, 127. https://doi.org/10.1007/s00190-021-01567-9

These two publications are cited using the usual citation style in this thesis. A short summary as well as the author's contribution are provided for each co-author publication in the Appendix.

Contents

Abstract **ii**

Kurzfassung **iv**

Preface **v**

1 Introduction **1**
1.1 Motivation . . . 1
1.2 Research questions and objectives . . . 3
1.3 Outline . . . 5

2 Fundamental theory **7**
2.1 Physical background . . . 7
2.2 Gravitational functionals . . . 9
2.3 Heights and height system . . . 10
2.4 Regional gravity field modeling . . . 13

3 Gravity data and models **15**
3.1 Satellite gravimetry . . . 15
3.2 Satellite altimetry . . . 16
3.3 Regional gravity measurements . . . 17
3.4 Global gravity models . . . 19
3.5 Topography models . . . 21

4 Methodology **23**
4.1 Spherical radial basis functions . . . 23
4.2 Multi-resolution representation . . . 25
4.3 Pyramid algorithm . . . 26
4.4 Scaling and wavelet functions . . . 29

5 Estimation model **33**
5.1 Model configuration . . . 33
5.2 Parameter estimation . . . 35
5.3 Sequential parameter estimation . . . 36
5.4 Regularization . . . 37

6 Results and discussion **43**
6.1 "1 cm geoid experiment" . . . 43
6.2 Spectral combination via MRR . . . 52

7 Summary and outlook **61**
7.1 Summary . . . 61
7.2 Outlook . . . 64

Abbreviations **67**

List of Figures **69**

List of Tables **71**

Bibliography **73**

Acknowledgements **85**

Appendix **87**
A1 Publication I 87
A2 Publication II 115
A3 Publication III 137
A4 Co-author publications 159

1 Introduction

1.1 Motivation

In 2003, a height difference of 54 cm was found when the two sides of a bridge (Laufenburg bridge) between Germany and Switzerland over the Rhine river were going to connect in the middle. How did this happen? What is the height of Mount Everest, and why did it vary between measurements from different countries? Is it possible that a river flows from a lower to a larger height value?

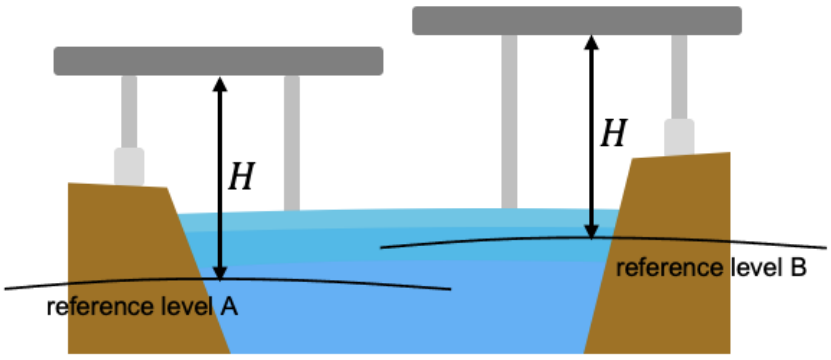


Figure 1.1: What happens when different height reference systems are used at the two sides of a bridge

One answer to all these questions is the usage of different local height reference systems in different countries, which all refer to local levels. As an example, the physical height (H in Fig. 1.1) in Germany and Switzerland refers to the sea level of the North Sea from the tide gauge in Amsterdam and the fundamental station Geneva, which is tightly linked to the tide gauge in Marseille, respectively. They differ 27 cm from each other. Instead of eliminating the difference caused by the local vertical datum before the construction of the bridge, it was doubled by mistake in the calculation. At present, hundreds of local height systems exist (Ihde et al., 2017), and the discrepancies between them can reach more than 2 m. There is a rapidly increasing need for the establishment of a global physical height reference system.

The definition and unification of physical height systems is an essential geodetic application of the Earth's gravity field. For both scientific and practical reasons, it is desirable to establish an accurate, consistent, and well-defined global height reference system (Sánchez et al., 2021). The general case for the realization and unification of height reference systems is the combination of the Global Navigation Satellite Systems (GNSS) positioning, which can reach an accuracy of a few millimeters, and the (quasi-) geoid modeling (Ihde et al., 2017). In 2015, the International Association of Geodesy (IAG) introduced the International Height Reference System (IHRS) as the conventional reference for the determination of physical heights worldwide (Drewes et al., 2016). The IHRS is a gravity potential based reference system (Ihde et al., 2017), and the determination of potential values as IHRS coordinates can be performed following the strategies applied for the (quasi-) geoid modeling.

Therefore, a high-resolution and high-precision (quasi-) geoid model is the key for the realization of the IHRS.

Observations from satellite missions, such as the CHAllenging Minisatellite Payload (CHAMP) (Reigber et al., 2002b), the Gravity Recovery And Climate Experiment (GRACE) (Tapley et al., 2004), the GRACE-Follow-On (GRACE-FO) (Kornfeld et al., 2019), and the Gravity field and steady-state Ocean Circulation Explorer (GOCE) (Rummel et al., 2002) are currently the main data sources for global geoid modeling. However, their main limitation is the spatial resolution, which is only around 100 km at the Earth's surface (Pail et al., 2011). The missing high-frequency part of the gravity signal can cause an omission error of 30 to 40 cm (in extreme cases even several meters) in the geoid models (Gruber et al., 2012; Sánchez et al., 2021). In contrast, other types of measurements such as terrestrial, airborne, and shipborne observations are able to provide a much higher spatial resolution of a few kilometers. Thus, they can be used on top of global models for regional geoid refinement to extend the spectral content and to improve the resolution and precision.

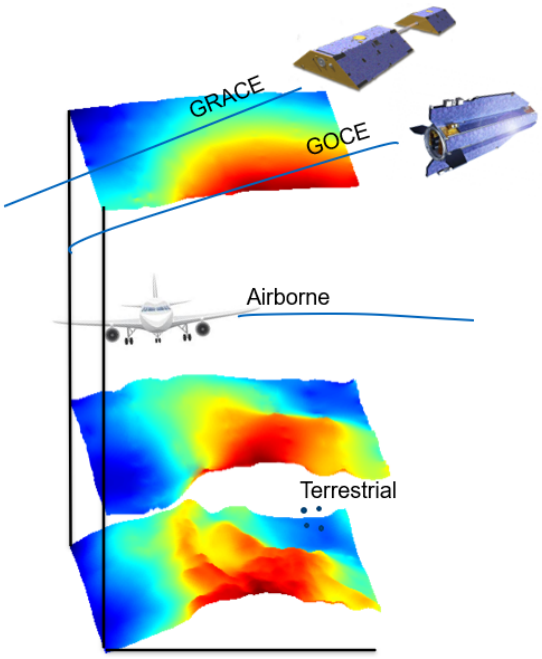


Figure 1.2: High-resolution regional gravity data (airborne and terrestrial measurements) in combination with global satellite data[1]

To optimally combine different types of observations, a proper modeling approach needs to be set up. Different regional gravity field modeling methods have been developed during the last decades, and among them, the method of Spherical Radial Basis Functions (SRBFs) is the focus of this work. The fundamentals of the SRBFs are introduced by Freeden et al. (1998), and further studies can be found in Freeden and Michel (2004); Schmidt et al. (2007); Klees et al. (2008); Eicker et al. (2014), among many others. SRBFs fulfill the Laplace equation such as the Spherical Harmonics (SHs). At the same time, they can be used appropriately for regional approaches to consider the heterogeneity of data sources, due to their localizing features. The SRBFs are computationally easy to implement, and the observations can be used directly at their original positions without applying any griding or interpolation procedures, which are often required in other regional modeling methods, e.g., the numerical evaluation of the Stoke's formula. Four properties in the SRBF setup influence the modeling accuracy, namely the type, the bandwidth, the location of the basis functions, and the extension of the data zone for reducing edge effects.

Heterogeneous data sets can be combined within a parameter estimation procedure (see Koch, 1999; Koch and Kusche, 2002). However, in the context of regional gravity field modeling, the derived least-squares adjustment system is in most cases ill-posed, due to three reasons: (1) the number of used basis functions is usually larger than required, (2) data gaps in the inhomogeneously distributed observations, and (3) the downward continuation of satellite and airborne data to the Earth's surface. Thus, a regularization is inevitable, and choosing an appropriate regularization parameter is a crucial issue. The Tikhonov regularization is applied in this work, which can be interpreted as a least-

[1]GRACE satellite image source: `http://geoid.colorado.edu/grace/`
GOCE satellite image source: `https://gisgeography.com/earth-satellite-list/`

squares estimation including prior information (Tikhonov and Arsenin, 1977). Various approaches have been developed and used for the regularization parameter determination, such as the L-curve method (Hansen, 1990), the Generalized Cross Validation (GCV) (Golub et al., 1979), and the Variance Component Estimation (VCE) (Koch and Kusche, 2002). However, when measurements from various observation techniques with different unknown variance factors are to be combined, all regularization methods may not be appropriately applicable unless the VCE is implemented (Xu et al., 2006). Nonetheless, it has been suspected that the regularization parameter generated by VCE might be unreliable (Liang, 2017). Lieb (2017) pointed out that in regional approaches, regularization is much more sensitive and less well-investigated than in global approaches.

Due to the different spectral sensitivities of each observation technique, the long wavelength parts, i.e., the large-scale structures, of the gravity field can only be evaluated by global satellite observations, while the short wavelength parts are mainly detectable by other types of gravity observations, such as terrestrial and airborne data. To take the spectral resolution of various observation techniques into consideration, a spectral combination (see e.g., Sjöberg, 1981; Kern et al., 2003; Denker, 2013) can be set up such that the different measurement techniques contribute their information in the spectral domain with the highest sensitivity. One way to realize the spectral combination is to set up a Multi-Resolution Representation (MRR), which was initially proposed, e.g., by Freeden et al. (1998); Freeden (1999); and Haagmans et al. (2002). Its realization has been investigated, e.g., by Beylkin and Cramer (2002); Schmidt et al. (2005); Panet et al. (2011); and Bolkas et al. (2016). The fundamental idea of the MRR is to split a given signal into a smoothed version, i.e., a low-pass filtered global gravity model, and a number of detail signals, i.e., band-pass filtered gravity signals (Schmidt et al., 2007). In this case, the final gravity model could benefit from the individual strengths of each observation technique. Furthermore, a pyramid algorithm (Freeden, 1999; Schmidt et al., 2005, 2006) can be applied to connect the different resolution levels, by consecutive low-pass filtering. However, although the proposal of using the pyramid algorithm dates back nearly two decades, its practical realization in regional cases faces several challenges (Lieb, 2017), e.g., the low-pass filter matrix needs to be set up properly, and the extension of the data zone should be adapted for each resolution level.

1.2 Research questions and objectives

This dissertation is aiming to investigate and realize the regional gravity refinement by optimally combining data from different observation techniques using SRBFs. This general goal leads to the following main research objectives:

1. To investigate and derive an appropriate regularization method when different data types are to be combined,
2. To develop a high-resolution regional (quasi-) geoid model using SRBFs based on real gravity measurements,
3. To realize the spectral combination of data from various observation techniques via MRR based on the pyramid algorithm.

These three objectives are accomplished by the three first-author papers **P-I** to **P-III** respectively, all published in peer-reviewed journals with open access. As a cumulative dissertation, the three papers are reprinted in the Appendix, along with a declaration of the author's contributions. To demonstrate how the corresponding objectives are addressed in each paper, a few research questions are defined.

P-I Determination of the regularization parameter to combine heterogeneous observations in regional gravity field modeling

By Qing Liu, Michael Schmidt, Roland Pail, and Martin Willberg. Published in "Remote Sensing".

This publication focuses on the determination of the regularization parameter, which is an inevitable issue in regional gravity field modeling. As mentioned in Sect. 1.1, VCE could give unreliable regularization results, and other conventional regularization methods are not properly applicable when the weight factors of different gravity measurements are unknown. To solve these issues, two combined approaches are proposed for the regularization parameter determination when different data sets are to be combined. The two approaches combine VCE and the L-curve method in such a way that the relative weights are estimated by VCE, but the regularization parameter is determined by the L-curve method. They differ in whether determining the relative weights between each observation type first (VCE-Lc) or the regularization parameter by the L-curve method first (Lc-VCE). Numerical experiments are carried out to compare the performance of these two approaches with the original L-curve method and VCE. In **P-I** (Liu et al., 2020a), we answer the following research questions:

Q-1. Is VCE sufficient for determining the regularization parameter?

Q-2. How to apply a conventional regularization method if various data sets are to be combined?

Q-3. How large is the impact of the regularization parameter on the modeling accuracy?

P-II Regional gravity field refinement for (quasi-) geoid determination based on spherical radial basis functions in Colorado

By Qing Liu, Michael Schmidt, Laura Sánchez, and Martin Willberg. Published in "Journal of Geodesy".

This publication applies SRBFs for computing the regional quasi-geoid and geoid models using real terrestrial and airborne gravity observations in Colorado, USA, which is a challenging study area with high elevation and rugged terrain. Thus, the topographic effect is also considered in the computation. The model settings, i.e., the type, the bandwidth, the location of the SRBFs, and the extension of the data zone, are explained in detail. The Cubic Polynomial (CuP) function, which has smoothing features, is applied to the airborne observations to further serve as a low-pass filter for reducing the high-frequency noise. In **P-II** (Liu et al., 2020b), we also discuss the contribution of each data set, namely the Global Gravity Model (GGM), the topography models, and the regional gravity observations, to the final (quasi-) geoid model. The results contribute to the "1 cm geoid experiment" (Wang et al., 2021; Sánchez et al., 2021), within which the (quasi-) geoid models calculated by fourteen institutes worldwide using different approaches are compared. Furthermore, the model accuracy is evaluated by the GNSS/leveling data from the Geoid Slope Validation Survey 2017 (GSVS17) in southern Colorado. The following research questions are defined in **P-II**:

Q-4. How to set up the estimation model using SRBFs?

Q-5. How much does each observation group contribute to the final (quasi-) geoid model?

Q-6. Which accuracy can the SRBF-based regional (quasi-) geoid model achieve, and how is its performance compared to other methods?

P-III Combination of different observation types through a multi-resolution representation of the regional gravity field using the pyramid algorithm and parameter estimation

By Qing Liu, Michael Schmidt, Laura Sánchez. Published in "Journal of Geodesy".

This paper develops an MRR scheme based on the pyramid algorithm and sequential parameter estimation for the spectral combination of data from various observation techniques. The challenges

in the practical realization of the pyramid algorithm are addressed. Different observation types are introduced successively into the evaluation process at the spectral levels of their highest sensitivities, which makes it possible to benefit from the individual strength of each data set. In **P-III** (Liu et al., 2022), we explain in detail how the estimation model is set up for the MRR, how the different resolution levels are connected by the pyramid algorithm, and how different observations are introduced into the estimation model at each level. The derived gravity model from the MRR based on the pyramid algorithm is then compared directly to the one computed by the single-level SRBF approach, using both simulated and real gravity measurements. Additionally, the advantages of applying the MRR based on the pyramid algorithm are demonstrated and discussed. The following research questions are answered in **P-III**:

Q-7. How can the MRR and the pyramid algorithm be realized in regional gravity field modeling?

Q-8. What and how large is the benefit of applying the MRR based on the pyramid algorithm?

Q-9. In which cases the MRR based on the pyramid algorithm should be applied?

These research questions are answered in the aforementioned papers, and will be structured and summarized in this dissertation. Although each publication is a self-contained study, this thesis will provide more insights, details, and connect them in a scientific context.

1.3 Outline

This thesis contains seven chapters. It covers the whole procedure of regional gravity field refinement using data from various observation techniques; from the theory and methodology to the estimation models and the results. Figure 1.3 shows the structure of this work, including the connection between the chapters as well as their connection to the three papers. Since this is a cumulative dissertation, there is a certain overlap between some contents presented in the following chapters, especially in the methodology and the result parts, and the three publications. They are repeated here to keep this work comprehensive on its own as much as possible. Nevertheless, this thesis will show in particular the insights and relations between the publications in a structured manner.

Chapter 2 explains the fundamentals. Section 2.1 introduces the background of the gravity and the potential theory. Section 2.2 lists different gravity functionals, which are obtained as the first or second order derivatives of the gravity potential. Section 2.3 is dedicated to the height systems. Different height definitions and the IHRS are introduced. It also explains why the physical height system can be realized by regional gravity refinement. Section 2.4 introduces different methods for regional gravity field modeling, and among them, the SRBFs will be explained in detail in Chap. 4.

Chapter 3 presents various gravity observation techniques which are involved in this work, including terrestrial, airborne, shipborne, satellite gravimetry, and satellite altimetry. Each observation technique corresponds to a certain type of gravity functionals and is characterized by its spectral sensitivity. The observation data, the GGMs, and the topography models used in this work are also introduced.

Chapter 4 is dedicated to the methodology. Section 4.1 introduces the SRBFs, and how they are adapted to different gravity functionals as given in Sect. 2.2. The spectral convolution of a gravity functional by SRBFs is also demonstrated. Sections 4.2 and 4.3 discuss the principle and the procedure of the MRR and the pyramid algorithm, respectively. These two sections explain how the resolution levels can be chosen, how the levels are connected, and how different observation techniques are used at these levels. Section 4.4 introduces and compares different types of scaling and wavelet functions, which can be interpreted as low-pass and band-pass filters, respectively.

Chapter 5 discusses how the methodologies presented in Chap. 4 are realized to compute regional gravity models using different types of gravity observations introduced in Chap. 3. Section 5.1 shows

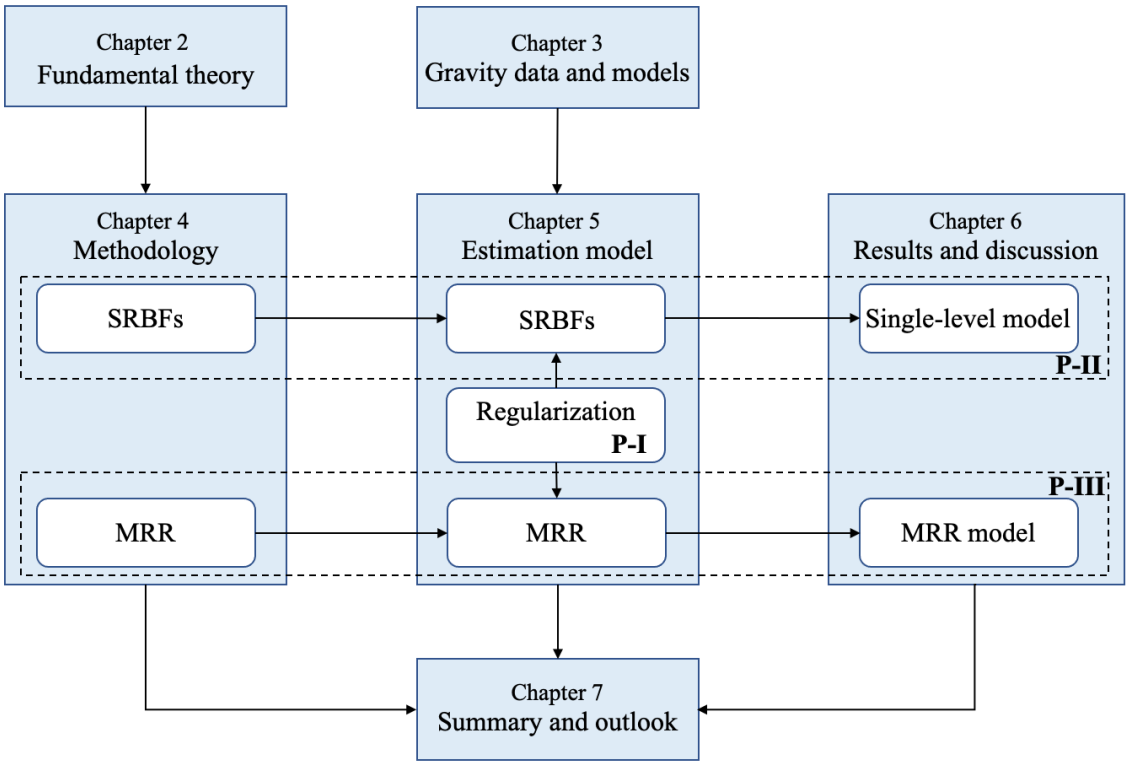


Figure 1.3: Structure of this dissertation, including the connection between the chapters, and in particular their connection to the three publications

the model settings, i.e., how the aforementioned four properties, namely the type, the bandwidth, the location of the SRBFs, and the extension of the data zone, are chosen. Sections 5.2 and 5.3 demonstrate how the estimation models are established for the single-level approach and the MRR, respectively. The combination of data from various observation techniques is explained in detail, including the relative weighting between each other. Section 5.4 introduces existing methods for determining the regularization parameter, discusses their drawbacks, and therefore, proposes a new approach when different data types are to be combined.

The estimation models derived in Chap. 5 are applied to different study cases, and the corresponding results are presented in Chap. 6. The results can be divided into two groups, one from the single-level approach using SRBFs (Sect. 6.1) and one from the multi-level approach, i.e. spectral combination through MRR (Sect. 6.2). In Sect. 6.1, the results from the "1 cm geoid experiment" are discussed, where the SRBF-based (quasi-) geoid model is thoroughly validated with the other thirteen independent solutions delivered by different modeling methods as well as the GNSS/leveling data. Section 6.2 presents the gravity model computed by the MRR based on the pyramid algorithm, and compares it directly with the single-level model.

Finally, Chap. 7 summarizes the findings of this dissertation, provides conclusions and the outlook for future work.

2 Fundamental theory

This chapter addresses the theoretical background of the Earth's gravity field, introduces different gravity related quantities and height systems, and provides a short summary of gravity field modeling approaches.

2.1 Physical background

Gravitation is a function of mass distribution. According to Newton's universal law of gravitation, the force $\boldsymbol{F}$ exerted by a body with attracting mass m on a unit mass located at a distance l from m reads

$$\boldsymbol{F} = G\,\frac{m}{l^3}\boldsymbol{l}, \tag{2.1}$$

where $G = 6.6742 \cdot 10^{-11}$ $\mathrm{m^3 kg^{-1} s^{-2}}$ is Newton's gravitational constant (Hofmann-Wellenhof and Moritz, 2006), $\boldsymbol{l}$ is a vector pointing from the unit mass to the attracting mass with length l. The Earth can be considered as an attracting mass with continuously distributed mass elements dm, and the gravitational potential V at any point P with coordinates (x, y, z) is the integral of the contributions of individual mass elements

$$V = G \iiint \frac{dm}{l} = G \iiint \frac{\rho}{l}\, dv \tag{2.2}$$

where dv is the volume element, and $\rho = dm/dv$ is the density of the attracting mass.

The gravitational potential V satisfies the Poisson equation

$$\nabla^2 V = -4\pi G\rho, \tag{2.3}$$

where $\nabla^2 = \partial^2/\partial x^2 + \partial^2/\partial y^2 + \partial^2/\partial z^2$ is the Laplace operator (Hofmann-Wellenhof and Moritz, 2006). Moreover, in the exterior space outside the Earth, under the assumption $\rho = 0$ by neglecting the density of the atmosphere, it further satisfies the Laplace equation

$$\nabla^2 V = 0. \tag{2.4}$$

Thus, the gravitational potential V is a harmonic function outside the attracting masses.

The gravity potential W is the sum of the gravitational potential V and the centrifugal potential Z

$$W = V + Z, \tag{2.5}$$

where Z at any point $P(x, y, z)$ can be calculated as

$$Z = \frac{1}{2}\,\omega^2(x^2 + y^2), \tag{2.6}$$

with ω being the angular velocity of the Earth.

The gravity acceleration $\boldsymbol{g}$ is derived as the gradient of the gravity potential W (Heiskanen and Moritz,

1967)

$$g = \nabla W = \left[\frac{\partial W}{\partial x}, \frac{\partial W}{\partial y}, \frac{\partial W}{\partial z}\right]^T. \tag{2.7}$$

The magnitude $g = |\boldsymbol{g}|$ is called gravity, which is usually measured in the unit Gal or mGal (1 mGal = 10^{-5} m/s^2). The direction of the gravity vector is pointing into the Earth along the plumb line, which intersects all equipotential surfaces of the Earth's gravity field perpendicularly.

The Earth can be first approximated as a sphere, and second as an ellipsoid of revolution, i.e., a spheroid, whose surface is an equipotential surface of the normal gravity field (Heiskanen and Moritz, 1967). The ellipsoid is regarded as the normal form of the geoid (see Fig. 2.1), which is an equipotential surface of the actual gravity field with $W = W_0$. The normal potential U of the ellipsoid is constant on its surface with $U = U_0 = W_0$. The value of this constant differs between different reference ellipsoids, e.g., the Geodetic Reference System 1980 (GRS80) (Moritz, 2000), and the World Geodetic System 1984 (WGS84) (Hofmann-Wellenhof and Moritz, 2006). The normal potential U is mathematically easy to handle; it can be determined by the constant GM value (with M being the total mass), the semi-axes of the ellipsoid, and the angular velocity ω (Heiskanen and Moritz, 1967). The Earth's gravity potential is then split into a "normal" and a remaining "disturbing" field

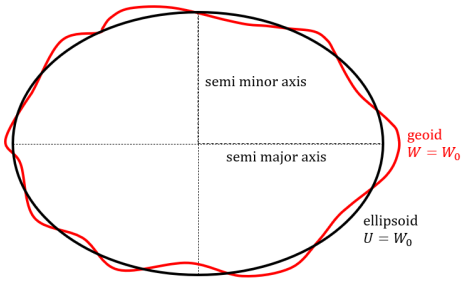


Figure 2.1: The geoid and the ellipsoid

$$T(x, y, z) = W(x, y, z) - U(x, y, z), \tag{2.8}$$

where T is called the disturbing potential. It also satisfies the Laplace equation $\nabla^2 T = 0$ outside the attracting masses, and thus, is a harmonic function. Gravity field modeling usually deals with T instead of W, since the latter can always be reconstructed by adding the normal potential (Heiskanen and Moritz, 1967).

Spherical harmonics

The global gravity field is usually modeled by a series expansion in terms of spherical harmonics (e.g., Heiskanen and Moritz, 1967; Torge, 1991). As a solution of the Laplace equation (2.4) in spherical coordinates, the series expansion of the disturbing potential T in terms of spherical harmonics in the exterior space reads

$$T(\varphi, \lambda, r) = \frac{GM}{R} \sum_{n=0}^{\infty} \left(\frac{R}{r}\right)^{n+1} \sum_{m=0}^{n} \left[\overline{C}_{nm} \cos(m\lambda) + \overline{S}_{nm} \sin(m\lambda)\right] \overline{P}_{nm}(\sin\varphi) \tag{2.9}$$

where φ and λ are the spherical latitude and longitude, R is the radius of the Earth, and $r \geq R$ is the radial distance. $\overline{C}_{nm}$ and $\overline{S}_{nm}$ are the fully normalized spherical harmonic coefficients, and $\overline{P}_{nm}$ are the fully normalized associated Legendre functions,

$$\overline{P}_{nm}(t) = \begin{cases} \sqrt{2n+1}\, P_{nm}(t), & \text{when } m = 0 \\ \sqrt{2\,(2n+1)\,\frac{(n-m)!}{(n+m)!}}\, P_{nm}(t), & \text{when } m \neq 0 \end{cases}. \tag{2.10}$$

P_{nm} is the associated Legendre function of degree n and order m, and it is defined by

$$P_{nm}(t) = (1 - t^2)^{m/2} \frac{\partial^m}{\partial t^m} P_n(t), \tag{2.11}$$

with $t = \sin\varphi$; P_n is the Legendre polynomial of degree n

$$P_n(t) = \frac{1}{2^n n!} \frac{\partial^n}{\partial t^n}(t^2 - 1)^n. \tag{2.12}$$

In practice, the Legendre polynomials P_n can be calculated more simply by the evaluation of the recursion formula

$$P_n(t) = -\frac{n-1}{n} P_{n-2}(t) + \frac{2n-1}{n} t P_{n-1}(t) \tag{2.13}$$

with $P_0(t) = 1$ and $P_1(t) = t$ (Hofmann-Wellenhof and Moritz, 2006).

2.2 Gravitational functionals

Various gravitational functionals can be derived from the disturbing potential T based on field transformations (Rummel and van Gelderen, 1995). This section introduces some of the functionals which are involved in this thesis, while more details related to different gravitational functionals are presented, e.g., by Heiskanen and Moritz (1967) and Hofmann-Wellenhof and Moritz (2006).

Geoid height

As mentioned in Sect. 2.1, the geoid is a unique equipotential surface with $W = W_0$ that coincides with the worldwide mean ocean surface; it was described as the "mathematical figure of the Earth" by Gauss. As shown in Fig. 2.2, the metric difference between the geoid (with $W = W_0$) and the reference ellipsoid (with $U = U_0 = W_0$) is denoted as the geoid height (also known as geoid undulation) N. According to Bruns' formula, it can be calculated as

$$N = \frac{T_{P_0}}{\gamma_0} \tag{2.14}$$

(Hofmann-Wellenhof and Moritz, 2006), where T_{P_0} is the disturbing potential of P_0 at the geoid, and γ_0 is the normal gravity of P_0' at the ellipsoid.

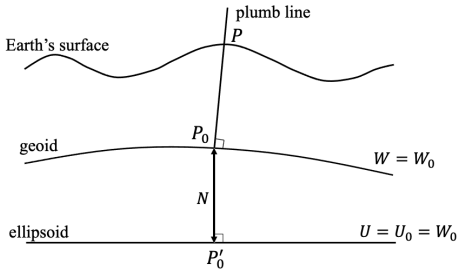


Figure 2.2: Geoid height N. Note that the curve of the ellipsoid is neglected in this and the following figures

Quasi-geoid height

The quasi-geoid is a surface identical to the geoid over the oceans, and close to the geoid anywhere else (Heiskanen and Moritz, 1967). In the same manner as the geoid height, the metric difference between the quasi-geoid and the reference ellipsoid is denoted as the quasi-geoid height (also known as height anomaly) ζ. According to Bruns' formula, it can be calculated as

$$\zeta = \frac{T_P}{\gamma_Q}, \tag{2.15}$$

where T_P is the disturbing potential at the Earth's surface point P, and γ_Q is the normal gravity of the corresponding point Q at the telluroid (Fig. 2.3), which is a surface that is composed of points which have the same normal potential as the gravity potential of the corresponding surface points, i.e., $U_Q = W_P$.

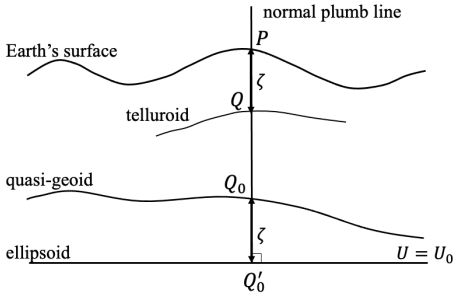


Figure 2.3: Quasi-geoid height ζ

Gravity disturbance

The gravity disturbance δg of the point P is defined as the difference between the gravity and normal gravity at this point

$$\delta g = g_P - \gamma_P. \tag{2.16}$$

Recalling Eq. (2.7), the gravity vector $\boldsymbol{g} = \boldsymbol{\nabla} W$, the normal gravity vector $\boldsymbol{\gamma} = \boldsymbol{\nabla} U$, thus, the gravity disturbance vector $\delta \boldsymbol{g}$ can be expressed as the gradient of the disturbing potential T

$$\delta \boldsymbol{g} = \boldsymbol{\nabla}(W - U) = \boldsymbol{\nabla} T. \tag{2.17}$$

Its magnitude in spherical approximation can be written as

$$\delta g = -\frac{\partial T}{\partial r}, \tag{2.18}$$

see e.g., Hofmann-Wellenhof and Moritz (2006).

Gravity anomaly

The (surface) gravity anomaly Δg is the difference between the gravity g_P at point P and the normal gravity γ_Q of the corresponding point Q at the telluroid (see Fig. 2.3)

$$\Delta g = g_P - \gamma_Q. \tag{2.19}$$

With Bruns' formula and the spherical approximation (Hofmann-Wellenhof and Moritz, 2006), it yields

$$\Delta g = -\frac{\partial T}{\partial r} - \frac{2}{R} T. \tag{2.20}$$

Gravity gradient

The gravity gradient tensor (also known as the Eötvös tensor) includes all second-order derivatives of the disturbing potential T, which quantifies the change of gravity

$$\boldsymbol{\nabla} \cdot \boldsymbol{\nabla} T = \begin{bmatrix} T_{xx} & T_{xy} & T_{xz} \\ T_{yx} & T_{yy} & T_{yz} \\ T_{zx} & T_{zy} & T_{zz} \end{bmatrix} \tag{2.21}$$

with $T_{xy} = T_{yx}, T_{xz} = T_{zx}, T_{yz} = T_{zy}$ (Torge, 1991). Moreover, the trace $\nabla^2 T = T_{xx} + T_{yy} + T_{zz} = 0$ outside the attracting mass, according to the Laplace equation (2.4). In spherical approximation, we obtain $T_{zz} = T_{rr}$.

2.3 Heights and height system

The definition and determination of heights include two aspects, the geometric part which provides the ellipsoidal height h (elevations above a reference ellipsoid), and the physical part which provides the physical height H (heights above a level surface of the Earth's gravity field, Ihde et al., 2017). These two parts are connected to each other by the geoid height N and the quasi-geoid height ζ, which were introduced in Sect. 2.2.

Ellipsoidal height

The ellipsoidal height (or geometric height) h of a point P is defined as the distance from this point to the ellipsoid along the normal plumb line (see Fig. 2.4). It can be directly measured by GNSS, with an accuracy of a few millimeters.

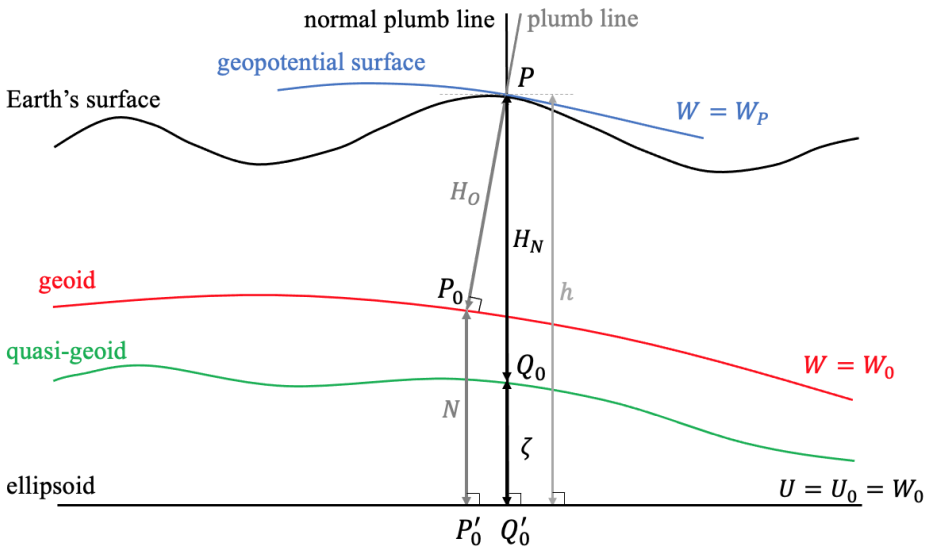


Figure 2.4: Overview of heights and reference surfaces, adapted from Sánchez et al. (2021)

Orthometric height

The orthometric height H_O of a point P is the distance from this point to the geoid, along the plumb line (Fig. 2.4). It can be calculated by

$$H_O = \frac{W_0 - W_P}{\overline{g}} = \frac{C_P}{\overline{g}} \tag{2.22}$$

(Heiskanen and Moritz, 1967), where W_0 and W_P are the potential values at the geoid and the point P, respectively; $C_P = W_0 - W_P$ is denoted as the geopotential number, and $\overline{g}$ is the mean value of the gravity along the plumb line between the point P_0 at the geoid and the point P. The relation between the orthometric height H_O and the ellipsoidal height h reads

$$h = H_O + N, \tag{2.23}$$

neglecting the deflection of the vertical and the curvature of the plumb line (Torge, 1991).

Normal height

The normal height H_N of a point P is the distance from this point to the quasi-geoid, along the normal plumb line (Fig. 2.4). The normal height can be derived as

$$H_N = \frac{W_0 - W_P}{\overline{\gamma}} = \frac{C_P}{\overline{\gamma}}, \tag{2.24}$$

(Heiskanen and Moritz, 1967), where $\overline{\gamma}$ is the mean normal gravity along the normal plumb line between the point Q_0 at the quasi-geoid and the point P. The relation between the normal height H_N and the ellipsoidal height h reads

$$h = H_N + \zeta. \tag{2.25}$$

The orthometric height H_O and the normal height H_N are the two most important types of physical heights. Although the ellipsoidal heights generally have a much better accuracy, they cannot replace the physical heights, due to their geometrical nature (Ihde et al., 2017). For applications related to geophysical fluids, e.g., sea level changes, the Earth's interior, or the river flow, the physical heights

need to be available. Two approaches can be applied to determine the physical heights. The first is spirit leveling combined with gravimetry, following Eq. (2.22) or Eq. (2.24). It is the classical technique that delivers precise results, but the disadvantages are that their measurement is time consuming and expensive, and it may contain systematic distortions. The second approach is to combine the ellipsoidal height from GNSS positioning with a (quasi-) geoid model from gravity field modeling, following Eq. (2.23) or Eq. (2.25). The costs of this approach are much lower, and it is regarded as the future trend for physical height determination (Rummel, 2012). Thanks to the recent advances in optical atomic clocks, a new approach that might be used for physical height determination in the future is the chronometric leveling by high-precision clocks (see e.g., Bjerhammar, 1985; Lion et al., 2017; Müller et al., 2018; Shen et al., 2019).

A physical height can be determined as orthometric height in combination with the geoid height following Stokes' theory or as normal height in combination with the quasi-geoid height following Molodensky's theory. The geoid height and the quasi-geoid height can be transformed from each other through a geoid-quasigeoid separation term. One formulation of this separation term reads

$$N - \zeta \approx \frac{\Delta g_B}{\bar{\gamma}} H_O, \tag{2.26}$$

$$\Delta g_B = g - A_B + F - \gamma \tag{2.27}$$

(Heiskanen and Moritz, 1967), where Δg_B is the simple Bouguer anomaly, $A_B = 0.1119 \cdot H_O$ mGal is the topographic mass effect, and $F \approx 0.3086 \cdot H_O$ mGal is the free-air reduction. More refined formulas for the geoid-quasigeoid separation have been derived, e.g., by Flury and Rummel (2009) and Sjöberg (2010). In this work, the quasi-geoid height is calculated directly at the Earth's surface following Molodensky's theory, and then it is transformed to the geoid height following the Eqs. (2.26) and (2.27). If the geoid is to be computed first, the gravity values should be reduced to gravity anomalies at the geoid, which includes the reduction of topographic masses. In this case, consistencies should be ensured between the gravity reductions in different regions to guarantee a globally consistent physical height system (Sánchez and Sideris, 2017).

Currently, the existing height reference frames around the world all refer to local sea levels. Ihde et al. (2017) pointed out that hundreds of national or regional physical height systems are in use, with discrepancies of more than 2 m between each other. This does not fulfill the demand of having global height systems consistent at the level of a few centimeters or better (Plag et al., 2009), for both scientific and practical reasons. Thus, it is important and necessary to establish a global physical height reference system and to integrate the regional height systems into the global one. Sánchez and Sideris (2017) showed that the height system unification is based on the comparison of the quasi-geoid height (or geoid height) obtained from the gravity field modeling and that derived from GNSS/leveling, i.e., $h - H$ (Eqs. (2.23) and (2.25)). The GNSS/leveling combination can also be used to validate the (quasi-) geoid models obtained by regional gravity field refinement, which is demonstrated in **P-II**, Sánchez et al. (2021), and Wang et al. (2021).

International Height Reference System

The Earth can be characterized by its geometry together with its geopotential. A globally unified geometric reference system was already introduced by the International Terrestrial Reference System (ITRS) and realized by the International Terrestrial Reference Frame (ITRF) (Petit and Luzum, 2010). However, an equivalent high-precision global physical reference system is still not available, and thus desired (Ihde et al., 2017). In 2015, the IHRS was introduced by the IAG as a global standard for the determination of physical heights (Drewes et al., 2016). The strategies for the definition and realization of the IHRS have been discussed in many publications, e.g., Sánchez (2012); Sánchez and Sideris (2017);

Ihde et al. (2017); and Sánchez et al. (2021).

The IHRS is defined as a geopotential reference system co-rotating with the Earth. It is realized by the establishment of the International Height Reference Frame (IHRF), by determining the coordinates of the selected stations worldwide following the definition of the IHRS. Station coordinates are determined (1) as gravity potential values $W(\boldsymbol{x})$ and their changes with time $dW(\boldsymbol{x})/dt$, defined within the Earth's gravity field and, (2) as geocentric Cartesian coordinates $\boldsymbol{x}$ and their changes with time $d\boldsymbol{x}/dt$, referring to the ITRS. For practical purposes, the geocentric position vector $\boldsymbol{x}$ can be transformed to the ellipsoidal height h, and the potential value $W(\boldsymbol{x})$ of point P should be transformed to the geopotential number C_P (see Eqs. (2.22) and (2.24)) by referring to an equipotential surface of the Earth's gravity field, i.e., the geoid, with conventional value W_0 (Ihde et al., 2017). According to the IAG Resolution No. 1 from Drewes et al. (2016), the conventional value is defined as $W_0 = 62,636,853.4\ \mathrm{m}^2/\mathrm{s}^2$, which was derived by Sánchez et al. (2016).

Sánchez et al. (2021) showed that there are three approaches for the determination of potential values as IHRF physical coordinates, namely (1) the unification of existing local height systems, (2) using high-resolution GGMs, and (3) using regional (quasi-) geoid models. The authors further stated that except for regions without or with very few surface gravity data, the IHRF coordinates should be determined by high-resolution regional gravity field modeling. The reliability of the potential estimation thus undergoes the same limitations of the precise (quasi-) geoid modeling. According to Ihde et al. (2017), the target uncertainty of $W(\boldsymbol{x})$ should be at the $10^{-2}\ \mathrm{m}^2/\mathrm{s}^2$ level, which is equivalent to ~ 1 mm for physical heights. This goal is unrealistic at the current moment due to the limitation of available resources, and Sánchez et al. (2021) stated that the possibility of reaching an accuracy at $10^{-1}\ \mathrm{m}^2/\mathrm{s}^2$ level (equivalent to ~ 1 cm in height) should be evaluated first.

To test the feasibility of reaching a 1 cm accuracy and to assess the repeatability of IHRS coordinates determination using different regional gravity field modeling methods, the "1 cm geoid experiment" (also known as the "Colorado experiment") was set up in 2017 (Sánchez et al., 2018). It was proposed by four scientific groups within the IAG, namely

- the Global Geodetic Observing System (GGOS) Joint Working Group (JWG) 0.1.2 "Strategy for the realization of the IHRS",
- the IAG JWG 2.2.2 "The 1 cm geoid experiment",
- the IAG Sub-Commission (SC) 2.2 "Methodology for geoid and physical height systems",
- the Inter-Commission Committee on Theory (ICCT) Joint Study Group (JSG) 0.15 "Regional geoid/quasi-geoid modeling – Theoretical framework for the sub-centimeter accuracy".

With high-resolution terrestrial and airborne gravity data provided by the National Geodetic Survey (NGS), fourteen institutions worldwide computed the (quasi-) geoid model and geopotential values (as IHRS coordinates) for Colorado, USA using different methodologies, within this experiment.

2.4 Regional gravity field modeling

SHs (see Sect. 2.1) are an appropriate method for global gravity field modeling. However, they are not ideal for regional cases, and the reasons are summarized, e.g., by Naeimi (2013) and Li (2018). Accordingly, different regional gravity modeling approaches have been developed during the last decades, e.g., the statistical method of Least Squares Collocation (LSC) (Krarup, 1970; Moritz, 1978), the Stokes' integral (Heiskanen and Moritz, 1967; Moritz, 1980), the method of mascons (mass concertrations, Rowlands et al., 2005; Jacob et al., 2012), and point masses (Barthelmes, 1988; Antunes et al., 2003), besides the SRBFs which are used in this work. Comparisons between the different

methods have been studied, e.g., by Tscherning (1981); Eicker (2008); and Ophaug and Gerlach (2017, 2020).

The method of LSC has been used in regional gravity field modeling for a long time, since its development by Krarup (1970). A detailed method description is given in Moritz (1978, 1980), and its application can be found in numerous studies, e.g., Pail et al. (2010); Reguzzoni and Sansò (2012); Tscherning (2013), and the references therein. Willberg et al. (2019) further developed the Residual Least Squares Collocation (RLSC) as an enhancement of LSC by applying the Remove-Compute-Restore (RCR) procedure and including the full variance-covariance information of the GGM. LSC is considered as a combination of least-squares adjustment, filtering, and prediction (Moritz, 1980). It tries to minimize the prediction error based on the knowledge of the signal covariance (Ophaug and Gerlach, 2017). The advantages of LSC are (1) it is flexible for handling and combining different types of observation data, (2) it is able to deliver error information with full covariance matrices, and (3) the measurements can be used directly without the need of grid interpolation (Denker, 2013). However, the challenges in applying the LSC are the proper computation of the covariance function (Alberts, 2009), and the high computational costs when dealing with a large number of point-wise data (Wittwer, 2009). For tackling the latter issue, Zingerle et al. (2021) made practical modifications to the original LSC and proposed a "partition-enhanced" LSC.

The Stokes' integral, also known as the Stokes' formula, is a classical method initiated by Stokes (1849), which delivers the disturbing potential T or geoid height N by an integration of gravity data in terms of gravity anomalies. The original form of the Stokes' integral has later been modified for the case of an arbitrary reference ellipsoid (Heiskanen and Moritz, 1967). For the more recent geoid determination, the Stokes' integral is usually employed in combination with SHs (Torge, 1991) in such a way that the long-wavelength features are represented by SHs, and the Stokes' integral furnishes the short-wavelength part. In this case, the modified Stokes' kernels should be used so as to minimize the resulting truncation error (Jekeli, 2015). Different modifications to the Stokes' kernel have been proposed, e.g., by Wong and Gore (1969); Sjöberg (1981, 1991, 2003); and Featherstone et al. (1998). Featherstone (2013) provided a detailed review and classification of the modifications applied to the Stokes' integral. The Stokes' integral is a widely used method with plenty of applications available, e.g., Saleh et al. (2013); Jiang and Wang (2016); McCubbine et al. (2018); Koji and Yuki (2020), among many others. However, one challenge in applying the Stokes' integral is the combination of heterogeneous data (Wu et al., 2017b), since a grid interpolation is needed in this approach, and the integral is formulated only for one data type each.

The method of SRBFs will be explained in detail in Chap. 4, as it is used in this thesis and the three publications **P-I** to **P-III**. These regional gravity field modeling methods have been applied in the "1 cm geoid experiment" by different institutions worldwide (e.g., Willberg et al., 2020; Claessens and Filmer, 2020; Wang et al., 2020), and their performances are compared and presented in the two co-author publications, i.e., Sánchez et al. (2021) and Wang et al. (2021). The (quasi-) geoid model calculated by SRBFs is also validated with the other methods in Sect. 6.1 and **P-II**.

3 Gravity data and models

This chapter introduces different gravity observation techniques, and presents the data and models that are involved in this thesis.

3.1 Satellite gravimetry

GOCE satellite mission

The GOCE mission was the first Earth Explorer mission within the framework of the Living Planet Programme of the European Space Agency (ESA) and the first gravity gradiometry satellite mission. It was launched by ESA in March 2009 and deorbited in November 2013. The primary objective of the GOCE mission was to provide gravity observations for modeling the Earth's gravity field and the geoid with high accuracy (Drinkwater et al., 2003; Johannessen et al., 2003), and more specifically

- to determine the Earth's gravity field with an accuracy of 1 mGal,
- to determine the geoid with an accuracy of 1 cm,
- to achieve both of the above goals at length scales down to 100 km, which corresponds to an SH degree and order (d/o) 200.

The core of the GOCE sensor system was a three axes gravity gradiometer with two accelerometers on each axis, which measured the difference in gravitational acceleration inside the spacecraft (Drinkwater et al., 2003). Each accelerometer was ultra sensitive along two orthogonal directions and less sensitive along the third one (Rummel et al., 2011). Gruber et al. (2014) reported that the gradient precision along the two sensitive axes was 10 mE/$\sqrt{\text{Hz}}$. The measured signal corresponds to the second derivatives of the gravitational potential V, i.e., the gravity gradient (Eicker et al., 2006). The gradiometer components V_{xx}, V_{yy}, V_{zz}, and V_{xz} have been derived with high precision, whereas the components V_{xy} and V_{yz} have much lower precision (Bouman et al., 2011; Fuchs and Bouman, 2011).

GOCE data products are provided in different level categories, depending on the processing status. Level 0 data are the raw observations. For Level 1a, the instrument time series with the calibration data are attached; after calibration and correction, Level 1b products are generated. Level 2 products are precise orbits, gravity gradients and GOCE gravity field models. The processing details for obtaining the Level 2 products can be found, e.g., in Gruber et al. (2007, 2014).

GRACE satellite mission

The GRACE mission was jointly implemented by the National Aeronautics and Space Administration (NASA) and the German Aerospace Center (DLR); it was launched in March 2002 and operated till October 2017. On 22 May 2018, its successor GRACE-FO was successfully launched as the continuation of the mission. The objectives of GRACE were to track changes in the Earth's gravity field and to map the global gravity field with a spatial resolution of 400 km and a temporal resolution of 30 days (Tapley et al., 2004). The GRACE mission consists of two satellites in the same orbit, with an inter-satellite distance of around 220 km, at an initial altitude of 500 km and an inclination of 89°. The measurements of GRACE include:

- the precise distance between the twin satellites, which reflects the changing gravity field of the Earth, obtained by a K-band microwave ranging system,
- the non-gravitational accelerations from high precision accelerometers,
- the position of the satellite using the onboard Global Positioning System (GPS) receiver (Tapley et al., 2005).

GRACE data are also provided from Level 0 (raw data) to Level 2 products, which include the satellite orbits as well as the estimated SH coefficients for the gravity field models (Dahle et al., 2013).

CHAMP satellite mission

The German satellite CHAMP was launched in July 2000; the mission generated gravity and magnetic field measurements simultaneously for 10 years and ended in September 2010. The CHAMP mission was operated in an almost circular and near-polar orbit with an inclination of 87.3°, which enables a homogeneous and complete global coverage of the Earth's sphere. The satellite was equipped with a GPS flight receiver and a three-axis accelerometer, which allow a Precise Orbit Determination (POD) as well as the separation of gravitational and non-gravitational accelerations to resolve the gravity field parameters (Reigber et al., 2002a).

CHAMP data products are categorized from Level 0 (raw data) to Level 4, which are the precise satellite orbits and global gravity models represented by the adjusted SH coefficients (Reigber et al., 2002b).

In **P-I** and **P-III** (simulated data case), satellite data are simulated from the GGMs in terms of the disturbing potential difference $\Delta T = T^A - T^B$ between the two satellites A and B for GRACE and the second-order derivative T_{rr} of the disturbing potential (see Sect. 2.2) for GOCE. In **P-II** and **P-III** (real data case), the satellite data are involved directly by the GGMs being subtracted within the RCR procedure.

3.2 Satellite altimetry

Satellite altimetry missions are initially not developed for gravity field modeling; however, gravity values such as the geoid height and the deflection of the vertical can be converted from the altimetry measurements and used as gravity observations. The derivation of different gravity functionals (including the gravity anomaly, vertical gravity gradient, deflection of the vertical, etc.) from altimetry data is discussed and applied, e.g., by Sandwell and Smith (1997); Hwang and Hsu (2008); and Sandwell et al. (2014). In this work, the altimetry observations are used in terms of geoid height.

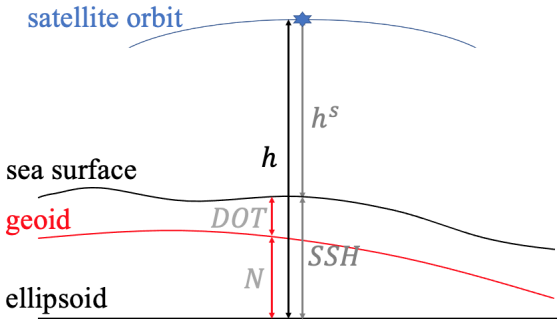


Figure 3.1: Quantities related to satellite altimetry

The direct observable of satellite altimetry is the traveling time for a radar signal to reach the sea surface and back using a pulse-limited radar. Thus, the distance h^s from the satellite to the sea surface is obtained. Meanwhile, the distance h from the satellite to the ellipsoid is given from POD (Sandwell and Smith, 1997). As shown in Fig. 3.1, the Sea Surface Height (SSH) can be calculated as the difference between the two distances h and h^s. The sea surface differs from the geoid due to different hydrodynamic processes, and their difference is

denoted as the Dynamic Ocean Topography (DOT). DGFI-TUM provides instantaneous DOT values through the Open Altimeter Database (OpenADB, https://openadb.dgfi.tum.de/en/), which are derived using a "profile approach" with cross-calibration between different missions (Bosch et al., 2014). The geoid height N is then obtained as

$$N = h - h^s - DOT. \tag{3.1}$$

Numerous satellite altimetry missions have been launched in the last four decades, and a list of past, active, and potential future missions is shown in Fig. 3.2. Detailed information about these missions can be found at the OpenADB. The precision of the derived SSH is listed in Vermeer (2020); it varies between different altimetry missions and averages around 3 cm. In **P-III**, geoid heights derived from the satellite altimetry mission ERS-1, Jason-1, Envisat, and Cryosat-2 are used as major offshore observations for regional gravity field modeling.

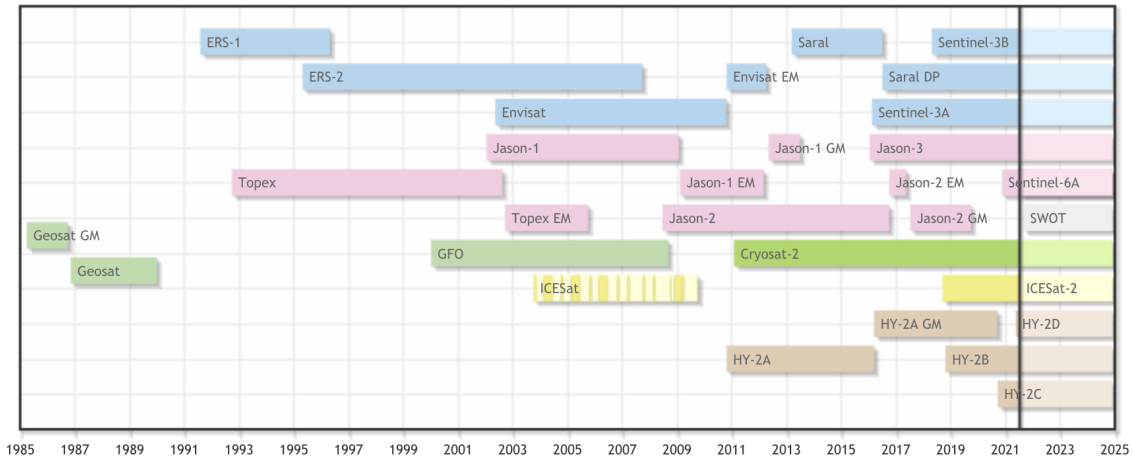


Figure 3.2: List of past, active, and potential future satellite altimetry missions[2]

3.3 Regional gravity measurements

As mentioned in Chap. 1, the main limitation of satellite data is their spatial resolution, which is around 100 km. Gravity measurements from terrestrial, airborne, and shipborne gravimetry deliver a much higher resolution of a few kilometers, and thus, are the major data contributors for regional gravity field refinement. Therefore, they are categorized here as regional gravity measurements. However, it is worth clarifying that terrestrial, airborne, and shipborne data can be used not only for regional gravity modeling but also for global gravity field modeling. Although the costs for collecting these data are generally much lower than for satellite missions, their availability and distribution vary between different regions. Hence, it is of great importance to develop approaches to optimally combine the heterogeneous regional observations in addition to global satellite data.

Terrestrial gravimetry

Terrestrial gravimetry measures the gravity field on the Earth's surface and can be divided into two types, absolute gravimetry and relative gravimetry. Absolute gravimetry delivers the magnitude of the gravity vector g directly at specific stations, while relative gravimetry measures the gravity difference with respect to the absolute stations. The measuring principle and related instruments of

[2]Image source: `https://openadb.dgfi.tum.de/en/missions/`

both types of gravimetry are explained, e.g., by Torge (1991) and Vermeer (2020). Absolute gravimetry can achieve an instrument uncertainty of 1 μGal (Niebauer et al., 1995), but it is expansive. Relative gravimeters are the standard instruments for rapid field measurements, and their measurement precision can reach 10μGal (Timmen, 2010). The most accurate and stable relative gravimeters, namely the superconducting gravimeters, are able to achieve a sensitivity of 1 μGal (Virtanen, 2006).

Airborne and shipborne gravimetry

Airborne gravimetry is conducted by the highly sensitive accelerometers on board an aircraft, following the principle of relative gravimetry. The details about its measuring principles can be found in Forsberg and Olesen (2010) and Vermeer (2020). Airborne gravimetry became a major tool for gravity field modeling in the 1990s, thanks to the development and availability of carrier-phase kinematic GPS, which measures the acceleration of the aircraft (Alberts, 2009). Removing it from the acceleration captured by the accelerometer, only gravity and system errors remain. Airborne gravimetry is important for geodesy, since it is able to collect data over areas that are difficult for other observation techniques to access, e.g., in polar, mountainous, and coastal regions. It is able to provide data with high spectral resolution over large scales, with relatively low costs. Nowadays, the airborne gravity measurements are at an accuracy level of 1-2 mGal (Forsberg and Olesen, 2010).

Like airborne gravimetry, shipborne gravimetry is conducted by gravimeters on board a ship, and it also follows the measuring principle of relative gravimetry. It is a major method for measuring the Earth's gravity field in coastal and offshore areas. Lu et al. (2019) reported that a measurement accuracy of sub-mGal can already be achieved by shipborne gravimetry.

Regional gravity data

As an example, the regional gravity data used in this work for the "1 cm geoid experiment" are visualized in Fig. 3.3a. The estimation model is then set up according to the resolution and quality of the data, and the corresponding modeling results are validated by the GNSS/leveling data at the GSVS17 benchmarks (red line in Fig. 3.3a) and presented in Sect. 6.1.

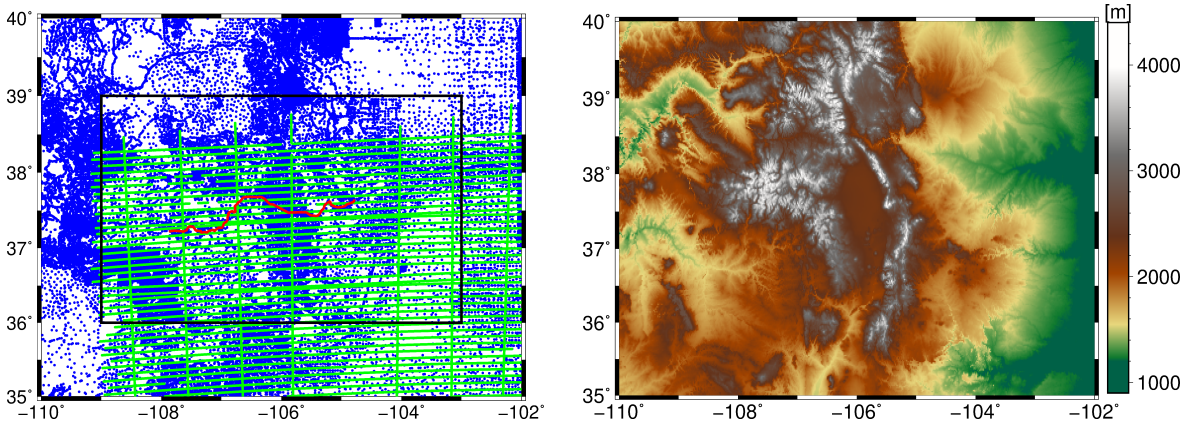


Figure 3.3: (a) terrestrial (blue dots) and airborne (green flight tracks) gravity measurements in Colorado, as well as GNSS/leveling data at the GSVS17 benchmarks (red line) for validation; (b) terrain map of the study area

Two types of observations are provided by the NGS in terms of gravity values g. The terrestrial gravity data (blue dots in Fig. 3.3a) were collected by different organizations during a large time span (since the late 1930s). Thus, their exact accuracy is unknown. However, Saleh et al. (2013) estimated that the NGS's surface gravity database generally contains high-frequency errors with a Root Mean Square

(RMS) of around 2.2 mGal, and the error is larger in mountainous areas such as the Rocky Mountains and the Appalachians. The terrestrial measurements have full coverage over the whole study area, with a total amount of 59,303 points, given with orthometric height H_O. Although they are not evenly distributed, the average point distance reaches approximately 3 km for the whole terrestrial data set.

The airborne gravity data (green flight tracks) were collected by the "Gravity for the Redefinition of the American Vertical Datum" (GRAV-D) project (GRAV-D Team, 2017) in recent years, and resampled to a 1 Hz observation frequency. The data consist of 56 flight lines, with a mean flight altitude of 6,186 m. They cover most of the study area in the southeastern part, generally between -109° and -102° longitude and between 35° and 38.5° latitude. The total number of airborne measurements amounts to 283,716 points, given with ellipsoidal height h. The along-track spatial resolution depends on the aircraft speed, with an average of around 100 m; the cross-track resolution is almost 10 km. A crossover error analysis has been done by the GRAV-D Team (2018), which suggests an RMS error of 2.32 mGal in the GRAV-D data for this region.

The following preprocessing steps are performed to the original terrestrial and airborne data before they are used for computation:

1. For the terrestrial data, duplicate values are removed. To be more specific, in case of several gravity observations located at the same position, only the first of these observations is kept. However, if the observations at the same position differ more than 2 mGal from each other, all of them are deleted. This step results in a deletion of 1,175 points.
2. Downsampling of the airborne data from 1 Hz to 1/8 Hz to save computation time, as the consecutive airborne observations are highly correlated (see **P-II** for more detail). Low-pass filtering is also required in the preprocessing for the airborne data (see e.g., Olesen et al., 2002; GRAV-D Team, 2018), and different low-pass filters have been applied by the participating groups in the "1 cm geoid experiment". However, in SRBFs, the low-pass filtering can be directly implemented in the computation by applying an SRBF with smoothing features (see Sect. 4.4).
3. Transformation of the orthometric heights H_O in the terrestrial data to the ellipsoidal heights h using a geoid model provided by the NGS following Eq. (2.23).
4. Transformation of both the terrestrial and airborne observations in terms of absolute gravity values g to gravity disturbance δg by subtracting the normal gravity γ following Eq. (2.16).
5. The normal gravity subtracted in the previous step contains the gravitation of the atmospheric mass, i.e., it considers the mass of the Earth's atmosphere on the ellipsoidal surface. However, gravity observations on or close to the Earth's surface are not affected by the atmospheric mass. Thus, the atmospheric correction (see Torge, 1989) is added to these two types of observations, which is calculated as

$$\delta g_{\mathrm{ATM}} = 0.874 - 9.9 \cdot 10^{-5} h + 3.56 \cdot 10^{-9} h^2. \tag{3.2}$$

3.4 Global gravity models

In this thesis, the global gravity field modeled by SHs serves as background model for regional gravity field refinement, using the RCR procedure (e.g., Forsberg and Tscherning, 1981; Forsberg, 1993). To be more specific, the long-wavelength component derived from a GGM is removed from the gravity measurements before computation, the remaining part is then modeled using regional gravity field modeling methods, and afterwards, this removed part is restored to the final gravity model. Existing global models approximate the long-wavelength component of the gravity field very accurately. Furthermore, it also solves the problem that regional gravimetry cannot estimate the long-wavelength parts (Lieb et al., 2016). Numerous GGMs are provided by the International Centre

for Global Earth Models (ICGEM) and available through http://icgem.gfz-potsdam.de/; the ones that are involved in this work are introduced in this section.

EGM2008

The Earth Gravitational Model 2008 (EGM2008) was developed and evaluated by Pavlis et al. (2012), and it is the first high-resolution GGM with SH expansion up to degree 2190 (calculated in terms of ellipsoidal harmonic coefficients up to degree 2159, and converted to the SH representation with degree 2190). This global model was developed by a combination of

- the GGM ITG-GRACE03S (Mayer-Gürr et al., 2010), which was developed using GRACE data up to d/o 180, along with its associated error covariance matrix,
- a global $5' \times 5'$ gravity anomaly grid formed by merging terrestrial, altimetry-derived, and airborne gravity data,
- gravitational information obtained from a detailed global topographic database over areas where only lower resolution gravity data were available.

Pavlis et al. (2012) further showed that over areas covered with high quality gravity data, the accuracy of the geoid heights calculated by EGM2008 is similar (or even better) compared to those obtained from corresponding regional geoid models w.r.t. independent GNSS/leveling data.

EIGEN-6C4

The EIGEN-6C4 (Förste et al., 2014) is a high-resolution global gravity model (up to degree 2190) of the European Improved Gravity model of the Earth by New techniques (EIGEN) series. It was calculated by a band-pass combination of normal equations from different types of data, namely Satellite Laser Ranging (SLR) data up to degree 30, GRACE data up to degree 175, GOCE data up to degree 300, and a $2' \times 2'$ global gravity anomaly grid of the Technical University of Denmark (DTU), which is obtained by altimetry over the oceans and EGM2008 over the continent (Andersen, 2010).

XGM2016 and XGM2019e

The eXperimental Gravity field Model 2016 (XGM2016) was derived by Pail et al. (2018) up to degree 719, as a successor of the model GOCO05c (Fecher et al., 2017). The main difference is that XGM2016 includes an improved terrestrial data set of $15' \times 15'$ gravity anomaly provided by the National Geospatial-Intelligence Agency (NGA), which improves the model especially in continental areas such as South America, Africa, parts of Asia, and Antarctica. In near-coastal regions, the model performance is also improved by a combination strategy of relative regional weighting.

The eXperimental Gravity field Model 2019 extended with topographic information (XGM2019e) (Zingerle et al., 2020) is the successor of XGM2016, with a highest degree of 5540. The same terrestrial data set as in XGM2016 is used up to degree 719. Beyond d/o 719, the topography-derived gravity information is taken from the Earth2014 spherical harmonic model (Rexer et al., 2016). Over the oceans, the DTU13 (Andersen et al., 2013) altimetry-derived gravity anomalies with a resolution of $1' \times 1'$ are used.

GECO

The GOCE and EGM2008 Combined model (GECO) (up to degree 2190, Gilardoni et al., 2016) merges gravity information derived from a GOCE satellite-only global model, namely GOCE-TIM-RL05 (up to d/o 280, Brockmann et al., 2014), with EGM2008. Gilardoni et al. (2016) pointed out that such a combination could improve the model accuracy in the low to medium frequencies in comparison to EGM2008, especially in areas where ground data were not available for the EGM2008 computation, such as Africa, South America and Antarctica.

As mentioned in Sect. 2.3, using high-resolution GGMs is also one way to determine the IHRF physical coordinates (Sánchez et al., 2021). However, how precise are the modeling results from the

high-resolution GGMs, and can they replace the regional (quasi-) geoid models? These questions are answered in Sect. 6.1, where the performance of here-listed GGMs is compared with the regional gravity model in the "1 cm geoid experiment".

3.5 Topography models

The consideration of topographic effects is important for high-resolution regional gravity field modeling, especially in mountainous areas (e.g., the Colorado study area shown in Fig. 3.3b), as the very short wavelengths are correlated with local topography to a large extent (Bucha et al., 2016). The following two topography models are used in this thesis to represent the high-frequency topographic effect.

dV_ELL_Earth2014

The topographic gravity field model dV_ELL_Earth2014 (Rexer et al., 2016) was developed by spectral forward modeling with volumetric mass layers using data from the Earth2014 topography model (Hirt and Rexer, 2015). Earth2014 is a set of global topography, bathymetry, and ice-sheet grids. It combines up-to-date digital elevation data with multi-source gridded surface data in terms of mean sea level heights, and delivers a high resolution of $1' \times 1'$. Rexer et al. (2016) established a layer concept, and derived the topography models relying on mass layer modeling based on two different levels of approximation, namely spherical and ellipsoidal. Rexer et al. (2016) pointed out that the ellipsoidal one should be used for applications requiring ultra-high-resolution or high accuracy, and thus, it is used in this study. dV_ELL_Earth2014 was initially calculated with a highest degree of 2190, and later extended to degree 5480 (Rexer et al., 2017); it is available through http://ddfe.curtin.edu.au/models/Earth2014/.

ERTM2160

The ERTM2160 (Earth Residual Terrain Modeled-gravity field with the spatial scales equivalent to spherical-harmonic coefficients up to degree 2160 removed, Hirt et al., 2014) was developed for the approximation of the short-scale gravity field, from degree 2160 to a degree of around 80,000 (equivalent to a spatial resolution of 250 m). It was calculated by high-resolution gravity forward modeling using the Shuttle Radar Topography Mission (SRTM) global topography model. ERTM2160 is the first model to represent the short scale gravity field characteristics at a near-global scale with ultra-high resolution (Hirt et al., 2014). It is provided as globally distributed $0.002^\circ \times 0.002^\circ$ grid points within $\pm 60^\circ$ latitude in terms of gravity disturbance, (quasi-) geoid height, and deflection of the vertical, and is accessible via http://ddfe.curtin.edu.au/models/ERTM2160/. Thus, interpolation is usually required when using ERTM2160 in regional gravity field modeling.

The influence of the topographic effect and the importance of including the topography models are demonstrated in **P-II**. In study areas with high elevation (e.g., Fig. 3.3b), the gravity field becomes much smoother after subtracting the topographic effect computed from these two topography models (see Fig. 3.4). The terrestrial and airborne observations (Fig. 3.3a) are smoothed by 69% and 61%, respectively, in terms of Standard Deviation (STD), after including the topography models. Such a significant smoothing effect enables a better least-squares fit in the parameter estimation (see Sect. 5.2), and thus, a better modeling result.

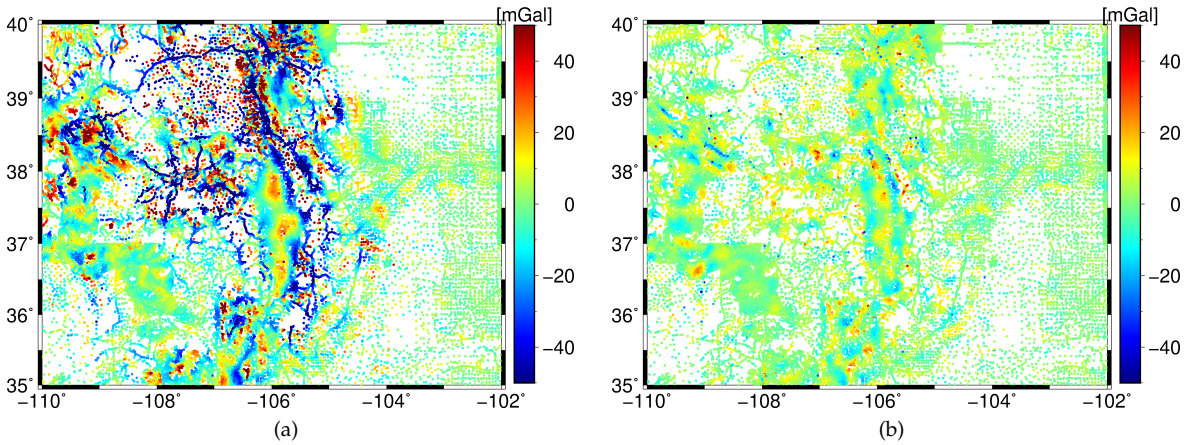


Figure 3.4: Terrestrial gravity observations (a) before and (b) after the topographic effect reduction (long-wavelength part from the GGM has already been removed)

4 Methodology

This chapter explains the methodology of SRBFs, as well as the principle of the MRR and the pyramid algorithm.

4.1 Spherical radial basis functions

The methodology of SRBFs is the base of this thesis, and it has been described and applied in all the three papers, **P-I**, **P-II**, and **P-III**. For completeness, this section reformats the related parts of the papers and explains the foundations of the method. SRBFs are an appropriate tool for regional gravity field modeling to consider the heterogeneity of different data sources, due to their localizing features. SRBFs are a good compromise between optimal spectral localization (SHs) and optimal spatial localization (Dirac delta function, Freeden et al., 1998).

In general, a spherical basis function $B(\boldsymbol{x}, \boldsymbol{x}_k)$ related to a point P_k with position vector $\boldsymbol{x}_k = R \cdot \boldsymbol{r}_k$ on a sphere Ω_R with radius R and an observation point P with position vector $\boldsymbol{x} = r \cdot \boldsymbol{r} = r \cdot [\cos\varphi\cos\lambda, \cos\varphi\sin\lambda, \sin\varphi]^T$ can be expressed by

$$B(\boldsymbol{x}, \boldsymbol{x}_k) = \sum_{n=0}^{\infty} \frac{2n+1}{4\pi R^2} \left(\frac{R}{r}\right)^{n+1} B_n P_n(\boldsymbol{r}^T \boldsymbol{r}_k) \tag{4.1}$$

(Schmidt et al., 2007). P_n is the Legendre polynomial (2.12) of degree n, and B_n is a Legendre coefficients which specifies the shape of the SRBF. When $B_n = 1$ for all n, $B(\boldsymbol{x}, \boldsymbol{x}_k)$ represents the Dirac delta function.

A harmonic funtion $F(\boldsymbol{x})$ given on the sphere Ω_R or in the exterior space of Ω_R, can be described as a series expansion in terms of the SRBFs (4.1)

$$F(\boldsymbol{x}) = \sum_{k=1}^{K} d_k B(\boldsymbol{x}, \boldsymbol{x}_k), \tag{4.2}$$

where K is the number of basis functions. For describing different gravity functionals listed in Sect. 2.2, e.g., the gravity disturbance δg or the gravity anomaly Δg, obtained from different observation techniques (see Chap. 3), the general expression of SRBFs (4.1) needs to be adapted. The adapted basis functions are listed in Table 1 of **P-I**, and a more complete version is presented here in Table 4.1 (Koop, 1993).

Spherical convolution

The content of this part is taken and adjusted from the Sect. 3.2 of **P-II**. SRBFs (4.1) can act as high-pass, low-pass or band-pass filter (Schmidt et al., 2007), and a harmonic function $F(\boldsymbol{x})$ can be filtered by it through a spherical convolution. The filtered function $F'(\boldsymbol{x})$ can be represented by

$$F'(\boldsymbol{x}) = (B * F)(\boldsymbol{x}) = \int_{\Omega_R} B(\boldsymbol{x}, \boldsymbol{x}_k) F(\boldsymbol{x}_k) d\Omega_R. \tag{4.3}$$

Table 4.1: The adapted basis functions for different gravity functionals obtained from various observation techniques

gravity functionals	units	adapted basis function $B(x, x_k)$
Disturbing potential T or gravitational potential V	m^2/s^2	$B(\boldsymbol{x},\boldsymbol{x}_k) = \sum_{n=0}^{\infty} \frac{2n+1}{4\pi R^2} \left(\frac{R}{r}\right)^{n+1} B_n P_n(\boldsymbol{r}^T\boldsymbol{r}_k)$
Gravitational potential difference (GRACE)	m^2/s^2	$B(\boldsymbol{x}^A,\boldsymbol{x}^B,\boldsymbol{x}_k) = \sum_{n=0}^{\infty} \frac{2n+1}{4\pi R^2} B_n \{ \left(\frac{R}{r^A}\right)^{n+1} P_n(\boldsymbol{r}^{A^T}\boldsymbol{r}_k) - \left(\frac{R}{r^B}\right)^{n+1} P_n(\boldsymbol{r}^{B^T}\boldsymbol{r}_k) \}$
Gravity disturbance δg (terrestrial, airborne, shipborne)	mGal	$B_r(\boldsymbol{x},\boldsymbol{x}_k) = \sum_{n=0}^{\infty} \frac{2n+1}{4\pi R^2} \frac{(n+1)}{r} \left(\frac{R}{r}\right)^{n+1} B_n P_n(\boldsymbol{r}^T\boldsymbol{r}_k)$
Gravity anomaly Δg (terrestrial, airborne, shipborne)	mGal	$B_r(\boldsymbol{x},\boldsymbol{x}_k) = \sum_{n=0}^{\infty} \frac{2n+1}{4\pi R^2} \frac{(n-1)}{r} \left(\frac{R}{r}\right)^{n+1} B_n P_n(\boldsymbol{r}^T\boldsymbol{r}_k)$
Gravity gradients T_{rr} or V_{rr} (GOCE)	E ($1E = 10^{-9}\ s^{-2}$)	$B_{rr}(\boldsymbol{x},\boldsymbol{x}_k) = \sum_{n=0}^{\infty} \frac{2n+1}{4\pi R^2} \frac{(n+1)(n+2)}{r^2} \left(\frac{R}{r}\right)^{n+1} B_n P_n(\boldsymbol{r}^T\boldsymbol{r}_k)$

In case of using a band-limited SRBF, which means setting the Legendre coefficient $B_n = 0$ for $n > n_{max}$, the SRBF acts as a low-pass or band-pass filter. Furthermore, the band-limited SRBF is defined as the reproducing kernel $K_{rep}(\boldsymbol{x},\boldsymbol{x}_k)$, in case of $B_n = 1$ for all degree values $n = 0, 1, \ldots, n_{max}$, i.e.,

$$K_{rep}(\boldsymbol{x},\boldsymbol{x}_k) = \sum_{n=0}^{n_{max}} \frac{2n+1}{4\pi R^2} \left(\frac{R}{r}\right)^{n+1} P_n(\boldsymbol{r}^T\boldsymbol{r}_k), \tag{4.4}$$

and it fulfills the condition that the spherical convolution of a harmonic function $F(\boldsymbol{x})$, which is band-limited with $n = 0, 1, \ldots, n' \leq n_{max}$, with $K_{rep}(\boldsymbol{x},\boldsymbol{x}_k)$ is equal to the original function

$$F(\boldsymbol{x}) = (K_{rep} * F)(\boldsymbol{x}) = \sum_{k=1}^{K} d_k K_{rep}(\boldsymbol{x},\boldsymbol{x}_k). \tag{4.5}$$

The band-limited basis functions $B(\boldsymbol{x},\boldsymbol{x}_k)$ span the Hilbert space $H_{0,1,\ldots,n_{max}}(\Omega_R)$ with finite dimension $\overline{n} = (n_{max}+1)^2$. The points P_k on the sphere Ω_R need to guarantee an admissible point system (Freeden et al., 1998)

$$S_K = \{\boldsymbol{x}_k \in \Omega_R \mid k = 1, 2, \ldots, K\}, \tag{4.6}$$

so that the series coefficients d_k can be estimated, i.e., the $K \times \overline{n}$ matrix containing the outer spherical harmonics possesses full column rank (see Schmidt et al., 2007 for more details). The point system S_K from Eq. (4.6) is admissible for $K \geq \overline{n} = (n_{max}+1)^2$, and it is called fundamental if the equality $K = (n_{max}+1)^2$ holds.

Theorem (cf. **P-II**): In a Hilbert space $H_{0,1,\ldots,n_{max}}(\Omega_R)$, let $B(\boldsymbol{x},\boldsymbol{x}_k)$, Eq. (4.1), be a band-limited SRBF with

$$B_n = \begin{cases} \neq 0 & \text{for } n = 0, 1, \ldots, n_{max} \\ = 0 & \text{for } n > n_{max} \end{cases}, \tag{4.7}$$

the filtered function $F_1(\boldsymbol{x})$ of the band-limited function $F(\boldsymbol{x})$ by the spherical convolution reads

$$F_1(\boldsymbol{x}) = (B * F)(\boldsymbol{x}) = \sum_{k=1}^{K} d_k B(\boldsymbol{x},\boldsymbol{x}_k). \tag{4.8}$$

If $C(\boldsymbol{x},\boldsymbol{x}_k) = \sum_{n=0}^{\infty} \frac{2n+1}{4\pi R^2} (\frac{R}{r})^{n+1} C_n P_n(\boldsymbol{r}^T\boldsymbol{r}_k)$ has the same upper band limitation with

$$C_n = 0 \quad \text{for} \quad n > n_{max} \tag{4.9}$$

then

$$F_2(\boldsymbol{x}) = (C * F)(\boldsymbol{x}) = \sum_{k=1}^{K} d_k C(\boldsymbol{x}, \boldsymbol{x}_k) \tag{4.10}$$

holds by using the same coefficients d_k as in Eq. (4.8). This theorem, which was proven by Freeden et al. (1998) and Schreiner (1999), shows that the coefficients d_k can be used to calculate different convolutions of a band-limited signal $F(\boldsymbol{x})$. Thus, it is possible to use different types of SRBFs for different data sets and to use different SRBFs in the analysis step (in which the unknown coefficients are estimated) and in the synthesis step (in which the estimated coefficients are used to calculate the output gravity functionals), respectively. Usually the reproducing kernel $K_{rep}(\boldsymbol{x}, \boldsymbol{x}_k)$ from Eq. (4.4) is used in the analysis step to avoid loss of spectral information, and any types of SRBFs (see Sect. 4.4) can be used in the synthesis, according to this theorem.

4.2 Multi-resolution representation

The publications **P-I** and **P-II** apply a conventional single-level approach to combine different types of observations, which is commonly implemented in current literature based on SRBFs (e.g., Bentel et al., 2013a; Lieb et al., 2016; Bucha et al., 2016; Wu et al., 2017a). In this case, all the data sets are combined at the maximum degree n_{max} of the expansion. However, as explained in Chap. 3, gravity data obtained from various observation techniques are not only heterogeneously distributed, but also characterized by different spectral sensitivities. To take into account the spectral resolution, a spectral combination based on SRBFs can be set up through the MRR (Freeden et al., 1998; Haagmans et al., 2002). The realization of the MRR has been investigated in many studies during the last decades, e.g., Beylkin and Cramer (2002); Panet et al. (2011); and Bolkas et al. (2016). The MRR approach suggested by Schmidt et al. (2005, 2006, 2007) is realized in **P-III**, where the gravity signal is decomposed into an expansion in terms of SHs for the long-wavelength part, and a number of frequency-dependent detail signals in terms of spherical wavelet functions (see Sect. 4.4) for the medium and high frequency parts.

This section outlines parts of **P-III**, while more details can be found there. To set up the MRR, the frequency domain should be discretized into different resolution levels, as shown in Fig. 4.1 (corresponds to Fig. 2 in **P-III**). Each resolution level defines a frequency band, and thus, includes a certain number of spectral degree values. In this study, the upper boundary (maximum degree value) n_i of each level is defined as

$$n_i = 2^i - 1. \tag{4.11}$$

Correspondingly, the maximum spatial resolution of level i reads $\rho_i = \pi R / n_i$, with R being the Earth's radius in km (Lieb et al., 2016). Different observation techniques can then be classified according to their spectral resolution.

The MRR of the gravity functional $F(\boldsymbol{x})$, which is band-limited to $n_I = 2^I - 1$, can be expressed as

$$F(\boldsymbol{x}) = \overline{F}(\boldsymbol{x}) + \sum_{i=i'}^{I} G_i(\boldsymbol{x}) \tag{4.12}$$

where $\overline{F}(\boldsymbol{x})$ is the smoothed version, i.e., usually the long-wavelength component evaluated by a GGM (Schmidt et al., 2006), and it is used as the background model within the RCR procedure. i' and I are the lowest and highest level of the MRR respectively, and $G_i(\boldsymbol{x})$ is the detail signal of resolution level i,

$$G_i(\boldsymbol{x}) = (\Psi_i * F)(\boldsymbol{x}) = \sum_{k=1}^{K_i} d_{k,i} \Psi_i(\boldsymbol{x}, \boldsymbol{x}_{k,i}) \tag{4.13}$$

where $\Psi_i(\boldsymbol{x}, \boldsymbol{x}_{k,i})$ is a spherical wavelet function (see Sect. 4.4), which acts as a band-pass filter. K_i and

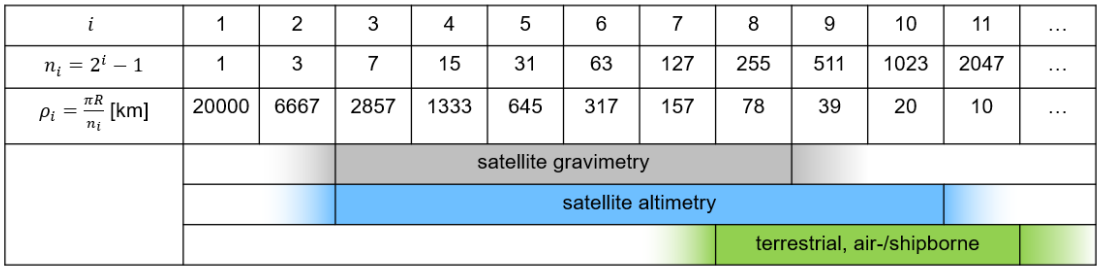


Figure 4.1: The discretization of the frequency domain, and the corresponding spectral degree value n_i as well as the approximate spatial resolution ρ_i of each level i, adapted from Lieb et al. (2016)

$d_{k,i}$ are the number of basis functions and the corresponding series coefficients of level i, respectively. Again, the system of grid points $P_{k,i}$ is required to guarantee an admissible point system of level i

$$S_{K_i} = \{\boldsymbol{x}_{k,i} \in \Omega_R \mid k = 1, 2, \ldots, K_i\} \tag{4.14}$$

with $K_i \geq (n_i + 1)^2 = 2^{i+1}$.

4.3 Pyramid algorithm

In existing publications applying this MRR approach, the coefficients are generally estimated at each level independently, using all or selected groups of observations (e.g., Lieb, 2017; Wu et al., 2018). However, a compromise is required in this case to balance the spectral range and the spatial distribution of the observations and to avoid the multiple use of the observation groups at different levels (Lieb, 2017). To be more specific, if all observation types are used at each level, the corresponding detail signals are strongly correlated. If only specific data sets are used, large data gaps may occur, and the prior information is insufficient for filling these data gaps at higher resolution levels. This leads to large erroneous effects in the output signals. Instead, a pyramid algorithm (Freeden et al., 1998) can be applied to consider all available information by connecting the different levels. Furthermore, Klees et al. (2018) applied a two-scale approach and suggested that it should be applied in combination with a sequential estimation of the scale-dependent coefficients. The pyramid algorithm is implemented in this work to connect the resolution levels and to estimate the coefficients sequentially. However, as pointed out by Lieb (2017), there are still challenges when applying the pyramid algorithm in the regional case: (1) it is difficult to set up a proper low-pass filter matrix in the regional case, and (2) the margin size has to be adapted appropriately at each level to minimize edge effects. In **P-III**, these issues are addressed, and the pyramid algorithm based on sequential parameter estimation is successfully implemented, for the first time. The setting up of the low-pass filter is discussed in this section, while the proposed strategies for adapting the extension of the data zone at each level will be explained in Sect. 5.1.

The pyramid algorithm starts with the calculation of the coefficient vector $\boldsymbol{d}_I = [d_{1,I}, d_{2,I}, \ldots, d_{K_I,I}]^T$ of the highest resolution level through the parameter estimation, which will be explained in Sect. 5.2. The coefficients of the lower resolution levels can then be determined from the coefficients of the highest level, by a low-pass filtering. With the pyramid algorithm, the coefficient vector at level i $(i = i', i'+1, \ldots, I-2, I-1)$ can be expressed as

$$\boldsymbol{d}_{i|i+1} = \boldsymbol{L}_i \boldsymbol{d}_{i+1} \tag{4.15}$$

$$\boldsymbol{\Sigma}_{d_{i|i+1}} = \boldsymbol{L}_i \boldsymbol{\Sigma}_{d_{i+1}} \boldsymbol{L}_i^T \tag{4.16}$$

where $\boldsymbol{L}_i$ is a $K_i \times K_{i+1}$ low-pass filter matrix, transforming the $K_{i+1} \times 1$ coefficient vector $\boldsymbol{d}_{i+1}$ of the higher level $i+1$ to the $K_i \times 1$ coefficient vector $\boldsymbol{d}_{i|i+1}$ of the lower level i. $\boldsymbol{\Sigma}_{d_{i|i+1}}$ is the covariance matrix of $\boldsymbol{d}_{i|i+1}$ obtained from the covariance matrix $\boldsymbol{\Sigma}_{d_{i+1}}$ following the law of error propagation.

According to Schreiner (1999) and Schmidt et al. (2007), the low-pass filter matrix $\boldsymbol{L}_i$ can be decomposed as

$$\boldsymbol{L}_i = \boldsymbol{W}_i \boldsymbol{H}_i, \tag{4.17}$$

where $\boldsymbol{H}_i$ is a $K_i \times K_{i+1}$ matrix containing the reproducing kernel $K_{rep}(\boldsymbol{x}_{k,i}, \boldsymbol{x}_{k,i+1})$ from Eq. (4.4) between the grid points $P_{k,i+1}$ $(k = 1, 2, ..., K_{i+1})$ of level $i+1$ and the grid points $P_{k,i}$ $(k = 1, 2, ..., K_i)$ of level i. Note that the grid points $P_{k,i+1}$ and $P_{k,i}$ guarantee admissible point systems $S_{K_{i+1}}$ of level $i+1$ and S_{K_i} of level i (4.14), respectively. $\boldsymbol{W}_i = \mathrm{diag}(w_{1,i}, w_{2,i}, \ldots, w_{K_i,i})$ is the $K_i \times K_i$ diagonal matrix of the integration weights $w_{k,i}$ associated with the grid points $P_{k,i}$ of level i, and it depends on the type of implemented grid.

The derivation of the low-pass filter matrix $\boldsymbol{L}_i$ is presented in the following. The band-limited function $F_i(\boldsymbol{x})$ in the Hilbert space $H_{0,1,\ldots,n_{max}}(\Omega_R)$ can be represented by the reproducing kernel as

$$F_i(\boldsymbol{x}) = \sum_{k=1}^{K_i} d_{k,i} K_{rep}(\boldsymbol{x}, \boldsymbol{x}_{k,i}) \tag{4.18}$$

according to Eq. (4.5).

On the other hand, the numerical integration of $F_i(\boldsymbol{x})$ can be expressed as

$$F_i(\boldsymbol{x}) = (K_{rep} * F_i)(\boldsymbol{x}) = \sum_{k=1}^{K_i} w_{k,i} F_i(\boldsymbol{x}_{k,i}) K_{rep}(\boldsymbol{x}, \boldsymbol{x}_{k,i}). \tag{4.19}$$

Comparing Eq. (4.18) with Eq. (4.19), we obtain

$$d_{k,i} = w_{k,i} F_i(\boldsymbol{x}_{k,i}). \tag{4.20}$$

As the grid points $P_{k,i+1}$ fulfill an admissible point system $S_{K_{i+1}}$ of level $i+1$ with $K_{i+1} \geq (n_{i+1}+1)^2 = 2^{i+2}$, it further fulfills an admissible point system S_{K_i} at level i with $K_{i+1} > (n_i+1)^2 = 2^{i+1}$. Replacing the admissible point system S_{K_i} in Eq. (4.18) by the admissible point system $S_{K_{i+1}}$, it can be rewritten as

$$F_i(\boldsymbol{x}) = \sum_{k=1}^{K_{i+1}} d_{k,i+1} K_{rep}(\boldsymbol{x}, \boldsymbol{x}_{k,i+1}). \tag{4.21}$$

By setting $\boldsymbol{x} = \boldsymbol{x}_{k,i}$ in Eq. (4.21), it follows

$$F_i(\boldsymbol{x}_{k,i}) = \sum_{k=1}^{K_{i+1}} d_{k,i+1} K_{rep}(\boldsymbol{x}_{k,i}, \boldsymbol{x}_{k,i+1}). \tag{4.22}$$

Combining Eq. (4.22) with Eq. (4.20), we obtain

$$d_{k,i} = w_{k,i} \sum_{k=1}^{K_{i+1}} d_{k,i+1} K_{rep}(\boldsymbol{x}_{k,i}, \boldsymbol{x}_{k,i+1}) \tag{4.23}$$

Collecting $d_{1,i}, d_{2,i}, \ldots, d_{K_i,i}$ to the vector $\boldsymbol{d}_{i|i+1} = [d_{1,i}, d_{2,i}, \ldots, d_{K_i,i}]^T$, collecting $d_{1,i+1}, d_{2,i+1}, \ldots, d_{K_{i+1},i+1}$ to the vector $\boldsymbol{d}_{i+1}$, the integration weights $w_{k,i}$ to the diagonal matrix $\boldsymbol{W}_i$, and the reproducing kernel

$K_{rep}(\boldsymbol{x}_{k,i}, \boldsymbol{x}_{k,i+1})$ to the matrix $\boldsymbol{H}_i$, it follows from Eq. (4.23) that

$$\boldsymbol{d}_{i|i+1} = \boldsymbol{W}_i \boldsymbol{H}_i \boldsymbol{d}_{i+1} \tag{4.24}$$

and thus, Eq. (4.15).

In this work, the Reuter grid (Reuter, 1982) is used. It generates a homogeneous coverage of grid points $P(\varphi_l, \lambda_{l,m})$ on the sphere with spherical coordinates

$$\varphi_0 = -\frac{\pi}{2} \quad \text{and} \quad \lambda_{0,0} = 0 \tag{4.25}$$

$$\varphi_l = -\frac{\pi}{2} + l\,\Delta\varphi \quad \text{and} \quad \lambda_{l,m} = m\,\frac{2\pi}{\gamma_l} \tag{4.26}$$

$$\varphi_\gamma = \frac{\pi}{2} \quad \text{and} \quad \lambda_{\gamma,0} = 0 \tag{4.27}$$

for $l = 1, 2, \ldots, \gamma - 1$ and $m = 0, 1, \ldots, \gamma_l - 1$. $\Delta\varphi$ and $\frac{2\pi}{\gamma_l}$ are the sampling intervals in the latitude and longitude direction, respectively

$$\Delta\varphi = \frac{\pi}{\gamma} \tag{4.28}$$

$$\gamma_l = \left\lfloor \frac{2\pi}{\arccos((\cos\Delta\varphi - \sin^2\varphi_l)/\cos^2\varphi_l)} \right\rfloor \tag{4.29}$$

where γ is a positive integer control parameter. Thus, the total amount of Reuter grid points Z on the sphere is determined by this positive integer γ. Figure 4.2 visualizes the generated Reuter grid points on the sphere at level 4 (red triangles in Fig. 4.2) and level 5 (green dots in Fig. 4.2), respectively. Reuter grids are regarded as equidistributed point systems on the sphere (Fengler et al., 2004; Eicker, 2008).

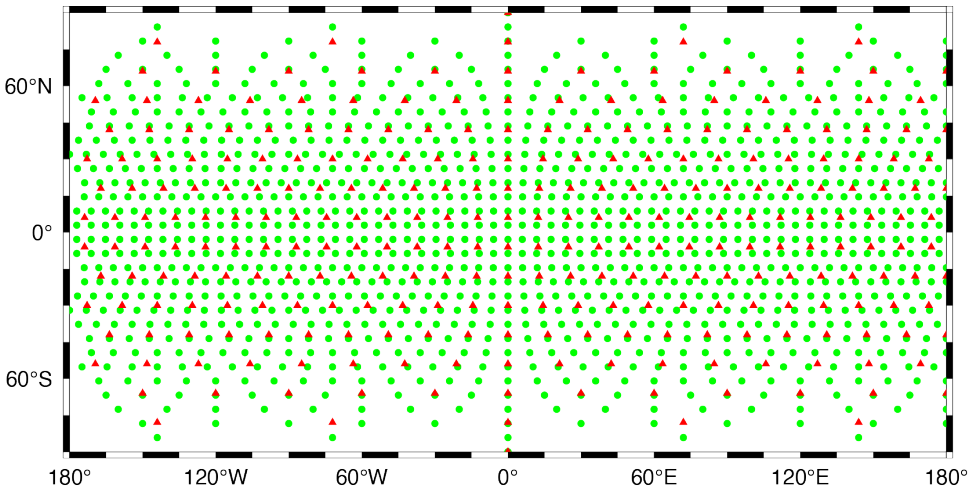


Figure 4.2: Reuter grid points on the sphere for level 4 (red triangles) and level 5 (green dots)

P-III proposes a way for computing the corresponding integration weights $w_{k,i}$ to set up the low-pass filter matrix $\boldsymbol{L}_i$ (4.17) in case of using the Reuter grid, which reads

$$w_{k,i} = \frac{4\pi R^2}{Z_i}, \tag{4.30}$$

where Z_i is the total number of Reuter grid points on the sphere at level i.

MRR based on the pyramid algorithm

The developed MRR scheme based on the pyramid algorithm and sequential parameter estimation is visualized in Fig. 4.3 (cf. Fig. 4 in **P-III**). The coefficient vector $\boldsymbol{d}_I$ of the highest level I is first estimated using only the high-resolution data set(s). It is used to compute the detail signal $\boldsymbol{G}_I$ and to start the pyramid algorithm, i.e., to calculate the coefficient vector $\boldsymbol{d}_{I-1|I}$ of the next lower level according to Eq. (4.24). At this level, the coefficient vector $\boldsymbol{d}_{I-1|I}$ is then updated by the direct combination with the lower-resolution data set(s) involved at the level $I-1$ through the parameter estimation (see Sect. 5.3). Continuing this process until the lowest level i' of the MRR, the scaling coefficients and the detail signals of each level can be obtained, and thus, the final gravity functional is computed according to Eq. (4.12). Typically, the terrestrial data are used at the highest level. Then the shipborne or airborne data can be introduced at a level lower, followed by the altimetry data and the satellite gravimetry data, if applicable (see Fig. 4.1).

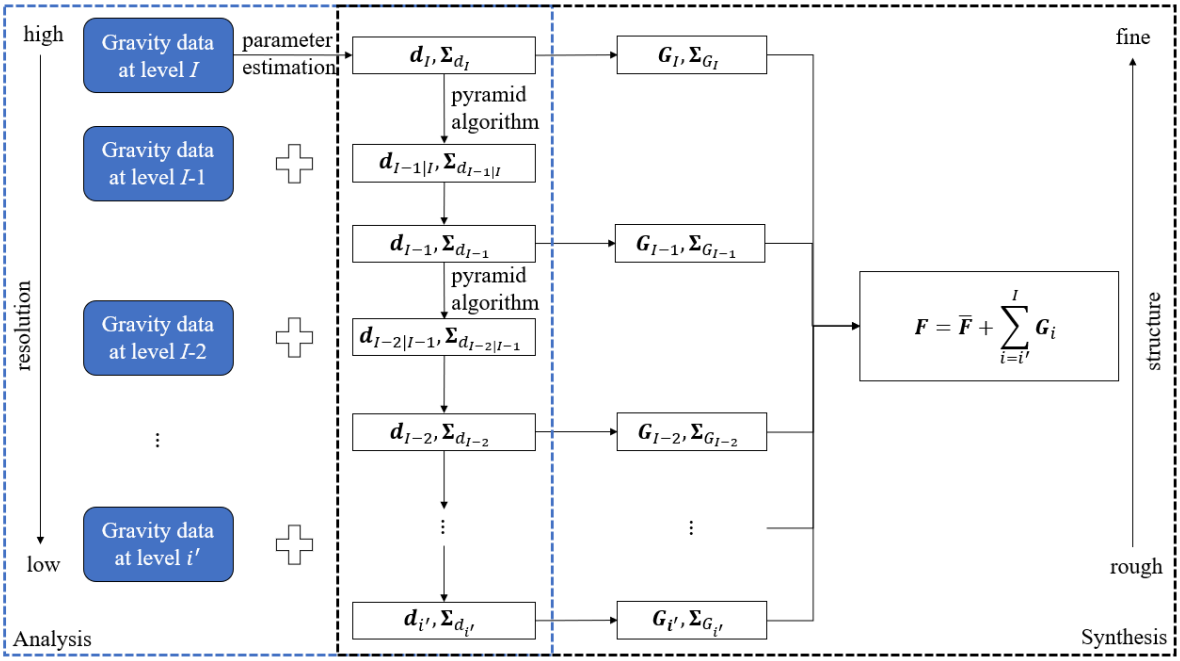


Figure 4.3: The multi-resolution representation (MRR) based on the pyramid algorithm (cf. **P-III**)

The advantages of applying the pyramid algorithm are demonstrated in **P-III** in detail, including

- different observation types can be used only once at the spectral level of their highest sensitivities,
- the covariance information can be calculated following the law of error propagation from the higher levels and serve as input for the lower levels,
- the computational effort is reduced when the observations are included at the lower levels, which require a smaller number of SRBFs.

4.4 Scaling and wavelet functions

A spherical scaling function of resolution i is a band-limited SRBF $B(\boldsymbol{x}, \boldsymbol{x}_k) =: \Phi_i(\boldsymbol{x}, \boldsymbol{x}_{k,i})$, which can act as a low-pass filter (see Sect. 4.1), with Legendre coefficient $B_n =: \phi_{n,i} > 0$ for degree

$n = 0, 1, \ldots, n_{max} =: 2^i - 1$ and $\phi_{n,i} = 0$ for degree values $n > 2^i - 1$. Based on the scaling function, a spherical wavelet function $\Psi_i(\boldsymbol{x}, \boldsymbol{x}_{k,i})$, which can be interpreted as a band-pass filter, can be defined as

$$\begin{aligned}\Psi_i(\boldsymbol{x}, \boldsymbol{x}_{k,i}) &= \Phi_i(\boldsymbol{x}, \boldsymbol{x}_{k,i}) - \Phi_{i-1}(\boldsymbol{x}, \boldsymbol{x}_{k,i}) \\ &= \sum_{n=0}^{2^i-1} \frac{2n+1}{4\pi R^2} \left(\frac{R}{r}\right)^{n+1} \psi_{n,i} P_n(\boldsymbol{r}^T \boldsymbol{r}_{k,i})\end{aligned} \tag{4.31}$$

(Schmidt et al., 2007), where its Legendre coefficients $\psi_{n,i}$ are computed as

$$\psi_{n,i} = \phi_{n,i} - \phi_{n,i-1}. \tag{4.32}$$

Different types of basis functions have been introduced and applied in numerous studies, including band-limited SRBF, e.g., the Shannon and Blackman function (Schmidt et al., 2007), as well as non-band-limited SRBF, e.g., the Poisson kernel (Klees et al., 2008) and radial multipoles (Marchenko, 1998). Wittwer (2009) and Bentel et al. (2013b) summarized and compared the characteristics of different types of SRBFs. Tenzer and Klees (2008) pointed out that the band-limited property of the basis functions is an advantage due to the reduced numerical complexity. Naeimi et al. (2015) and Bucha et al. (2016) showed the advantages of applying the Shannon function in regional gravity field modeling for satellite and terrestrial data, respectively. Lieb (2017) demonstrated that it is beneficial to use the non-smoothing Shannon function in the analysis but apply the Blackman or CuP function with smoothing features in the synthesis. These three types of band-limited SRBF, i.e., scaling functions, are considered in this work:

1. The Shannon function, which is a reproducing kernel (4.4), its Legendre coefficients $\phi_{n,i}^{Sha}$ are given by

$$\phi_{n,i}^{Sha} = \begin{cases} 1 & \text{for } n \in [0, 2^i) \\ 0 & \text{else} \end{cases} \tag{4.33}$$

2. The Blackman function, its Legendre coefficients $\phi_{n,i}^{Bla}$ are given by

$$\phi_{n,i}^{Bla} = \begin{cases} 1 & \text{for } n \in [0, 2^{i-1}) \\ (A(n))^2 & \text{for } n \in [2^{i-1}, 2^i) \\ 0 & \text{else} \end{cases} \tag{4.34}$$

   where

$$A(n) = \frac{21}{50} - \frac{1}{2}\cos\left(\frac{2\pi n}{2^i}\right) + \frac{2}{25}\cos\left(\frac{4\pi n}{2^i}\right) \tag{4.35}$$

3. The Cubic Polynomial (CuP) function, its Legendre coefficients $\phi_{n,i}^{CuP}$ are given by

$$\phi_{n,i}^{CuP} = \begin{cases} (1 - \frac{n}{2^i})^2 (1 + \frac{n}{2^{i-1}}) & \text{for } n \in [0, 2^i) \\ 0 & \text{else} \end{cases} . \tag{4.36}$$

Correspondingly, three types of wavelet functions can be obtained, with Legendre coefficients $\psi_{n,i}^{Sha} = \phi_{n,i}^{Sha} - \phi_{n,i-1}^{Sha}$, $\psi_{n,i}^{Bla} = \phi_{n,i}^{Bla} - \phi_{n,i-1}^{Bla}$, and $\psi_{n,i}^{CuP} = \phi_{n,i}^{CuP} - \phi_{n,i-1}^{CuP}$. Figure 4.4 visualizes the characteristics of these three types of scaling functions (left column) as well as their corresponding wavelet functions (right column). In each sub-plot, the upper and bottom panels show the spatial and spectral domain, correspondingly. According to Heisenberg's uncertainty principle (Heisenberg, 1927; Freeden and Michel, 2004), the spatial and spectral domain cannot be sharply localized at the same time, and a trade-off between these two localizations is required in the choice of SRBFs. The comparison between the different types of basis functions, i.e., between the Figs. 4.4a, 4.4c, 4.4e, shows that the Shannon

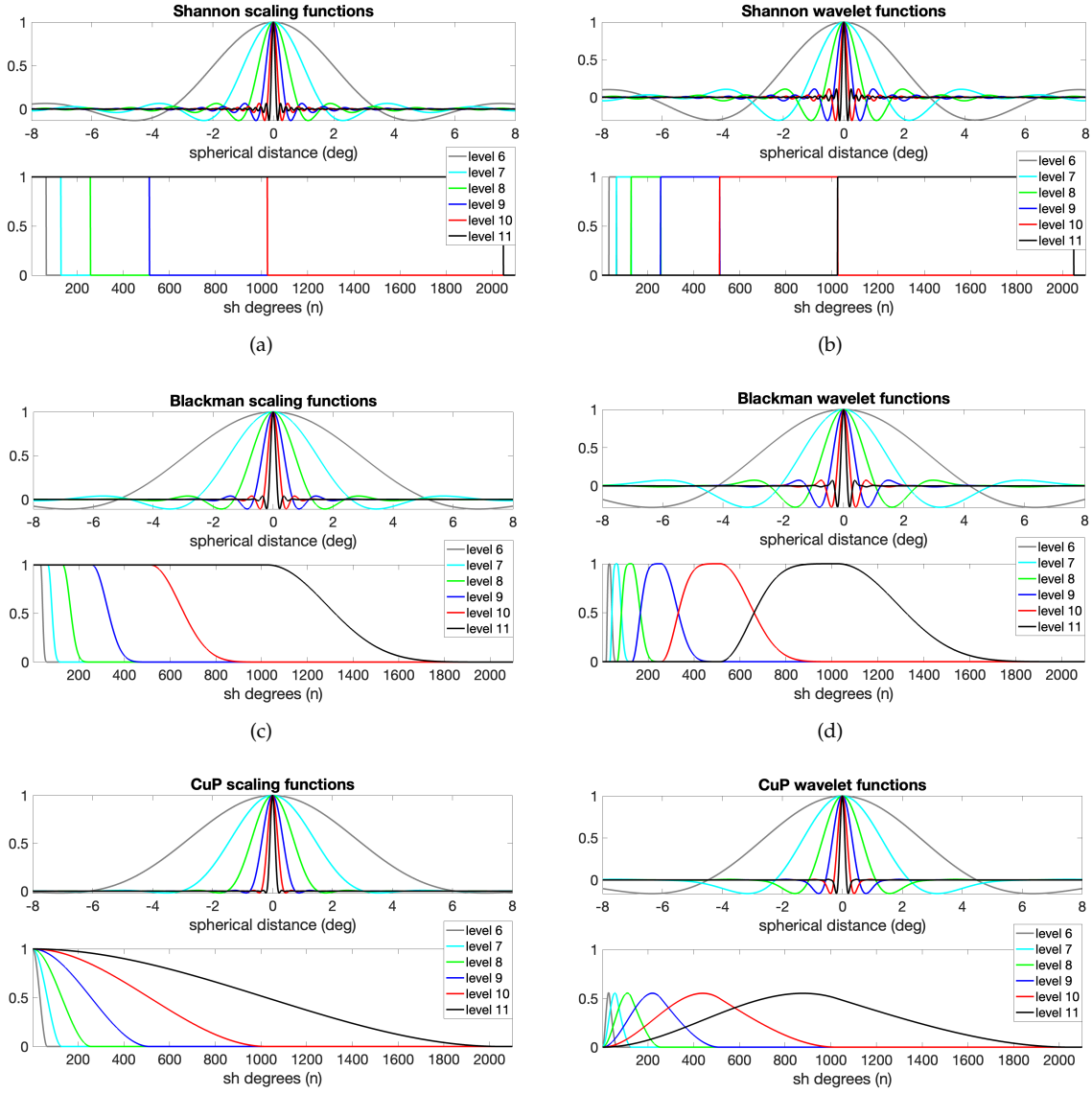


Figure 4.4: The (a) Shannon scaling functions, (b) Shannon wavelet functions, (c) Blackman scaling functions, (d) Blackman wavelet functions, (e) CuP scaling functions, and (f) CuP wavelet functions at different resolution levels, in the spatial domain (upper panel, ordinate values are normalized to 1), and in the spectral domain (bottom panel, ordinate values are not normalized)

function has the highest localization in the spectral domain, but it also has the strongest oscillations in the spatial domain. In contrast, the CuP function has the least oscillations in the spatial domain but has a smoothing decay and extracts the least spectral information in the spectral domain. The Blackman function is regarded as a compromise between these two domains. When the resolution level i increases, the peak becomes sharper, but stronger oscillations show up in the spatial domain. In the spectral domain, the corresponding frequency band becomes wider at higher resolution level. Comparing the plots in the right with those in the left, it is clear that the wavelet function is the difference between two scaling functions of neighboring levels in the spectral domain. In the spatial

domain, the wavelet function has stronger oscillations than the scaling function of the same resolution level.

In **P-I**, both the Shannon and CuP scaling functions are applied for comparing different regularization methods, as Naeimi et al. (2015) stated that the performance of regularization methods differs when using SRBFs with or without smoothing features. In **P-II** and **P-III**, the Shannon scaling function is implemented in the analysis to avoid the loss of spectral information, and a smoothing function is applied in the synthesis to reduce erroneous systematic effects, as suggested by Lieb (2017). Furthermore, **P-II** shows that the SRBF with smoothing features can be applied to the airborne data as a low-pass filter to reduce the high-frequency noise. The results also indicate the validity of combining different SRBFs for different observations, which is applied to real data for the first time, in **P-II**. When the terrestrial and airborne data are combined at a high maximum degree of the expansion, the noise in the high frequency of the airborne data needs additional filtering (Childers et al., 1999; Forsberg and Olesen, 2010). This issue can be solved either by applying a smoothing SRBF, which is done in **P-II**, or by implementing the MRR based on the pyramid algorithm to include the airborne data at a lower resolution level, which is realized in **P-III**. And in the latter case, the Shannon function can be applied to all types of observations in the analysis.

5 Estimation model

Based on the methodologies of the SRBFs discussed in Chap. 4, estimation models are set up. This chapter discusses the model settings, how different types of observations are included and combined within the estimation model in terms of both the SRBFs and the MRR, how the regularization parameter is determined, and how the unknown coefficients are calculated.

5.1 Model configuration

As mentioned in Chap. 1, there are four properties that influence the modeling accuracy, and thus, need to be specified in the model settings. The type of the SRBFs has been discussed in Sect. 4.4, and this section explains the other three, namely the bandwidth and location of the SRBFs as well as the extension of the data zone. Detailed explanations regarding the settings of these four properties are given in **P-II**; in **P-III** these settings are adapted in case of the MRR.

Bandwidth of the SRBFs

In this work, the maximum degree n_{max} of the expansion is defined according to the spatial resolution ρ of the observations (Bucha et al., 2016; Lieb et al., 2016), and it is chosen following

$$n_{max} \leq \frac{\pi R}{\rho}, \tag{5.1}$$

with ρ calculated as the average spatial resolution of all types of observations used in the whole study area. For instance, in the "1 cm geoid experiment", the average spatial resolution of the terrestrial and airborne gravity data (see Fig. 3.3a) amounts to 3.5 km, and correspondingly, the maximum degree of the expansion is chosen as $n_{max} = 5600$.

Extension of data zone

Three areas need to be defined in regional gravity modeling, the observation area $\partial\Omega_O$ where the observations are available, the computation area $\partial\Omega_C$ where the SRBFs are located, and the investigation (target) area $\partial\Omega_I$ in which the final gravity functionals are computed as output. The observation area $\partial\Omega_O$ is fixed by the given data, and as shown in Fig. 5.1, $\partial\Omega_C$ and $\partial\Omega_I$ are chosen following $\partial\Omega_I \subset \partial\Omega_O \subset \partial\Omega_C$ to mitigate edge effects. The detailed reasons for such settings are explained in **P-II**, which include:

- the oscillations of the SRBFs cannot overlap and balance with each other at the boundaries of the computation area $\partial\Omega_C$ due to the neglect of SRBFs outside $\partial\Omega_C$, and thus, the computation area $\partial\Omega_C$ needs to be chosen larger than the observation area $\partial\Omega_O$, i.e., $\partial\Omega_C \supset \partial\Omega_O$.
- the unknown coefficients d_k cannot be estimated appropriately at the border of the observation area $\partial\Omega_O$ due to the lack of fully surrounding observations, and thus, the observation area $\partial\Omega_O$ should be larger than the investigation area $\partial\Omega_I$, i.e., $\partial\Omega_O \supset \partial\Omega_I$.

The margin size between the three areas is influenced by the shape of the SRBFs; if n_{max} is chosen higher, the SRBFs become narrower (see Fig. 4.4), and thus, a smaller margin size can be selected. In

this work, the margin size $\eta_{C,O}$ between $\partial\Omega_C$ and $\partial\Omega_O$ is determined following a method described by Lieb et al. (2016), but modified to

$$\eta_{C,O} = \frac{360^\circ}{n_{max}\,\cos(|\phi_{max}|)} \tag{5.2}$$

where ϕ_{max} is the maximum latitude value of the investigation area. In case of applying the MRR, the margin size $\eta_{C,O}$ increases by multiples of 2 from the highest level to the lowest level, as $n_{max} = 2^i - 1$ for each resolution level i. The margin size $\eta_{O,I}$ between $\partial\Omega_O$ and $\partial\Omega_I$ is usually chosen equal to the margin size $\eta_{C,O}$ (Bentel et al., 2013a), which is applied in **P-I**. Depending on the desired final model size (target area), any value $\eta_{O,I} \geq \eta_{C,O}$ is valid, which is the case in **P-II**. When the MRR is applied, the margin size $\eta_{C,O}$ differs between different resolution levels, and **P-III** shows that the margin size $\eta_{O,I}$ can be chosen as the median of the applied $\eta_{C,O}$ of each level.

Location of the SRBFs

The location of the SRBFs depends on the type and the number of grid points. Eicker (2008) examined four types of grids, and the results indicate that the Reuter grid and the triangle vertex grid are the most suitable choices for space localizing basis functions. According to Bentel et al. (2013a) and Naeimi (2013), different grid types do not have a strong impact on the modeling results, especially comparing to the other three properties. In this work, the Reuter grid is implemented, which generates a homogeneous coverage of equidistributed grid points on the sphere. As explained in Sect. 4.3, the total number of Reuter grid points Z on the sphere is set by a control parameter γ (Eicker, 2008), and it is estimated by

$$Z \leq 2 + \frac{4}{\pi}\,\gamma^2. \tag{5.3}$$

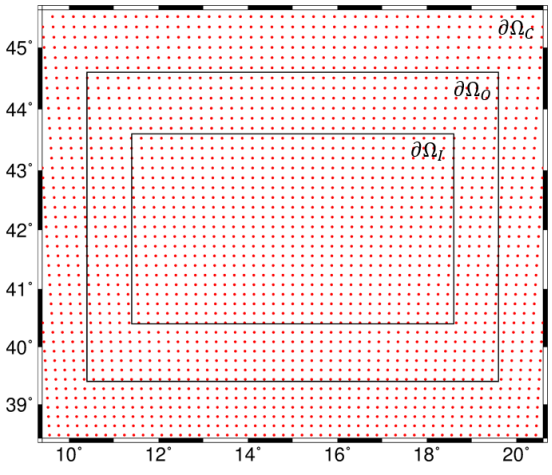


Figure 5.1: The different extensions for the areas of computation $\partial\Omega_C$, of observations $\partial\Omega_O$ and of investigation $\partial\Omega_I$, as well as the distribution of the Reuter grid points in $\partial\Omega_C$

The minimum total number of required grid points on the sphere depends on the maximum degree n_{max} of the expansion. When n_{max} increases, the SRBFs need to be placed at denser grid points in order to cover the full spectral content of the gravity observations. As already mentioned in Sect. 4.1, the system of grid points needs to be admissible, which means

$$Z \geq (n_{max} + 1)^2, \tag{5.4}$$

and it is fundamental if $Z = (n_{max} + 1)^2$ holds (Schmidt et al., 2007). In practice, it is difficult to generate grids with the exact amount of points fulfilling a fundamental system. In case of an admissible system, linear dependencies exist between the SRBFs, which yield a global rank deficiency of $Z - (n_{max} + 1)^2$. This is one of the reasons why regularization is required. The choice of the total amount of Reuter grid points Z thus needs to guarantee an admissible grid point system, and to minimize the rank deficiency at the same time. For these reasons, the control parameter γ is usually chosen as $\gamma = n_{max} + 1$ (Bucha et al., 2016; Lieb et al., 2016) or $\gamma = n_{max}$ (Wittwer, 2009; Bentel, 2013) in existing literature. In this thesis, $\gamma = n_{max}$ is applied, and those Reuter grid points that are distributed inside the computation area $\partial\Omega_C$ are used as the locations of the SRBFs (see Fig. 5.1).

5.2 Parameter estimation

To calculate the unknown coefficients, a classical numerical integration technique (de Min, 1995) or a parameter estimation procedure (Koch, 1999) can be applied. The advantages of numerical integration are that each coefficient can be computed independently of the others and no (ill-conditioned) linear system needs to be solved (Schmidt et al., 2007). The advantages of parameter estimation include:

- data from different observation techniques can be used directly at their original observation sites, without the need of grid interpolation,
- the covariance, and thus, the standard deviations can be estimated along with the coefficients and the gravity model, which evaluate their uncertainty,
- the downward continuation of the airborne and satellite data can be directly performed in the estimation step,

(Bentel et al., 2013b). Thus, in geodesy the parameter estimation is usually applied to combine heterogeneous data sets (Schmidt et al., 2015). The procedure of parameter estimation has been discussed in all the three publications, **P-I** to **P-III**, and the key points are repeated here for completeness.

The following estimation models are developed based on the Eq. (4.2). For each gravity data set $p = 1, 2, \cdots, P$, collecting the observations $y_p(\boldsymbol{x}_1), y_p(\boldsymbol{x}_2), \ldots, y_p(\boldsymbol{x}_{n_p})$ with position vector $\boldsymbol{x}_1, \boldsymbol{x}_2, \ldots, \boldsymbol{x}_{n_p}$ into the $n_p \times 1$ observation vector $\boldsymbol{y}_p$, the Gauss–Markov model

$$\boldsymbol{y}_p + \boldsymbol{e}_p = \boldsymbol{A}_p \boldsymbol{d} \qquad \text{with} \qquad D(\boldsymbol{y}_p) = \sigma_p^2 \boldsymbol{P}_p^{-1} \tag{5.5}$$

can be set up. $\boldsymbol{e}_p = [e_p(\boldsymbol{x}_1), e_p(\boldsymbol{x}_2), \ldots, e_p(\boldsymbol{x}_{n_p})]^T$ is the $n_p \times 1$ vector of the observation errors, and $\boldsymbol{A}_p = [B_p(\boldsymbol{x}, \boldsymbol{x}_k)]$ is the $n_p \times K$ design matrix, which contains the corresponding (adapted) scaling functions between the observation points and the grid points. $D(\boldsymbol{y}_p)$ is the covariance matrix of the observation vector $\boldsymbol{y}_p$, with σ_p^2 being the unknown variance factor and $\boldsymbol{P}_p$ being the given positive definite weight matrix. However, the model (5.5) is in most cases ill-posed due to three reasons, namely

- the number of used basis functions is larger than required (as explained in Sect. 5.1),
- existing data gaps,
- the downward continuation of airborne and satellite data.

Thus, regularization is inevitable. To solve this problem, an additional linear model

$$\boldsymbol{\mu}_d + \boldsymbol{e}_d = \boldsymbol{d} \qquad \text{with} \qquad D(\boldsymbol{\mu}_d) = \sigma_d^2 \boldsymbol{P}_d^{-1} \tag{5.6}$$

is introduced as prior information. $\boldsymbol{\mu}_d$ is the $K \times 1$ expectation vector of the coefficient vector $\boldsymbol{d}$, $\boldsymbol{e}_d$ is the corresponding error vector, and $D(\boldsymbol{\mu}_d)$ is the covariance matrix of the prior information, with σ_d^2 being its variance factor and $\boldsymbol{P}_d$ being the positive definite weight matrix.

Combining the two models (5.5) and (5.6), an extended Gauss–Markov model can be formulated

$$\begin{bmatrix} \boldsymbol{y}_1 \\ \boldsymbol{y}_2 \\ \vdots \\ \boldsymbol{y}_P \\ \boldsymbol{\mu}_d \end{bmatrix} + \begin{bmatrix} \boldsymbol{e}_1 \\ \boldsymbol{e}_2 \\ \vdots \\ \boldsymbol{e}_P \\ \boldsymbol{e}_d \end{bmatrix} = \begin{bmatrix} \boldsymbol{A}_1 \\ \boldsymbol{A}_2 \\ \vdots \\ \boldsymbol{A}_P \\ \boldsymbol{I} \end{bmatrix} \cdot \boldsymbol{d} \;\text{ with }\; D\left(\begin{bmatrix} \boldsymbol{y}_1 \\ \boldsymbol{y}_2 \\ \vdots \\ \boldsymbol{y}_P \\ \boldsymbol{\mu}_d \end{bmatrix} \right) = \begin{bmatrix} \sigma_1^2 \boldsymbol{P}_1^{-1} & \boldsymbol{0} & \boldsymbol{0} & \ldots & \boldsymbol{0} \\ \boldsymbol{0} & \sigma_2^2 \boldsymbol{P}_2^{-1} & \vdots & \vdots & \vdots \\ \vdots & \boldsymbol{0} & \ddots & \vdots & \vdots \\ \vdots & \vdots & \vdots & \sigma_P^2 \boldsymbol{P}_P^{-1} & \boldsymbol{0} \\ \boldsymbol{0} & \boldsymbol{0} & \ldots & \boldsymbol{0} & \sigma_d^2 \boldsymbol{P}_d^{-1} \end{bmatrix} \tag{5.7}$$

Applying the least-squares adjustment to Eq. (5.7), the unknown coefficient vector $\widehat{\boldsymbol{d}}$ can be estimated as

$$\widehat{\boldsymbol{d}} = \left(\sum_{p=1}^{P} \omega_p \boldsymbol{A}_p^T \boldsymbol{P}_p \boldsymbol{A}_p + \lambda \boldsymbol{P}_d \right)^{-1} \left(\sum_{p=1}^{P} \omega_p \boldsymbol{A}_p^T \boldsymbol{P}_p \boldsymbol{y}_p + \lambda \boldsymbol{P}_d \boldsymbol{\mu}_d \right), \tag{5.8}$$

with the covariance matrix

$$\widehat{\boldsymbol{\Sigma}}_d = \sigma_1^2 \left(\sum_{p=1}^{P} \omega_p \boldsymbol{A}_p^T \boldsymbol{P}_p \boldsymbol{A}_p + \lambda \boldsymbol{P}_d \right)^{-1}. \tag{5.9}$$

$\omega_p = \widehat{\sigma}_1^2 / \widehat{\sigma}_p^2$ denotes the relative weights between the observation groups, which are estimated by VCE. $\lambda = \widehat{\sigma}_1^2 / \widehat{\sigma}_d^2$ can be interpreted as the regularization parameter (Koch and Kusche, 2002), and its determination is discussed in Sect. 5.4. In this work, the expectation vector $\boldsymbol{\mu}_d$ is set to the zero vector, since the background model subtracted in the remove step of the RCR procedure serves as the prior information.

The estimated coefficient vector $\widehat{\boldsymbol{d}}$ and its covariance matrix $\widehat{\boldsymbol{\Sigma}}_d$ are then used to calculate the output gravity functional $\widehat{\boldsymbol{F}}$ as well as its covariance matrix $\widehat{\boldsymbol{\Sigma}}_F$ in the synthesis step

$$\widehat{\boldsymbol{F}} = \boldsymbol{B}\widehat{\boldsymbol{d}} \tag{5.10}$$

$$\widehat{\boldsymbol{\Sigma}}_F = \boldsymbol{B}\widehat{\boldsymbol{\Sigma}}_d \boldsymbol{B}^T, \tag{5.11}$$

where $\boldsymbol{B}$ is the design matrix, which contains the scaling functions between the grid points and the computation points of the final gravity model.

5.3 Sequential parameter estimation

As explained in Sect. 4.2, the unknown coefficients need to be estimated at each resolution level when the MRR is applied. They are estimated sequentially in this work, by implementing the pyramid algorithm (see Sect. 4.3). In this procedure, the unknown coefficient vector $\widehat{\boldsymbol{d}}_I$ as well as its covariance matrix $\widehat{\boldsymbol{\Sigma}}_{d_I}$ of the highest level I are estimated first by the parameter estimation procedure explained in Sect. 5.2, i.e., the Eqs. (5.8) and (5.9). Afterwards, they are transformed to the lower levels by low-pass filtering according to the Eqs. (4.15) and (4.16), and updated by including observations successively at each level. The combination of the coefficient vector $\boldsymbol{d}_{i|i+1}$ from the pyramid algorithm with the observations of level i is realized again by parameter estimation, and it is detailed in **P-III**.

Assuming that Q data groups with observation vector $\boldsymbol{y}_{q,i}$ are introduced at level i, the combination of $\boldsymbol{d}_{i|i+1}$ and $\boldsymbol{y}_{q,i}$ reads

$$\begin{bmatrix} \boldsymbol{y}_{1,i} \\ \boldsymbol{y}_{2,i} \\ \vdots \\ \boldsymbol{y}_{Q,i} \\ \boldsymbol{d}_{i|i+1} \end{bmatrix} + \begin{bmatrix} \boldsymbol{e}_{1,i} \\ \boldsymbol{e}_{2,i} \\ \vdots \\ \boldsymbol{e}_{Q,i} \\ \boldsymbol{e}_d \end{bmatrix} = \begin{bmatrix} \boldsymbol{A}_{1,i} \\ \boldsymbol{A}_{2,i} \\ \vdots \\ \boldsymbol{A}_{Q,i} \\ \boldsymbol{I} \end{bmatrix} \cdot \boldsymbol{d}_i \quad \text{with } D \left(\begin{bmatrix} \boldsymbol{y}_{1,i} \\ \boldsymbol{y}_{2,i} \\ \vdots \\ \boldsymbol{y}_{Q,i} \\ \boldsymbol{d}_{i|i+1} \end{bmatrix} \right) = \begin{bmatrix} \sigma_{1,i}^2 \boldsymbol{P}_{1,i}^{-1} & \boldsymbol{0} & \boldsymbol{0} & \dots & \boldsymbol{0} \\ \boldsymbol{0} & \sigma_{2,i}^2 \boldsymbol{P}_{2,i}^{-1} & \vdots & \vdots & \vdots \\ \vdots & \boldsymbol{0} & \ddots & \vdots & \vdots \\ \vdots & \vdots & \vdots & \sigma_{Q,i}^2 \boldsymbol{P}_{Q,i}^{-1} & \boldsymbol{0} \\ \boldsymbol{0} & \boldsymbol{0} & \dots & \boldsymbol{0} & \boldsymbol{\Sigma}_{d_{i|i+1}} \end{bmatrix} \tag{5.12}$$

The updated coefficient vector $\widehat{\boldsymbol{d}}_i$ of level i is derived as

$$\widehat{\boldsymbol{d}}_i = \left(\sum_{q=1}^{Q} \frac{1}{\sigma_{q,i}^2} \boldsymbol{A}_{q,i}^T \boldsymbol{P}_{q,i} \boldsymbol{A}_{q,i} + \boldsymbol{\Sigma}_{d_{i|i+1}}^{-1} \right)^{-1} \left(\sum_{q=1}^{Q} \frac{1}{\sigma_{q,i}^2} \boldsymbol{A}_{q,i}^T \boldsymbol{P}_{q,i} \boldsymbol{y}_{q,i} + \boldsymbol{\Sigma}_{d_{i|i+1}}^{-1} \boldsymbol{d}_{i|i+1} \right) \tag{5.13}$$

with the covariance matrix

$$\widehat{\boldsymbol{\Sigma}}_{d_i} = \left(\sum_{q=1}^{Q} \frac{1}{\sigma_{q,i}^2} \boldsymbol{A}_{q,i}^T \boldsymbol{P}_{q,i} \boldsymbol{A}_{q,i} + \boldsymbol{\Sigma}_{d_{i|i+1}}^{-1} \right)^{-1}. \tag{5.14}$$

The variance factors $\sigma_{1,i}^2, \sigma_{2,i}^2, \ldots, \sigma_{Q,i}^2$ of the data sets $\boldsymbol{y}_{1,i}, \boldsymbol{y}_{2,i}, \ldots, \boldsymbol{y}_{Q,i}$ are estimated by VCE.

The combination of $\boldsymbol{y}_i = [\boldsymbol{y}_{1,i}^T,\ \boldsymbol{y}_{2,i}^T,\ \ldots,\ \boldsymbol{y}_{Q,i}^T]^T$ and $\boldsymbol{d}_{i|i+1}$ can also be solved in analogy to a Kalman filter (Kalman, 1960), where the $\boldsymbol{d}_{i|i+1}$ and $\boldsymbol{\Sigma}_{d_{i|i+1}}$ can be regarded as the predicted state vector and the related predicted covariance matrix, respectively. Then the corrected state vector $\boldsymbol{d}_i$ as well as its covariance matrix $\boldsymbol{\Sigma}_{d_i}$ are computed by incorporating the involved measurements $\boldsymbol{y}_i$ at level i

$$\widehat{\boldsymbol{d}}_i = \boldsymbol{d}_{i|i+1} + \boldsymbol{K}_i \left(\boldsymbol{y}_i - \boldsymbol{A}_i \boldsymbol{d}_{i|i+1} \right) \tag{5.15}$$

$$\widehat{\boldsymbol{\Sigma}}_{d_i} = (\boldsymbol{I} - \boldsymbol{K}_i \boldsymbol{A}_i)\, \boldsymbol{\Sigma}_{d_{i|i+1}} \tag{5.16}$$

where $\boldsymbol{K}_i$ is the gain matrix

$$\boldsymbol{K}_i = \boldsymbol{\Sigma}_{d_{i|i+1}} \boldsymbol{A}_i^T \left(\boldsymbol{A}_i \boldsymbol{\Sigma}_{d_{i|i+1}} \boldsymbol{A}_i^T + \boldsymbol{\Sigma}_{y_i} \right)^{-1} \tag{5.17}$$

with $\boldsymbol{A}_i = [\boldsymbol{A}_{1,i}^T,\ \boldsymbol{A}_{2,i}^T,\ \ldots,\ \boldsymbol{A}_{Q,i}^T]^T$, and $\boldsymbol{\Sigma}_{y_i} = \text{diag}\left(\sigma_{1,i}^2 \boldsymbol{P}_{1,i}^{-1}, \sigma_{2,i}^2 \boldsymbol{P}_{2,i}^{-1}, \ldots, \sigma_{Q,i}^2 \boldsymbol{P}_{Q,i}^{-1} \right)$ being the covariance matrix of the observation vector $\boldsymbol{y}_i$. After taking into account the matrix identities (Koch, 1999)

$$\boldsymbol{D}^{-1}\boldsymbol{C}(\boldsymbol{A} - \boldsymbol{B}\boldsymbol{D}^{-1}\boldsymbol{C})^{-1} = (\boldsymbol{D} - \boldsymbol{C}\boldsymbol{A}^{-1}\boldsymbol{B})^{-1}\boldsymbol{C}\boldsymbol{A}^{-1} \tag{5.18}$$

and

$$(\boldsymbol{A} - \boldsymbol{B}\boldsymbol{D}^{-1}\boldsymbol{C})^{-1} = \boldsymbol{A}^{-1} + \boldsymbol{A}^{-1}\boldsymbol{B}(\boldsymbol{D} - \boldsymbol{C}\boldsymbol{A}^{-1}\boldsymbol{B})^{-1}\boldsymbol{C}\boldsymbol{A}^{-1} \tag{5.19}$$

the solution delivered by the Eqs. (5.15) and (5.16) ends up identical to the Eqs. (5.13) and (5.14).

In the synthesis step, the estimated coefficient vector $\widehat{\boldsymbol{d}}_i$ and its covariance matrix $\widehat{\boldsymbol{\Sigma}}_{d_i}$ are used to calculate the estimated detail signal $\widehat{\boldsymbol{G}}_i$ as well as its covariance matrix $\widehat{\boldsymbol{\Sigma}}_{G_i}$ of level i

$$\widehat{\boldsymbol{G}}_i = \boldsymbol{B}_i \widehat{\boldsymbol{d}}_i \tag{5.20}$$

$$\widehat{\boldsymbol{\Sigma}}_{G_i} = \boldsymbol{B}_i \widehat{\boldsymbol{\Sigma}}_{d_i} \boldsymbol{B}_i^T, \tag{5.21}$$

where $\boldsymbol{B}_i$ is the design matrix containing the corresponding wavelet functions between the computation points of the gravity model and the grid points of level i.

5.4 Regularization

As mentioned in Sect. 5.2, regularization is in most cases inevitable in the parameter estimation. Bouman (1998) discussed and compared different regularization methods, and among them, the

Tikhonov regularization (Tikhonov and Arsenin, 1977) is applied here. It finds the solution $\boldsymbol{d}_\lambda$ that solves the minimization problem

$$\boldsymbol{d}_\lambda = \arg\min_{\boldsymbol{d}}\{(\boldsymbol{A}\boldsymbol{d}-\boldsymbol{y})^T\boldsymbol{P}(\boldsymbol{A}\boldsymbol{d}-\boldsymbol{y}) + \lambda(\boldsymbol{d}-\boldsymbol{\mu}_d)^T\boldsymbol{R}(\boldsymbol{d}-\boldsymbol{\mu}_d)\}. \tag{5.22}$$

The residual term $\|\boldsymbol{A}\boldsymbol{d}-\boldsymbol{y}\|_{\boldsymbol{P}}$ measures the least-squares fit, and the penalty term $\|\boldsymbol{d}-\boldsymbol{\mu}_d\|_{\boldsymbol{R}}$ quantifies the regularity, where $\boldsymbol{\mu}_d$ is the prior information of $\boldsymbol{d}$, λ and $\boldsymbol{R}$ are the regularization parameter and regularization matrix, respectively. Ilk (1993) concluded that the modeling result is insensitive to the choice of the regularization matrix $\boldsymbol{R}$. In this thesis, it is chosen as the identity matrix, i.e., $\boldsymbol{R} = \boldsymbol{I}$, which is commonly applied in existing literature (see e.g., Naeimi et al., 2015; Klees et al., 2018; Slobbe et al., 2019). Eicker et al. (2014) explained why the regularization matrix can be approximated by $\boldsymbol{I}$. Other choices for $\boldsymbol{R}$ are given, e.g., by Kusche and Klees (2002) and Wu et al. (2017a). However, a detailed discussion about the regularization matrix is beyond the scope of this study.

This section focuses on the determination of the regularization parameter λ when different data types are to be combined, which is the first main research objective of the thesis (see Sect. 1.2), accomplished by **P-I**. The regularization parameter determination is a crucial issue, and it directly influences the modeling results. A weak regularization, i.e., λ chosen too small, leads still to instabilities in the results, and if λ is chosen too large, some information contained in the observations would be lost (Naeimi, 2013). Different methods have been developed and applied for the regularization parameter determination, e.g., the L-curve criterion (Hansen, 1990; Hansen and O'Leary, 1993), the GCV (Golub et al., 1979; Wahba, 1990), and the VCE (Koch and Kusche, 2002). Each method has its own advantages and disadvanteges, and a comparison between different methods can be found, e.g., in Farquharson and Oldenburg (2004); Naeimi et al. (2015); and Xu et al. (2016). Xu et al. (2006) modified the VCE and proposed a bias-corrected variance component estimator. Tanir et al. (2009) combined two regularization methods, namely the VCE and GCV for the Very Long Baseline Interferometry (VLBI) intra-technique combination. Naeimi (2013) proposed a Parameter-Signal Correlation (PSC) approach based on the idea that in case of SRBFs, an appropriate regularization parameter gives the maximum correlation between the estimated coefficients and the gravitational potential.

Koch and Kusche (2002) demonstrated that the Tikhonov regularization can be interpreted by Bayesian statistics as estimation with prior information, and it is realized by adding a positive definite matrix $\boldsymbol{P}_d$ times the regularization parameter λ to the normal equations for stabilizing the solution, as shown in Eq. (5.8). In this case, the regularization parameter is regarded as an additional variance component for the prior information $\boldsymbol{\mu}_d$ of the unknown coefficients, i.e., the prior information is treated as an additional observation group. The VCE is commonly used in regional gravity field applications (see e.g., Bentel et al., 2013a; Eicker et al., 2014; Bucha et al., 2016; Wu et al., 2017b), especially when different types of observations are combined. It estimates the relative weights between different observation groups and the regularization parameter simultaneously. However, it has been suspected that the regularization parameter generated by VCE could be unreliable (Liang, 2017), due to the fact that the prior information is required to be of random character (Koch and Kusche, 2002), and this is not fulfilled when a background model serves as prior information. Naeimi et al. (2015) showed that VCE delivers larger RMS errors in the calculated geoid model than the L-curve method and GCV, and further concluded that the L-curve method should be applied when the Shannon function is used. However, the L-curve or other conventional regularization methods cannot deliver the relative weights between heterogeneous observations (Xu et al., 2006). Thus, **P-I** proposes to combine the L-curve method and VCE in such a way that the relative weights are estimated by VCE, but the regularization parameters are determined by the L-curve method.

Variance component estimation

VCE is an iterative process; it starts with given initial values for the variance factors σ_p^2 and σ_d^2 to calculate an initial solution for $\widehat{\boldsymbol{d}}$, following Eq. (5.8). This leads to new estimations for $\widehat{\sigma}_p^2$ and $\widehat{\sigma}_d^2$, with

$$\begin{cases} \widehat{\sigma}_p^2 = \frac{\widehat{\boldsymbol{e}}_p^T \boldsymbol{P}_p \widehat{\boldsymbol{e}}_p}{r_p} \\ \widehat{\sigma}_d^2 = \frac{\widehat{\boldsymbol{e}}_d^T \boldsymbol{P}_d \widehat{\boldsymbol{e}}_d}{r_d} \end{cases} \tag{5.23}$$

where $\widehat{\boldsymbol{e}}_p$ and $\widehat{\boldsymbol{e}}_d$ are the residual vectors, which read

$$\begin{cases} \widehat{\boldsymbol{e}}_p = \boldsymbol{A}_p \widehat{\boldsymbol{d}} - \boldsymbol{y}_p \\ \widehat{\boldsymbol{e}}_d = \widehat{\boldsymbol{d}} - \boldsymbol{\mu}_d \end{cases} \tag{5.24}$$

r_p and r_d are the partial redundancies, which can be computed as

$$\begin{cases} r_p = n_p - \text{trace}(\frac{1}{\sigma_p^2} \boldsymbol{A}_p^T \boldsymbol{P}_p \boldsymbol{A}_p \boldsymbol{N}^{-1}) \\ r_d = K - \text{trace}(\frac{1}{\sigma_d^2} \boldsymbol{P}_d \boldsymbol{N}^{-1}) \end{cases} \tag{5.25}$$

(Koch and Kusche, 2002). n_p denotes the number of observations in the p^{th} data set, K is the number of coefficients, and $\boldsymbol{N} = \sum_{p=1}^{P} \frac{1}{\sigma_p^2} \boldsymbol{A}_p^T \boldsymbol{P}_p \boldsymbol{A}_p + \frac{1}{\sigma_d^2} \boldsymbol{P}_d$ is the extended normal equation matrix. The procedure iterates until a convergence point is reached.

L-curve method

The L-curve is a graphical procedure. As shown in Fig. 5.2, the plot of the regularized solution norm $\|\widehat{\boldsymbol{d}}_\lambda - \boldsymbol{\mu}_d\|_{\boldsymbol{P}_d}$ against the residual norm $\|\boldsymbol{A}\widehat{\boldsymbol{d}}_\lambda - \boldsymbol{y}\|_{\boldsymbol{P}}$ by changing the numerical value for the regularization parameter λ shows a typical L-curve behavior. The corner point in this L-shaped curve corresponds to the desired regularization parameter. The L-shaped curve can be examined on a logarithmic scale (Hansen and O'Leary, 1993), or a linear scale when the variation of the residual norm is low (Eriksson, 2000).

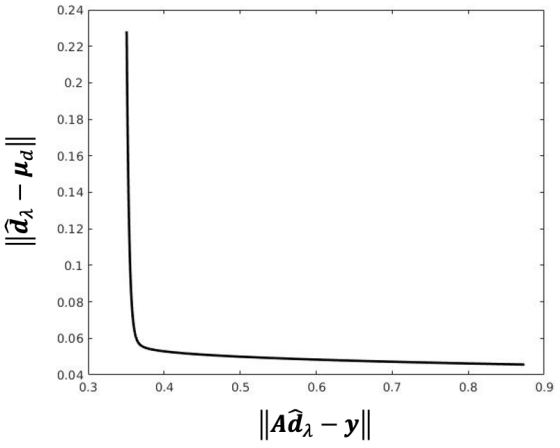


Figure 5.2: An example of the L-curve function

Based on these two methods, two combined approaches are proposed, namely VCE-Lc and Lc-VCE. The following descriptions about these two approaches are taken from **P-I**, which answer the research question **Q-2** raised in Sect. 1.2: how to apply a conventional regularization method, i.e., the L-curve method, if various data sets are combined.

VCE-Lc

The first approach (VCE-Lc) is visualized in Fig. 5.3 (Fig. 3 in **P-I**). It starts with the calculation of the relative weights between the observation groups by means of VCE; a regularization parameter λ_{VCE} is also generated. In the second step, the weighting factors ω_p are kept, but the regularization parameter λ_{VCE} is not used. Instead, a new regularization parameter is regenerated using the L-curve method, based on these weights. The final solution is then computed using Eq. (5.8) with the weights ω_p from VCE and the new regularization parameter $\lambda_{\text{L-curve}}$ from the L-curve criterion.

Lc-VCE

Figure 5.4 (Fig. 4 in **P-I**) illustrates the procedure of the Lc-VCE. In contrast to the VCE-Lc, in the Lc-VCE the L-curve method is applied first based on empirically chosen values for the relative weights ω_p.

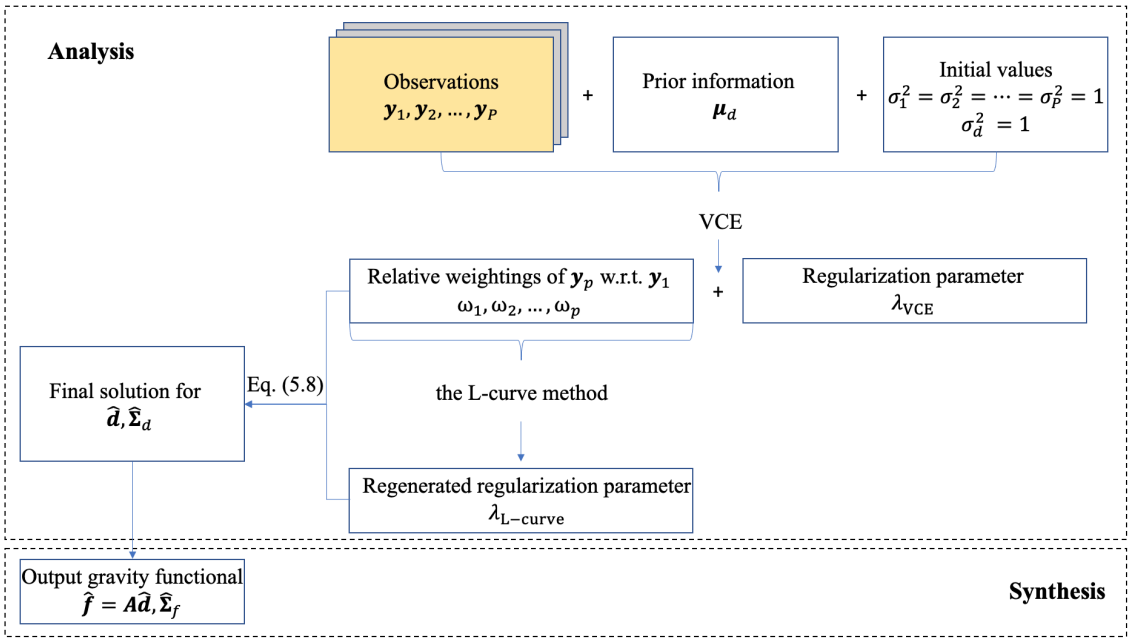


Figure 5.3: Combination of different types of observations based on the regularization method VCE-Lc (adapted from **P-I**)

A regularization parameter $\lambda_{\text{L-curve}}$ is obtained in the first step, and it is used for defining the value of σ_d^2 in the VCE. In the second step, the VCE is applied with initial values $\sigma_1^2 = \sigma_2^2 = \ldots = \sigma_P^2$ and $\sigma_d^2 = \sigma_1^2/\lambda_{\text{L-curve}}$. After each iteration within the VCE, the value of σ_d^2 is set to $\sigma_1^2/\lambda_{\text{L-curve}}$ again, with the new value of σ_1^2 obtained in this iteration. In this case, the regularization parameter λ calculated from the L-curve method will be kept, but the relative weighting factors ω_p are recomputed in each iteration step.

In **P-I**, these two combined approaches are compared with the L-curve method and VCE using simulated terrestrial, airborne, and satellite gravimetry data in six study cases, based on different combinations of data groups. Two comparison criteria are used; the RMS error between the computed disturbing potential and the validation data, as well as the correlation between the estimated coefficients and the validation data. A higher correlation indicates a better representation of the gravity signal (see Sect. 4.2 in **P-I** for more details). Numerical results and detailed discussions can be found in **P-I**, while the key findings and conclusions are summarized here. The investigation shows that the L-curve method or the VCE alone does not guarantee a reliable regularization result. The answer to **Q-1** is that VCE fails to provide a sufficient regularization in study cases where strong regularization is required, e.g., when only satellite gravity data are used, and when large data gaps exist (see Sect. 5.1 in **P-I** for more details). In such cases, the RMS error obtained from VCE-Lc decreases by up to 60% compared to the one delivered by the VCE. This conclusion is further verified in **P-II** by the modeling results using real gravity observations. In the "1 cm Geoid Experiment", when calculating the airborne-only solution (see Sect. 6.1), the regularization parameter delivered by VCE is almost two magnitudes smaller than the one given by the VCE-Lc, due to the data gaps and downward continuation of the airborne observations (see Fig. 3.3a).

On the other hand, the L-curve method relies heavily on the empirically chosen relative weights, and it cannot deliver reasonable modeling results if these weights are not chosen accurately. When various types of observations are combined, the L-curve method delivers an RMS error 75% larger than the one given by the combined approaches if the relative weights are chosen equally, i.e., $\omega_p = 1$. These results answer **Q-3**: the impact of the regularization parameter on the modeling accuracy is significant.

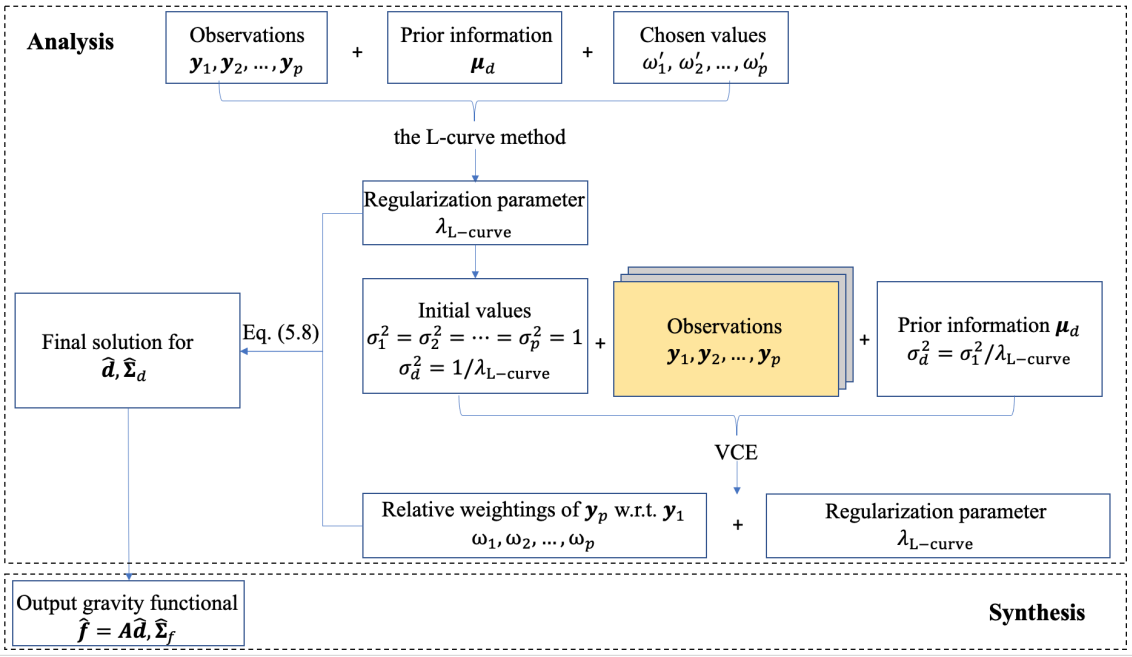


Figure 5.4: Combination of different types of observations based on the regularization method Lc-VCE (adapted from **P-I**)

When the regularization parameter is not estimated properly, i.e., when the L-curve method or VCE is applied alone, the gravity model could deliver an RMS error up to two times larger. The drawbacks of these two methods are overcome by applying the proposed combined approaches. Among the two combined approaches, the VCE-Lc generally gives better results in terms of both the two criteria. Furthermore, the performance of the Lc-VCE also depends on the empirically chosen weights, as the regularization parameter generated by the L-curve method in the first step will be kept. Thus, the VCE-Lc approach is then applied throughout this work for determining the regularization parameter.

6 Results and discussion

This chapter presents the major results of this work, i.e., regional gravity models derived from both the single-level SRBF approach and the MRR using various types of gravity observations in different study areas. These regional models are computed by setting up the estimation models (Chap. 5) based on the methodologies presented in Chap. 4 using gravity data and models as introduced in Chap. 3. The connection between related sections are shown in Fig. 6.1.

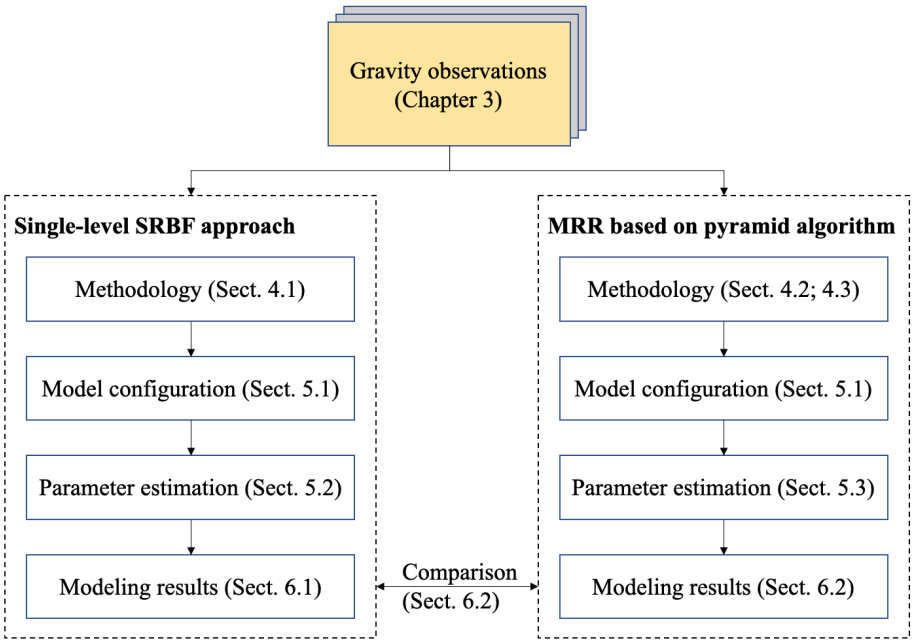


Figure 6.1: Flowchart regarding the procedure for calculating regional gravity models

6.1 "1 cm geoid experiment"

The "1 cm Geoid Experiment" means a milestone in the international effort towards the high-accuracy geoid determination for the realization of the IHRS, and it provides a basis for the evaluation and further development of procedures. This experiment is of great interest and importance for three reasons:

- Colorado is a mountainous area with high elevations (with an average of 2017 m and a maximum of 4386 m) and rugged topography (see Fig. 3.3b), which makes the gravity field modeling challenging. If a 1 cm accuracy is obtained in this study area, even higher accuracies can be expected in other study areas by the applied modeling procedure, since the accuracy of the geoid determination decreases when the topographic heights increase (Foroughi et al., 2019).

- The NGS provides not only high-resolution terrestrial and airborne gravity observations (see Sect. 3.3), but also a set of GNSS/leveling data at 223 GSVS17 benchmarks (red line in Fig. 3.3a) with a mean distance of 1.6 km along the U.S. Highway 160. Thus, the accuracy of the modeling results can be evaluated.
- With altogether fourteen participated groups from thirteen countries involved in this experiment with different methodologies, the comparison of the results highlights the disparities of each method.

Each group calculates the height anomaly, the geoid height, and the geopotential values at the GSVS17 benchmarks and for the whole target area (black rectangle in Fig. 3.3a), respectively, without the knowledge of the GNSS/leveling data. The involved computation methods include the Stokes' integral (Claessens and Filmer, 2020; Wang et al., 2020), the LSC (Willberg et al., 2020; Grigoriadis et al., 2021), the least-squares modification of Stokes' formula (Jiang et al., 2020; Varga et al., 2021), and the SRBFs (**P-II**), which well-represent the state-of-art methodologies in regional (quasi-) geoid modeling. Beside the methodologies, discrepancies exist in processing strategies regarding

- the filtering and downward continuation of the airborne data,
- the combination of terrestrial and airborne observations,
- the handling of terrain effects,
- the choice of the GGMs.

The detailed comparison of the height anomaly and the geoid height results delivered by each participating group is presented in Wang et al. (2021), and the comparison of geopotential values is given in Sánchez et al. (2021). Among the fourteen contributions, eleven groups followed Molodensky's theory, i.e., calculated the height anomaly directly, and converted it to geoid height by including a geoid-quasigeoid separation term (see Sect. 2.3); three groups calculated the geoid height first following Stokes' theory. As our geoid height result is obtained from the height anomaly by adding the geoid-quasigeoid separation term given by Heiskanen and Moritz (1967), i.e., the Eqs. (2.26) and (2.27), which includes an approximation, it is expected to be less accurate than the height anomaly result. Consequently, the evaluation in **P-II** and this section focuses only on the height anomaly results.

As the only group implementing the method of SRBFs, we documented the computation procedure step by step in **P-II**, where the research question **Q-4** is answered in detail. Due to the high elevation and rugged terrain in this study area, not only a GGM but also topography models (see Sect. 3.5) are included in the RCR procedure. The remaining part is then modeled by the combination of the terrestrial and the airborne observations, and the estimation model is set up following Eq. (5.7). The relative weight between the two data types and the regularization parameter are determined by the VCE-Lc approach proposed in **P-I**. An innovation of **P-II** is the combination of two different types of SRBFs for the terrestrial and the airborne data, respectively. To be more specific, the Shannon function is used for the terrestrial data and the CuP function is applied to the airborne data as a low-pass filter for reducing the high-frequency noise. Although the idea of using different SRBFs for different observations was proven in theory to be possible by the Theorem presented in Sect. 4.1, it is applied to real data for the first time, in **P-II**.

An internal validation, i.e., the statistical analysis of the residuals is presented in **P-II**, and the Figs. 6.2a and 6.2b (cf. Fig. 7 in **P-II**) show the residuals of the terrestrial and the airborne data, respectively. These residuals give STD values of 2.13 mGal and 1.25 mGal for the terrestrial and the airborne data, which indicate that the estimation model fits the airborne data better than the terrestrial data. This is explainable as the terrestrial observations were gathered during a large time span with varying quality, and the GRAV-D airborne measurements were collected in recent years (see Sect. 3.3). The largest residuals in Fig. 6.2 are located in high-elevation areas, and a correlation with the terrain map (Fig. 3.3b) can be seen. This indicates that a further improvement in the quasi-geoid model

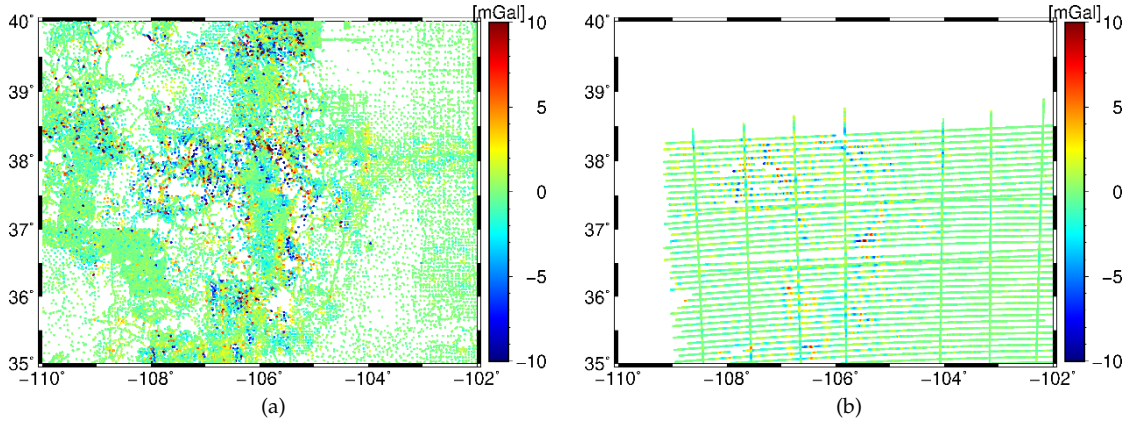


Figure 6.2: Residuals of (a) the terrestrial gravity data, and (b) the airborne gravity data from the least-squares estimation

could be achieved by applying a more accurate topography model that might be available in the near future. The SRBF-based modeling results are evaluated w.r.t. the mean results of all contributions in **P-II**, as the GNSS/leveling data have not been available to the participating groups until recently. Compared to the mean results, the SRBF-based height anomaly values give RMS errors of 1.0 cm and 1.6 cm along the GSVS17 benchmarks and in the whole study area, respectively, which are the smallest among all the contributions. This section focuses on the validation of the SRBF-based results w.r.t. the GNSS/leveling data. Note that the GNSS/leveling data actually contain 222 instead of 223 benchmarks, as the benchmark Nr. 77 was ultimately omitted because of its location on a sharp switchback in the route (see van Westrum et al., 2021 for more details).

Validation with the GNSS/leveling data

Compared to the GNSS/leveling data, the SRBF-based height anomaly result gives an STD of 2.64 cm, which is among the five models of the best agreement (Wang et al., 2021). This comparison confirms that the modeling result delivered by the SRBFs is comparable to those obtained by other methods, and also answers the research question **Q-6**. The differences between the SRBF-based height anomaly result and the GNSS/leveling data are plotted in Fig. 6.3 (red line), and the statistics are listed in Table 6.1. It is worth mentioning that a bias of 88 cm between the models and the GNSS/leveling data has been removed (Wang et al., 2021), which is due to the difference between the adapted W_0 value used in this experiment and that of the North American Vertical Datum of 1988 (NAVD88). As a reference, the differences between the mean result of all contributions and the GNSS/leveling data are also plotted (cyan line in Fig. 6.3). The mean result is close to the SRBF-based solution, giving an STD of 2.55 cm.

In Fig. 6.3, there is a noticeable sudden increase of almost 10 cm after benchmark Nr. 160 (vertical line in Fig. 6.3) in both the SRBF-based result and the mean result in comparison to the GNSS/leveling data, and such behavior is observed in all the fourteen contributions (see Wang et al., 2021 for more details). The fourteen groups performed the computation independently with different methods and procedures. Thus, it is unlikely that this increase comes from computation errors. Although this slope seems to be correlated with the peak in the ellipsoidal height (black line in Fig. 6.3), there is no such behavior at the first peak of height (around Nr. 86) where the elevation raises from 2200 m to 3300 m in about 60 km distance. Wang et al. (2021) pointed out that the exact reason for such a behavior is unknown yet, but it could be caused by errors in the GSVS17 validation data or in the gravity data.

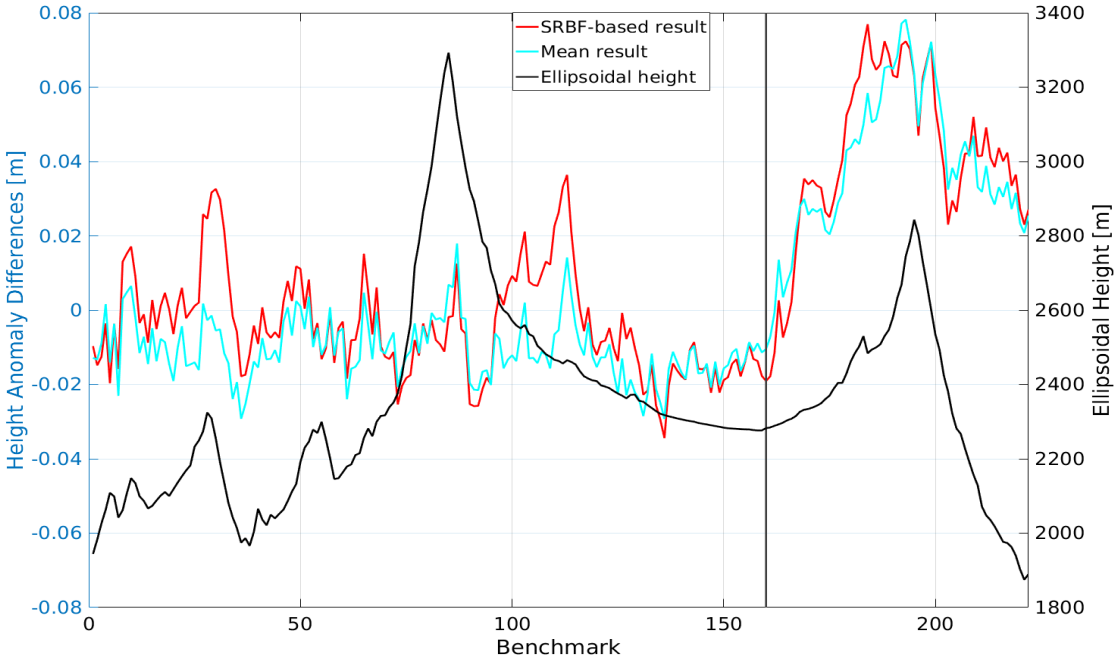


Figure 6.3: Differences between the GSVS17 validation data and the SRBF-based height anomaly result (red line) as well as the mean result (cyan line). The ellipsoidal height (black line) of the GSVS17 benchmarks and the benchmark Nr. 160 (vertical line) are plotted for interpretation reasons

Table 6.1: Comparison between the GNSS/leveling data and the height anomaly results, unit [cm]

		Min	Max	Mean	STD
222 benchmarks	SRBF	-3.44	7.69	0.85	2.64
	Mean of all contributions	-2.92	7.82	0.33	2.55
160 benchmarks	SRBF	-3.44	3.64	-0.43	1.37
	Mean of all contributions	-2.92	1.79	-1.06	0.82

In either case, it makes sense to exclude the benchmarks after Nr. 160 in the validation for a fair comparison. The statistics of the comparison at the first 160 benchmarks are also listed in Table 6.1. The STD values of the SRBF-based result and the mean result are 1.37 cm and 0.82 cm, respectively. van Westrum et al. (2021) estimated the accuracy of the GNSS/leveling data to be around 1.3 cm, and thus, the accuracies of both the mean result and the SRBF-based result are generally within the uncertainty of the GNSS/leveling data. Providing validation data with sub-cm accuracy to verify the 1 cm geoid accuracy could be as challenging as calculating the 1 cm geoid itself (Wang et al., 2021). Nevertheless, the results obtained in this experiment indicate that the 1 cm (quasi-) geoid is achievable even in areas with rugged terrain.

Contribution of the regional gravity measurements

To assess how much the quasi-geoid model benefits from the regional terrestrial and airborne gravity data, i.e., to answer the research question **Q-5**, four solutions are computed and compared,

namely the terrestrial and airborne combined solution, the terrestrial-only, the airborne-only, and the models-only solution, i.e., only the GGM (XGM2016 up to degree 719) and the topography models (dV_ELL_Earth2014 from degree 720 to 2159 and ERTM2160 from degree 2160 to $\sim 80,000$) are used without any regional observations. The terrestrial-only and the airborne-only solutions are computed in the same manner as the combined solution, i.e., the same GGM and topographic models as for the combined solution are used in the RCR procedure, and the remaining part is then modeled by the terrestrial or airborne data individually. In **P-II**, each solution is validated by the mean result of the other thirteen contributions along the GSVS17 benchmarks. Compared to the mean result, the models-only solution gives the worst result, with an RMS error of 4.04 cm; it is improved to 1.76 cm by adding the terrestrial data, and further improved to 1.08 cm by including the airborne data. The detailed comparison is presented and discussed in Sect. 5.2 of **P-II**. Here these four solutions are validated by the GNSS/leveling data, and the differences between each solution and the GNSS/leveling data are plotted in Fig. 6.4. The corresponding statistics are listed in Table 6.2. In this validation, the models-only solution (grey line in Fig. 6.4) still shows the worst performance, delivering the largest variation compared to the GNSS/leveling data (zero value line), with an STD of 4.39 cm (3.85 cm at the first 160 benchmarks). As explained in **P-II**, the topography models cannot represent the true high-frequency gravity signal accurately despite their high resolution, as they assume the topographic masses to have constant density, which is not the case in reality.

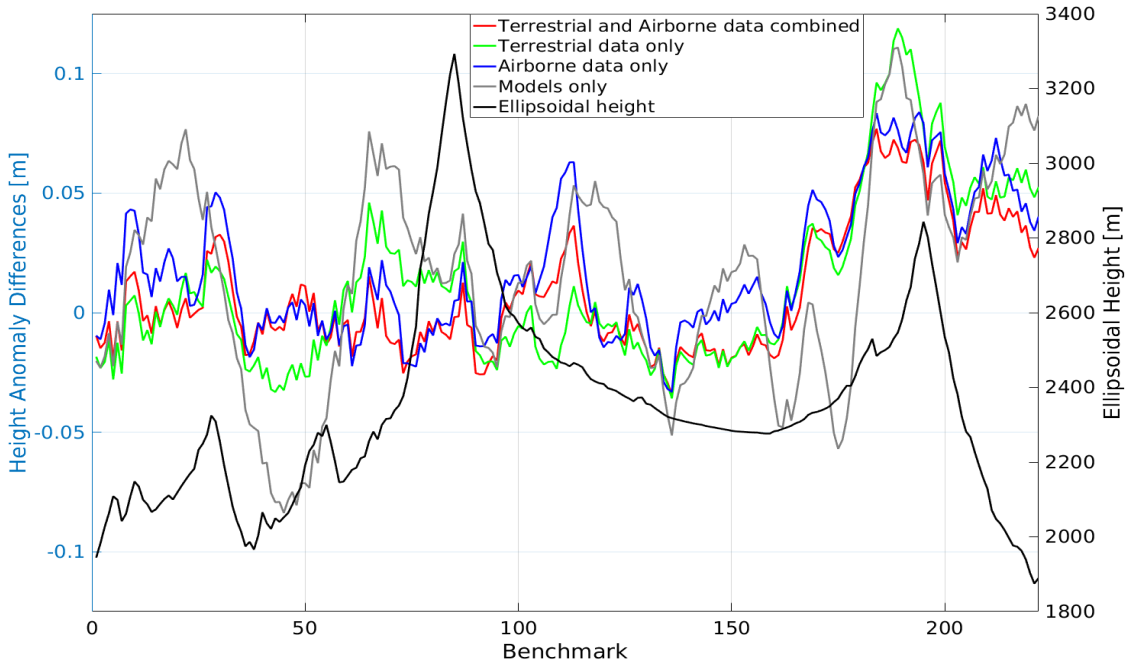


Figure 6.4: Differences between the GSVS17 validation data and the combined solution (red line), the terrestrial-only solution (green line), the airborne-only solution (blue line), as well as the models-only solution (grey line)

The statistics listed in Table 6.2 indicate that the airborne-only solution, with an STD of 2.84 cm, is better than the terrestrial-only solution, which gives an STD of 3.47 cm. However, Fig. 6.4 shows that the airborne-only solution (blue line in Fig. 6.4) actually has larger oscillations than the terrestrial-only solution (green line in Fig. 6.4), compared to the GNSS/leveling data. The reason for the smaller STD value in the airborne-only solution is that it shows a smaller slope after benchmark Nr. 160. This further indicates that the benchmarks after Nr. 160 should be excluded from the validation data to guarantee a fair comparison. At the first 160 benchmarks, the obtained STD values are 3.85 cm, 1.88 cm, 1.68 cm, and 1.37 cm for the models-only, airborne-only, terrestrial-only, and combined solution, respectively.

Table 6.2: Comparison between the GNSS/leveling data and the different solutions, unit [cm]

		Min	Max	Mean	STD
222 benchmarks	Combined	-3.44	7.69	0.85	2.64
	Terrestrial-only	-3.58	11.89	1.13	3.47
	Airborne-only	-3.31	8.39	1.78	2.84
	Models-only	-8.38	11.08	1.44	4.39
160 benchmarks	Combined	-3.44	3.64	-0.43	1.37
	Terrestrial-only	-3.58	4.60	-0.57	1.68
	Airborne-only	-3.31	6.29	0.52	1.88
	Models-only	-8.38	7.67	0.62	3.85

The possible reasons for the terrestrial-only solution to be better than the airborne-only solution are explained in **P-II**, which include (1) the terrestrial data have a larger coverage, and (2) the downward continuation of the airborne data, i.e., the airborne measurements are collected at an average altitude of 6 km to model the gravity field on the Earth surface, and thus, the modeling results are expected to be less accurate than using the surface gravity data.

For the terrestrial-only solution, its differences w.r.t. the GNSS/leveling data are highly correlated to the variations of the topography (black line in Fig. 6.4) at the GSVS17 benchmarks. This phenomenon is also reported in **P-II**, where the comparison is made with the mean results of the other thirteen groups. To be more specific, when the ellipsoidal heights are constant (between around benchmark Nr. 110 to Nr. 180), the terrestrial-only solution is almost identical to the combined solution. However, when there are big changes in the ellipsoidal heights (e.g. between around benchmark Nr. 40 to Nr. 90 as well as after benchmark Nr. 180), larger differences between the terrestrial-only solution and the validation data are observed. Including the airborne data seems to improve the terrestrial-only solution the most in rugged regions. This is reasonable due to the varying gravity in such regions, and thus, denser gravity observations are necessary to achieve a higher modeling accuracy.

The improvement in the combined solution is 18% compared to using terrestrial data only and 27% compared to using airborne data only, and it reaches 64% compared to using no regional gravity observations. Such significant improvements indicate the importance of high-resolution regional gravity data. It is clear from both Table 6.2 and Fig. 6.4 that the combined solution (red line in Fig. 6.4) benefits from both the terrestrial and the airborne data. Moreover, an interesting observation in Fig. 6.4 is that the combined solution always coincides with the solution (terrestrial-only or airborne-only) which shows less variation to the GNSS/leveling data. To be more specific, from benchmark Nr. 1 to Nr. 36 and from Nr. 116 to Nr. 180, the terrestrial-only solution shows smaller differences than the airborne-only solution w.r.t. the GNSS/leveling data, and the combined solution is close to the terrestrial-only solution at these parts. In contrast, from Nr. 37 to Nr. 100 and from Nr. 181 to Nr. 210, the combined solution coincides to the airborne-only solution, as it is better than the terrestrial-only solution. This indicates that the two types of gravity data are combined in a proper way.

Figure 6.5 shows the comparison between the combined solution and the models-only solution (Fig. 6.5a), the terrestrial-only solution (Fig. 6.5b), as well as the airborne-only solution (Fig. 6.5c), in the whole study area. Significant differences are observed between the combined solution and the models-only solution, especially at locations with high elevation. A correlation between Fig. 6.5a and the terrain map (Fig. 3.3b) can be seen. In the eastern part of the study area, which is more flat than the western and central part, smaller differences appear between the combined solution and the

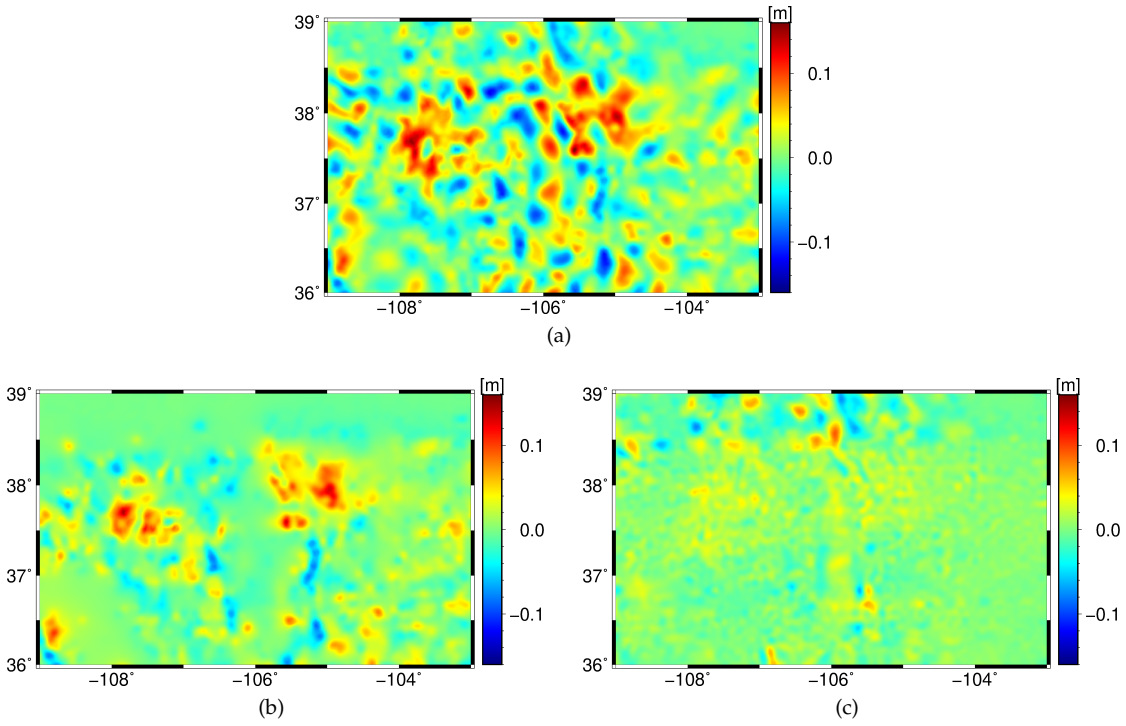


Figure 6.5: The differences between the combined solution and (a) the models-only solution, (b) the terrestrial-only solution, as well as (c) the airborne-only solution, in the whole study area

models-only solution. This comparison shows the necessity and importance of including regional gravity observations despite the high resolution of the used GGM and topography models, especially in high-elevation areas with rugged topography. The comparison between the combined solution and the terrestrial-only solution reveals the contribution of the airborne data to the quasi-geoid model. Larger differences in Fig. 6.5b show up in rugged region (central part of the study area), which coincides with the conclusion drawn from the validation w.r.t. the GNSS/leveling data. This gives some hints about where to place new airborne measurements in mountainous study areas. According to the findings in this study, airborne observations should be performed in rugged terrain in addition to the local terrestrial data. In the comparison between the combined solution and the airborne-only solution (Fig. 6.5c), differences mainly occur in areas without the airborne data coverage (see Fig. 3.3a), which is reasonable. In the area with airborne observations, the airborne-only solution is closer to the combined-solution than the terrestrial-only solution. This can be explained by the fact that the estimation model fits the airborne data better than the terrestrial data (see Fig. 6.2), since the airborne observations have been collected in recent years and are expected to have a higher quality than the terrestrial observations. Nevertheless, additional contribution of the terrestrial data is still observed, especially in high-elevation regions.

Performance of the GGMs

To answer the questions raised in Sect. 3.4, i.e., to compare the GGMs with the regional quasi-geoid model, the performance of different high-resolution GGMs, namely EGM2008, EIGEN-6C4, GECO, and XGM2019, is also validated in comparison to the GNSS/leveling data. Each GGM is truncated to degree 2159, and the topography model ERTM2160 is added to count for the very high frequency parts from degree 2160 to $\sim$ 80,000. The differences between the GNSS/leveling data and the quasi-geoid

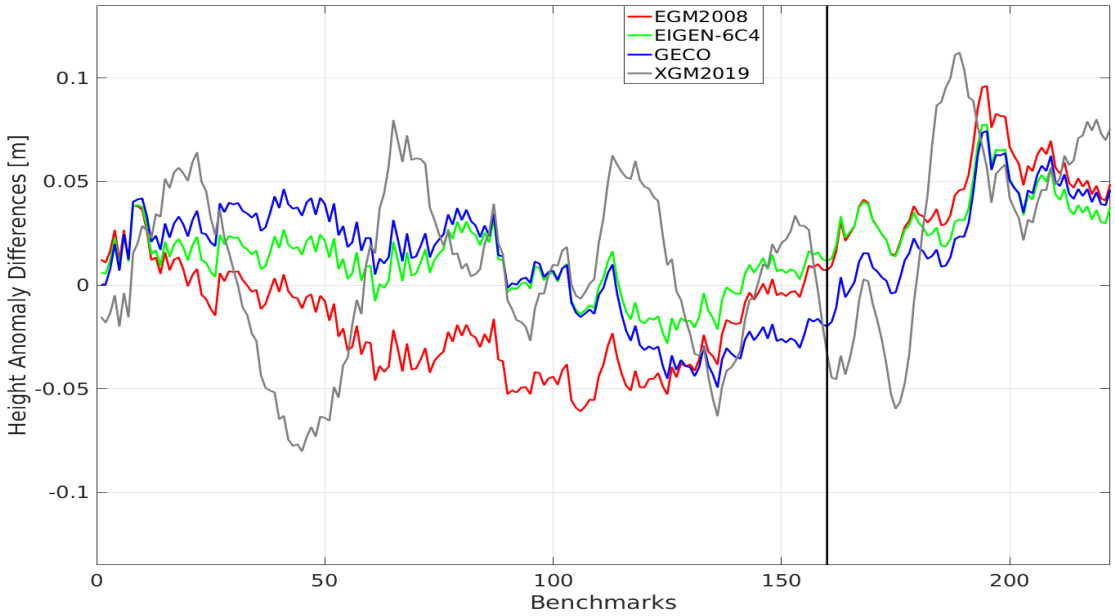


Figure 6.6: Differences between the GNSS/leveling data and the four GGMs (in combination with ERTM2160) at the GSVS17 benchmarks

Table 6.3: Comparison between the GNSS/leveling data and the GGMs (in combination with ERTM2160) at the first 160 benchmarks, unit [cm]

	Min	Max	Mean	STD
EGM2008	-6.08	3.83	-1.92	2.32
EIGEN-6C4	-2.82	3.86	0.80	1.39
GECO	-4.93	4.63	0.65	2.66
XGM2019	-8.02	7.97	0.48	3.80

calculated directly by the four GGMs in combination with ERTM2160 are shown in Fig. 6.6, and the statistics at the first 160 benchmarks are listed in Table 6.3. As shown in Fig. 6.6, the four tested GGMs differ significantly in comparison to the GNSS/leveling data, giving STD values ranging from 1.39 cm (EIGEN-6C4) to 3.80 cm (XGM2019). EGM2008, EIGEN-6C4, and GECO show the same pattern in the variation to the GNSS/leveling data, since the latter two models are developed based on EGM2008. However, EGM2008 gives a much larger mean value (-1.92 cm) at the first 160 benchmarks compared to the other three models, which could be due to the absence of GOCE data in the development of this model (see Sect. 3.4). Although EIGEN-6C4 and GECO are both based on EGM2008, EIGEN-6C4 delivers the smallest STD, thanks to the contribution of GOCE, GRACE, and SLR data to the long-wavelength component as well as the usage of a high-resolution gravity anomaly grid ($2' \times 2'$, see Sect. 3.4 for more details). XGM2019 shows a pretty different pattern than the other three models, and it gives the largest STD. This could be explained by the low resolution of the terrestrial gravity anomaly data set ($15' \times 15'$) used in the model determination of XGM2019 (Sánchez et al., 2021). In contrary, much denser gravity anomaly grids are employed by EGM2008 ($5' \times 5'$), GECO ($5' \times 5'$), and EIGEN-6C4 ($2' \times 2'$). Furthermore, in XGM2019 the gravity information above d/o 719 is derived from the topography model Earth2014, which assumes the topographic masses to have constant density. Thus, it is less accurate than using a high-resolution gravity anomaly grid formed by real gravity

observations, which contain signals of density mass changes. Nevertheless, it is worth clarifying that the performance of the GGMs depends on the testing region, and the validation here is not intended to rank the different GGMs but to compare the GGMs with the regional (quasi-) geoid model.

The comparison results show that it is not reliable to use only the GGMs in combination with topography models for (quasi-) geoid determination. The significantly varying performance of the GGMs implies that they are not sufficient for engineering purposes or geophysical investigation (Wu et al., 2017a), especially in mountainous areas. The standard deviations delivered by three of the test GGMs are much larger than the one given by the regional model, which demonstrates the necessity and importance of regional gravity field refinement with local gravity measurements. Thus, the GGMs cannot replace the regional (quasi-) geoid models, and high-resolution regional gravity field modeling is preferred for the determination of the IHRF coordinates, except for regions without or with very few surface gravity data (Sánchez et al., 2021).

Table 6.4: Comparison between the GNSS/leveling data and the regional quasi-geoid model calculated using different GGMs, truncated at different SH degrees, as background model (at the first 160 benchmarks), unit [cm]

	2159		1079		719		359	
	Mean	STD	Mean	STD	Mean	STD	Mean	STD
EGM2008	-2.13	1.40	-2.24	1.31	-2.29	1.33	-2.54	1.42
EIGEN-6C4	-0.25	1.19	-0.54	1.21	-0.88	1.29	-1.83	1.48
GECO	-0.01	1.51	-0.31	1.45	-0.69	1.39	-1.74	1.53
XGM2019	-0.54	1.37	-0.55	1.37	-0.55	1.35	-1.65	1.53

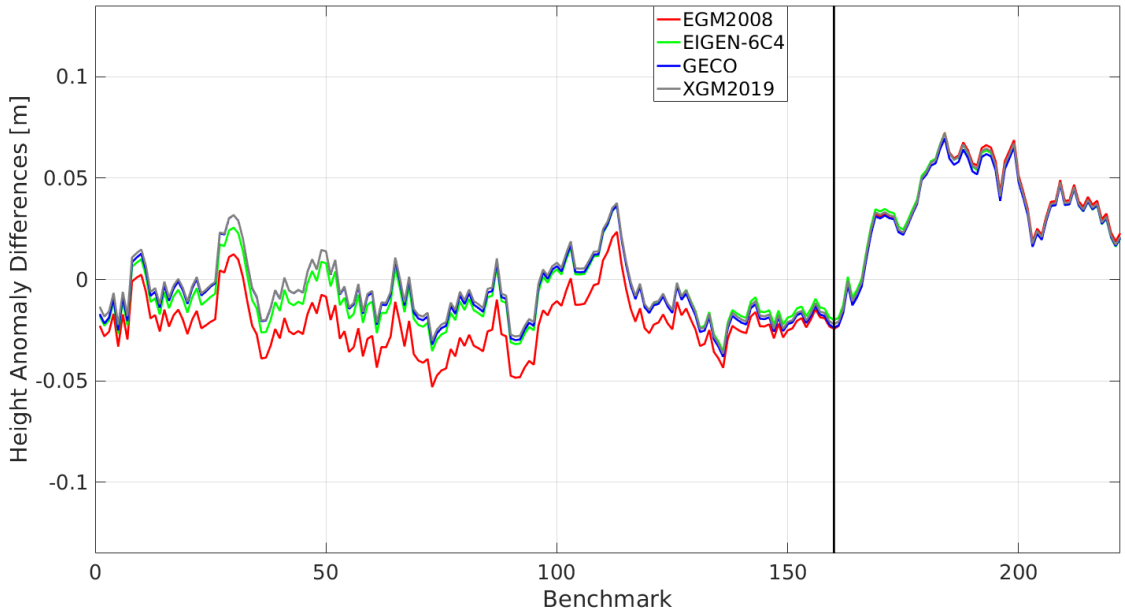


Figure 6.7: Differences between the GNSS/leveling data and the regional quasi-geoid model calculated using the four GGMs (truncated at degree 719) as background model

These four GGMs are also tested as background model within the RCR procedure for regional quasi-geoid modeling, i.e., in replacement of XGM2016. Each reference model is truncated to degree values

2159, 1079, 719, and 359, respectively, and the parts above the truncation degree are covered by the topography models (dV_ELL_Earth2014 and ERTM2160). The statistics (at the first 160 benchmarks) of the differences between the GNSS/leveling data and the regional quasi-geoid model based on each GGM are listed in Table 6.4. The regional models based on the different GGMs deliver similar results in terms of STD, with discrepancies less than 2 mm between each other. Among the four truncation degree values, 1079 and 719 generally give better results, i.e., smaller STD values. However, the differences between the four truncation degrees are also less than 2 mm in terms of STD. As an example, the differences between the GNSS/leveling data and the regional quasi-geoid model based on the four GGMs with truncation degree 719 are shown in Fig. 6.7. Despite the large discrepancies between the four GGMs (Fig. 6.6), they are able to provide almost identical result after regional quasi-geoid modeling. These results further show the reliability of the SRBF-based regional (quasi-) geoid determination method, as it is able to deliver stable modeling results regardless the choice of the GGMs. However, in Fig. 6.7 an offset (large mean value) is again observed in the solution based on EGM2008 at the first 160 benchmarks, and it disappears after the benchmark 160. The exact reason for such behavior of EGM2008 still requires further investigation.

6.2 Spectral combination via MRR

The gravity models calculated by the spectral combination via MRR are presented and discussed in **P-III**, and this section summarizes the key findings. The developed approach, i.e., the MRR based on the pyramid algorithm is firstly tested using simulated data and then applied to real gravity observations in different study areas, as shown in the Figs. 6.8a and 6.8b, respectively. The results obtained from the MRR are directly compared with those delivered by the single-level SRBF approach in order to highlight the benefits of the MRR based on the pyramid algorithm.

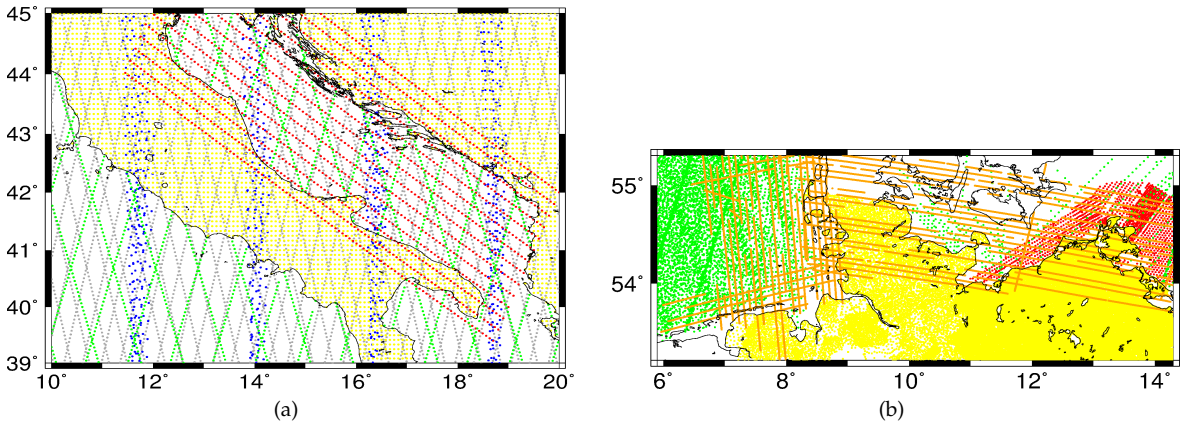


Figure 6.8: The study areas and the distributions of gravity data in (a) the simulated case, including terrestrial (yellow dots), airborne (orange dots), altimetry (green dots), GOCE (grey dots), and GRACE (blue dots) data, and (b) the real case, including terrestrial (yellow dots), shipborne (red dots), airborne (orange dots), and altimetry (green dots) data

In the simulated case, five types of gravity data are involved, namely terrestrial, airborne, and altimetry data, as well as satellite gravimetry data from GOCE and GRACE. These data are simulated from GECO, with the position of the observations (except the altimetry data) provided by the IAG-ICCT JWG 0.3, running from 2011 to 2015. The position of the altimetry data is obtained from the real ground track of Envisat (Extended Mission, see Sect. 3.2). All observations are simulated in the sense of disturbing gravity field quantities, i.e., first order radial derivatives of the disturbing potential for

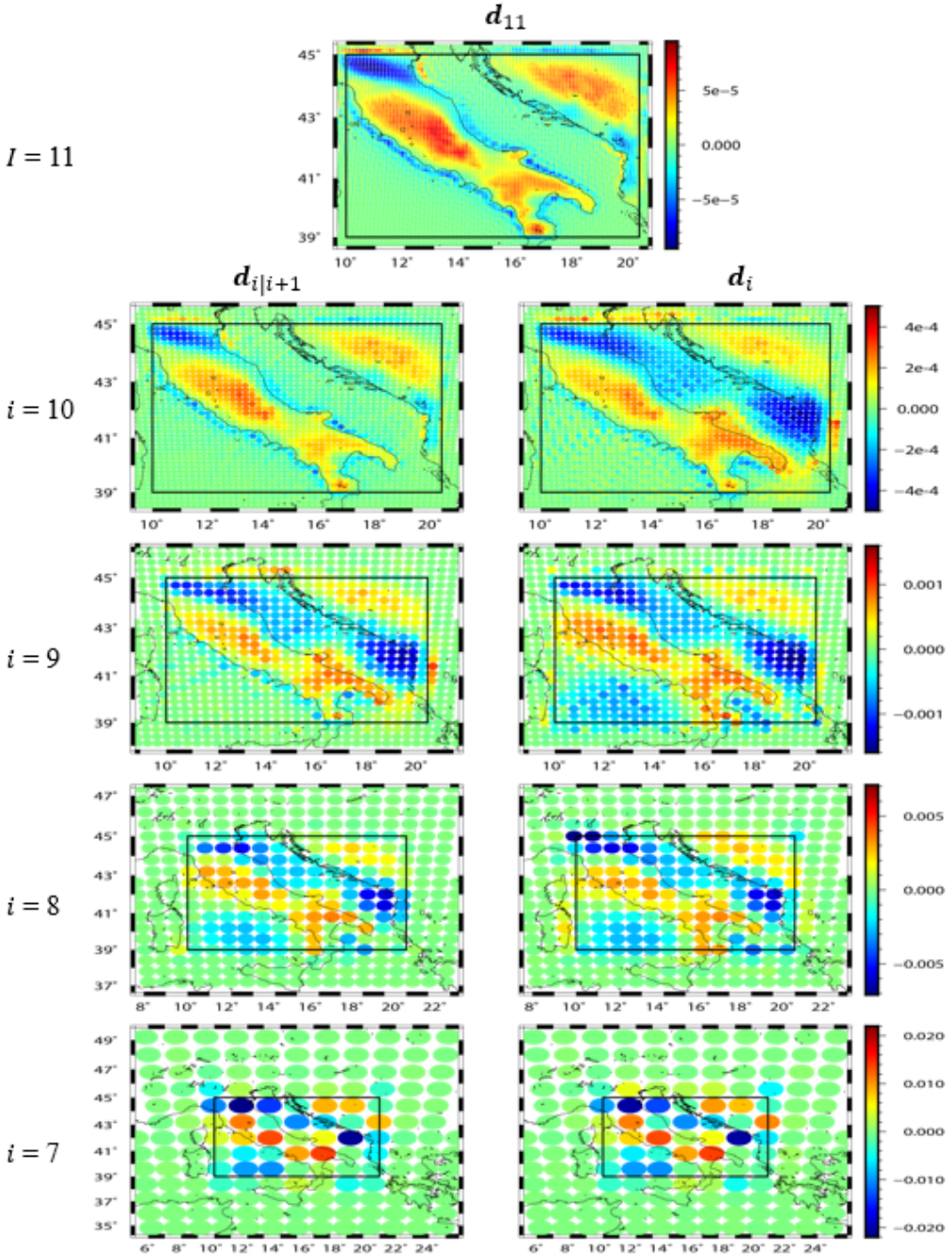


Figure 6.9: The estimated scaling coefficients at level $I = 11$ (first row), and levels $i = 10, 9, 8, 7$ (second to fifth row). From the second to the fifth row, the left column represents the coefficients $\boldsymbol{d}_{i|i+1}$ computed directly from the pyramid algorithm, and the right column represents the updated coefficients $\boldsymbol{d}_i$ after including the gravity data involved at this level. The black rectangle inside each plot shows the observation area $\partial\Omega_O$

the terrestrial and airborne data, geoid height for the altimetry data, second order radial derivatives of the disturbing potential for GOCE, and disturbing potential differences between the two satellites for GRACE. White noise with standard deviations of 0.01 mGal, 1 mGal, and 0.03 m is added to the terrestrial, airborne, and altimetry data; colored noise with standard deviations of 10 mE and

$8 \cdot 10^{-4}$ m^2/s^2 is added to the satellite data of GOCE and GRACE, respectively. The observation area $\partial\Omega_O$ is located between 39° and 45° latitude and between 10° and 20° longitude (Fig. 6.8a). Following the pyramid algorithm shown in Fig. 4.3, only the terrestrial data, which cover almost half of the study area, are used at the highest resolution level $I = 11$, according to the spatial resolution of the data. The coefficient vector $\boldsymbol{d}_{11}$ and its covariance matrix $\boldsymbol{\Sigma}_{d_{11}}$ are estimated according to the Eqs. (5.8) and (5.9) and transformed to $\boldsymbol{d}_{10|11}$ and $\boldsymbol{\Sigma}_{d_{10|11}}$ of level $i = 10$ by low-pass filtering according to the Eqs. (4.15) and (4.16). They are then updated by including the airborne data at level 10, and the updated coefficient vector $\boldsymbol{d}_{10}$ as well as $\boldsymbol{\Sigma}_{d_{10}}$ are calculated by the Eqs. (5.13) and (5.14). Continuing this process, the altimetry data are added at level $i = 9$, the GOCE data at level $i = 8$, and the GRACE data at level $i = i' = 7$; the coefficient vector of each resolution level is then estimated. Figure 6.9 (cf. Fig. 6 in **P-III**) visualizes the updated coefficients (right column) and those obtained directly from the pyramid algorithm (left column) at each resolution level. From the first row (level $I = 11$) to the last row (level $i' = 7$), the margin size $\eta_{C,O}$ increases from 0.3° to 4.8° following Eq. (5.2), and the density of the coefficients decreases gradually, as explained in Sect. 5.1. The top row shows the scaling coefficients collected in the vector $\boldsymbol{d}_{11}$ at level $I = 11$, which are estimated from the terrestrial observations only. Comparing it with Fig. 6.8a, additional gravity signals are only captured at the locations with terrestrial data coverage, which is reasonable. The comparison between the left plots and the right ones shows that the gravity observations at each level insert additional information in the areas where they are located, and at the same time, the gravity signals captured from the previous levels are preserved.

Figure 6.10 (cf. Fig. 7 in **P-III**) visualizes the estimated detail signals $\boldsymbol{G}_i$ of the MRR as well as the gravity signals $\boldsymbol{F}_i$ at each level i. The detail signals (left column in Fig. 6.10) at different levels show the spectral information contained in the corresponding frequency ranges (see Fig. 4.1). When the resolution level increases from level $i' = 7$ (fifth row) to level $I = 11$ (first row), more and more fine structures show up. At level $I = 11$, the detail signal $\boldsymbol{G}_{11}$ captures gravity information only in the onshore area where the terrestrial data are located. However, at the border of the terrestrial data, strong edge effects appear due to the Gibbs phenomenon. At level 10 where only terrestrial and airborne data are involved, large edge effects are also observed at the border of the data coverage, i.e., in the coastal area of the Tyrrhenian Sea. After level 9, the involved observations have full coverage over the observation area $\partial\Omega_O$ (Fig. 6.8a), and no edge effects are visible within $\partial\Omega_I$. The edge effects in $\boldsymbol{G}_{11}$ and $\boldsymbol{G}_{10}$ will further contaminate the final gravity model, as shown in Fig. 6.11b. To address this issue, a strategy is developed in **P-III** to reduce the edge effects in the calculated detail signals $\boldsymbol{G}_i$. Besides the observation area $\partial\Omega_O$ and the investigation area $\partial\Omega_I$ for the whole study area (see Sect. 5.1), we also define $\partial\Omega_{O_i}$ and $\partial\Omega_{I_i}$ for each resolution level i when calculating the detail signals. $\partial\Omega_{O_i}$ depends on the data coverage of the observation groups involved at this level i, and $\partial\Omega_{I_i}$ is adapted to $\partial\Omega_{I_i} = \partial\Omega_{O_i} \cap \partial\Omega_I$. The detail signals $\boldsymbol{G}_i$ of level i are then calculated within $\partial\Omega_{I_i}$. As an example, $\partial\Omega_{O_{11}}$ is defined as the onshore areas in Fig. 6.8a since only terrestrial observations are involved at level 11. Consequently, $\partial\Omega_{I_{11}}$ is adapted to the onshore areas within the investigation area $\partial\Omega_I$. The new detail signals of level 11 and 10 after adapting $\partial\Omega_{I_i}$ are presented in Fig. 6.10 (mid column), and the edge effects are significantly reduced. Figure 6.10 (right column) shows the gravity signal (in terms of disturbing potential) $\boldsymbol{F}_{I'} = \bar{\boldsymbol{F}} + \sum_{i=7}^{I'} \boldsymbol{G}_i$ of each level, with the gravity signal $\bar{\boldsymbol{F}} = \boldsymbol{F}_6$ in the bottom panel of the right column being the long wavelength component modeled from GECO.

Figures 6.11a and 6.11b (cf. Fig. 8 in **P-III**) show the differences between the validation data and the gravity model in terms of disturbing potential calculated from the MRR based on the pyramid algorithm after and before applying the proposed strategy for reducing the edge effects, respectively. The corresponding statistics are listed in Table 6.5 (Table 2 in **P-III**). Comparing Fig. 6.11a to Fig. 6.11b, the edge effects at the border (outside the coverage) of the terrestrial data are significantly reduced. The improvement achieved by applying this strategy is 21% in terms of RMS, w.r.t. the validation data. However, at the border (inside the coverage) of the terrestrial observations, the edge effects remain the same after adapting $\partial\Omega_{I_i}$, as also shown in the calculated detail signals at levels 11 and level 10

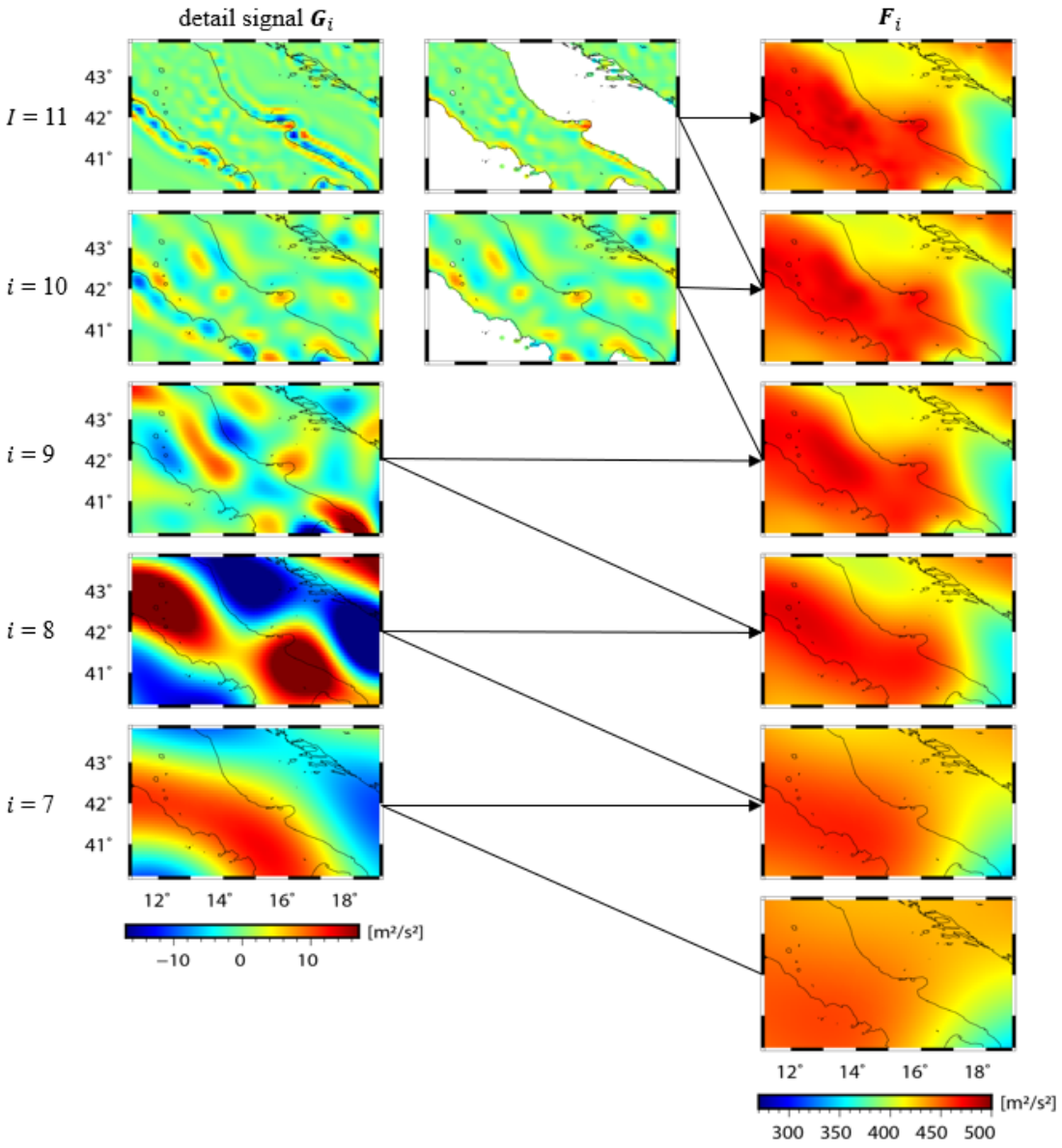


Figure 6.10: The detail signal G_i of the MRR based on the pyramid algorithm before (left column) and after (mid column) adapting the investigation area $\partial\Omega_{I_i}$, as well as the estimated gravity signal (in terms of disturbing potential) $F_{I'} = \bar{F} + \sum_{i=7}^{I'} G_i$ (right column) from level $I' = 11$ (first row) to level $I' = 7$ (fifth row), with $\bar{F}$ (right column, last row) modeled from GECO

(Fig. 6.10, mid column). Thus, it is planned for future work to develop strategies that further reduce these edge effects, e.g., implementing a tapering at the border of the high-resolution gravity data.

To demonstrate the benefits of the spectral combination through MRR, the gravity model based on the single-level approach is computed, and Fig. 6.11c shows it differences w.r.t. the validation data. In the single-level model, much larger differences are obtained in offshore than in onshore regions, where the terrestrial data are available. It indicates that the single-level approach majorly recovers gravity information from the terrestrial observations, and the contribution of other measurements which are sensitive to lower spectral bands is not captured sufficiently. In contrast, such terrestrial-data-

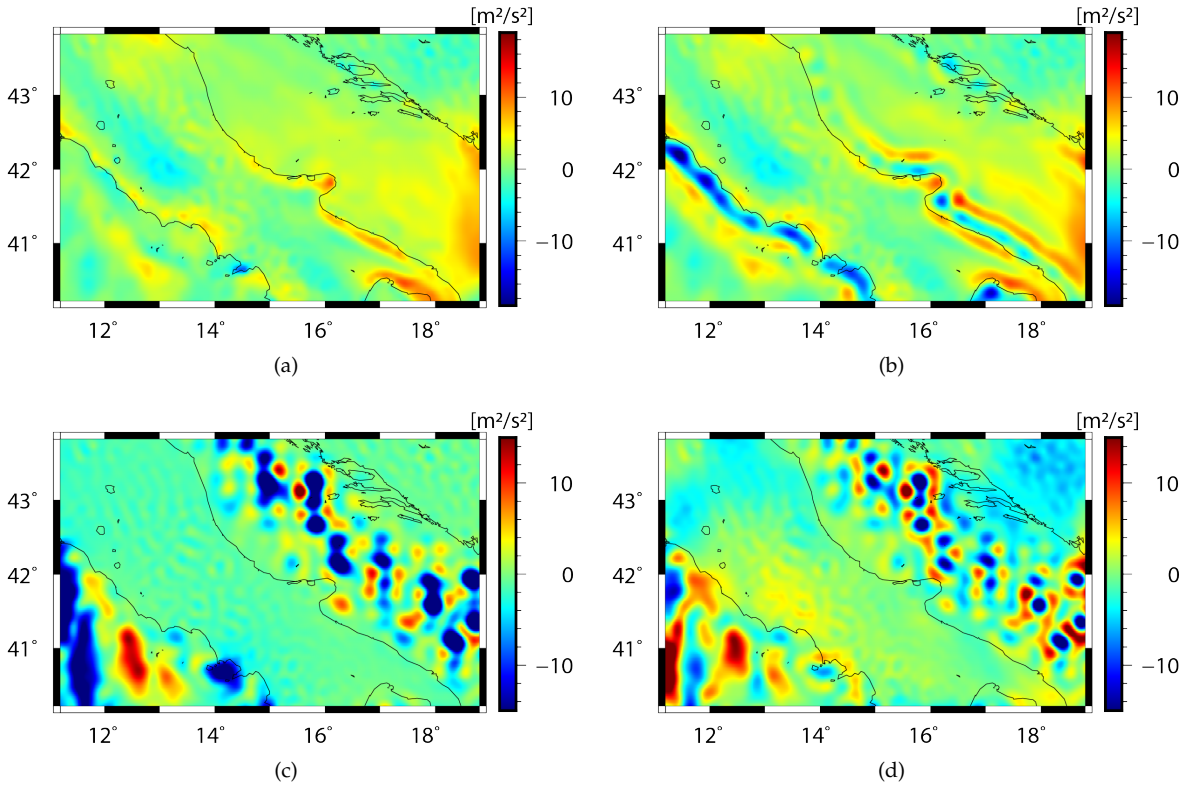


Figure 6.11: Differences between the estimated disturbing potential and the validation data, delivered by (a) the MRR based on the pyramid algorithm, (b) the MRR based on the pyramid algorithm before applying the developed strategy for reducing edge effects, (c) the single-level approach, and (d) the MRR without pyramid algorithm

dependent pattern is not visible in the solution of the MRR based on pyramid algorithm (Fig. 6.11a). The RMS error delivered by the MRR based on the pyramid algorithm is 2.72 m^2/s^2, which is 50% smaller than the value given by the single-level approach. These results answer the research question **Q-8**, and demonstrate the necessity and benefits of the developed MRR approach.

Table 6.5: Evaluation of the MRR and the single-level model with respect to the validation data in terms of disturbing potential values (unit $[m^2/s^2]$)

	Min	Max	RMS
MRR based on pyramid algorithm (Fig. 6.11a)	-11.63	11.41	2.72
MRR based on pyramid algorithm (before adapting $\partial\Omega_{I_i}$ to reduce edge effects, Fig. 6.11b)	-20.98	12.82	3.44
Single-level model (Fig. 6.11c)	-38.22	21.64	5.48
MRR without pyramid algorithm (Fig. 6.11d)	-27.13	27.64	4.21

Furthermore, to verify the advantages of applying the pyramid algorithm, an additional comparison is

conducted with the MRR without applying the pyramid algorithm, i.e., the coefficients are estimated independently at each level using all types of observations. The differences between the validation data and the calculated model are shown in Fig. 6.11d, and the statistics are listed in Table 6.5. Compared with the single-level approach, its differences w.r.t. the validation data decrease in offshore regions, which indicates that the gravity information in lower-resolution observations are better captured. Consequently, the RMS error delivered by the MRR without pyramid algorithm is 23% smaller than that of the single-level model. However, the same pattern as the single-level model is observed in Fig. 6.11d, i.e., larger differences show up in the offshore regions comparing to the onshore area. After applying the pyramid algorithm (Fig. 6.11a), the differences in the offshore area become much smaller, and an improvement of 35% is obtained in terms of RMS value. These results further contribute to the answer of the research question **Q-8**, i.e., show the benefit of applying the pyramid algorithm.

In the case of real data, the developed method is applied to calculate the regional quasi-geoid and gravity anomaly models in Northern Germany, i.e., between 53.2° and 55.3° latitude and between 5.9° and 14.3° longitude (see Fig. 6.8b). Four types of gravity observations are used, namely terrestrial, shipborne, airborne, and altimetry data, and a detailed data description can be found in **P-III**. The computation of the MRR based on the pyramid algorithm is carried out in the same manner as the simulated case, following Fig. 4.3. The terrestrial observations are used at the highest level $I = 12$ to calculate the unknown coefficients of this level and to start the pyramid algorithm. The shipborne, airborne, and altimetry measurements are included at levels 11, 10, and 9, respectively. The number of grid points at each resolution level as well as the margin sizes $\eta_{C,O}$ and $\eta_{O,I}$ are chosen following Sect. 5.1. The developed strategy as explained in the simulated case, i.e., adapting $\partial\Omega_{I_i}$ to reduce edge effects in the calculated detail signals, is applied as well.

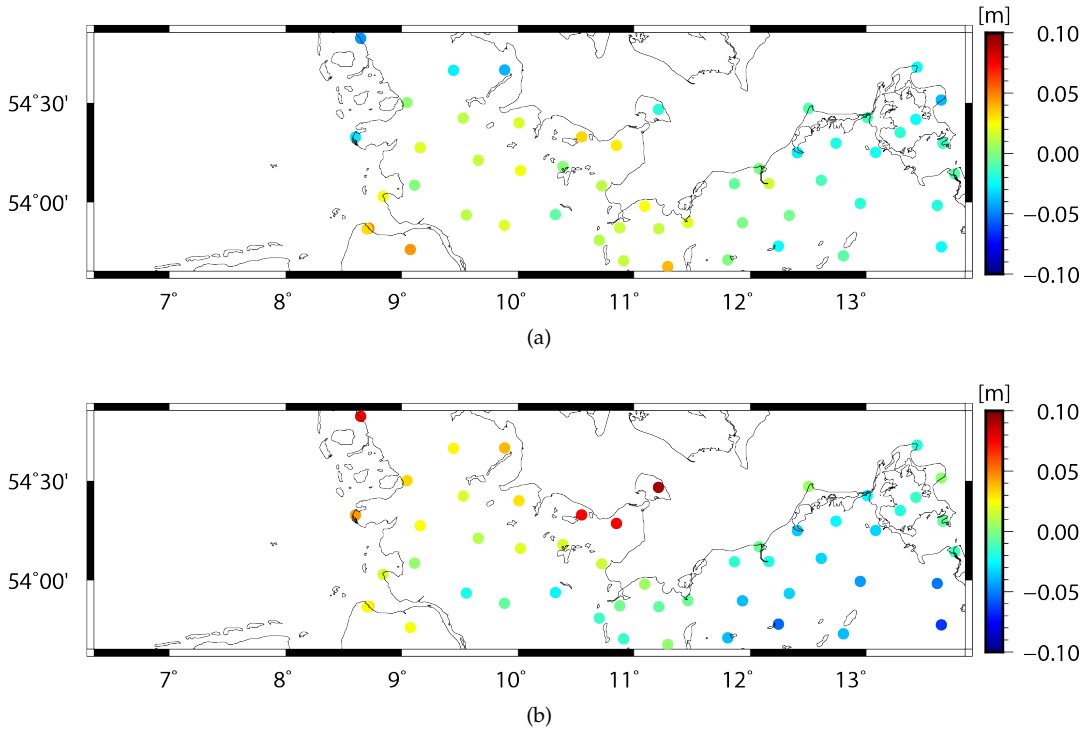


Figure 6.12: Differences between the calculated quasi-geoid model and the GNSS/leveling data in the onshore area, delivered by (a) the MRR based on the pyramid algorithm, and (b) the single-level approach. Note that the mean values of the differences are removed

The quasi-geoid models calculated by the MRR based on the pyramid algorithm and the single-level

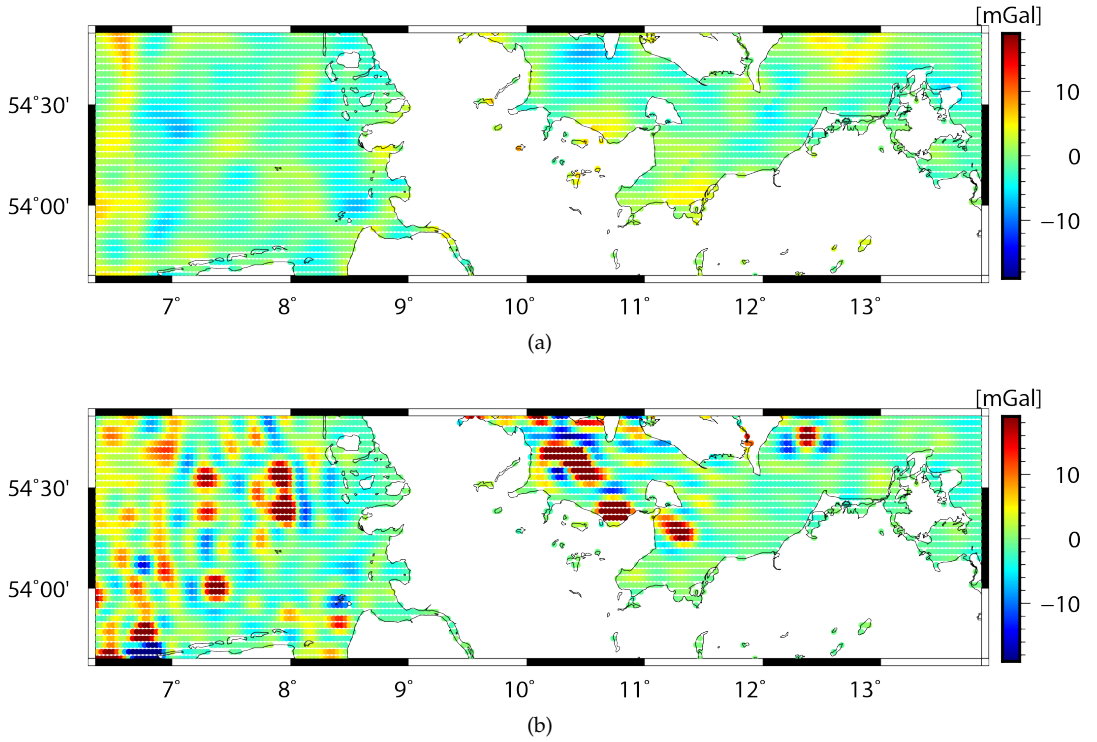


Figure 6.13: Differences between the calculated gravity anomaly model and the DTU17 in the offshore area, delivered by (a) the MRR based on the pyramid algorithm, and (b) the single-level approach

approach are validated using GNSS/leveling data in Northern Germany (Gruber et al., 2011), and their differences are visualized in Fig. 6.12 (cf. Fig. 11 in **P-III**). The MRR based on the pyramid algorithm delivers smaller differences w.r.t. the GNSS/leveling data, giving an RMS error of 2.23 cm, as shown in Table 6.6, which is 35% smaller than that of the single-level approach (3.43 cm). The calculated gravity anomaly models are validated with a DTU $2' \times 2'$ gravity anomaly grid (DTU17, Andersen and Knudsen, 2019) in the offshore area. Figure 6.13 (cf. Fig. 12 in **P-III**) shows the differences between the computed gravity anomaly models and the DTU17, delivered by the MRR based on pyramid algorithm (Fig. 6.13a) and the single-level approach (Fig. 6.13b), respectively. The corresponding statistics are listed in Table 6.6. In the single-level model, much smaller differences are observed in regions with shipborne data coverage (see Fig. 6.8b), which suggests that it majorly recovers gravity information from the high-resolution shipborne data, and information from other measurement types is not captured sufficiently. The MRR based on pyramid algorithm again delivers smaller differences, and the obtained RMS value decreases by 63% in comparison to the single-level approach. The improvement achieved by applying the MRR based on the pyramid algorithm is even larger in the offshore area than in the onshore area, where the high-resolution terrestrial data are available. These results agree with the conclusion drawn from the simulated study case, and further answer the research question **Q-8**.

In these two study cases, gravity data from various observation techniques with different spectral and spatial resolution are combined, and the high-resolution measurements do not have coverage over the whole study area. In such case, it is especially beneficial to apply the MRR, as the single-level approach would be biased towards the high-resolution data and is not able to extract the full information from measurements with medium to low resolution. The improvement by applying the MRR based on the pyramid algorithm is significant in these study cases, with the RMS values decrease by more than

Table 6.6: Evaluation of the MRR based on the pyramid algorithm and the single-level model w.r.t. GNSS/leveling data (in terms of quasi-geoid, note that the mean differences are removed) in the onshore area, and w.r.t. DTU17 (in terms of gravity anomaly) in the offshore area

	w.r.t. GNSS/leveling data (unit [cm])			w.r.t. the DTU17 grid (unit [mGal])		
	Min	Max	RMS	Min	Max	RMS
MRR based on pyramid algorithm	-4.50	5.15	2.23	-7.98	8.70	2.67
Single-level	-6.48	9.36	3.43	-53.24	60.46	7.22

30% compared to those obtained from the single-level approach, w.r.t. the validation data. However, when the high-resolution data have almost full coverage, the single-level approach is not expected to deliver worse results than the MRR. For instance, in the "1 cm geoid experiment", only the terrestrial and airborne gravity observations are involved with high data quality and almost full coverage, the single-level quasi-geoid model actually gives slightly smaller STD than the one calculated by the MRR. This could be due to the fact that less erroneous effects, e.g., edge effects, are included in the synthesis step in the single-level than in the multi-level. Thus, the choice of applying the single-level SRBF or the MRR based on the pyramid algorithm depends on each study case, i.e., depends on the involved data types and distributions. The answer to research question **Q-9** is: the MRR based on the pyramid algorithm should be applied when there are many types of gravity observations with different spectral resolution, especially in study areas where the high-resolution data do not have full coverage, such as offshore regions and developing areas with sparse terrestrial data.

7 Summary and outlook

7.1 Summary

This thesis focuses on regional gravity field modeling based on the combination of data from various observation techniques, for the realization of physical height systems. Chapter 2 presents the fundamental theory of gravity and the definition of different heights and height systems. Chapter 3 introduces various types of gravity observation techniques, as well as the gravity data and models involved in this work. The method of SRBFs is used, and based on it, a spectral combination is further implemented through the MRR by means of the pyramid algorithm to consider the spectral sensitivity of different observation techniques. Chapter 4 explains the methodologies of the SRBFs, the MRR, and the pyramid algorithm. The estimation models based on both the SRBFs and the MRR are then set up in Chap. 5, with the model configuration discussed in detail, including the type, bandwidth, location of the SRBFs, as well as the extension of the data zone. Different types of gravity observations are combined by the parameter estimation procedure, and the Tikhonov regularization is applied for solving the ill-posed problem. A new approach is proposed and recommended for the determination of the regularization parameter, which combines VCE and the L-curve method (**P-I**). The modeling results based on the SRBFs (**P-II**) and the MRR (**P-III**) are discussed in Chap. 6. In the single-level SRBF approach, the calculated high-resolution regional (quasi-) geoid model in Colorado contributes to the "1 cm geoid experiment", where it is compared with thirteen independent solutions from different modeling methods. The comparison shows that the STD of the SRBF-based (quasi-) geoid model is among the smallest w.r.t. both the mean result of all fourteen contributions and the GNSS/leveling data. In the MRR case, regional gravity models calculated by the MRR based on the pyramid algorithm are compared with those obtained from the single-level SRBF approach. The results show that it is beneficial to apply the MRR based on the pyramid algorithm, especially when the high-resolution gravity observations do not have full coverage over the study area, as it is able to extract information from measurements with medium to low resolution better than the single-level approach.

In summary, the research objectives listed in the Introduction are accomplished, and the research questions raised in Sect. 1.2 are answered:

Regularization method

Q-1. Is VCE sufficient for determining the regularization parameter?

VCE is not sufficient for the regularization parameter determination when a strong regularization is required, e.g., when large data gaps exist. In regions without data coverage, the estimation model relies heavily on the background model. However, as explained in Sect. 5.4, the prior information is regarded as an additional observation technique in VCE, and thus, is expected to be of random character. This requirement cannot be fulfilled as the background model, which is not stochastic, is used as the prior information. In such case, the regularization parameter generated by VCE is not reliable. Results in **P-I** show that in study areas with large data gaps, the regularization parameter λ generated by VCE is not strong enough, and it could be more than two magnitudes smaller than the one obtained by the VCE-Lc method. Consequently, the RMS error w.r.t. the validation data delivered by VCE is almost 100% larger than that given by the proposed VCE-Lc method in such study cases.

Q-2. How to apply a conventional regularization method if various data sets are to be combined?

When various types of gravity observations with unknown weight factors are to be combined, a conventional regularization method, e.g., the L-curve method, can be applied in combination with VCE, such that the relative weights between the data sets are estimated by VCE but the regularization parameter is determined by the L-curve method. This study further suggests that it is preferred to apply the VCE first, and then determine the regularization parameter by the L-curve method based on the estimated weights. **P-I** shows that the VCE-Lc method generally delivers smaller RMS errors as well as higher correlations between the estimated coefficients and the validation data, compared to the Lc-VCE. Furthermore, as mentioned in Sect. 5.4, the relative weights need to be selected empirically if the L-curve method is to be applied first, and wrongly chosen weights could lead to the degradation of modeling results.

Q-3. How large is the impact of the regularization parameter on the modeling accuracy?

As mentioned in the answer to **Q-1**, if VCE is applied alone in study cases that require a strong regularization, the calculated gravity model could deliver an RMS error up to 100% larger, compared to the one acquired when the regularization parameter is chosen appropriately by the proposed VCE-Lc method. On the other hand, numerical investigations in **P-I** show that if the L-curve method is used solely when different types of observations are combined, the obtained RMS error is 75% larger than that of the VCE-Lc method. These results demonstrate that the regularization parameter has a significant impact on the modeling accuracy in regional gravity field refinement. Thus, the regularization parameter determination plays a crucial role in regional gravity field modeling.

High-resolution regional (quasi-) geoid model based on SRBFs

Q-4. How to set up the estimation model using SRBFs?

To set up the estimation model, the settings need to be chosen first, including the type, the bandwidth, the location of the SRBFs, as well as the margin size for the extension of the data zone. The bandwidth of the SRBFs, i.e., the maximum degree n_{max} of the series expansion, depends on the spatial resolution of the gravity observations following Eq. (5.1). The number of the SRBFs as well as the margin size are then chosen based on the maximum degree n_{max} of the expansion, following the rules defined in Sect. 5.1. Generally, the Shannon function is applied in the analysis to avoid the loss of spectral information, and an SRBF with smoothing features, such as the Blackman or the CuP function is used in the synthesis to reduce erroneous effects. However, the SRBFs with smoothing features can also be used in the analysis as a low-pass filter to reduce the high-frequency noise in the gravity data. The validity of combining different types of SRBFs for different types of observations is proven in **P-II**. The extended Gauss–Markov model (Eq. (5.7)) is then set up to estimate the unknown coefficients, with the relative weights between different observation groups estimated by VCE, and the regularization parameter determined by the L-curve method, i.e., using the VCE-Lc method proposed in **P-I**.

Q-5. How much does each observation group contribute to the final (quasi-) geoid model?

In the "1 cm geoid experiment", the regional quasi-geoid model is calculated using terrestrial and airborne gravity measurements in combination with a GGM and topography models. The final quasi-geoid model benefits from all the data types. Including the topography models is of great importance in mountainous areas, as it smoothens the input observations, which enables a better least-squares fit. However, the topography models alone do not guarantee an accurate modeling result, despite their high resolution. Compared to the GNSS/leveling data, the STD value of the height anomaly result delivered by the combined solution decreases by 18% compared to using terrestrial data only and 27% compared to using airborne data only, and it reaches 64% compared to using only the GGM and the topography models. The calculated quasi-geoid model is also compared with those directly obtained by different high-resolution GGMs, namely EGM2008, EIGEN6C4, GECO, and XGM2019, in combination of the topography models. This comparison shows that the performance of the GGMs varies significantly, delivering larger STDs compared to the regional model. Thus, regional (quasi-) geoid modeling based on local gravity observations is preferred for determining the IHRF coordinates,

compared to using the high-resolution GGMs directly. Furthermore, the SRBF-based regional (quasi-) geoid models deliver stable results regardless of the choice of the GGMs as background model.

Q-6. Which accuracy can the SRBF-based regional (quasi-) geoid model achieve, and how is its performance compared to other methods?

Compared with the mean result of all the fourteen contributions in the "1 cm geoid experiment", the SRBF-based quasi-geoid model delivers RMS errors of 1.0 cm and 1.6 cm at the GSVS17 benchmarks and in the whole target area, respectively. They are both the smallest among all the solutions calculated by different regional gravity field modeling methods. Compared with the GNSS/leveling data, the STD obtained by the SRBF-based quasi-geoid model is 2.64 cm, which is among the five results with the smallest STD values. However, the goal of having a (quasi-) geoid with 1 cm accuracy is not reached yet. As shown in Fig. 6.3, there is a noticeable sudden increase in the differences between the height anomaly results and the GNSS/leveling data after benchmark Nr. 160, which could be caused by errors in the leveling data or in the gravity data. The exact reason for this increase needs further investigation. Nevertheless, the STD at the first 160 benchmarks reaches 1.37 cm, which is close to the 1.3 cm uncertainty of the GNSS/leveling data. These results show the reliability of the SRBFs for regional (quasi-) geoid modeling, and its performance is comparable with other methods, such as the Stoke's formula and the LSC.

Spectral combination via MRR based on pyramid algorithm

Q-7. How can the MRR and the pyramid algorithm be realized in regional gravity field modeling?

To set up the MRR based on the SRBFs, the frequency domain needs to be discretized into different resolution levels. From the highest level to the lowest level, the density of the required basis functions decreases gradually but the margin size increases to reduce edge effects. The exact values for the number of basis functions and the margin size at each level are chosen following the discussions in Sect. 5.1. In this work, an MRR scheme is developed based on the pyramid algorithm and sequential parameter estimation. The different resolution levels are connected by the pyramid algorithm, which means the estimated coefficients of the highest level are transformed to the lower levels by successive low-pass filtering. One choice of the low-pass filter in case of using the Reuter grid is proposed in **P-III**. The coefficients obtained from the pyramid algorithm are updated by the gravity data included at each lower resolution level through the parameter estimation. These updated coefficients are then used in combination with spherical wavelet functions to calculate the corresponding detail signals of each level, and thus, the final gravity model is obtained.

Q-8. What and how large is the benefit of applying the MRR based on the pyramid algorithm?

This question is answered in both Sect. 6.2 and **P-III**. The detailed benefits of applying the MRR based on the pyramid algorithm are listed in Sect. 4.3. The major advantage is that different types of observations can be included into the estimation procedure at the spectral level of their highest sensitivities, which makes it possible to benefit from the individual strength of each data set. It has been pointed out in the existing literature that the single-level approach might be biased towards the high-resolution measurements, and the contribution of measurements with medium to low resolution (e.g., altimetry data, satellite gravimetry data) could be understated, since they are not sensitive at high spectral degrees. Numerical results based on both simulated and real gravity observations in this work confirm this suspicion. The single-level gravity models show much larger differences w.r.t. the validation data in regions without high-resolution gravity data. In the two study cases presented in **P-III**, where the high-resolution terrestrial data do not have full coverage over the study area, the improvement achieved by the MRR based on the pyramid algorithm is more than 30% in terms of RMS, compared to the single-level SRBF approach.

Q-9. In which cases the MRR based on the pyramid algorithm should be applied?

In **P-III**, different types of gravity observation techniques with varying spectral sensitivities are involved, including high-resolution terrestrial, airborne, and shipborne data, medium-resolution

altimetry data, as well as low-resolution satellite gravimetry data. Moreover, the high-resolution data do not have coverage over the whole study area. In such cases, applying the developed MRR scheme, i.e., MRR based on the pyramid algorithm and sequential parameter estimation, is especially beneficial. The MRR models do not show larger differences w.r.t. the validation data in areas without coverage of high-resolution observations than in areas with coverage, which is the case in the single-level model. These results demonstrate that the MRR based on the pyramid algorithm is able to capture gravity information from measurements that are sensitive to different spectral bands. Thus, it should be applied when gravity observations with varying spectral resolution are used, and especially when the high-resolution gravity data do not have a large coverage, e.g., in offshore regions and developing areas with sparse terrestrial data. However, it is worth mentioning that the choice of applying the single-level SRBF or the MRR based on the pyramid algorithm depends on each study case. As shown in Sect. 6.2, the MRR does not deliver smaller STD w.r.t. the GNSS/leveling data than the single-level approach in the "1 cm geoid experiment", where the terrestrial and airborne data cover almost the whole study area with high density.

7.2 Outlook

Based on the results and discussions of this thesis, the following open research questions need to be investigated in future studies.

Combination of VCE and other regularization methods

In this thesis, VCE is combined with the L-curve method for regularization parameter determination. It solves the problem that VCE could deliver unreliable regularization results, and the L-curve method cannot be applied when the relative weights between different types of gravity data are not available. However, besides the L-curve method, there are other conventional regularization methods, such as the GCV and the quasi-optimality method (Morozov, 1984; Bouman, 1998), that should be used with the knowledge of weight matrices. Thus, they can also be combined with VCE, and it would be interesting to compare the performance of these new "combined approaches" (e.g., VCE-GCV) with the VCE-Lc method.

Inclusion of the covariance information

In the parameter estimation, i.e., Eq. (5.7), the weight matrix of each observation vector is set to be the identity matrix, $\boldsymbol{P}_p = \boldsymbol{I}$, under the assumption that observations within the same group have the same accuracy and are uncorrelated. Furthermore, the weight matrix of the prior information is also set to $\boldsymbol{P}_d = \boldsymbol{I}$ assuming that the coefficients are not correlated and have the same accuracy. These assumptions are commonly used in existing publications, but they are not necessarily the ideal choices. It is usually difficult to acquire the realistic full error variance-covariance matrix of the observations, since information about the real data quality is often not available. If an improper $\boldsymbol{P}_p$ is included, it might not improve the modeling results, and at the same time increase the computation effort. Thus, it is reasonable to set $\boldsymbol{P}_p = \boldsymbol{I}$. However, the weight matrix $\boldsymbol{P}_d$ of the prior information could be obtained from the covariance matrix of the GGM. Although this procedure would be computationally intensive, more realistic modeling results might be obtained (Willberg et al., 2019). The full covariance matrix of the GGM can also be included in the MRR based on the pyramid algorithm during the parameter estimation of the highest resolution level.

Further reduction of edge effects in the MRR based on the pyramid algorithm

In case of the MRR based on pyramid algorithm, larger differences in the calculated gravity model w.r.t. the validation data show up near the border of the high-resolution observations, due to edge effects. To address this issue, a strategy is proposed and developed in **P-III** and Sect. 6.2, which adapts the investigation area according to the observations involved at each level when calculating

the detail signals. The edge effects at the border outside the coverage of the high-resolution data are significantly reduced by applying this procedure. However, those at the border inside the coverage of the high-resolution data remain. Thus, further work is planned to develop strategies for further reducing these edge effects, which could lead to an even better performance of the MRR based on the pyramid algorithm.

Error assessment in the "1 cm geoid experiment"

As reported in Wang et al. (2021), the STD of the height anomaly results delivered by the fourteen contributions ranges from 1.5 cm to 5.3 cm in comparison to the mean result in the whole target area, and it ranges from 1.7 cm to 3.6 cm in comparison to the GNSS/leveling data at the GSVS17 benchmarks. Thus, the next step of the "1 cm geoid experiment" is to study and understand the possible reasons for the differences between the individual solutions. Actually, the JWG 2.2.1 "Error assessment of the 1 cm geoid experiment" has been set up for this purpose in the IAG period 2019-2023. Currently, different contributions have discrepancies not only in the computation method but also in the data pre-processing. Thus, it is planned within the JWG that the data-driven errors should first be removed by using a common database, i.e., a common joint data grid of free-air gravity anomalies, and then the method-driven errors could be quantified. Moreover, the reason for the sudden increase after the GSVS17 benchmark Nr. 160 (see Fig. 6.3) in the validation between the height anomaly results and the GNSS/leveling data needs to be investigated within this JWG.

For the SRBF-based quasi-geoid model, there are also a few possibilities for further improving the model accuracy according to the numerical investigation and discussions in Sect. 6.1 and **P-II**.

> **Handing of the topographic effect** As shown in Fig. 6.2, the modeling residuals are highly correlated to the topography, which indicate that improvements in the quasi-geoid model could be achieved by a more accurate topography modeling. Currently, the applied topography models (dV_ELL_Earth2014 and ERTM2160) have a spatial resolution of around 250 m. Thus, higher-resolution topography models that are newly available (e.g., TerraSAR/TanDEM 30 m) can be considered, and the results should be compared to study the impact of topography models in regional gravity field modeling.
>
> **Bias/outlier detection in the gravity data** Data pre-processing strategies could be further applied and assessed. A bias detection or an outlier detection could be implemented by a cross-over adjustment or newly proposed methods (e.g., Li, 2018). Furthermore, the measurement accuracy might be derived from these pre-processing procedures.
>
> **Improvement of stochastic models** Further improvement could be obtained by considering the covariance information of the global quasi-geoid background model, instead of using an identity matrix in the parameter estimation. In addition, the measurement accuracy derived from the pre-processing procedures could also be included as the stochastic information.

In summary, significant advances have been made in regional gravity field modeling by numerous research groups using different methodologies in order to achieve the goal of geoid determination with 1 cm accuracy. This thesis presents a contribution towards this goal based on the method of SRBFs; procedures for the combination of data from various observation techniques are developed, and potential improvements for future work are proposed accordingly.

Abbreviations

CHAMP	CHAllenging Minisatellite Payload
CuP	Cubic Polynomial
DLR	German Aerospace Center
DOT	Dynamic Ocean Topography
DTU	Technical University of Denmark
EGM2008	Earth Gravitational Model 2008
EIGEN	European Improved Gravity model of the Earth by New techniques
ESA	European Space Agency
GBVP	Geodetic Boundary Value Problem
GCV	Generalized Cross Validation
GECO	GOCE and EGM2008 Combined model
GGM	Global Gravity Model
GGOS	Global Geodetic Observing System
GNSS	Global Navigation Satellite Systems
GOCE	Gravity field and steady-state Ocean Circulation Explorer
GPS	Global Positioning System
GRACE	Gravity Recovery And Climate Experiment
GRACE-FO	GRACE-Follow-On
GRAV-D	"Gravity for the Redefinition of the American Vertical Datum"
GRS80	Geodetic Reference System 1980
GSVS17	Geoid Slope Validation Survey 2017
IAG	International Association of Geodesy
ICCT	Inter-Commission Committee on Theory
ICGEM	International Centre for Global Earth Models
IHRF	International Height Reference Frame
IHRS	International Height Reference System
ITRF	International Terrestrial Reference Frame
ITRS	International Terrestrial Reference System
JSG	Joint Study Group
JWG	Joint Working Group
LSC	Least Squares Collocation

MRR	Multi-Resolution Representation
NASA	National Aeronautics and Space Administration
NAVD88	North American Vertical Datum of 1988
NGA	National Geospatial-Intelligence Agency
NGS	National Geodetic Survey
POD	Precise Orbit Determination
PSC	Parameter-Signal Correlation
RCR	Remove-Compute-Restore
RLSC	Residual Least Squares Collocation
RMS	Root Mean Square
SC	Sub-Commission
SH	Spherical Harmonic
SLR	Satellite Laser Ranging
SRBF	Spherical Radial Basis Function
SRTM	Shuttle Radar Topography Mission
SSH	Sea Surface Height
STD	Standard Deviation
VCE	Variance Component Estimation
VLBI	Very Long Baseline Interferometry
WGS84	World Geodetic System 1984
XGM2016	eXperimental Gravity field Model 2016
XGM2019e	eXperimental Gravity field Model 2019 extended with topographic information

List of Figures

1.1 What happens when different height reference systems are used at the two sides of a bridge . . . 1
1.2 High-resolution regional gravity data (airborne and terrestrial measurements) in combination with global satellite data[1] . . . 2
1.3 Structure of this dissertation, including the connection between the chapters, and in particular their connection to the three publications . . . 6

2.1 The geoid and the ellipsoid . . . 8
2.2 Geoid height N. Note that the curve of the ellipsoid is neglected in this and the following figures . . . 9
2.3 Quasi-geoid height ζ . . . 9
2.4 Overview of heights and reference surfaces, adapted from Sánchez et al. (2021) . . . 11

3.1 Quantities related to satellite altimetry . . . 16
3.2 List of past, active, and potential future satellite altimetry missions[2] . . . 17
3.3 (a) terrestrial (blue dots) and airborne (green flight tracks) gravity measurements in Colorado, as well as GNSS/leveling data at the GSVS17 benchmarks (red line) for validation; (b) terrain map of the study area . . . 18
3.4 Terrestrial gravity observations (a) before and (b) after the topographic effect reduction (long-wavelength part from the GGM has already been removed) . . . 22

4.1 The discretization of the frequency domain, and the corresponding spectral degree value n_i as well as the approximate spatial resolution ρ_i of each level i, adapted from Lieb et al. (2016) . . . 26
4.2 Reuter grid points on the sphere for level 4 (red triangles) and level 5 (green dots) . . . 28
4.3 The multi-resolution representation (MRR) based on the pyramid algorithm (cf. **P-III**) 29
4.4 The (a) Shannon scaling functions, (b) Shannon wavelet functions, (c) Blackman scaling functions, (d) Blackman wavelet functions, (e) CuP scaling functions, and (f) CuP wavelet functions at different resolution levels, in the spatial domain (upper panel, ordinate values are normalized to 1), and in the spectral domain (bottom panel, ordinate values are not normalized) . . . 31

5.1 The different extensions for the areas of computation $\partial\Omega_C$, of observations $\partial\Omega_O$ and of investigation $\partial\Omega_I$, as well as the distribution of the Reuter grid points in $\partial\Omega_C$ . . . 34
5.2 An example of the L-curve function . . . 39
5.3 Combination of different types of observations based on the regularization method VCE-Lc (adapted from **P-I**) . . . 40
5.4 Combination of different types of observations based on the regularization method Lc-VCE (adapted from **P-I**) . . . 41

6.1 Flowchart regarding the procedure for calculating regional gravity models . . . 43
6.2 Residuals of (a) the terrestrial gravity data, and (b) the airborne gravity data from the least-squares estimation . . . 45

6.3 Differences between the GSVS17 validation data and the SRBF-based height anomaly result (red line) as well as the mean result (cyan line). The ellipsoidal height (black line) of the GSVS17 benchmarks and the benchmark Nr. 160 (vertical line) are plotted for interpretation reasons 46
6.4 Differences between the GSVS17 validation data and the combined solution (red line), the terrestrial-only solution (green line), the airborne-only solution (blue line), as well as the models-only solution (grey line) 47
6.5 The differences between the combined solution and (a) the models-only solution, (b) the terrestrial-only solution, as well as (c) the airborne-only solution, in the whole study area 49
6.6 Differences between the GNSS/leveling data and the four GGMs (in combination with ERTM2160) at the GSVS17 benchmarks 50
6.7 Differences between the GNSS/leveling data and the regional quasi-geoid model calculated using the four GGMs (truncated at degree 719) as background model 51
6.8 The study areas and the distributions of gravity data in (a) the simulated case, including terrestrial (yellow dots), airborne (orange dots), altimetry (green dots), GOCE (grey dots), and GRACE (blue dots) data, and (b) the real case, including terrestrial (yellow dots), shipborne (red dots), airborne (orange dots), and altimetry (green dots) data . . 52
6.9 The estimated scaling coefficients at level $I = 11$ (first row), and levels $i = 10, 9, 8, 7$ (second to fifth row). From the second to the fifth row, the left column represents the coefficients $\boldsymbol{d}_{i|i+1}$ computed directly from the pyramid algorithm, and the right column represents the updated coefficients $\boldsymbol{d}_i$ after including the gravity data involved at this level. The black rectangle inside each plot shows the observation area $\partial\Omega_O$ 53
6.10 The detail signal $\boldsymbol{G}_i$ of the MRR based on the pyramid algorithm before (left column) and after (mid column) adapting the investigation area $\partial\Omega_{I_i}$, as well as the estimated gravity signal (in terms of disturbing potential) $\boldsymbol{F}_{I'} = \bar{\boldsymbol{F}} + \sum_{i=7}^{I'} \boldsymbol{G}_i$ (right column) from level $I' = 11$ (first row) to level $I' = 7$ (fifth row), with $\bar{\boldsymbol{F}}$ (right column, last row) modeled from GECO 55
6.11 Differences between the estimated disturbing potential and the validation data, delivered by (a) the MRR based on the pyramid algorithm, (b) the MRR based on the pyramid algorithm before applying the developed strategy for reducing edge effects, (c) the single-level approach, and (d) the MRR without pyramid algorithm 56
6.12 Differences between the calculated quasi-geoid model and the GNSS/leveling data in the onshore area, delivered by (a) the MRR based on the pyramid algorithm, and (b) the single-level approach. Note that the mean values of the differences are removed 57
6.13 Differences between the calculated gravity anomaly model and the DTU17 in the offshore area, delivered by (a) the MRR based on the pyramid algorithm, and (b) the single-level approach 58

List of Tables

4.1 The adapted basis functions for different gravity functionals obtained from various observation techniques 24

6.1 Comparison between the GNSS/leveling data and the height anomaly results, unit [cm] 46
6.2 Comparison between the GNSS/leveling data and the different solutions, unit [cm] . . 48
6.3 Comparison between the GNSS/leveling data and the GGMs (in combination with ERTM2160) at the first 160 benchmarks, unit [cm] 50
6.4 Comparison between the GNSS/leveling data and the regional quasi-geoid model calculated using different GGMs, truncated at different SH degrees, as background model (at the first 160 benchmarks), unit [cm] 51
6.5 Evaluation of the MRR and the single-level model with respect to the validation data in terms of disturbing potential values (unit [m^2/s^2]) 56
6.6 Evaluation of the MRR based on the pyramid algorithm and the single-level model w.r.t. GNSS/leveling data (in terms of quasi-geoid, note that the mean differences are removed) in the onshore area, and w.r.t. DTU17 (in terms of gravity anomaly) in the offshore area 59

1 Contribution of Qing Liu to P-I 87
2 Contribution of Qing Liu to P-II 115
3 Contribution of Qing Liu to P-III 137

Bibliography

Alberts, B. A. (2009). *Regional gravity field modeling using airborne gravity data*. PhD thesis, Delft University of Technology.

Andersen, O. B. (2010). The DTU10 global gravity field and mean sea surface - improvements in the Arctic. In *Second international symposium of the gravity field of the Earth (IGFS2)*.

Andersen, O. B. and Knudsen, P. (2019). The DTU17 global marine gravity field: First validation results. In *Fiducial Reference Measurements for Altimetry*, pages 83–87. Springer. https://doi.org/10.1007/1345_2019_65.

Andersen, O. B., Knudsen, P., Kenyon, S., Factor, J., and Holmes, S. (2013). The DTU13 global marine gravity field - first evaluation. In *Ocean Surface Topography Science Team Meeting, Boulder, Colorado*.

Antunes, C., Pail, R., and Catalão, J. (2003). Point mass method applied to the regional gravimetric determination of the geoid. *Studia Geophysica et Geodaetica*, 47(3):495–509. https://doi.org/10.1023/A:1024836032617.

Barthelmes, F. (1988). Local gravity field approximation by point masses with optimized positions. In *Proceedings 6th international symposium "Geodesy and Physics of the Earth"*. https://doi.org/10.2312/zipe.1989.102.02.

Bentel, K. (2013). *Regional gravity modeling in spherical radial basis functions–on the role of the basis function and the combination of different observation types*. PhD thesis, Norwegian University of Life Sciences.

Bentel, K., Schmidt, M., and Denby, C. R. (2013a). Artifacts in regional gravity representations with spherical radial basis functions. *Journal of Geodetic Science*, 3:173–187. https://doi.org/10.2478/jogs-2013-0029.

Bentel, K., Schmidt, M., and Gerlach, C. (2013b). Different radial basis functions and their applicability for regional gravity field representation on the sphere. *GEM-International Journal on Geomathematics*, 4:67–96. https://doi.org/10.1007/s13137-012-0046-1.

Beylkin, G. and Cramer, R. (2002). Toward multiresolution estimation and efficient representation of gravitational fields. *Celestial Mechanics and Dynamical Astronomy*, 84(1):87–104. https://doi.org/10.1023/A:1019941111529.

Bjerhammar, A. (1985). On a relativistic geodesy. *Bulletin géodésique*, 59(3):207–220. https://doi.org/10.1007/BF02520327.

Bolkas, D., Fotopoulos, G., and Braun, A. (2016). Comparison and fusion of satellite, airborne, and terrestrial gravity field data using wavelet decomposition. *Journal of Surveying Engineering*, 142(2):04015010. https://doi.org/10.1061/(ASCE)SU.1943-5428.0000162.

Bosch, W., Dettmering, D., and Schwatke, C. (2014). Multi-mission cross-calibration of satellite altimeters: Constructing a long-term data record for global and regional sea level change studies. *Remote Sensing*, 6(3):2255–2281. https://doi.org/10.3390/rs6032255.

Bouman, J. (1998). Quality of regularization methods. DEOS Report 98.2. Technical report, Delft University Press, Delft, The Netherlands.

Bouman, J., Fiorot, S., Fuchs, M., Gruber, T., Schrama, E., Tscherning, C., Veicherts, M., and Visser, P. (2011). GOCE gravitational gradients along the orbit. *Journal of Geodesy*, 85(11):791–805. https://doi.org/10.1007/s00190-011-0464-0.

Brockmann, J. M., Zehentner, N., Höck, E., Pail, R., Loth, I., Mayer-Gürr, T., and Schuh, W.-D. (2014). EGM_TIM_RL05: An independent geoid with centimeter accuracy purely based on the GOCE mission. *Geophysical Research Letters*, 41(22):8089–8099. https://doi.org/10.1002/2014GL061904.

Bucha, B., Janák, J., Papčo, J., and Bezděk, A. (2016). High-resolution regional gravity field modelling in a mountainous area from terrestrial gravity data. *Geophysical Journal International*, 207:949–966. https://doi.org/10.1093/gji/ggw311.

Childers, V. A., Bell, R. E., and Brozena, J. M. (1999). Airborne gravimetry: An investigation of filtering. *Geophysics*, 64:61–69. https://doi.org/10.1190/1.1444530.

Claessens, S. and Filmer, M. (2020). Towards an International Height Reference System: insights from the Colorado geoid experiment using AUSGeoid computation methods. *Journal of Geodesy*, 94:1–19. https://doi.org/10.1007/s00190-020-01379-3.

Dahle, C., Flechtner, F., Gruber, C., König, D., König, R., Michalak, G., and Neumayer, K.-H. (2013). GFZ GRACE Level-2 Processing Standards Document for Level-2 Product Release 0005. Technical report. https://gfzpublic.gfz-potsdam.de/rest/items/item_108022_2/component/file_108023/content.

de Min, E. (1995). A comparison of Stokes' numerical integration and collocation, and a new combination technique. *Bulletin géodésique*, 69(4):223–232. https://doi.org/10.1007/BF00806734.

Denker, H. (2013). Regional gravity field modeling: theory and practical results. In *Sciences of geodesy-II*, pages 185–291. Springer. https://doi.org/10.1007/978-3-642-28000-9_5.

Drewes, H., Kuglitsch, F., Adám, J., and Rózsa, S. (2016). The geodesists' handbook 2016. *Journal of Geodesy*, 90:907–1205. https://doi.org/10.1007/s00190-016-0948-z.

Drinkwater, M., Floberghagen, R., Haagmans, R., Muzi, D., and Popescu, A. (2003). VII: Closing session: GOCE: ESA's first earth explorer core mission. *Space science reviews*, 108(1):419–432. https://doi.org/10.1023/A:1026104216284.

Eicker, A. (2008). *Gravity field refinement by radial basis functions from in-situ satellite data*. PhD thesis, Universität Bonn.

Eicker, A., Mayer-Gürr, T., and Ilk, K. H. (2006). An integrated global/regional gravity field determination approach based on GOCE observations. In *Observation of the Earth System from Space*, pages 225–237. Springer. https://doi.org/10.1007/3-540-29522-4_16.

Eicker, A., Schall, J., and Kusche, J. (2014). Regional gravity modelling from spaceborne data: case studies with GOCE. *Geophysical Journal International*, 196(3):1431–1440. https://doi.org/10.1093/gji/ggt485.

Eriksson, P. (2000). Analysis and comparison of two linear regularization methods for passive atmospheric observations. *Journal of Geophysical Research: Atmospheres*, 105(D14):18157–18167. https://doi.org/10.1029/2000JD900172.

Farquharson, C. G. and Oldenburg, D. W. (2004). A comparison of automatic techniques for estimating the regularization parameter in non-linear inverse problems. *Geophysical Journal International*, 156(3):411–425. https://doi.org/10.1111/j.1365-246X.2004.02190.x.

Featherstone, W. (2013). Deterministic, stochastic, hybrid and band-limited modifications of Hotine's integral. *Journal of Geodesy*, 87(5):487–500. https://doi.org/10.1007/s00190-013-0612-9.

Featherstone, W., Evans, J., and Olliver, J. (1998). A Meissl-modified Vaníček and Kleusberg kernel to reduce the truncation error in gravimetric geoid computations. *Journal of Geodesy*, 72(3):154–160. https://doi.org/10.1007/s001900050157.

Fecher, T., Pail, R., Gruber, T., and GOCO Consortium (2017). GOCO05c: a new combined gravity field model based on full normal equations and regionally varying weighting. *Surveys in geophysics*, 38(3):571–590. https://doi.org/10.1007/s10712-016-9406-y.

Fengler, M., Freeden, W., and Michel, V. (2004). The Kaiserslautern multiscale geopotential model SWITCH-03 from orbit perturbations of the satellite CHAMP and its comparison to the models EGM96, UCPH2002_02_0. 5, EIGEN-1s and EIGEN-2. *Geophysical Journal International*, 157(2):499–514. https://doi.org/10.1111/j.1365-246X.2004.02209.x.

Flury, J. and Rummel, R. (2009). On the geoid–quasigeoid separation in mountain areas. *Journal of Geodesy*, 83(9):829–847. https://doi.org/10.1007/s00190-009-0302-9.

Foroughi, I., Vaníček, P., Kingdon, R. W., Goli, M., Sheng, M., Afrasteh, Y., Novák, P., and Santos, M. C. (2019). Sub-centimetre geoid. *Journal of Geodesy*, 93:849–868. https://doi.org/10.1007/s00190-018-1208-1.

Forsberg, R. (1993). Modelling the fine-structure of the geoid: methods, data requirements and some results. *Surveys in geophysics*, 14(4-5):403–418. https://doi.org/10.1007/BF00690568.

Forsberg, R. and Olesen, A. V. (2010). Airborne gravity field determination. In *Sciences of geodesy-I*, pages 83–104. Springer. https://doi.org/10.1007/978-3-642-11741-1_3.

Forsberg, R. and Tscherning, C. C. (1981). The use of height data in gravity field approximation by collocation. *Journal of Geophysical Research: Solid Earth*, 86(B9):7843–7854. https://doi.org/10.1029/JB086iB09p07843.

Förste, C., Bruinsma, S., Abrikosov, O., Lemoine, J.-M., Marty, J.-C., Flechtner, F., Balmino, G., Barthelmes, F., and Biancale, R. (2014). *EIGEN-6C4-The latest combined global gravity field model including GOCE data up to degree and order 2190 of GFZ Potsdam and GRGS Toulouse*. https://doi.org/10.5880/icgem.2015.1.

Freeden, W. (1999). *Multiscale modelling of spaceborne geodata*. Teubner.

Freeden, W., Gervens, T., and Schreiner, M. (1998). *Constructive approximation on the sphere with applications to geomathematics*. Oxford University Press on Demand, New York.

Freeden, W. and Michel, V. (2004). *Multiscale potential theory: with applications to geoscience*. Birkhäuser, Basel.

Fuchs, M. J. and Bouman, J. (2011). Rotation of GOCE gravity gradients to local frames. *Geophysical Journal International*, 187(2):743–753. https://doi.org/10.1111/j.1365-246X.2011.05162.x.

Gilardoni, M., Reguzzoni, M., and Sampietro, D. (2016). GECO: a global gravity model by locally combining GOCE data and EGM2008. *Studia Geophysica et Geodaetica*, 60(2):228–247. https://doi.org/10.1007/s11200-015-1114-4.

Golub, G. H., Heath, M., and Wahba, G. (1979). Generalized cross-validation as a method for choosing a good ridge parameter. *Technometrics*, 21:215–223. https://doi.org/10.2307/1268518.

GRAV-D Team (2017). *GRAV-D Airborne Gravity Data User Manual*. https://www.ngs.noaa.gov/GRAV-D/data/NGS_GRAV-D_General_Airborne_Gravity_Data_User_Manual_v2.1.pdf.

GRAV-D Team (2018). *Block MS05 (Mountain South 05); GRAV-D Airborne Gravity Data User Manual*. https://www.ngs.noaa.gov/GRAV-D/data_ms05.shtml.

Grigoriadis, V. N., Vergos, G. S., Barzaghi, R., Carrion, D., and Koç, Ö. (2021). Collocation and FFT-based geoid estimation within the Colorado 1 cm geoid experiment. *Journal of Geodesy*, 95(5):1–18. https://doi.org/10.1007/s00190-021-01507-7.

Gruber, T., Gerlach, C., and Haagmans, R. (2012). Intercontinental height datum connection with GOCE and GPS-levelling data. *Journal of Geodetic Science*, 2(4):270–280. https://doi.org/10.2478/v10156-012-0001-y.

Gruber, T., Rummel, R., Abrikosov, O., and van Hees, R. (2014). GOCE Level 2 Product Data Handbook. Technical report, The European GOCE Gravity Consortium. https://earth.esa.int/documents/10174/1650485/GOCE_Product_Data_Handbook_Level-2.

Gruber, T., Rummel, R., and Koop, R. (2007). How to use GOCE level 2 products. In *Proceedings of the 3rd International GOCE User Workshop, ESA SP-627*.

Gruber, T., Visser, P., Ackermann, C., and Hosse, M. (2011). Validation of GOCE gravity field models by means of orbit residuals and geoid comparisons. *Journal of geodesy*, 85(11):845–860. https://doi.org/10.1007/s00190-011-0486-7.

Haagmans, R., Prijatna, K., and Omang, O. (2002). An alternative concept for validation of GOCE gradiometry results based on regional gravity. In *Proceedings of the 3rd Meeting of the International Gravity and Geoid Commission*, pages 281–286.

Hansen, P. C. (1990). Truncated singular value decomposition solutions to discrete ill-posed problems with ill-determined numerical rank. *SIAM Journal on Scientific and Statistical Computing*, 11:503–518. https://doi.org/10.1137/0911028.

Hansen, P. C. and O'Leary, D. P. (1993). The use of the L-curve in the regularization of discrete ill-posed problems. *SIAM journal on scientific computing*, 14(6):1487–1503. https://doi.org/10.1137/0914086.

Heisenberg, W. (1927). Über den anschaulichen inhalt der quantentheoretischen kinematik und mechanik. *Zeitschrift für Physik*, 43:172–198. https://doi.org/10.1007/BF01397280.

Heiskanen, W. A. and Moritz, H. (1967). *Physical geodesy*. San Francisco W. H. Freeman and Company, USA.

Hirt, C., Kuhn, M., Claessens, S., Pail, R., Seitz, K., and Gruber, T. (2014). Study of the Earth's short-scale gravity field using the ERTM2160 gravity model. *Computers & geosciences*, 73:71–80. https://doi.org/10.1016/j.cageo.2014.09.001.

Hirt, C. and Rexer, M. (2015). Earth2014: 1 arc-min shape, topography, bedrock and ice-sheet models–available as gridded data and degree-10,800 spherical harmonics. *International Journal of Applied Earth Observation and Geoinformation*, 39:103–112. https://doi.org/10.1016/j.jag.2015.03.001.

Hofmann-Wellenhof, B. and Moritz, H. (2006). *Physical geodesy*. Springer Science & Business Media.

Hwang, C. and Hsu, H.-Y. (2008). Shallow-water gravity anomalies from satellite altimetry: Case studies in the east China sea and Taiwan strait. *Journal of the Chinese Institute of Engineers*, 31(5):841–851. http://dx.doi.org/10.1080/02533839.2008.9671437.

Ihde, J., Sánchez, L., Barzaghi, R., Drewes, H., Foerste, C., Gruber, T., Liebsch, G., Marti, U., Pail, R., and Sideris, M. (2017). Definition and proposed realization of the International Height Reference System (IHRS). *Surveys in geophysics*, 38:549–570. https://doi.org/10.1007/s10712-017-9409-3.

Ilk, K. (1993). Regularization for high resolution gravity field recovery by future satellite techniques. In *Inverse Problems: Principles and Applications in Geophysics, Technology and Medicine. Mathematical Research*, pages 189–214. Akademie-Verlag. https://doi.org/10.1142/9789812836182_2008.

Jacob, T., Wahr, J., Pfeffer, W. T., and Swenson, S. (2012). Recent contributions of glaciers and ice caps to sea level rise. *Nature*, 482(7386):514–518. https://doi.org/10.1038/nature10847.

Jekeli, C. (2015). Potential theory and the static gravity field of the Earth. In *Treatise on Geophysics (Second Edition)*, pages 9–35. Elsevier, Oxford. https://doi.org/10.1016/B978-0-444-53802-4.00056-7.

Jiang, T., Dang, Y., and Zhang, C. (2020). Gravimetric geoid modeling from the combination of satellite gravity model, terrestrial and airborne gravity data: a case study in the mountainous area, Colorado. *Earth, Planets and Space*, 72(1):1–15. https://doi.org/10.1186/s40623-020-01287-y.

Jiang, T. and Wang, Y. M. (2016). On the spectral combination of satellite gravity model, terrestrial and airborne gravity data for local gravimetric geoid computation. *Journal of Geodesy*, 90:1405–1418. https://doi.org/10.1007/s00190-016-0932-7.

Johannessen, J. A., Balmino, G., Le Provost, C., Rummel, R., Sabadini, R., Sünkel, H., Tscherning, C., Visser, P., Woodworth, P., Hughes, C., Legrand, P., Sneeuw, N., Perosanz, F., Aguirre-Martinez, M., Rebhan, H., and Drinkwater, M. (2003). The European gravity field and steady-state ocean circulation explorer satellite mission its impact on geophysics. *Surveys in Geophysics*, 24(4):339–386. https://doi.org/10.1023/B:GEOP.0000004264.04667.5e.

Kalman, R. E. (1960). A new approach to linear filtering and prediction problems. *Journal of Basic Engineering*, 82(1):35–45. https://doi.org/10.1115/1.3662552.

Kern, M., Schwarz, K., and Sneeuw, N. (2003). A study on the combination of satellite, airborne, and terrestrial gravity data. *Journal of Geodesy*, 77(3-4):217–225. https://doi.org/10.1007/s00190-003-0313-x.

Klees, R., Slobbe, D., and Farahani, H. (2018). A methodology for least-squares local quasi-geoid modelling using a noisy satellite-only gravity field model. *Journal of Geodesy*, 92:431–442. https://doi.org/10.1007/s00190-017-1076-0.

Klees, R., Tenzer, R., Prutkin, I., and Wittwer, T. (2008). A data-driven approach to local gravity field modelling using spherical radial basis functions. *Journal of Geodesy*, 82:457–471. https://doi.org/10.1007/s00190-007-0196-3.

Koch, K.-R. (1999). *Parameter estimation and hypothesis testing in linear models*. Springer-Verlag Berlin Heidelberg.

Koch, K.-R. and Kusche, J. (2002). Regularization of geopotential determination from satellite data by variance components. *Journal of Geodesy*, 76:259–268. https://doi.org/10.1007/s00190-002-0245-x.

Koji, M. and Yuki, K. (2020). Refinement of a gravimetric geoid model for Japan using GOCE and an updated regional gravity field model. *Earth, Planets and Space (Online)*, 72(1). https://doi.org/10.1186/s40623-020-01158-6.

Koop, R. (1993). *Global gravity field modelling using satellite gravity gradiometry*. Nederlandse Commissie voor Geodesie, Delft.

Kornfeld, R. P., Arnold, B. W., Gross, M. A., Dahya, N. T., Klipstein, W. M., Gath, P. F., and Bettadpur, S. (2019). GRACE-FO: the gravity recovery and climate experiment follow-on mission. *Journal of spacecraft and rockets*, 56(3):931–951. https://doi.org/10.2514/1.A34326.

Krarup, T. (1970). The method of least squares collocation. *Studia Geophysica et Geodaetica*, 14(2):107–109. https://doi.org/10.1007/BF02585604.

Kusche, J. and Klees, R. (2002). Regularization of gravity field estimation from satellite gravity gradients. *Journal of Geodesy*, 76(6-7):359–368. https://doi.org/10.1007/s00190-002-0257-6.

Li, X. (2018). Using radial basis functions in airborne gravimetry for local geoid improvement. *Journal of Geodesy*, 92(5):471–485. https://doi.org/10.1007/s00190-017-1074-2.

Liang, W. (2017). *A regional physics-motivated electron density model of the ionosphere*. PhD thesis, Technische Universität München.

Lieb, V. (2017). *Enhanced regional gravity field modeling from the combination of real data via MRR*. PhD thesis, Technische Universität München.

Lieb, V., Schmidt, M., Dettmering, D., and Börger, K. (2016). Combination of various observation techniques for regional modeling of the gravity field. *Journal of Geophysical Research: Solid Earth*, 121:3825–3845. https://doi.org/10.1002/2015JB012586.

Lion, G., Panet, I., Wolf, P., Guerlin, C., Bize, S., and Delva, P. (2017). Determination of a high spatial resolution geopotential model using atomic clock comparisons. *Journal of Geodesy*, 91(6):597–611. https://doi.org/10.1007/s00190-016-0986-6.

Liu, Q., Schmidt, M., Pail, R., and Willberg, M. (2020a). Determination of the regularization parameter to combine heterogeneous observations in regional gravity field modeling. *Remote Sensing*, 12(10):1617. https://doi.org/10.3390/rs12101617.

Liu, Q., Schmidt, M., and Sánchez, L. (2022). Combination of different observation types through a multi-resolution representation of the regional gravity field using the pyramid algorithm and parameter estimation. *Journal of Geodesy*, 96(80):1–20. https://doi.org/10.1007/s00190-022-01670-5.

Liu, Q., Schmidt, M., Sánchez, L., and Willberg, M. (2020b). Regional gravity field refinement for (quasi-) geoid determination based on spherical radial basis functions in Colorado. *Journal of Geodesy*, 94(99):1–19. https://doi.org/10.1007/s00190-020-01431-2.

Lu, B., Barthelmes, F., Li, M., Förste, C., Ince, E. S., Petrovic, S., Flechtner, F., Schwabe, J., Luo, Z., Zhong, B., and He, K. (2019). Shipborne gravimetry in the Baltic Sea: data processing strategies, crucial findings and preliminary geoid determination tests. *Journal of Geodesy*, 93(7):1059–1071. https://doi.org/10.1007/s00190-018-01225-7.

Marchenko, A. N. (1998). *Parameterization of the Earth's gravity field : point and line singularities*. Lviv Astronomical and Geodetic Society. ISBN: 9785776346040.

Mayer-Gürr, T., Eicker, A., Kurtenbach, E., and Ilk, K.-H. (2010). ITG-GRACE: global static and temporal gravity field models from GRACE data. In *System Earth via geodetic-geophysical space techniques*, pages 159–168. Springer. https://doi.org/10.1007/978-3-642-10228-8_13.

McCubbine, J., Amos, M., Tontini, F., Smith, E., Winefied, R., Stagpoole, V., and Featherstone, W. (2018). The New Zealand gravimetric quasigeoid model 2017 that incorporates nationwide airborne gravimetry. *Journal of geodesy*, 92(8):923–937. https://doi.org/10.1007/s00190-017-1103-1.

Moritz, H. (1978). Least-squares collocation. *Reviews of geophysics*, 16(3):421–430. https://doi.org/10.1029/RG016i003p00421.

Moritz, H. (1980). *Advanced physical geodesy*. Herbert Wichmann Verlag: Kalsruhe, Germany.

Moritz, H. (2000). Geodetic reference system 1980. *Journal of Geodesy*, 74:128–133. https://doi.org/10.1007/s001900050278.

Morozov, V. A. (1984). *Methods for solving incorrectly posed problems*. Springer Verlag, New York.

Müller, J., Dirkx, D., Kopeikin, S. M., Lion, G., Panet, I., Petit, G., and Visser, P. (2018). High performance clocks and gravity field determination. *Space Science Reviews*, 214(1):1–31. https://doi.org/10.1007/s11214-017-0431-z.

Naeimi, M. (2013). *Inversion of satellite gravity data using spherical radial base functions*. PhD thesis, Leibniz Universität Hannover.

Naeimi, M., Flury, J., and Brieden, P. (2015). On the regularization of regional gravity field solutions in spherical radial base functions. *Geophysical Journal International*, 202:1041–1053. https://doi.org/10.1093/gji/ggv210.

Niebauer, T., Sasagawa, G., Faller, J. E., Hilt, R., and Klopping, F. (1995). A new generation of absolute gravimeters. *Metrologia*, 32(3):159.

Olesen, A. V., Andersen, O. B., and Tscherning, C. C. (2002). Merging of airborne gravity and gravity derived from satellite altimetry: test cases along the coast of Greenland. *Studia geophysica et geodaetica*, 46(3):387–394. https://doi.org/10.1023/A:1019577232253.

Ophaug, V. and Gerlach, C. (2017). On the equivalence of spherical splines with least-squares collocation and Stokes's formula for regional geoid computation. *Journal of Geodesy*, 91(11):1367–1382. https://doi.org/10.1007/s00190-017-1030-1.

Ophaug, V. and Gerlach, C. (2020). Error propagation in regional geoid computation using spherical splines, least-squares collocation, and Stokes's formula. *Journal of Geodesy*, 94(12):1–19. https://doi.org/10.1007/s00190-020-01443-y.

Pail, R., Bruinsma, S., Migliaccio, F., Förste, C., Goiginger, H., Schuh, W.-D., Höck, E., Reguzzoni, M., Brockmann, J. M., Abrikosov, O., Veicherts, M., Fecher, T., Mayrhofer, R., Krasbutter, I., Sansò, F., and Tscherning, C. (2011). First GOCE gravity field models derived by three different approaches. *Journal of Geodesy*, 85:819. https://doi.org/10.1007/s00190-011-0467-x.

Pail, R., Fecher, T., Barnes, D., Factor, J., Holmes, S., Gruber, T., and Zingerle, P. (2018). Short note: the experimental geopotential model XGM2016. *Journal of geodesy*, 92:443–451. https://doi.org/10.1007/s00190-017-1070-6.

Pail, R., Reguzzoni, M., Sansó, F., and Kühtreiber, N. (2010). On the combination of global and local data in collocation theory. *Studia Geophysica et Geodaetica*, 54(2):195–218. https://doi.org/10.1007/s11200-010-0010-1.

Panet, I., Kuroishi, Y., and Holschneider, M. (2011). Wavelet modelling of the gravity field by domain decomposition methods: an example over Japan. *Geophysical Journal International*, 184(1):203–219. https://doi.org/10.1111/j.1365-246X.2010.04840.x.

Pavlis, N. K., Holmes, S. A., Kenyon, S. C., and Factor, J. K. (2012). The development and evaluation of the Earth Gravitational Model 2008 (EGM2008). *Journal of geophysical research: solid earth*, 117. https://doi.org/10.1029/2011JB008916.

Petit, G. and Luzum, B. (2010). IERS conventions (2010). Technical report, Verlag des Bundesamts für Kartographie und Geodäsie, Frankfurt am Main. https://www.iers.org/IERS/EN/Publications/TechnicalNotes/tn36.html.

Plag, H.-P., Rothacher, M., Pearlman, M., Neilan, R., and Ma, C. (2009). The global geodetic observing system. In *Advances in Geosciences: Volume 13: Solid Earth (SE)*, pages 105–127. World Scientific. https://doi.org/10.1142/9789812836182_2008.

Reguzzoni, M. and Sansò, F. (2012). On the combination of high-resolution and satellite-only global gravity models. *Journal of Geodesy*, 86(6):393–408. https://doi.org/10.1007/s00190-011-0526-3.

Reigber, C., Balmino, G., Schwintzer, P., Biancale, R., Bode, A., Lemoine, J.-M., König, R., Loyer, S., Neumayer, H., Marty, J.-C., Barthelmes, F., Perosanz, F., and Zhu, S. (2002a). A high-quality global gravity field model from CHAMP GPS tracking data and accelerometry (EIGEN-1S). *Geophysical Research Letters*, 29(14):37–1. https://doi.org/10.1029/2002GL015064.

Reigber, C., Lühr, H., and Schwintzer, P. (2002b). CHAMP mission status. *Advances in space research*, 30(2):129–134. https://doi.org/10.1016/S0273-1177(02)00276-4.

Reuter, R. (1982). *Über Integralformeln der Einheitssphäre und harmonische Splinefunktionen*. PhD thesis, RWTH Aachen University.

Rexer, M., Hirt, C., Claessens, S., and Tenzer, R. (2016). Layer-based modelling of the Earth's gravitational potential up to 10-km scale in spherical harmonics in spherical and ellipsoidal approximation. *Surveys in Geophysics*, 37:1035–1074. https://doi.org/10.1007/s10712-016-9382-2.

Rexer, M., Hirt, C., and Pail, R. (2017). High-resolution global forward modelling: a degree-5480 global ellipsoidal topographic potential model. In *EGU general assembly conference abstracts*, page 7725.

Rowlands, D. D., Luthcke, S., Klosko, S., Lemoine, F. G., Chinn, D., McCarthy, J., Cox, C., and Anderson, O. (2005). Resolving mass flux at high spatial and temporal resolution using grace intersatellite measurements. *Geophysical Research Letters*, 32(4). https://doi.org/10.1029/2004GL021908.

Rummel, R. (2012). Height unification using GOCE. *Journal of Geodetic Science*, 2:355–362. https://doi.org/10.2478/v10156-011-0047-2.

Rummel, R., Balmino, G., Johannessen, J., Visser, P., and Woodworth, P. (2002). Dedicated gravity field missions - principles and aims. *Journal of Geodynamics*, 33:3–20. https://doi.org/10.1016/S0264-3707(01)00050-3.

Rummel, R. and van Gelderen, M. (1995). Meissl scheme-spectral characteristics of physical geodesy. *Manuscripta geodaetica*, 20(5):379–385.

Rummel, R., Yi, W., and Stummer, C. (2011). GOCE gravitational gradiometry. *Journal of Geodesy*, 85(11):777. https://doi.org/10.1007/s00190-011-0500-0.

Saleh, J., Li, X., Wang, Y. M., Roman, D. R., and Smith, D. A. (2013). Error analysis of the NGS' surface gravity database. *Journal of Geodesy*, 87(3):203–221. https://doi.org/10.1007/s00190-012-0589-9.

Sánchez, L. (2012). Towards a vertical datum standardisation under the umbrella of Global Geodetic Observing System. *Journal of Geodetic Science*, 2:325–342. https://doi.org/10.2478/v10156-012-0002-x.

Sánchez, L., Agren, J., Huang, J., Wang, Y., and Forsberg, R. (2018). *Basic agreements for the computation of station potential values as IHRS coordinates, geoid undulations and height anomalies within the Colorado 1 cm geoid experiment*. https://ihrs.dgfi.tum.de/fileadmin/JWG_2015/Colorado_Experiment_Basic_req_V0.5_Oct30_2018.pdf.

Sánchez, L., Ågren, J., Huang, J., Wang, Y., Mäkinen, J., Pail, R., Barzaghi, R., Vergos, G. S., Ahlgren, K., and Liu, Q. (2021). Strategy for the realisation of the International Height Reference System (IHRS). *Journal of Geodesy*, 95(33):1–33. https://doi.org/10.1007/s00190-021-01481-0.

Sánchez, L., Cunderlík, R., Dayoub, N., Mikula, K., Minarechová, Z., Šíma, Z., Vatrt, V., and Vojtíšková, M. (2016). A conventional value for the geoid reference potential W_0. *Journal of Geodesy*, 90:815–835. https://doi.org/10.1007/s00190-016-0913-x.

Sánchez, L. and Sideris, M. G. (2017). Vertical datum unification for the International Height Reference System (IHRS). *Geophysical journal international*, 209:570–586. https://doi.org/10.1093/gji/ggx025.

Sandwell, D. T., Müller, R. D., Smith, W. H., Garcia, E., and Francis, R. (2014). New global marine gravity model from CryoSat-2 and Jason-1 reveals buried tectonic structure. *Science*, 346(6205):65–67. https://doi.org/10.1126/science.1258213.

Sandwell, D. T. and Smith, W. H. (1997). Marine gravity anomaly from Geosat and ERS 1 satellite altimetry. *Journal of Geophysical Research: Solid Earth*, 102(B5):10039–10054. https://doi.org/10.1029/96JB03223.

Schmidt, M., Fabert, O., and Shum, C. (2005). On the estimation of a multi-resolution representation of the gravity field based on spherical harmonics and wavelets. *Journal of geodynamics*, 39(5):512–526. https://doi.org/10.1016/j.jog.2005.04.007.

Schmidt, M., Fengler, M., Mayer-Gürr, T., Eicker, A., Kusche, J., Sánchez, L., and Han, S.-C. (2007). Regional gravity modeling in terms of spherical base functions. *Journal of Geodesy*, 81:17–38. https://doi.org/10.1007/s00190-006-0101-5.

Schmidt, M., Göttl, F., and Heinkelmann, R. (2015). Towards the combination of data sets from various observation techniques. In *The 1st International Workshop on the Quality of Geodetic Observation and Monitoring Systems (QuGOMS'11)*, pages 35–43. Springer. https://doi.org/10.1007/978-3-319-10828-5_6.

Schmidt, M., Han, S.-C., Kusche, J., Sanchez, L., and Shum, C. (2006). Regional high-resolution spatiotemporal gravity modeling from GRACE data using spherical wavelets. *Geophysical Research Letters*, 33. https://doi.org/10.1029/2005GL025509.

Schreiner, M. (1999). A pyramid scheme for spherical wavelets. Technical report, Technische Universität Kaiserslautern. https://kluedo.ub.uni-kl.de/frontdoor/index/index/docId/605.

Shen, W.-B., Sun, X., Cai, C., Wu, K., and Shen, Z. (2019). Geopotential determination based on a direct clock comparison using two-way satellite time and frequency transfer. *Terr. Atmos. Ocean. Sci*, 30(1):1–11. https://doi.org/10.3319/TAO.2018.07.09.02.

Sjöberg, L. E. (1981). Least squares combination of satellite and terrestrial data in physical geodesy. *An Geophys*, 37:25–30.

Sjöberg, L. E. (1991). Refined least squares modification of Stokes' formula. *Manuscripta geodaetica*, 16(6):367–375.

Sjöberg, L. E. (2003). A computational scheme to model the geoid by the modified Stokes formula without gravity reductions. *Journal of Geodesy*, 77(7):423–432. https://doi.org/10.1007/s00190-003-0338-1.

Sjöberg, L. E. (2010). A strict formula for geoid-to-quasigeoid separation. *Journal of Geodesy*, 84:699–702. https://doi.org/10.1007/s00190-010-0407-1.

Slobbe, C., Klees, R., Farahani, H. H., Huisman, L., Alberts, B., Voet, P., and Doncker, F. D. (2019). The impact of noise in a GRACE/GOCE global gravity model on a local quasi-geoid. *Journal of Geophysical Research: Solid Earth*, 124(3):3219–3237. https://doi.org/10.1029/2018JB016470.

Stokes, G. G. (1849). On the variation of gravity on the surface of the Earth. *Trans. Camb. Phil. Soc.*, 8:672–695.

Tanir, E., Heinkelmann, R., Schuh, H., Kusche, J., and van Loon, J. (2009). Assessment of the results of VLBI intra-technique combination using regularization methods. In *Geodetic Reference Frames*, pages 45–51. Springer.

Tapley, B., Bettadpur, S., Watkins, M., and Reigber, C. (2004). The gravity recovery and climate experiment: Mission overview and early results. *Geophysical Research Letters*, 31. https://doi.org/10.1029/2004GL019920.

Tapley, B., Ries, J., Bettadpur, S., Chambers, D., Cheng, M., Condi, F., Gunter, B., Kang, Z., Nagel, P., Pastor, R., Pekker, T., Poole, S., and Wang, F. (2005). GGM02–An improved Earth gravity field model from GRACE. *Journal of Geodesy*, 79(8):467–478. https://doi.org/10.1007/s00190-005-0480-z.

Tenzer, R. and Klees, R. (2008). The choice of the spherical radial basis functions in local gravity field modeling. *Studia Geophysica et Geodaetica*, 52:287. https://doi.org/10.1007/s11200-008-0022-2.

Tikhonov, A. N. and Arsenin, V. I. (1977). *Solutions of ill-posed problems*. Winston, Washington DC, USA.

Timmen, L. (2010). Absolute and relative gravimetry. In *Sciences of Geodesy-I*, pages 1–48. Springer. https://doi.org/10.1007/978-3-642-11741-1_1.

Torge, W. (1989). *Gravimetry*. Walter de Gruyter, Berlin.

Torge, W. (1991). *Geodesy*. Walter de Gruyter, Berlin, Germany.

Tscherning, C. C. (1981). Comparison of some methods for the detailed representation of the Earth's gravity field. *Reviews of Geophysics*, 19(1):213–221. https://doi.org/10.1029/RG019i001p00213.

Tscherning, C. C. (2013). Geoid determination by 3D least-squares collocation. In Sansò, F. and Sideris, M., editors, *Geoid Determination. Lecture Notes in Earth System Sciences*, pages 311–336. Springer. https://doi.org/10.1007/978-3-540-74700-0_7.

van Westrum, D., Ahlgren, K., Hirt, C., and Guillaume, S. (2021). A Geoid Slope Validation Survey (2017) in the rugged terrain of Colorado, USA. *Journal of Geodesy*, 95(1):1–19. https://doi.org/10.1007/s00190-020-01463-8.

Varga, M., Pitoňák, M., Novák, P., and Bašić, T. (2021). Contribution of GRAV-D airborne gravity to improvement of regional gravimetric geoid modelling in Colorado, USA. *Journal of Geodesy*, 95(5):1–23. https://doi.org/10.1007/s00190-021-01494-9.

Vermeer, M. (2020). *Physical geodesy*. Aalto University.

Virtanen, H. (2006). *Studies of earth dynamics with the superconducting gravimeter*. PhD thesis, University of Helsinki.

Wahba, G. (1990). *Spline Models for Observational Data*. SIAM, Philadelphia, USA.

Wang, Y., Li, X., Ahlgren, K., and Krcmaric, J. (2020). Colorado geoid modeling at the US National Geodetic Survey. *Journal of Geodesy*, 94(10):1–8. https://doi.org/10.1007/s00190-020-01429-w.

Wang, Y., Sánchez, L., Ågren, J., Huang, J., Forsberg, R., Abd-Elmotaal, H., Barzaghi, R., Bašić, T., Carrion, D., Claessens, S., Erol, B., Erol, S., Filmer, M., Grigoriadis, V., Isik, M., Jiang, T., Koç, Ö., Li, X., Ahlgren, K., Krcmaric, J., Liu, Q., Matsuo, K., Natsiopoulos, D., Novák, P., Pail, R., Pitoňák, M., Schmidt, M., Varga, M., Vergos, G., Véronneau, M., Willberg, M., and Zingerle, P. (2021). Colorado geoid computation experiment - Overview and Summary. *Journal of Geodesy*, 95(127):1–21. https://doi.org/10.1007/s00190-021-01567-9.

Willberg, M., Zingerle, P., and Pail, R. (2019). Residual least-squares collocation: use of covariance matrices from high-resolution global geopotential models. *Journal of Geodesy*, 93(9):1739–1757. https://doi.org/10.1007/s00190-019-01279-1.

Willberg, M., Zingerle, P., and Pail, R. (2020). Integration of airborne gravimetry data filtering into residual least-squares collocation: example from the 1 cm geoid experiment. *Journal of Geodesy*, 94(8):1–17. https://doi.org/10.1007/s00190-020-01396-2.

Wittwer, T. (2009). *Regional gravity field modelling with radial basis functions*. PhD thesis, Netherlands Geodetic Commission.

Wong, L. and Gore, R. (1969). Accuracy of geoid heights from modified Stokes kernels. *Geophysical Journal International*, 18(1):81–91. https://doi.org/10.1111/j.1365-246X.1969.tb00264.x.

Wu, Y., Luo, Z., Chen, W., and Chen, Y. (2017a). High-resolution regional gravity field recovery from Poisson wavelets using heterogeneous observational techniques. *Earth, Planets and Space*, 69:34. https://doi.org/10.1186/s40623-017-0618-2.

Wu, Y., Luo, Z., Zhong, B., and Xu, C. (2018). A multilayer approach and its application to model a local gravimetric quasi-geoid model over the North Sea: QGNSea V1.0. *Geoscientific Model Development*, 11(12):4797–4815. https://10.5194/gmd-11-4797-2018.

Wu, Y., Zhou, H., Zhong, B., and Luo, Z. (2017b). Regional gravity field recovery using the GOCE gravity gradient tensor and heterogeneous gravimetry and altimetry data. *Journal of Geophysical Research: Solid Earth*, 122(8):6928–6952. https://doi.org/10.1002/2017JB014196.

Xu, J., Schreier, F., Doicu, A., and Trautmann, T. (2016). Assessment of Tikhonov-type regularization methods for solving atmospheric inverse problems. *Journal of Quantitative Spectroscopy and Radiative Transfer*, 184:274–286. https://doi.org/10.1016/j.jqsrt.2016.08.003.

Xu, P., Shen, Y., Fukuda, Y., and Liu, Y. (2006). Variance component estimation in linear inverse ill-posed models. *Journal of Geodesy*, 80(2):69–81. https://doi.org/10.1007/s00190-006-0032-1.

Zingerle, P., Pail, R., Gruber, T., and Oikonomidou, X. (2020). The combined global gravity field model XGM2019e. *Journal of Geodesy*, 94(7):1–12. https://doi.org/10.1007/s00190-020-01398-0.

Zingerle, P., Pail, R., Willberg, M., and Scheinert, M. (2021). A partition-enhanced least-squares collocation approach (PE-LSC). *Journal of Geodesy*, 95(8):1–16. https://doi.org/10.1007/s00190-021-01540-6.

Acknowledgements

At the end of this thesis, I would like to take the opportunity to thank those who kindly offered help and support during the journey of my Ph.D.

First and foremost, I would like to show my deepest gratitude to my supervisor Prof. Michael Schmidt for his continuous guidance, valuable suggestions, and constant encouragement throughout the whole Ph.D. period. He gives me the freedom to pursue my own ideas, and at the same time, he is always there for help with patience. I have learned a lot from him both professionally and personally. This research work would not have been possible without his support.

Many thanks to Prof. Roland Pail for all the fruitful discussions, for being the co-author of my paper, and for reviewing this thesis. He is always willing to help regardless of his busy schedule, and I am very grateful for that. I would like to thank Dr. Laura Sánchez for providing me the insights into the height system, for taking the time to answer my questions, and for the constant support. Special thanks to Prof. Annette Eicker, who is very friendly and gives her valuable comments and input that help improve this thesis.

All current and former colleagues at DGFI-TUM are greatly acknowledged. They have been really helpful and made the working environment pleasant. I appreciate very much that all colleagues are willing to share their knowledge unreservedly from different research domains. I would like to thank Prof. Florian Seitz for giving me the opportunity to work at DGFI first of all, and for all the kind help related to my contracts and visa. Many thanks to Dr. Denise Dettmering for being my mentor and answering my questions related to altimetry. I would like to express my gratitude to the DGFI "Atmosphere and Regional Gravity Field" group. My thanks also go to Dr. Martin Willberg for the nice cooperation and meaningful discussions.

Last but not least, I want to thank my parents and my brother for loving me and supporting me unconditionally. I especially thank my husband, Ramzi, who always stands by me, believes in me more than I could myself, and makes this journey more enjoyable. Thank you all for the constant encouragement and support.

Appendix

A1 Publication I

Reference

Liu, Q., Schmidt, M., Pail, R., and Willberg, M. (2020a). **Determination of the regularization parameter to combine heterogeneous observations in regional gravity field modeling**. *Remote Sensing*, 12(10), 1617. https://doi.org/10.3390/rs12101617

Copyright

This work originally has been published in Remote Sensing, an open access journal. The publication is available under the creative commons license. The copyright remains with the authors.

Declaration of own contribution

The overall own contribution of Qing Liu to P-I is estimated to be 83%, which is a weighted average of the five contribution parts listed in the Table 1.

Table 1: Contribution of Qing Liu to P-I

	Weight	Estimated contribution
Ideas and conceptual design	30%	80%
Realization and computation	10%	95%
Analysis and discussion	30%	80%
Figure compilation	10%	95%
Manuscript writing	20%	80%
Overall		**83%**

Confirmation by the Co-authors

I hereby confirm the correctness of the declaration of own contribution by Qing Liu for the publication
Liu, Q., Schmidt, M., Pail, R., and Willberg, M. (2020a). Determination of the Regularization Parameter to Combine Heterogeneous Observations in Regional Gravity Field Modeling. *Remote Sensing*, 12(10):1617. https://doi.org/10.3390/rs12101617

Michael Schmidt
Deutsches Geodätisches Forschungsinstitut der Technischen Universität München (DGFI-TUM), Germany

Signature: ..... Date: 24.05.2022

Roland Pail
Institute for Astronomical and Physical Geodesy, Technical University of Munich, Germany

Signature: ..... Date: 25.03.2021

Martin Willberg
Institute for Astronomical and Physical Geodesy, Technical University of Munich, Germany

Signature: ..... Date: 25.3.2021

remote sensing

MDPI

Article

Determination of the Regularization Parameter to Combine Heterogeneous Observations in Regional Gravity Field Modeling

Qing Liu [1,*], Michael Schmidt [1], Roland Pail [2] and Martin Willberg [2]

[1] Deutsches Geodätisches Forschungsinstitut der Technischen Universität München (DGFI-TUM), Arcisstr. 21, 80333 Munich, Germany; mg.schmidt@tum.de

[2] Institute for Astronomical and Physical Geodesy, Technical University of Munich, Arcisstr. 21, 80333 Munich, Germany; roland.pail@tum.de (R.P.); martin.willberg@tum.de (M.W.)

* Correspondence: qingqing.liu@tum.de

Received: 16 April 2020; Accepted: 17 May 2020; Published: 19 May 2020



Abstract: Various types of heterogeneous observations can be combined within a parameter estimation process using spherical radial basis functions (SRBFs) for regional gravity field refinement. In this process, regularization is in most cases inevitable, and choosing an appropriate value for the regularization parameter is a crucial issue. This study discusses the drawbacks of two frequently used methods for choosing the regularization parameter, which are the L-curve method and the variance component estimation (VCE). To overcome their drawbacks, two approaches for the regularization parameter determination are proposed, which combine the L-curve method and VCE. The first approach, denoted as "VCE-Lc", starts with the calculation of the relative weights between the observation techniques by means of VCE. Based on these weights, the L-curve method is applied to determine the regularization parameter. In the second approach, called "Lc-VCE", the L-curve method determines first the regularization parameter, and it is set to be fixed during the calculation of the relative weights between the observation techniques from VCE. To evaluate and compare the performance of the two proposed methods with the L-curve method and VCE, all these four methods are applied in six study cases using four types of simulated observations in Europe, and their modeling results are compared with the validation data. The RMS errors (w.r.t the validation data) obtained by VCE-Lc and Lc-VCE are smaller than those obtained from the L-curve method and VCE in all the six cases. VCE-Lc performs the best among these four tested methods, no matter if using SRBFs with smoothing or non-smoothing features. These results prove the benefits of the two proposed methods for regularization parameter determination when different data sets are to be combined.

Keywords: regional gravity field modeling; spherical radial basis functions; combination of heterogeneous observations; regularization parameter; VCE; the L-curve method

1. Introduction

Gravity field modeling is a major topic in geodesy, and it supports many applications, including physical height system realization, orbit determination, and solid earth geophysics. To model the gravity field, approaches need to be set up to represent the input data as well as possible. The global gravity field is usually described by spherical harmonics (SH), due to the fact that they fulfill the Laplacian differential equation and are orthogonal basis functions on a sphere; see, e.g., [1,2] for more detailed explanations. However, the computation of the corresponding spherical harmonic coefficients requires a global homogeneous coverage of input data. As this requirement cannot be fulfilled,

SHs cannot represent data of heterogeneous density and quality in a proper way [3,4]. Regional gravity refinement is, thus, performed for combining different observation types such as airborne, shipborne, or terrestrial measurements, which are only available in specific regions. Different regional gravity modeling methods have been developed during the last decades, e.g., the statistical method of Least Squares Collocation (LSC) [5–7], the method of mascons (mass concentrations) [8–10], and the Slepian functions [11,12]. The method based on SRBFs will be the focus of this work.

The fundamentals of SRBFs can be found among others in [13–15]. SRBFs are kernel functions given on a sphere which only depend on the spherical distance between two points on this sphere [16]. They are a good compromise between ideal frequency localization (SHs) and ideal spatial localization (Dirac delta functions) [17,18]. Due to the fact that SRBFs are isotropic and characterized by their localizing feature, they can be used for regional approaches to consider the heterogeneity of data sources; examples are given by [4,19,20]. Li et al. [21] listed the advantages of using SRBFs in regional gravity field modeling: they can be directly established at the observation points without gridding, and they are computationally easy to implement. There are four major factors in SRBF modeling that influence the accuracy of the regional gravity model [22,23]: (1) the shape, (2) the bandwidth, (3) the location of the SRBFs, and (4) the extension of the data zone for reducing the edge effects. Tenzer and Klees [24] compared the performance of different types of SRBFs using terrestrial data and concluded that comparable results could be obtained for each tested type of SRBFs. Naeimi et al. [23] showed that SRBFs with smoothing features (e.g., the cubic polynomial function) or without (the Shannon function) deliver different modeling results. Bentel et al. [25] studied the location of the SRBFs, which depends on the point grids; the results showed that the differences between SRBFs types are much more significant than the differences between different point grids. Another detailed investigation about the location of SRBFs can be found in [26], where the bandwidth of the SRBFs was also studied, and methods for choosing a proper bandwidth were introduced. Lieb [27] discussed the edge effects and provided a way to choose area margins in order to minimize edge effects.

After setting up the aforementioned four factors, heterogeneous data sets can be combined within a parameter estimation process. Regional gravity modeling is usually an ill-posed problem due to (1) the number of unknowns related to the basis functions, i.e., here the SRBFs; (2) data gaps; and (3) the downward continuation. Thus, regularization is in most cases inevitable in the parameter estimation process. Bouman 1998 [28] discussed and compared different regularization methods, including Tikhonov regularization [29], truncated singular value decomposition [30], and iteration methods [31]. We apply the Tikhonov regularization in this study, which can be interpreted as an estimation including prior information [32]. Instead of minimizing only the residual norm, the norm of the estimated coefficients is minimized in this procedure. Moreover, it is realized by introducing an additional condition (also called penalty term) containing the regularization parameter. Choosing an appropriate value for the regularization parameter is, however, a crucial issue.

Different methods have been developed for estimating the regularization parameter in the last decades, such as the L-curve criterion [33,34], the variance component estimation (VCE) [32,35,36], the generalized cross-validation (GCV) [37–41], and Akaike's Bayesian information criterion [42–46]. Recently, some new methods have been proposed [47–50], and a summary of existing methods can be found in [28,51–53]. As two of the most commonly used methods for determining the regularization parameter, the L-curve method and VCE have been applied in numerous studies for different research fields. Ramillien et al. [54] applied the L-curve method for the inversion of surface water mass anomalies; Xu et al. [53] used the L-curve method for solving atmospheric inverse problems; Xu et al. [55] applied VCE for the geodetic-geophysical joint inversion; and Kusche [56], Bucha et al. [57], and Wu et al. [58] used VCE in global and regional gravity field modeling; similar applications can be found in the references therein.

The L-curve method is a graphical procedure. The plot of the solution norm versus the residual norm displays an "L-shape" with a corner point, which corresponds to the desired regularization parameter. Koch and Kusche [32] demonstrated that the relative weighting

between different observation types, as well as the regularization parameter, could be determined simultaneously by VCE. The prior information is added and regarded as an additional observation technique, and thus the regularization parameter can be interpreted as an additional variance component. However, in this case, the prior information is required to be of random character [32]. In most of the regional gravity modeling studies, a background model serves as prior information. In this case, the prior information has no random character, and the regularization parameter generated by VCE is not reliable [59]. Lieb [27] presented a case that shows the instability of VCE. Naeimi [60] showed that VCE delivers larger geoid RMS errors than the L-curve method, based on GRACE and GOCE data.

As VCE does not guarantee a reliable regularization solution, and the L-curve method (or other conventional regularization methods) cannot weight heterogeneous observations [61], the purpose of this paper is to combine VCE and the L-curve method to improve the stability and reliability of the gravity solutions. The idea of combining VCE for weighting different data sets only, and a method for determining the regularization parameter was introduced in the Section "future work" of both works in [59,60], but have not yet been applied in any further publications. The study in this manuscript is also inspired by the authors of [62,63]; the formal combines VCE for VLBI intra-technique combination and GCV for regularization; the latter combines a U-curve method for determining the regularization parameter and discriminant function minimization (DFM) for estimating the relative weighting between GPS and InSAR data. Our novel contribution focus on applying this idea for combining heterogeneous observations in regional gravity field modeling. Thus, we introduce and discuss in this paper two methods that combine VCE for determining the relative weighting between different observation types and the L-curve method for determining the regularization parameter, denoted as "VCE-Lc" and "Lc-VCE", depending on the order of the applied procedures. Numerical experiments are carried out to compare their performance to the original L-curve method and VCE.

This work is organized as follows. Section 2 presents the fundamental concepts of SRBFs, different types of gravitational functionals, and their adapted basis functions. The parameter estimation, the Gauss–Markov model as well as the combination model are also introduced. Section 3 is dedicated to the regularization method, the L-curve method, VCE, and the two proposed combination methods. In Section 4, the study area, the data used in this study, and the model configuration are explained. Section 5 discusses the results. The performance of these four regularization methods is compared. Finally, the summary and conclusions are given in Section 6.

2. Regional Gravity Field Modelling Using SRBF

In general, a spherical basis function $B(\boldsymbol{x}, \boldsymbol{x}_k)$ related to a point P_k with position vector $\boldsymbol{x}_k$ on a sphere Ω_R with radius R and an observation point P with position vector $\boldsymbol{x}$ can be expressed by

$$B(\boldsymbol{x}, \boldsymbol{x}_k) = \sum_{n=0}^{\infty} \frac{2n+1}{4\pi} \left(\frac{R}{r}\right)^{n+1} B_n P_n(\boldsymbol{r}^T \boldsymbol{r}_k) \tag{1}$$

Ref. [4], with $\boldsymbol{x} = r \cdot \boldsymbol{r} = r \cdot [\cos\phi\cos\lambda, \cos\phi\sin\lambda, \sin\phi]^T$, where λ is the spherical longitude, ϕ is the spherical latitude, $\boldsymbol{x}_k = R \cdot \boldsymbol{r}_k$, P_n is the Legendre polynomial of degree n, and B_n is the Legendre coefficient which specifies the shape of the SRBF. When $B_n = 1$ for all n, $B(\boldsymbol{x}, \boldsymbol{x}_k)$ represents the Dirac delta function, which has ideal spatial localization. With the spherical basis function (1), a harmonic signal $F(\boldsymbol{x})$ given on the sphere Ω_R or in the exterior space of Ω_R, can be described as

$$F(\boldsymbol{x}) = \sum_{k=1}^{K} d_k B(\boldsymbol{x}, \boldsymbol{x}_k), \tag{2}$$

where K is the number of basis functions. The unknown coefficients d_k can be evaluated from the observations. As will be shown in the following subsection, using these coefficients, any functional of $F(\boldsymbol{x})$ can be described.

2.1. Gravity Representations

Various functionals can be derived from the gravitational potential V or from the disturbing potential T based on field transformations. The corresponding kernels can be derived from the definition (1) of the basis functions, and are listed in Table 1.

Disturbing potential: The disturbing potential T is defined as the difference between the gravity potential W and the normal gravity potential U,

$$T = W - U, \tag{3}$$

where the latter is the potential related to the level ellipsoid. The gravity potential W consists of two parts: the gravitational potential V and the centrifugal potential Z, i.e.,

$$W = V + Z. \tag{4}$$

Combining Equation (3) and Equation (4) yields [2]

$$T = V - U + Z. \tag{5}$$

The disturbing potential T can be represented by

$$T(\boldsymbol{x}) = \sum_{k=1}^{K} d_k B(\boldsymbol{x}, \boldsymbol{x}_k). \tag{6}$$

Gravitational potential difference: The satellite gravity field mission Gravity Recovery and Climate Experiment (GRACE) [64] consists of two satellites A and B. The main observable is the exact separation distance between the two satellites and its rate of change [65]. Several GRACE products exist (level 0 to level 2) [66,67]; the gravitational potential V can be computed from the level 2 products. In many studies (see, e.g., [20,27,60,68]), the differences between the gravitational potential values V of A and B are used as observations ΔV, i.e., $\Delta V(\boldsymbol{x}^A, \boldsymbol{x}^B) = V(\boldsymbol{x}^A) - V(\boldsymbol{x}^B)$. Including the measurement error e, the observation equation reads

$$\Delta V(\boldsymbol{x}^A, \boldsymbol{x}^B) + e(\boldsymbol{x}^A, \boldsymbol{x}^B) = V(\boldsymbol{x}^A) - V(\boldsymbol{x}^B) + e(\boldsymbol{x}^A, \boldsymbol{x}^B) = \sum_{k=1}^{K} d_k B(\boldsymbol{x}^A, \boldsymbol{x}^B, \boldsymbol{x}_k). \tag{7}$$

Gravity disturbance: The gravity disturbance is used in airborne and terrestrial gravity field determination. The gravity disturbance vector $\delta \boldsymbol{g}$ is expressed as the gradient of the disturbing potential T

$$\delta \boldsymbol{g} = \left[\frac{\partial T}{\partial x}, \frac{\partial T}{\partial y}, \frac{\partial T}{\partial z} \right]^T = \mathrm{grad} T. \tag{8}$$

In spherical approximation, the magnitude of the gravity disturbance can be written as

$$\delta g = -\frac{\partial T}{\partial r} = -T_r, \tag{9}$$

its observation equation reads

$$\delta g(\boldsymbol{x}) + e(\boldsymbol{x}) = \sum_{k=1}^{K} d_k B_r(\boldsymbol{x}, \boldsymbol{x}_k). \tag{10}$$

Gravity gradient: Equipped with a 3-axis gradiometer, the satellite mission Gravity Field and Steady-State Ocean Circulation Explorer (GOCE) [69] observed the gravity gradients V_{ab} with $a, b \in \{x, y, z\}$, i.e., all second-order derivatives of the gravitational potential V

$$\boldsymbol{V} = \begin{bmatrix} V_{xx} & V_{xy} & V_{xz} \\ V_{yx} & V_{yy} & V_{yz} \\ V_{zx} & V_{zy} & V_{zz} \end{bmatrix} \tag{11}$$

with $V_{xy} = V_{yx}, V_{xz} = V_{zx}, V_{yz} = V_{zy}$ and trace $\boldsymbol{V} = 0$ due to the Laplacian differential equation. The observation data of GOCE used in this study are simulated as the radial component $V_{rr} = \frac{\partial^2 V}{\partial r^2}$, and the observation equation reads

$$V_{rr}(\boldsymbol{x}) + e(\boldsymbol{x}) = \sum_{k=1}^{K} d_k B_{rr}(\boldsymbol{x}, \boldsymbol{x}_k). \tag{12}$$

For each type of gravitational functional, the adapted basis functions are derived by the zeroth, first, or second order derivatives of Equation (1), and they are listed in Table 1. Basis functions adapted to other functionals of the disturbing potential which are not used here can be found in [20,27,70].

Table 1. Kernels, i.e., the adapted basis functions for different gravitational functionals.

Gravitational Functionals	**Adapted Basis Function $B(\boldsymbol{x}, \boldsymbol{x}_k)$**
Disturbing potential	$B(\boldsymbol{x}, \boldsymbol{x}_k) = \sum_{n=0}^{\infty} \frac{2n+1}{4\pi} \left(\frac{R}{r}\right)^{n+1} B_n P_n(\boldsymbol{r}^T \boldsymbol{r}_k)$
ine Gravitational potential difference	$B(\boldsymbol{x}^A, \boldsymbol{x}^B, \boldsymbol{x}_k) = \sum_{n=0}^{\infty} \frac{2n+1}{4\pi} B_n \{ \left(\frac{R}{r^A}\right)^{n+1} P_n(\boldsymbol{r}^{A^T} \boldsymbol{r}_k) - \left(\frac{R}{r^B}\right)^{n+1} P_n(\boldsymbol{r}^{B^T} \boldsymbol{r}_k) \}$
ine Gravity disturbance	$B_r(\boldsymbol{x}, \boldsymbol{x}_k) = \sum_{n=0}^{\infty} \frac{2n+1}{4\pi} \frac{(n+1)}{r} \left(\frac{R}{r}\right)^{n+1} B_n P_n(\boldsymbol{r}^T \boldsymbol{r}_k)$
ine Gravity gradients	$B_{rr}(\boldsymbol{x}, \boldsymbol{x}_k) = \sum_{n=0}^{\infty} \frac{2n+1}{4\pi} \frac{(n+1)(n+2)}{r^2} \left(\frac{R}{r}\right)^{n+1} B_n P_n(\boldsymbol{r}^T \boldsymbol{r}_k)$

2.2. Types of Spherical Radial Basis Functions

Different types of SRBFs can be found among others in [4,68]; the frequently used types include the Shannon function, the Blackman function, the cubic polynomial (CuP) function, and the Poisson function. Two types of band-limited SRBFs are used in this work, one without smoothing features (Shannon function), i.e., their shape coefficients (Legendre coefficients) equal to 1 for all frequencies within a certain bandwidth, and the other one with smoothing features (CuP function). The Shannon function has the simplest representation; its Legendre coefficients are given by

$$B_n = \begin{cases} 1 & \text{for } n \in [0, N_{max}] \\ 0 & \text{else} \end{cases} \tag{13}$$

In case of the CuP function, the Legendre coefficients are given by a cubic polynomial, namely,

$$B_n = \begin{cases} (1 - \frac{n}{N_{max}})^2 (1 + \frac{2n}{N_{max}}) & \text{for } n \in [0, N_{max}] \\ 0 & \text{else} \end{cases} \tag{14}$$

N_{max} is a certain degree to which the SRBFs are expanded, representing the cut-off degree. These two functions for $N_{max} = 255$ are plotted in Figure 1, the top sub-plot and the bottom one visualize the characteristics in the spatial and the spectral domain, respectively. In the spatial domain, the Shannon function shows the sharper transition but also the stronger oscillations compared to the CuP function. In the spectral domain, the Shannon function is characterized by its exact band limitation without any smoothing features. The CuP function, however, has a smoothing decay. In this study, we apply both the Shannon function and the CuP function in the same experiments to test the performance of our proposed regularization methods.

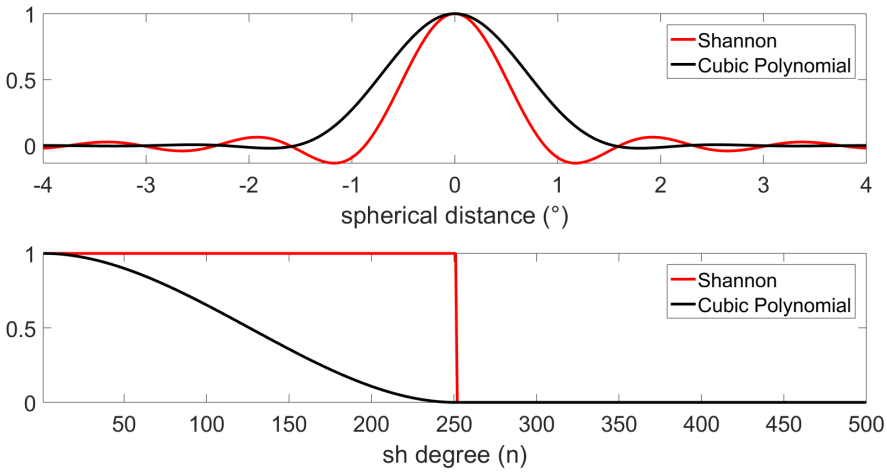


Figure 1. The different spherical radial basis functions (SRBFs) in the spatial domain (**top**, ordinate values are normalized to 1) and the spectral domain (**bottom**) for $N_{max} = 255$.

2.3. Parameter Estimation

To determine the unknown coefficients d_k in Equation (2), parameter estimation [36] is used in this study. This process allows the combination of different types of observations with varying resolutions, accuracies and distributions [71].

2.3.1. Gauss–Markov Model

For one single observation $F(\boldsymbol{x})$, the observation equation reads

$$F(\boldsymbol{x}) + e(\boldsymbol{x}) = \sum_{k=1}^{K} d_k B(\boldsymbol{x}, \boldsymbol{x}_k), \tag{15}$$

$B(\boldsymbol{x}, \boldsymbol{x}_k)$ represents the adapted SRBFs as listed in Table 1. Collecting the observations $F(\boldsymbol{x}_1)$, $F(\boldsymbol{x}_2), \ldots,$ $F(\boldsymbol{x}_n)$ in the $n \times 1$ observation vector $\boldsymbol{f}$, the Gauss–Markov model

$$\boldsymbol{f} + \boldsymbol{e} = \boldsymbol{A}\boldsymbol{d} \text{ (deterministic part)} \quad \text{with} \quad D(\boldsymbol{f}) = \sigma^2 \boldsymbol{P}^{-1} \text{ (stochastic part)} \tag{16}$$

can be set up. In the deterministic part, $\boldsymbol{e} = [e(\boldsymbol{x}_1), e(\boldsymbol{x}_2), \ldots, e(\boldsymbol{x}_n)]^T$ is the $n \times 1$ vector of the observation errors and $\boldsymbol{A} = [B(\boldsymbol{x}, \boldsymbol{x}_k)]$ is the $n \times K$ design matrix containing the corresponding basis functions. In the stochastic part, $D(\boldsymbol{f})$ is the $n \times n$ covariance matrix of the observation vector $\boldsymbol{f}$ with σ^2 being the unknown variance factor and $\boldsymbol{P}$ being the given positive definite weight matrix.

Due to the three reasons mentioned in the introduction, namely, (1) the number of unknowns related to the basis functions, (2) data gaps, and (3) the downward continuation, the normal equation matrix $\boldsymbol{N} = \boldsymbol{A}^T \boldsymbol{P} \boldsymbol{A}$ is ill-posed or even singular. For handling this problem, we introduce an additional linear model

$$\boldsymbol{\mu}_d + \boldsymbol{e}_d = \boldsymbol{d} \quad \text{with} \quad D(\boldsymbol{\mu}_d) = \sigma_d^2 \boldsymbol{P}_d^{-1} \tag{17}$$

as prior information. $\boldsymbol{\mu}_d$ is the $K \times 1$ expectation vector of the coefficient vector $\boldsymbol{d}$, $\boldsymbol{e}_d$ is the corresponding error vector, and $D(\boldsymbol{\mu}_d)$ is the $K \times K$ covariance matrix of the prior information with σ_d^2 the unknown variance factor and $\boldsymbol{P}_d$ the positive definite weight matrix. Combining the two models (16) and (17) yields the extended linear model

$$\begin{bmatrix} \boldsymbol{f} \\ \boldsymbol{\mu}_d \end{bmatrix} + \begin{bmatrix} \boldsymbol{e} \\ \boldsymbol{e}_d \end{bmatrix} = \begin{bmatrix} \boldsymbol{A} \\ \boldsymbol{I} \end{bmatrix} \boldsymbol{d} \quad \text{with} \quad D\left(\begin{bmatrix} \boldsymbol{f} \\ \boldsymbol{\mu}_d \end{bmatrix} \right) = \sigma^2 \begin{bmatrix} \boldsymbol{P}^{-1} & \boldsymbol{0} \\ \boldsymbol{0} & \boldsymbol{0} \end{bmatrix} + \sigma_d^2 \begin{bmatrix} \boldsymbol{0} & \boldsymbol{0} \\ \boldsymbol{0} & \boldsymbol{P}_d^{-1} \end{bmatrix} \tag{18}$$

Now the least-squares adjustment can be applied and leads to the normal equations

$$\left(\frac{1}{\sigma^2}\boldsymbol{A}^T\boldsymbol{P}\boldsymbol{A}+\frac{1}{\sigma_d^2}\boldsymbol{P}_d\right)\widehat{\boldsymbol{d}}=\frac{1}{\sigma^2}\boldsymbol{A}^T\boldsymbol{P}\boldsymbol{f}+\frac{1}{\sigma_d^2}\boldsymbol{P}_d\boldsymbol{\mu}_d \tag{19}$$

The variance factors σ^2 and σ_d^2 can either be chosen or estimated within a VCE, and the solution reads

$$\widehat{\boldsymbol{d}}=(\boldsymbol{A}^T\boldsymbol{P}\boldsymbol{A}+\lambda\boldsymbol{P}_d)^{-1}(\boldsymbol{A}^T\boldsymbol{P}\boldsymbol{f}+\lambda\boldsymbol{P}_d\boldsymbol{\mu}_d) \tag{20}$$

$$D(\widehat{\boldsymbol{d}})=\sigma^2(\boldsymbol{A}^T\boldsymbol{P}\boldsymbol{A}+\lambda\boldsymbol{P}_d)^{-1}, \tag{21}$$

wherein $\lambda=\sigma^2/\sigma_d^2$ can be interpreted as the regularization parameter, see [4,32]. When $\boldsymbol{\mu}_d$ is set to the zero vector, Equation (20) reduces to the Tikhonov regularization, and the regularization parameter λ can be determined by the L-curve method.

2.3.2. Combination Model

To combine different types of heterogeneous data sets for regional gravity field modeling, combination model (CM) needs to be set up (see, e.g., [4,32]). In general, let $\boldsymbol{f}_l$ with $l=1,\ldots,L$ be the observation vector of the l^{th} observation technique, such as $\boldsymbol{f}_l=[F_l(\boldsymbol{x}_1),F_l(\boldsymbol{x}_2),\ldots,F_l(\boldsymbol{x}_{n_l})]^T$, $\boldsymbol{e}_l$ and $\boldsymbol{A}_l$ are the corresponding error vector and the design matrix. Note that for different techniques, the data are observed as different gravitational functionals and thus, the adapted SRBFs as discussed in the Section 2.1 must be applied accordingly, $\boldsymbol{A}_l=[B_l(\boldsymbol{x},\boldsymbol{x}_k)]$. For the combination of the L observation techniques, an extended Gauss–Markov model can be formulated by including the additional linear model (17) for the prior information

$$\begin{bmatrix}\boldsymbol{f}_1\\ \boldsymbol{f}_2\\ \vdots\\ \boldsymbol{f}_L\\ \boldsymbol{\mu}_d\end{bmatrix}+\begin{bmatrix}\boldsymbol{e}_1\\ \boldsymbol{e}_2\\ \vdots\\ \boldsymbol{e}_L\\ \boldsymbol{e}_d\end{bmatrix}=\begin{bmatrix}\boldsymbol{A}_1\\ \boldsymbol{A}_2\\ \vdots\\ \boldsymbol{A}_L\\ \boldsymbol{I}\end{bmatrix}\cdot\boldsymbol{d}\ \text{ with }\ D\left(\begin{bmatrix}\boldsymbol{f}_1\\ \boldsymbol{f}_2\\ \vdots\\ \boldsymbol{f}_L\\ \boldsymbol{\mu}_d\end{bmatrix}\right)=\begin{bmatrix}\sigma_1^2\boldsymbol{P}_1^{-1} & \boldsymbol{0} & \boldsymbol{0} & \ldots & \boldsymbol{0}\\ \boldsymbol{0} & \sigma_2^2\boldsymbol{P}_2^{-1} & \vdots & \vdots & \vdots\\ \vdots & \boldsymbol{0} & \ddots & \vdots & \vdots\\ \vdots & \vdots & \vdots & \sigma_L^2\boldsymbol{P}_L^{-1} & \boldsymbol{0}\\ \boldsymbol{0} & \boldsymbol{0} & \ldots & \boldsymbol{0} & \sigma_d^2\boldsymbol{P}_d^{-1}\end{bmatrix} \tag{22}$$

Ref. [27], where $\boldsymbol{P}_l$ is the $n_l\times n_l$ positive definite weight matrix of the lth observation technique.

Applying the least-squares method to Equation (22), the extended normal equations read

$$\left(\sum_{l=1}^{L}\left(\frac{1}{\sigma_l^2}\boldsymbol{A}_l^T\boldsymbol{P}_l\boldsymbol{A}_l\right)+\frac{1}{\sigma_d^2}\boldsymbol{P}_d\right)\widehat{\boldsymbol{d}}=\sum_{l=1}^{L}\left(\frac{1}{\sigma_l^2}\boldsymbol{A}_l^T\boldsymbol{P}_l\boldsymbol{f}_l\right)+\frac{1}{\sigma_d^2}\boldsymbol{P}_d\boldsymbol{\mu}_d. \tag{23}$$

The values for the variance factors can either be chosen or estimated by VCE (refer to Section 3.2). Consequently, the solution of Equation (23) reads

$$\widehat{\boldsymbol{d}}=\left(\sum_{l=1}^{L}\left(\frac{1}{\sigma_l^2}\boldsymbol{A}_l^T\boldsymbol{P}_l\boldsymbol{A}_l\right)+\frac{1}{\sigma_d^2}\boldsymbol{P}_d\right)^{-1}\left(\sum_{l=1}^{L}\left(\frac{1}{\sigma_l^2}\boldsymbol{A}_l^T\boldsymbol{P}_l\boldsymbol{f}_l\right)+\frac{1}{\sigma_d^2}\boldsymbol{P}_d\boldsymbol{\mu}_d\right). \tag{24}$$

The covariance matrix of the unknown parameter vectors reads

$$D(\widehat{\boldsymbol{d}})=\left(\sum_{l=1}^{L}\left(\frac{1}{\sigma_l^2}\boldsymbol{A}_l^T\boldsymbol{P}_l\boldsymbol{A}_l\right)+\frac{1}{\sigma_d^2}\boldsymbol{P}_d\right)^{-1}. \tag{25}$$

Equation (24) can be rewritten as

$$\widehat{\boldsymbol{d}} = \left(\sum_{l=1}^{L} (\omega_l \boldsymbol{A}_l^T \boldsymbol{P}_l \boldsymbol{A}_l) + \lambda \boldsymbol{P}_d \right)^{-1} \left(\sum_{l=1}^{L} \left(\omega_l \boldsymbol{A}_l^T \boldsymbol{P}_l \boldsymbol{f}_l \right) + \lambda \boldsymbol{P}_d \boldsymbol{\mu}_d \right), \tag{26}$$

such that $\lambda = \widehat{\sigma}_1^2 / \widehat{\sigma}_d^2$ is the regularization parameter, and the factors $\omega_1 = \widehat{\sigma}_1^2 / \widehat{\sigma}_1^2 = 1$, $\omega_2 = \widehat{\sigma}_1^2 / \widehat{\sigma}_2^2, \ldots, \omega_L = \widehat{\sigma}_1^2 / \widehat{\sigma}_L^2$ express the relative weights of the observation vector $\boldsymbol{f}_l$ with respect to $\boldsymbol{f}_1$.

3. Determination of the Regularization Parameter

A critical question of regularization is the selection of an appropriate regularization parameter λ [72]. In the following, the L-curve method and the VCE will be explained in more detail. Finally, two new proposed methods are presented as combinations of VCE and the L-curve method.

3.1. L-Curve Method

The L-curve is a graphical procedure for regularization [28,33,34,73]. The norm of the regularized solution $\|\widehat{\boldsymbol{d}}_\lambda - \boldsymbol{\mu}_d\|$ is plotted against the norm of the residuals $\|\widehat{\boldsymbol{e}}\| = \|\boldsymbol{A}\widehat{\boldsymbol{d}}_\lambda - \boldsymbol{f}\|$ by changing the numerical value for the regularization parameter λ. Moreover, the plot shows a typical L-curve behavior, i.e., it looks like the capital letter "L" (see Figure 2). The corner point in this L-shaped curve means a compromise of the minimization of the solution norm (which measures the regularity of the solution) and the residual norm (which quantifies the quality of fit to the given data), and thus can be interpreted as the "best fit" point that corresponds to the desired regularization parameter.

It should be mentioned that if the L-curve method is to be applied when different types of observations are combined, the relative weights ω_l in Equation (24) need to be chosen. However, as it is not possible to know the accurate weights, the solution delivered by the L-curve method alone is, thus, not reliable.

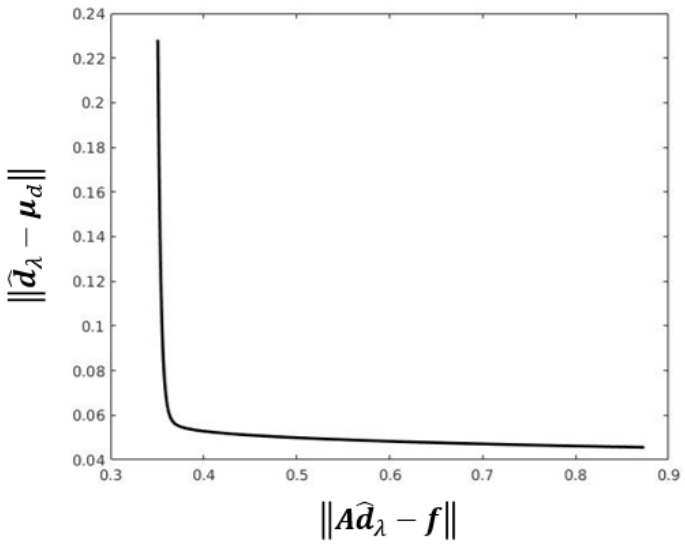


Figure 2. An example of the L-curve function.

3.2. Variance Component Estimation

Variance component estimation not only estimates the relative weighting between each data set but also determines the regularization parameter simultaneously. The variance components are estimated by an iterative process [20,32]. It starts from initial values for σ_l^2, σ_d^2, and ends in the convergence point. The estimations read

$$\begin{cases} \widehat{\sigma}_l^2 = \frac{\widehat{\boldsymbol{e}}_l^T \boldsymbol{P}_l \widehat{\boldsymbol{e}}_l}{r_l} \\ \widehat{\sigma}_d^2 = \frac{\widehat{\boldsymbol{e}}_d^T \boldsymbol{P}_d \widehat{\boldsymbol{e}}_d}{r_d} \end{cases} \tag{27}$$

where the residual vectors $\widehat{\boldsymbol{e}}_l$ and $\widehat{\boldsymbol{e}}_d$ are given as

$$\begin{cases} \widehat{\boldsymbol{e}}_l = \boldsymbol{A}_l \widehat{\boldsymbol{d}} - \boldsymbol{f}_l \\ \widehat{\boldsymbol{e}}_d = \widehat{\boldsymbol{d}} - \boldsymbol{\mu}_d \end{cases} \tag{28}$$

and r_l, r_d are the partial redundancies, which are the contributions of the observations $\boldsymbol{f}_l$ and the prior information $\boldsymbol{\mu}_d$ to the overall redundancy of Equation (22). The redundancy numbers r_l, r_d are computed following Koch and Kusche [32],

$$\begin{cases} r_l = n_l - \text{trace}(\frac{1}{\sigma_l^2} \boldsymbol{A}_l^T \boldsymbol{P}_l \boldsymbol{A}_l \boldsymbol{N}^{-1}) \\ r_\mu = K - \text{trace}(\frac{1}{\sigma_d^2} \boldsymbol{P}_d \boldsymbol{N}^{-1}) \end{cases} \tag{29}$$

where n_l denotes the number of observations in the l^{th} data set, K is the number of coefficients, and

$$\boldsymbol{N} = \left(\sum_{l=1}^{L} (\frac{1}{\sigma_l^2} \boldsymbol{A}_l^T \boldsymbol{P}_l \boldsymbol{A}_l) + \frac{1}{\sigma_d^2} \boldsymbol{P}_d \right). \tag{30}$$

Starting with initial values for σ_l^2, σ_d^2, an initial solution for $\widehat{\boldsymbol{d}}$ can be calculated, and it leads to the new estimations for $\widehat{\sigma}_l^2$, $\widehat{\sigma}_d^2$ in Equation (27). The procedure iterates until the convergence point is reached.

As in the model represented by Equation (17) the prior information is regarded as an additional type of noisy observation, $\boldsymbol{\mu}_d$ is expected to be of stochastic character. However, when the background model serves as prior information, $\boldsymbol{\mu}_d$ is a deterministic vector. Consequently, $\boldsymbol{e}_d = \boldsymbol{d} - \boldsymbol{\mu}_d$ is also deterministic, and the requirements for the Equation (17) are in fact not fulfilled. Thus, in this case the regularization parameter λ generated by VCE is not reliable.

3.3. Combination of VCE and the L-Curve Method

To overcome the drawbacks in the L-curve method and in the VCE for combining heterogenous observations, two methods are proposed and applied in this study, namely, VCE-Lc and Lc-VCE.

3.3.1. VCE-Lc

Figure 3 illustrates the procedure of the VCE-Lc. In the first step, the VCE is applied to determine the relative weights between the observation types. This step gives the relative weighting factors ω_l, and a regularization parameter λ_{VCE} simultaneously, after the iteration converges. In the second step, the weighting factors ω_l are kept, but the regularization parameter λ_{VCE} is not used. Instead, a new regularization parameter is regenerated using the L-curve method. The corner point in the plot of the regularized solution norm $\|\widehat{\boldsymbol{d}}_\lambda - \boldsymbol{\mu}_d\|_{\boldsymbol{P}_d}$ against the the residual norm $\|\widehat{\boldsymbol{e}}\| = \|\boldsymbol{A}\widehat{\boldsymbol{d}}_\lambda - \boldsymbol{f}\|_{\boldsymbol{P}}$ corresponds to the new regularization parameter. In this case, the L-curve method is applied based on the variance factors $\widehat{\sigma}_l^2$ of each observation type generated by VCE. The corner point in Figure 2 corresponds to the new regularization parameter $\lambda_{\text{L-curve}}$.

Thus, the final solution is computed using Equation (26) with the weights ω_l from VCE and the new regularization parameter $\lambda_{\text{L-curve}}$ from the L-curve criterion.

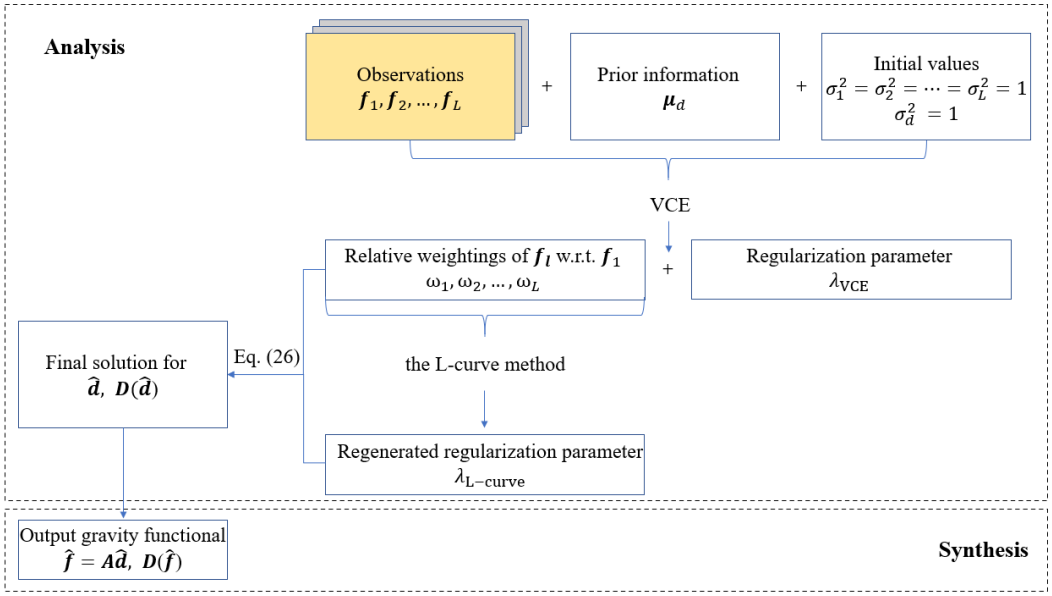


Figure 3. Analysis and synthesis for combining different types of observations based on the VCE-Lc.

3.3.2. Lc-VCE

Figure 4 illustrates the procedure of the Lc-VCE. In contrast to the VCE-Lc, in the Lc-VCE the L-curve method is applied first based on chosen values for the relative weights ω_l in Equation (24). A regularization parameter $\lambda_{\text{L-curve}}$ is obtained in the first step, and it is used for defining the value of σ_d^2 in the variance component estimation.

In the second step, the VCE is applied with initial values $\sigma_1^2 = \sigma_2^2 = \ldots = \sigma_L^2$ and $\sigma_d^2 = \sigma_1^2/\lambda_{\text{L-curve}}$. After each iteration within the VCE, the value of σ_d^2 is set to $\sigma_1^2/\lambda_{\text{L-curve}}$ again, with the new value of σ_1^2 obtained in this iteration. In this case, the regularization parameter λ calculated from the L-curve method will be kept, but the relative weighting factors ω_l are recomputed in each iteration step. The final solution is computed using Equation (26) with the relative weights ω_l and the regularization parameter $\lambda_{\text{L-curve}}$.

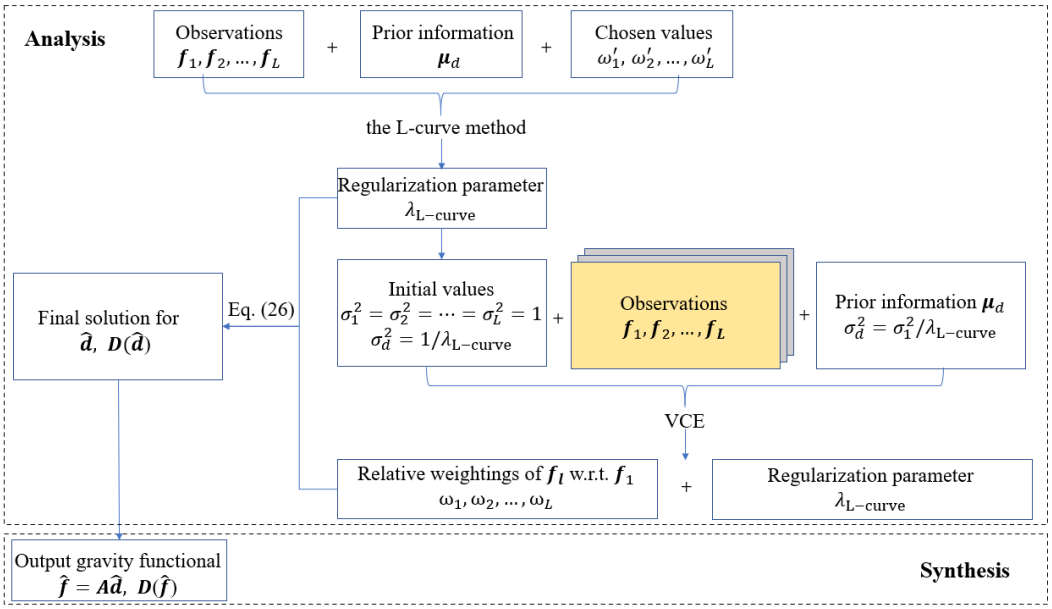


Figure 4. Analysis and synthesis for combining different types of observations based on the Lc-VCE.

It is worth clarifying that the solution obtained from the Lc-VCE is not unique. Due to the fact that the regularization parameter $\lambda_{\text{L-curve}}$ is fixed during VCE, the results change when $\lambda_{\text{L-curve}}$ refers to different observation techniques. To be more specific, as already mentioned in the last paragraph, the value of σ_d^2 is set to $\sigma_1^2/\lambda_{\text{L-curve}}$ after each iteration. Thus, the value of σ_d^2 changes by setting different observation types as σ_1^2, and the results of Equation (24) change, consequently.

To summarize, the purpose of these two proposed methods is to benefit from the L-curve method and VCE, and thus to overcome the drawbacks when using each method individually. VCE-Lc fixes the relative weights of each observation technique first and tries to find a "best fit" regularization parameter, whereas Lc-VCE fixes the regularization parameter first and then tries to find the relative weights for each observation technique.

4. Numerical Investigation

4.1. Data Description

The data used in this study are provided by the ICCT (Inter-Commission Committee on Theory) Joint Study Group (JSG) 0.3 "Comparison of current methodologies in regional gravity field modelling", part of the IAG (International Association of Geodesy) programme running from 2011 to 2015. The observation data are simulated from the Earth Gravitational Model EGM2008 [74] and are provided along with simulated observation noise. In this study, all observations are simulated in the sense of disturbing gravity field quantities, i.e., functionals of the disturbing potential T: disturbing potential differences ΔT for GRACE, the first order radial derivatives T_r for the terrestrial and airborne observations as well as the second order radial derivatives T_{rr} for GOCE. The standard deviations of the given white noise are $8 \cdot 10^{-4}$ m^2/s^2 for GRACE, 10 mE for GOCE, 0.01 mGal for the terrestrial data and 1 mGal for the airborne data. The study area chosen here is "Europe", where the validation data are also simulated from the EGM2008 and provided on geographic grid points in terms of disturbing potential values T.

Figure 5 illustrates the available observation data as well as the validation data. The two validation areas are presented with black rectangles: the larger area (Synthesis Data I) has a spatial resolution of $30' \times 30'$ and is simulated with a maximum degree of 250; the smaller area (Synthesis Data II) has a spatial resolution of $5' \times 5'$ and with a maximum degree of 2190. Four types of observations are included:

1. GRACE data: provided along the real satellite orbits of GRACE (green tracks in Figure 5), with a time span of one month.
2. GOCE data: provided along the real satellite orbits of GOCE (red tracks), covering a full repeat cycle of 61 days.
3. Terrestrial data: provided in a regular grid on the surface of the topography (DTM2006.0 [75]) with two different resolutions: one over an area of $20^\circ \times 30^\circ$ (latitude $\times$ longitude) with a grid spacing of $30'$ (blue dots) and the other one over an inner area of $6^\circ \times 10^\circ$ with a grid spacing of $5'$ (yellow highlighted area).
4. Airborne data: provided on two different flight tracks: one over the Adriatic Sea (magenta striped area) and the other one over Corsica connecting Southern Europe with Northern Africa (cyan striped area).

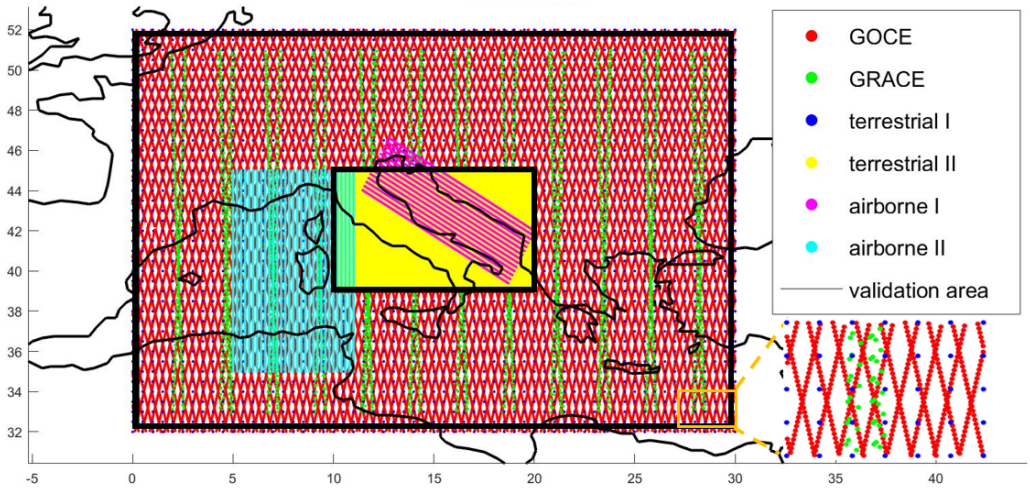


Figure 5. The study area as well as the GRACE, GOCE, terrestrial and airborne observations

This study uses simulated data to take advantage of the availability of validation data. As this is a conceptual study to compare different methods, it is important to have an accurate validation data serving as the "true value" so that the gravity modeling result from each method can be evaluated and compared. Although validation when using real data is also possible, e.g., by comparing to GNSS/leveling data or to existing regional gravity models in the same region, the accuracy of the validation data then needs to be assessed beforehand.

4.2. Model Configuration

A Remove–Compute–Restore approach [76,77] is applied in this study, i.e., from each type of observation, the background model EGM2008 up to spherical harmonic degree 60 is removed and restored in the synthesis step. The background model serves additionally as prior information, and thus the vector $\boldsymbol{d}$ of the unknown coefficients contains the gravity information referring to a reference field (background model) up to degree and order 60. Koch and Kusche [32] pointed out that in this case, the expectation vector $\boldsymbol{\mu}_d$ can be set to the zero vector [4,27]. We assume that the coefficients have the same accuracy and are uncorrelated; thus, $\boldsymbol{P}_d = \boldsymbol{I}$, where $\boldsymbol{I}$ denotes the identity matrix. Further, we set $\boldsymbol{P}_l = \boldsymbol{I}$ by assuming the measurement errors to be uncorrelated and the same type of observations to have the same accuracy. These assumptions are commonly used in the existing publications for both simulated and real data, since it is usually difficult to acquire the realistic full error variance-covariance matrix, and examples can be found in, e.g., [27,57,58].

As discussed in Section 3.1, the values of σ_l^2 need to be chosen beforehand for the L-curve method. In studies where different observation types are involved, one might conduct an analysis on the relative weighting between the data sets in order to apply the L-curve method. Thus, in this study, empirically chosen values of σ_l^2 are used for each observation type to have a more realistic result for the L-curve method. Lieb et al. [20] pointed out that the variance factors σ_l^2 depend on the measurement accuracy, but also on the number, the spectral resolution, and the spatial distribution of the data. By using only the noise levels of each data set for calculating the variance factors, the σ_l^2 values should be $0.64 \cdot 10^{-6}$ for the GRACE data, 10^{-22} for the GOCE data, 10^{-10} for the airborne data, and 10^{-14} for the terrestrial data. However, Lieb (2017) showed that the airborne and terrestrial data are less sensitive in the low-frequency part, and their weights could degrade up to six orders of magnitude when the maximum degree of expansion is low. Taking both factors into consideration, the values of σ_l^2 are chosen as 10^{-6} for the GRACE data, 10^{-22} for the GOCE data, and 10^{-8} for the terrestrial data and the airborne data in this study. It is worth mentioning that these values of σ_l^2 are only approximations, and they are a choice for applying the L-curve method when VCE is not considered.

Moreover, the purpose of this study is not to compare between the L-curve method and VCE, but to compare the two proposed methods with using the L-curve method or VCE individually. The results for the L-curve method without relative weights (equal weighting between each data set) are also presented in Section 5.1 as a comparison scenario.

In this study, different observation types are combined in a "one-level" manner, which is also applied in, e.g., [20,58,68]. The relative weights indicate the contributions of different observation types [20]. Another way for combining different types of observations is the spectral combination (see, e.g., in [78–80]), where the (spectral) weights depend on the spectral degree. The spectral weights at each degree can be incorporated into the (kernel) functions [79], and studies about how to find the optimal kernels can be found in, e.g., [80,81]. However, details about the spectral combination technique would go beyond the scope of this study.

Figure 6 presents the computation area $\partial\Omega_C$, the observation area $\partial\Omega_O$, as well as the investigation area $\partial\Omega_I$. The computation area $\partial\Omega_C$ should be larger than the observation area $\partial\Omega_O$, due to the oscillations of the SRBFs. The observation area $\partial\Omega_O$ should be larger than the investigation area $\partial\Omega_I$, because the unknown coefficients d_k cannot be accurately estimated in the border of the observation area $\partial\Omega_O$. Thus, $\partial\Omega_I \subset \partial\Omega_O \subset \partial\Omega_C$, and detailed explanations for this extension can be found in [27,60]. In the analysis step, we estimate the vector $\widehat{\boldsymbol{d}}$ of the unknown coefficients $\boldsymbol{d}_k$ related to the grid points P_k within the computation area $\partial\Omega_C$, from the measurements available within the area $\partial\Omega_O$. In the following synthesis step, these coefficients are used for calculating the output gravity functional within the area $\partial\Omega_I$. It has to be mentioned that the points P_k within the computation area $\partial\Omega_C$ are defined by a Reuter grid [82]. The Reuter's algorithm generates a system of homogeneous points on the sphere [22]. Margins η between the computation area $\partial\Omega_C$ and the observation area $\partial\Omega_O$ as well as between the observation area $\partial\Omega_O$ and the investigation area $\partial\Omega_I$ are chosen equally, and they have to be defined to minimize edge effects in the computation process [20]. In this study, we conducted the experiments using different margin sizes (from 1° to 4°), and the ones (values given in Section 5) which result in the smallest difference between the estimated disturbing potential and the validation data are finally chosen.

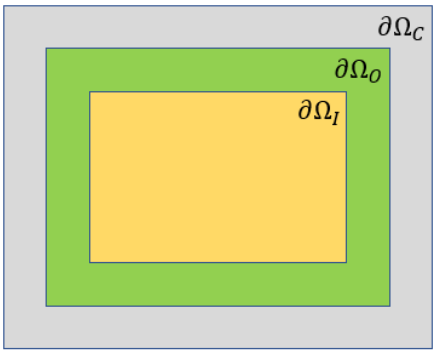


Figure 6. Extensions for the different areas $\partial\Omega_C$ of computation, $\partial\Omega_O$ of observations, and $\partial\Omega_I$ of investigation.

The aforementioned four methods for choosing the regularization parameter, i.e., (1) L-curve method, (2) VCE, (3) VCE-Lc, and (4) Lc-VCE, are applied to six groups of data sets, respectively. The types of observations involved in the six study cases as well as the corresponding validation data for each study case are listed in Table 2. These six groups cover the possible combination among the four data types, to make sure that the comparisons of these four methods are conducted in different data combination scenario. The computed disturbing potential T_c is compared with the corresponding validation data T_v and assessed following two criteria:

1. Root mean square error (RMS) of the computed disturbing potential T_c with respect to the validation data T_v over the investigation area $\partial\Omega_I$

$$\mathrm{RMS} = \sqrt{\frac{\sum_{n_{\mathrm{points}}} (T_v - T_c)^2}{n_{\mathrm{points}}}} \tag{31}$$

where n_{points} is the number of points in the validation data.

2. Correlation coefficient between the estimated coefficients d_k collected in the vector $\widehat{\boldsymbol{d}}$ and the validation data T_v. It has to be clarified that the estimated coefficients d_k and the validation data T_v are located at different points, and an interpolation is conducted to transit d_k to the grid of the validation data.

   The reason that this correlation can be used as a criterion is that the coefficients d_k reflect the energy of the gravity field at their locations. On a sphere embedded in a three-dimensional space, the energy of a signal $F(\boldsymbol{x})$ can be expressed by

$$E = \int_{\Omega_R} |F(\boldsymbol{x})|^2 d\Omega_R. \tag{32}$$

   Combining Equation (2) with Equation (32), it yields

$$E = \int_{\Omega_R} |\sum_{k=1}^{K} d_k B(\boldsymbol{x}, \boldsymbol{x}_k)|^2 d\Omega_R = \sum_{k=1}^{K} d_k \sum_{i=1}^{K} d_i \int_{\Omega_R} B(\boldsymbol{x}, \boldsymbol{x}_k) B(\boldsymbol{x}, \boldsymbol{x}_i) d\Omega_R. \tag{33}$$

   By inserting the series expansion of the SRBFs (Equation 1) on Ω_R to Equation (33) and applying the addition theorem (details about the equation manipulation can be found in [27]), the energy contribution E_k ($k = 1, 2, \ldots, K$) at location $\boldsymbol{x}_k$ is given as

$$E_k = d_k \sum_{i=1}^{K} d_i \sum_{n=0}^{N_{max}} \frac{2n+1}{4\pi} B_n^2 P_n(\boldsymbol{r}_i^T \boldsymbol{r}_k). \tag{34}$$

   When N_{max} goes to ∞, and B_n=1 for all n, i.e., in the case of the Dirac delta function, $E_k = d_k^2$. In the case of SRBFs where $N_{max} \neq \infty$, and B_n is not necessarily equal to 1, the relation $E_k = d_k^2$ is only approximately valid. However, a higher correlation between the coefficients d_k and the validation data still indicates a better representation of the gravity signal. The same criterion is used as a quality measure by [23,25].

Table 2. Study cases.

Study Case	Data Combination	Validation Data
A	GRACE + GOCE	Synthesis Data I
B	GRACE + Airborne I + Airborne II	
C	GRACE + Terrestrial I	
D	GOCE + Terrestrial I	Synthesis Data II
ine E	Terrestrial II + Airborne I	
F	GRACE + GOCE + Terrestrial II +Airborne I	

5. Results

The experiments are carried out using the Shannon function for both analysis and synthesis. However, to test the performance of these four methods when a smoothing SRBF is used, the same experiments are also applied using the CuP function for analysis and synthesis as a comparison scenario. The maximum degree in the expansion in terms of SRBF is chosen based

on the spatial resolution of the observations [20,57], and it is set to $N_{max} = 250$ for the study cases A and B; $N_{max} = 400$ for the study cases C and D; $N_{max} = 2190$ for the study cases E; and $N_{max} = 1050$ for the study case F. The margin η between the different areas (Figure 6) is chosen to be 4° for the study cases A, B, C, and D, and 2° for the study cases E and F.

For the sake of brevity, only the results of two study cases (case A in Table 3 and case F in Table 4) are detailed here. Results from the case A and the case F clearly show the drawbacks of VCE and the L-curve method, respectively. However, results obtained from all study cases, including the RMS errors and the correlations between the estimated coefficients d_k and the validation data T_v of each method are summarized in the Tables 5 and 6, respectively. The results when using the CuP function are listed in the Tables 7 and 8.

5.1. Results Using the Shannon Function

5.1.1. Study Case A

GRACE and GOCE observations are combined. Four solutions are estimated according to the aforementioned four methods for determining the regularization parameter. For each solution, the RMS error as well as the correlation between the estimated coefficients d_k and the validation data T_v are listed in Table 3. Two scenarios are considered, depending on how the relative weights ω_l (or the variance factors σ_l^2) between each observation type are chosen in the L-curve method and Lc-VCE. In the first scenario, the relative weights ω_l are chosen empirically (see Section 4.2). The lowest RMS error is obtained from the VCE-Lc which is 4.59 m^2/s^2. This method also delivers the highest correlation between the estimated coefficients d_k and the validation data. Lc-VCE gives the second best RMS value which is 4.61 m^2/s^2 (Referring to Section 3.3.2, the solution obtained from Lc-VCE is not unique, and the results listed here for Lc-VCE are always the best ones, i.e., the solution which gives the lowest RMS and largest correlation). For each solution, the estimated coefficients d_k, the calculated disturbing potential T_c, as well as its difference to the validation data are plotted in Figure 7. VCE gives the smallest correlation and the largest difference compared to the validation data. The RMS error obtained from VCE is 7.84 m^2/s^2, which is ~70% larger than those obtained from VCE-Lc or Lc-VCE.

In reality, it is difficult to choose the empirical weights between different observation types accurately, as the accuracy of different observation types is not available. As listed in Table 3, in the second scenario, when no relative weights are applied (equal weighting between data sets), the performance of the L-curve method decreases, with a 56% increase in RMS error. This increase demonstrates the importance of accurately weighting different data sets. The result obtained from the Lc-VCE also decreases slightly, with the RMS error increases from 4.61 m^2/s^2 to 5.17 m^2/s^2. In this scenario, VCE-Lc and Lc-VCE still deliver the lowest and second lowest RMS error, respectively. The same order applies to the correlation between the estimated coefficients d_k and the validation data. The RMS error from VCE-Lc is 36% and 41% smaller than that delivered by the L-curve method and VCE, respectively. The RMS error from Lc-VCE is 28% and 34% smaller than that delivered by the L-curve method and VCE, respectively. VCE still gives the largest RMS error as well as the smallest correlation, which proves that VCE does not determine the regularization parameter as successful as the L-curve method, since it gives a worse result than the L-curve method which is based on an equal weighting between each observation type.

Table 3. Results of Study Case A: the root mean square error (RMS) values (unit [m^2/s^2]) as well as the correlations for each regularization method, when different relative weights ω_l are chosen for the L-curve method

Regularization Method	ω_l Chosen Empirically		$\omega_l = 1$	
	RMS	Correlation	RMS	Correlation
L-curve method	4.6185	0.9376	7.2153	0.9078
VCE	7.8374	0.8965	7.8374	0.8965
VCE-Lc	4.5876	0.9384	4.5876	0.9384
Lc-VCE	4.6062	0.9382	5.1655	0.9310

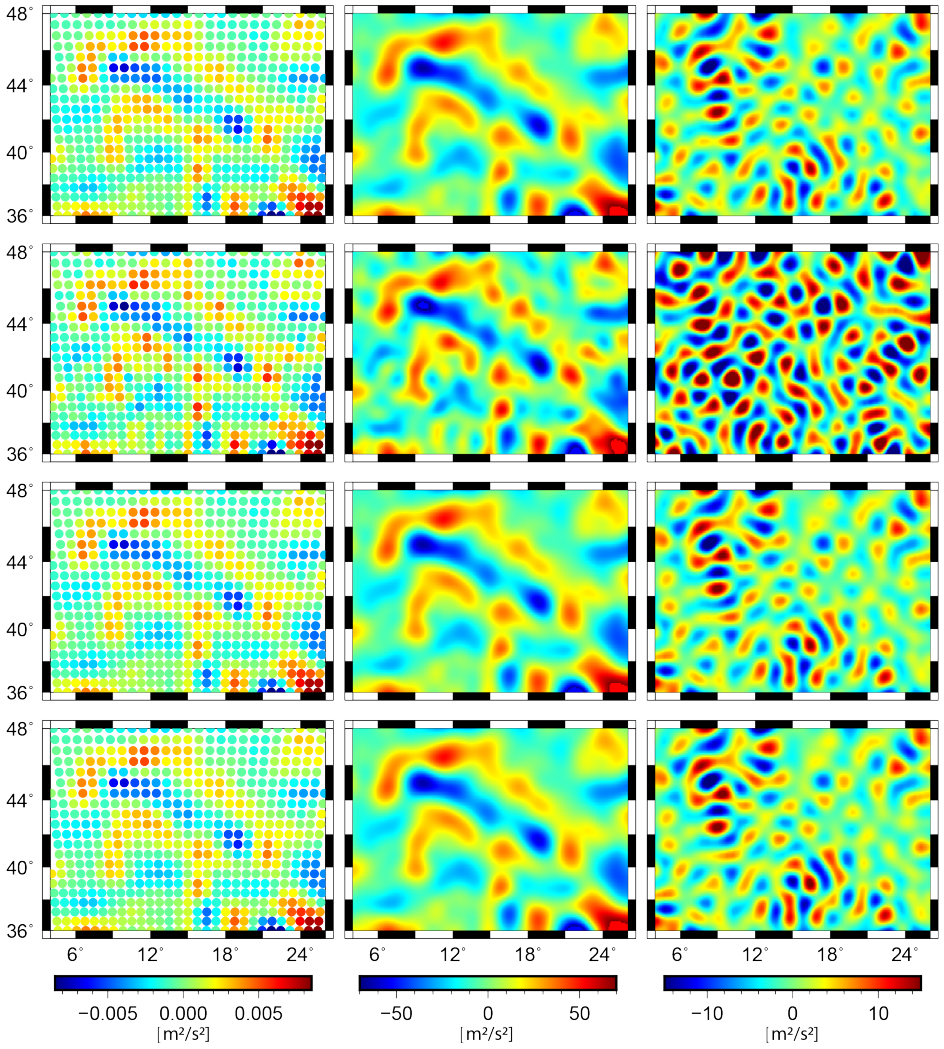


Figure 7. The estimated coefficients d_k (**left column**), the recovered disturbing potential T_c (**mid column**), and the differences w.r.t the validation data (**right column**) for study case A. The results are obtained using: the L-curve method (**first row**), VCE (**second row**), VCE-Lc (**third row**), and Lc-VCE (**fourth row**).

5.1.2. Study Case F

In case F, four data sets (GRACE, GOCE, the terrestrial II, and the airborne I observations) are combined. Compared to the study case A, the results in the study case F (listed in Table 4) show a general improvement, in terms of both the two criteria. When the relative weights ω_l are chosen empirically (see Section 4.2), VCE-Lc provides the smallest RMS error 0.84 m^2/s^2, followed by

the Lc-VCE. The same order applies to the correlation between the estimated coefficients d_k and the validation data. The L-curve method delivers the largest RMS value with 0.91 m^2/s^2, as well as the smallest correlation. It shows that the empirically chosen relative weights between different observation types are not accurate, and it is necessary to estimate the weights with VCE. For each solution, the estimated coefficients d_k, the calculated disturbing potential T_c as well as its difference to the validation data are plotted in Figure 8. It shows that the L-curve method delivers the largest difference compared to the validation data.

When no relative weights are applied (equal weighting), the performance of the L-curve method decreases, with a 61% increase in RMS error. Further, in this case, it delivers the worst results, with an RMS error 75% larger than the ones obtained by VCE-Lc or Lc-VCE. It shows that when more types of observation are involved, combining each observation technique with a relative weight becomes even more important. VCE-Lc again delivers the smallest RMS error as well as the highest correlation, followed by Lc-VCE.

Table 4. Results of Study Case F: the RMS values (unit [m^2/s^2]) as well as the correlations for each regularization method, when different relative weights ω_l are chosen for the L-curve method

Regularization Method	ω_l Chosen Empirically		$\omega_l = 1$	
	RMS	Correlation	RMS	Correlation
L-curve method	0.9106	0.9803	1.4687	0.9766
VCE	0.8410	0.9807	0.8410	0.9807
VCE-Lc	0.8377	0.9916	0.8377	0.9916
Lc-VCE	0.8394	0.9842	0.8403	0.9831

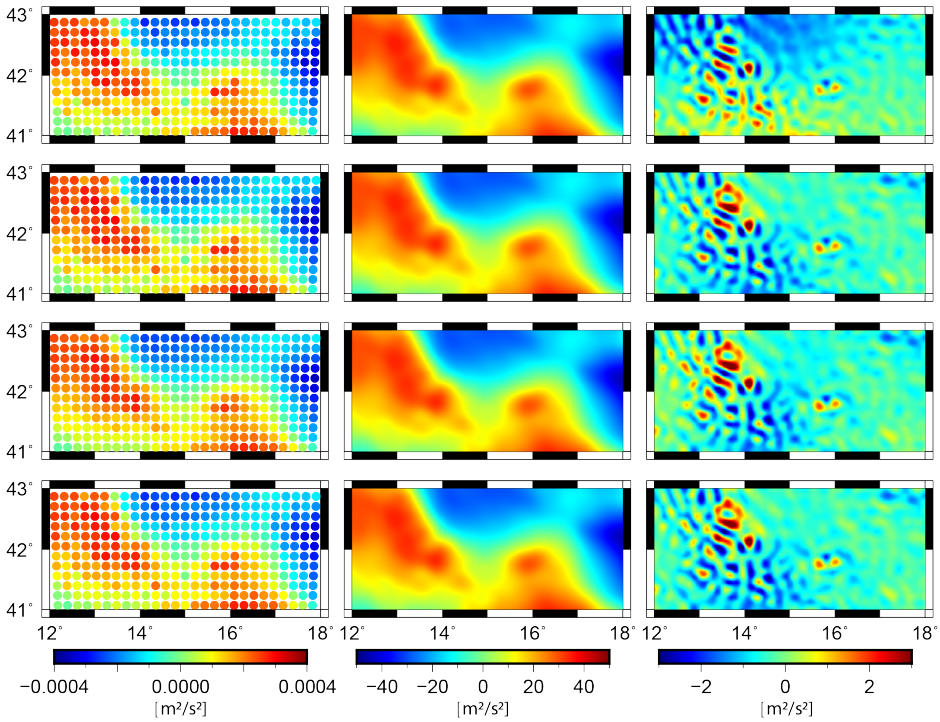


Figure 8. The estimated coefficients d_k (**left column**), the recovered disturbing potential T_c (**mid column**), and the differences w.r.t the validation data (**right column**) for study case F. The results are obtained using: the L-curve method (**first row**), VCE (**second row**), VCE-Lc (**third row**) and Lc-VCE (**fourth row**).

5.1.3. Results of All Six Cases

For all the six study cases, the RMS error obtained from each regularization method using the Shannon function are summarized in Table 5, the correlations between the estimated coefficients and the validation data are listed in Table 6.

Table 5. RMS values (unit [m^2/s^2]) of each method for different study cases using the Shannon function.

Regularization Method	A	B	C	D	E	F
L-curve method	4.6185	6.4345	5.0590	4.7712	0.1396	0.9106
VCE	7.8374	15.7168	5.1393	4.7724	0.1421	0.8410
VCE-Lc	4.5876	6.1696	4.9435	4.3974	0.1345	0.8377
Lc-VCE	4.6062	6.1610	4.9554	4.4549	0.1367	0.8394

Table 6. Correlations between the estimated coefficients and the validation data of each method for different study cases.

Regularization Method	A	B	C	D	E	F
L-curve method	0.9376	0.9159	0.9432	0.9468	0.9923	0.9803
VCE	0.8965	0.7424	0.9430	0.9463	0.9923	0.9807
VCE-Lc	0.9384	0.9194	0.9451	0.9511	0.9923	0.9916
Lc-VCE	0.9382	0.9184	0.9449	0.9499	0.9923	0.9842

Comparing to VCE, the two proposed methods, VCE-Lc and Lc-VCE, give smaller RMS errors as well as larger correlations in all the six study cases. In study cases A and B, the differences between the results delivered by VCE and the ones from the proposed methods are large, i.e., the RMS errors obtained from the VCE-Lc or Lc-VCE are 41% and 61% smaller than the ones obtained by VCE in case A and B, respectively. It indicates that VCE is unable to regularize the solutions properly in these two cases. In case A, when GRACE and GOCE are combined, the downward continuation of the satellite data requires strong regularization. VCE cannot provide sufficient regularization in this case. This result coincides with the conclusion drawn by Naeimi [60], who showed that VCE gives similar RMS errors as the L-curve method at the orbit level, but it is not able to provide sufficient regularization at the Earth surface for the regional solutions based on satellite data. Moreover, the high errors in the satellite data could be another reason for the large RMS error from VCE in this study case. And if the data errors are reduced by two orders of magnitude, the RMS error delivered by VCE-Lc or Lc-VCE becomes 22% smaller than that from VCE in case A. In case B, when the GRACE data are combined with the two airborne data sets, large data gaps exist along the study area, which also requires strong regularization. As we have mentioned in the Introduction, data gaps and the downward continuation are two of the major reasons why regularization is needed in regional gravity field modeling. Thus, VCE is also not able to provide sufficient regularization in study case B due to both large data gaps and the downward continuation of the data. The study cases A and B could be two extreme cases, i.e., in realistic applications of regional gravity field modeling, usually not only satellite data are used, and data gaps will not be as large as in study case B. However, we present these two cases here to give a complete view for the comparisons of the four regularization methods in different combination scenarios.

In the other four cases, when the terrestrial data are included, and there are much less data gaps, the RMS errors obtained from VCE differ with VCE-Lc and Lc-VCE less. The RMS errors from the VCE-Lc decrease by 4%, 8%, 5%, and 0.4%, and the RMS errors from the Lc-VCE decrease by 4%, 7%, 4%, and 0.2% in study cases C, D, E, F, compared to the ones obtained from VCE. These results show a more unbiased view of the benefits of the two proposed approaches compared to VCE, in realistic applications when different regional gravity observations are involved. Although the improvements

obtained by VCE-Lc or Lc-VCE compared to VCE are not as large as in the cases A and B, the two proposed methods still deliver smaller RMS errors and higher correlations in all the study cases.

The RMS errors from the VCE-Lc decrease by 0.7%, 4%, 2%, 8%, 4%, and 8%, and the RMS errors from the Lc-VCE decrease by 0.3%, 4%, 2%, 7%, 2%, and 8% compared to the ones from the L-curve method, in the six study cases. The improvements of the proposed methods compared to the L-curve method are not that large because the relative weights between different data sets were chosen empirically, with the knowledge of the data accuracy. In reality, the relative weights are not necessarily to be chosen accurately, especially when the accuracy of different real data sets is not available. Moreover, the results from the L-curve method heavily depend on the chosen relative weights. As shown in Sections 5.1.1 and 5.1.2, if different data sets are combined without relative weights (equal weighting), the RMS error from VCE-Lc decreases by 36% and 43% compared to the L-curve method in case A and F, respectively. These results show that the empirically chosen weights are important for the L-curve method, and wrongly chosen weights will lead to unreliable modeling results. VCE-Lc not only reduces the RMS errors compared to the L-curve method, but it also avoids the need for determining empirical weights, and thus, avoids the effect of wrongly chosen weights.

As the results delivered by Lc-VCE also change slightly when different relative weights are chosen (see Sections 5.1.1 and 5.1.2), it is worth mentioning that we have also conducted an iterative procedure for the Lc-VCE, which means applying the Lc-VCE repeatedly until the regularization parameter stays unchanged. At each iteration, the L-curve method is applied based on the relative weights obtained from the last VCE procedure. To be more specific, based on the relative weights obtained from the Lc-VCE, the L-curve method is applied again to generate the regularization parameter; VCE is then applied based on this regularization parameter to generate the relative weights, and the L-curve method is applied again, and so on. The L-curve method and VCE are applied successively until the regularization parameter and the relative weights do not change anymore. However, no significant improvements have been observed compared to the results delivered by the Lc-VCE; furthermore, this iterative procedure is time-consuming. Thus, we do not propose it in this paper.

To summarize, the two proposed methods improve the modeling results compared to using the L-curve method or VCE alone in all the six study cases. Among the two proposed methods, VCE-Lc delivers not only smaller RMS errors but also higher correlations than the Lc-VCE in five out of six study cases. Lc-VCE also shows good performance; however, the reference observation type in this method needs to be chosen carefully. Another advantage of using the VCE-Lc is that there is no need for determining the empirical weights in this approach, which is required in the L-curve method and Lc-VCE. Moreover, the results in terms of RMS value and correlation are consistent, i.e., the method which gives a smaller RMS error also delivers a larger correlation. However, the correlations differ much less than the RMS errors do between each method.

5.2. Results Using the CuP Function

Tables 7 and 8 list the RMS values as well as the correlations between the estimated coefficients d_k and the validation data T_v of each method when the CuP function is used.

Table 7. RMS values (unit [m^2/s^2]) of each method for different study cases using the CuP function.

Regularization Method	A	B	C	D	E	F
L-curve method	4.5501	6.9931	3.7021	3.3181	0.2262	0.9191
VCE	4.6870	7.7205	4.1689	3.7096	0.2497	0.8814
VCE-Lc	4.5104	6.4675	3.5848	2.9911	0.2232	0.8810
Lc-VCE	4.5106	6.4665	3.6076	2.9913	0.2237	0.8811

Table 8. Correlations between the estimated coefficients and the validation data of each method using the CuP function.

Regularization Method	A	B	C	D	E	F
L-curve method	0.9002	0.8722	0.8848	0.9019	0.7536	0.7650
VCE	0.8705	0.4721	0.7896	0.7926	0.1791	0.7632
VCE-Lc	0.9117	0.8734	0.8996	0.9189	0.7658	0.7652
Lc-VCE	0.9055	0.8875	0.8866	0.9061	0.7662	0.7652

When the CuP function is used, the proposed two methods still always deliver better results than the L-curve method and VCE, in terms of both RMS value and correlation for all the six study cases. The RMS errors from the VCE-Lc decrease by 4%, 16%, 14%, 19%, 11%, and 0.05% compared to those obtained from VCE, and by 1%, 8%, 3%, 10%, 1%, and 4% compared to the results from the L-curve method, in the six study cases. The RMS errors from the Lc-VCE decrease by 4%, 16%, 13%, 19%, 10%, and 0.03% compared to those obtained from VCE, and by 1%, 8%, 3%, 10%, 1%, and 4% compared to the results from the L-curve method, in the six study cases. These results show that improvements are achieved in the proposed methods, no matter using SRBFs with or without smoothing features. VCE-Lc still performs the best among the four regularization methods. When the CuP function is used, the differences between VCE and VCE-Lc become smaller in terms of RMS error (especially in cases A and B) but larger in terms of correlation. This behavior is consistent with the publication [23], which demonstrated that the SRBFs with smoothing features have a built-in regularity. Naeimi [60] concluded that VCE should be used with SRBFs which have smoothing features (e.g., the CuP function), based on both simulated and real satellite observations. The results using the CuP function in this study show that even when using an SRBF with smoothing features, the proposed VCE-Lc and Lc-VCE can still achieve improvements compared to using VCE alone.

6. Summary and Conclusions

This study discusses the regularization methods when heterogeneous observations are to be combined in regional gravity field modeling. We analyze the drawbacks of the two traditional regularization methods, namely, the L-curve method and VCE. When the L-curve method is applied, the relative weights between different observation types need to be chosen beforehand, and the modeling results heavily depend on if the relative weights are chosen accurately. In VCE, the prior information is regarded to be another observation type and is required to be stochastic. However, in regional gravity modeling, the prior information is not stochastic, and in this case, the regularization parameter generated by VCE could be unreliable. We propose two "combined methods" which combine VCE and the L-curve method in such a way that the relative weights are estimated by VCE, but the regularization parameters are determined by the L-curve method. The two proposed methods differ in whether determining the relative weights between each observation type first (VCE-Lc) or the regularization parameter by the L-curve method first (Lc-VCE).

We compare the two proposed methods, VCE-Lc and Lc-VCE, with the L-curve method and VCE. Each method is applied to six groups of data sets with simulated satellite, terrestrial and airborne data in Europe, and the results are compared to the validation data with corresponding spatial and spectral resolutions. These data are simulated from EGM2008 and are provided by the IAG ICCT JSG 0.3, along with the simulated observation noise. The RMS error between the computed disturbing potential and the validation data, as well as the correlation between the estimated coefficients and the validation data are used as the comparison criteria. The investigation shows that the two proposed methods deliver smaller RMS errors and larger correlations than the L-curve method and VCE, in all the six study cases. In cases A and B, VCE fails to provide sufficient regularization due to large data gaps, the downward continuation, and high errors in the satellite data. In cases C–F, the RMS errors from VCE-Lc decrease by 4%, 8%, 5%, and 0.4%, respectively, compared to those obtained from VCE. The

RMS errors from VCE-Lc decrease by 0.7%, 4%, 2%, 8%, 4%, and 8% compared to the results from the L-curve method (when the relative weights are chosen empirically), in the six study cases. However, when the relative weights are chosen inaccurately (e.g. equal weighting), the RMS error obtained by VCE-Lc reaches a value 43% smaller than that from the L-curve method. Among the four tested methods, the VCE-Lc gives the best results in terms of both RMS error and the correlation between the estimated coefficients and the validation data. Moreover, another advantage of using the VCE-Lc is that there is no need for determining the empirical weights beforehand, which is required in both the L-curve method and Lc-VCE.

We also carry out the same investigation using the CuP function, which has smoothing features as a comparison scenario. VCE-Lc and Lc-VCE still give the best and second best results in terms of both RMS error and the correlation. From our investigation, we conclude that VCE-Lc is the best choice among the applied methods for the determination of the regularization parameter when heterogeneous observations are to be combined, no matter using SRBFs with or without smoothing features.

In the future, a primary concern is to apply the newly devised methods using more types of SRBFs, so that the performance of different SRBFs can be compared while making sure that the differences in results are not coming from the regularization method. In addition, after validating the proposed methods with simulated data in this study, they have also been applied to real observations for the regional geoid modeling in Colorado, USA, within the "1 cm Geoid Experiment" [83]. The experiment was proposed within four scientific groups, namely, (1) the Global Geodetic Observing System (GGOS) Joint Working Group (JWG) 0.1.2, (2) the IAG JWG 2.2.2, (3) the IAG Sub-Commission (SC) 2.2, and (4) the ICCT JSG 0.15. We are currently preparing a related publication; the validation and comparison of different methodologies applied in this experiment can be found in [84].

Author Contributions: Conceptualization, Q.L.; Methodology, Q.L. and M.S.; Software, Q.L.; Validation, Q.L. and M.S.; Formal Analysis, Q.L.; Investigation, Q.L.; Resources, Q.L. and M.S.; Data Curation, Q.L.; Writing—Original Draft Preparation, Q.L.; Writing—Review and Editing, Q.L., M.S., R.P., and M.W.; Visualization, Q.L.; Supervision, M.S.; Project Administration, M.S. and R.P.; Funding Acquisition, M.S. and R.P. All authors have read and agreed to the published version of the manuscript.

Funding: This research was funded by Deutsche Forschungsgemeinschaft (DFG), grant number, SCHM 2433/11-1. The APC was funded by Institutional Open Access Program of the Technichal University of Munich (TUM).

Acknowledgments: This study was conducted in the framework of the project "Optimally combined regional geoid models for the realization of height systems in developing countries", the authors would like to thank the German Research Foundation (DFG) for funding this project. We also acknowledge the ICCT Joint Study Group 0.3 for providing the data sets. We are grateful to Katrin Bentel for kindly providing support and the basic programme related to this work. Furthermore, the authors acknowledge the developers of the Generic Mapping Tool (GMT) mainly used for generating the figures in this work. The authors thank the editor and three reviewers for their comments that allowed them to improve this paper.

Conflicts of Interest: The authors declare no conflicts interest.

References

1. Heiskanen, W.A.; Moritz, H. *Physical Geodesy*; San Francisco W. H. Freeman and Company: San Francisco, CA, USA, 1967; ISBN 978-3-211-33544-4.
2. Hofmann-Wellenhof, B.; Moritz, H. *Physical Geodesy*; Springer-Verlag Wien: Vienna, Austria, 2005; ISBN 3-211-23584-1.
3. Jekeli, C. *Spline Representations of Functions on a Sphere for Geopotential Modeling*; Technical Report; Ohio State University: Columbus, OH, USA, 2005.
4. Schmidt, M.; Fengler, M.; Mayer-Gürr, T.; Eicker, A.; Kusche, J.; Sánchez, L.; Han, S.C. Regional gravity modeling in terms of spherical base functions. *J. Geod.* **2007**, *81*, 17–38. [CrossRef]
5. Krarup, T. The method of least squares collocation. *Stud. Geophys. Geod.* **1970**, *14*, 107–109. [CrossRef]
6. Moritz, H. *Advanced Physical Geodesy*; Herbert Wichmann Verlag: Kalsruhe, Germany, 1980; ISBN 978-3879071951.
7. Pail, R.; Reguzzoni, M.; Sansó, F.; Kühtreiber, N. On the combination of global and local data in collocation theory. *Stud. Geophys. Geod.* **2010**, *54*, 195–218. [CrossRef]

8. Rowlands, D.D.; Luthcke, S.; Klosko, S.; Lemoine, F.G.; Chinn, D.; McCarthy, J.; Cox, C.; Anderson, O. Resolving mass flux at high spatial and temporal resolution using GRACE intersatellite measurements. *Geophys. Res. Lett.* **2005**, *32*. [CrossRef]
9. Rowlands, D.; Luthcke, S.; McCarthy, J.; Klosko, S.; Chinn, D.; Lemoine, F.; Boy, J.P.; Sabaka, T. Global mass flux solutions from GRACE: A comparison of parameter estimation strategies—Mass concentrations versus Stokes coefficients. *J. Geophys. Res. Solid Earth* **2010**, *115*. [CrossRef]
10. Jacob, T.; Wahr, J.; Pfeffer, W.T.; Swenson, S. Recent contributions of glaciers and ice caps to sea level rise. *Nature* **2012**, *482*, 514–518. [CrossRef]
11. Simons, F.J.; Dahlen, F.; Wieczorek, M.A. Spatiospectral concentration on a sphere. *SIAM Rev.* **2006**, *48*, 504–536. [CrossRef]
12. Simons, F.J. Slepian functions and their use in signal estimation and spectral analysis. In *Handbook of Geomathematics*; Freeden, W., Nashed, Z.M., Sonar, T., Eds.; Springer: Berlin, Germany, 2009; pp. 891–923.
13. Marchenko, A.N. *Parameterization of the Earth's Gravity Field: Point and Line Singularities*; Lviv Astronomical and Geodetic Society: Lviv, Ukraine, 1998; ISBN 9785776346040.
14. Holschneider, M.; Chambodut, A.; Mandea, M. From global to regional analysis of the magnetic field on the sphere using wavelet frames. *Phys. Earth Planet. Inter.* **2003**, *135*, 107–124. [CrossRef]
15. Freeden, W.; Michel, V. *Multiscale Potential Theory: With Applications to Geoscience*; Birkhäuser: Basel, Switzerland, 2004; ISBN 978-1-4612-2048-0.
16. Freeden, W.; Schreiner, M. *Spherical Functions of Mathematical Geosciences: A Scalar, Vectorial, and Tensorial Setup*; Springer Science & Business Media: Berlin, Germany, 2009; ISBN 978-3-642-09881-9.
17. Freeden, W.; Gervens, T.; Schreiner, M. *Constructive Approximation on the Sphere with Applications to Geomathematics*; Oxford University Press on Demand: New York, NY, USA, 1998; ISBN 978-0198536826.
18. Freeden, W. *Multiscale Modelling of Spaceborne Geodata*; Teubner: Stuttgart, Germany, 1999.
19. Marchenko, A.N. Regional gravity field model from satellite altimetry, gravimetry, and GPS-leveling data in the Black Sea area. *BOllettino Geod. Sci. Affin. LXII* **2003**, *4*, 245–259.
20. Lieb, V.; Schmidt, M.; Dettmering, D.; Börger, K. Combination of various observation techniques for regional modeling of the gravity field. *J. Geophys. Res. Solid Earth* **2016**, *121*, 3825–3845. [CrossRef]
21. Li, X. Using radial basis functions in airborne gravimetry for local geoid improvement. *J. Geod.* **2018**, *92*, 471–485. [CrossRef]
22. Wittwer, T. Regional Gravity Field Modelling with Radial Basis Functions. Ph.D. Thesis, Netherlands Geodetic Commission, Delft, The Netherlands, 2009.
23. Naeimi, M.; Flury, J.; Brieden, P. On the regularization of regional gravity field solutions in spherical radial base functions. *Geophys. J. Int.* **2015**, *202*, 1041–1053. [CrossRef]
24. Tenzer, R.; Klees, R. The choice of the spherical radial basis functions in local gravity field modeling. *Stud. Geophys. Geod.* **2008**, *52*, 287–304. [CrossRef]
25. Bentel, K.; Schmidt, M.; Denby, C.R. Artifacts in regional gravity representations with spherical radial basis functions. *J. Geod. Sci.* **2013**, *3*, 173–187. [CrossRef]
26. Eicker, A. Gravity field Refinement by Radial Basis Functions from In-Situ Satellite Data. Ph.D. Thesis, University of Bonn, Bonn, Germany, 2008.
27. Lieb, V. Enhanced Regional Gravity Field Modeling from the Combination of Real Data via MRR. Ph.D. Thesis, Technische Universität München, Munich, Germany, 2017.
28. Bouman, J. *Quality of Regularization Methods. DEOS Report 98.2*; Technical Report; Delft University Press: Delft, The Netherlands, 1998.
29. Tikhonov, A.N.; Arsenin, V.I. *Solutions of ill-posed Problems*; Winston: Washington, DC, USA, 1977; ISBN 978-0470991244.
30. Xu, P. Truncated SVD methods for discrete linear ill-posed problems. *Geophys. J. Int.* **1998**, *135*, 505–514. [CrossRef]
31. Schuh, W.D. *Tailored Numerical Solution Strategies for the Global Determination of the Earth's Gravity Field*; Technical Report; Technischen Universität Graz: Graz, Austria, 1996.
32. Koch, K.R.; Kusche, J. Regularization of geopotential determination from satellite data by variance components. *J. Geod.* **2002**, *76*, 259–268. [CrossRef]
33. Hansen, P.C. Truncated singular value decomposition solutions to discrete ill-posed problems with ill-determined numerical rank. *SIAM J. Sci. Stat. Comput.* **1990**, *11*, 503–518. [CrossRef]

34. Hansen, P.C.; O'Leary, D.P. The use of the L-curve in the regularization of discrete ill-posed problems. *SIAM J. Sci. Comput.* **1993**, *14*, 1487–1503. [CrossRef]
35. Grafarend, E.; Kleusberg, A.; Schaffrin, B. An introduction to the variance-covariance component estimation of Helmert type. *Z. FüR Vermess.* **1980**, *105*, 161–180.
36. Koch, K.R. *Parameter Estimation and Hypothesis Testing in Linear Models*; Springer: Berlin/Heidelberg, Germany, 1999; ISBN 978-3-642-08461-4.
37. Wahba, G. *Spline Models for Observational Data*; SIAM: Philadelphia, PA, USA, 1990; ISBN 978-0-89871-244-5.
38. Haber, E. Numerical Strategies for the Solution of Inverse Problems. Ph.D. Thesis, The University of British Columbia, Vancouver, BC, Canada, 1997.
39. Li, Y.; Oldenburg, D.W. Fast inversion of large-scale magnetic data using wavelet transforms and a logarithmic barrier method. *Geophys. J. Int.* **2003**, *152*, 251–265. [CrossRef]
40. Liu, X. Global Gravity Field Recovery from Satellite-to-Satellite Tracking Data with the Acceleration Approach. Ph.D. Thesis, Technical University of Delft, Delft, The Netherlands, 2008.
41. Van Loon, J. Functional and Stochastic Modelling of Satellite Gravity Data. Ph.D. Thesis, Technical University of Delft, Delft, The Netherlands, 2008.
42. Akaike, H. Likelihood and the Bayes procedure. *Trab. Estad. Investig. Oper.* **1980**, *31*, 143–166. [CrossRef]
43. Yabuki, T.; Matsu'Ura, M. Geodetic data inversion using a Bayesian information criterion for spatial distribution of fault slip. *Geophys. J. Int.* **1992**, *109*, 363–375. [CrossRef]
44. Mitsuhata, Y.; Uchida, T.; Amano, H. 2.5-D inversion of frequency-domain electromagnetic data generated by a grounded-wire source. *Geophysics* **2002**, *67*, 1753–1768. [CrossRef]
45. Fukahata, Y.; Nishitani, A.; Matsu'ura, M. Geodetic data inversion using ABIC to estimate slip history during one earthquake cycle with viscoelastic slip-response functions. *Geophys. J. Int.* **2004**, *156*, 140–153. [CrossRef]
46. Liu, Y.; Fok, H.S.; Tenzer, R.; Chen, Q.; Chen, X. Akaike's Bayesian Information Criterion for the Joint Inversion of Terrestrial Water Storage Using GPS Vertical Displacements, GRACE and GLDAS in Southwest China. *Entropy* **2019**, *21*, 664. [CrossRef]
47. Wu, L. A parameter choice method for Tikhonov regularization. *Electron. Trans. Numer. Anal.* **2003**, *16*, 107–128.
48. Ceccherini, S. Analytical determination of the regularization parameter in the retrieval of atmospheric vertical profiles. *Opt. Lett.* **2005**, *30*, 2554–2556. [CrossRef]
49. Ridolfi, M.; Sgheri, L. Iterative approach to self-adapting and altitude-dependent regularization for atmospheric profile retrievals. *Opt. Express* **2011**, *19*, 26696–26709. [CrossRef]
50. Albani, V.; De Cezaro, A.; Zubelli, J.P. On the Choice of the Tikhonov Regularization Parameter and the Discretization Level: A Discrepancy-Based Strategy. *Inverse Probl. Imaging* **2016**, *10*, 1–25. [CrossRef]
51. Steck, T. Methods for determining regularization for atmospheric retrieval problems. *Appl. Opt.* **2002**, *41*, 1788–1797. [CrossRef]
52. Farquharson, C.G.; Oldenburg, D.W. A comparison of automatic techniques for estimating the regularization parameter in non-linear inverse problems. *Geophys. J. Int.* **2004**, *156*, 411–425. [CrossRef]
53. Xu, J.; Schreier, F.; Doicu, A.; Trautmann, T. Assessment of Tikhonov-type regularization methods for solving atmospheric inverse problems. *J. Quant. Spectrosc. Radiat. Transf.* **2016**, *184*, 274–286. [CrossRef]
54. Ramillien, G.; Biancale, R.; Gratton, S.; Vasseur, X.; Bourgogne, S. GRACE-derived surface water mass anomalies by energy integral approach: Application to continental hydrology. *J. Geod.* **2011**, *85*, 313–328. [CrossRef]
55. Xu, C.; Ding, K.; Cai, J.; Grafarend, E.W. Methods of determining weight scaling factors for geodetic–geophysical joint inversion. *J. Geodyn.* **2009**, *47*, 39–46. [CrossRef]
56. Kusche, J. Noise variance estimation and optimal weight determination for GOCE gravity recovery. *Adv. Geosci.* **2003**, *1*, 81–85. [CrossRef]
57. Bucha, B.; Janák, J.; Papčo, J.; Bezděk, A. High-resolution regional gravity field modelling in a mountainous area from terrestrial gravity data. *Geophys. J. Int.* **2016**, *207*, 949–966. [CrossRef]
58. Wu, Y.; Zhou, H.; Zhong, B.; Luo, Z. Regional gravity field recovery using the GOCE gravity gradient tensor and heterogeneous gravimetry and altimetry data. *J. Geophys. Res. Solid Earth* **2017**, *122*, 6928–6952. [CrossRef]
59. Liang, W. A Regional Physics-Motivated Electron Density Model of the Ionosphere. Ph.D. Thesis, Technische Universität München, Munich, Germany, 2017.

60. Naeimi, M. Inversion of Satellite Gravity Data Using Spherical Radial Base Functions. Ph.D. Thesis, Leibniz Universität Hannover, Hanover, Germany, 2013.
61. Xu, P.; Shen, Y.; Fukuda, Y.; Liu, Y. Variance component estimation in linear inverse ill-posed models. *J. Geod.* **2006**, *80*, 69–81. [CrossRef]
62. Tanir, E.; Heinkelmann, R.; Schuh, H.; Kusche, J.; van Loon, J. Assessment of the results of VLBI intra-technique combination using regularization methods. In *Geodetic Reference Frames*; Springer: Berlin, Germany, 2009; pp. 45–51.
63. Wang, L.; Zhao, X.; Gao, H. A method for determining the regularization parameter and the relative weight ratio of the seismic slip distribution with multi-source data. *J. Geodyn.* **2018**, *118*, 1–10. [CrossRef]
64. Tapley, B.D.; Bettadpur, S.; Watkins, M.; Reigber, C. The gravity recovery and climate experiment: Mission overview and early results. *Geophys. Res. Lett.* **2004**, *31*. [CrossRef]
65. Reigber, C.; Schmidt, R.; Flechtner, F.; König, R.; Meyer, U.; Neumayer, K.H.; Schwintzer, P.; Zhu, S.Y. An Earth gravity field model complete to degree and order 150 from Grace: Eigen-Grace02s. *J. Geodyn.* **2005**, *39*, 1–10. [CrossRef]
66. GRACE Data Product, ESA. Available online: https://earth.esa.int/web/guest/data-access/browse-data-products?p_p_id=datasetlist_WAR_ospportlet&missions=GRACE (accessed on 27 March 2020).
67. GRACE Data Product, GFZ. Available online: https://www.gfz-potsdam.de/en/grace/grace-products/ (accessed on 27 March 2020).
68. Bentel, K. Regional Gravity Modeling in Spherical Radial Basis Functions—On the Role of the Basis Function and the Combination of Different Observation Types. Ph.D. Thesis, Norwegian University of Life Sciences, Ås, Norway, 2013.
69. Rummel, R.; Balmino, G.; Johannessen, J.; Visser, P.; Woodworth, P. Dedicated gravity field missions—Principles and aims. *J. Geodyn.* **2002**, *33*, 3–20. [CrossRef]
70. Koop, R. *Global Gravity Field Modelling Using Satellite Gravity Gradiometry*; Nederlandse Commissie voor Geodesie: Delft, The Netherlands, 1993; ISBN 978-90-6132-246-7.
71. Schmidt, M.; Göttl, F.; Heinkelmann, R. Towards the combination of data sets from various observation techniques. In *The 1st International Workshop on the Quality of Geodetic Observation and Monitoring Systems (QuGOMS'11)*; Kutterer, H., Seitz, F., Alkhatib, H., Schmidt, M., Eds.; Springer: Cham, Switzerland, 2015; pp. 35–43.
72. Kusche, J.; Klees, R. Regularization of gravity field estimation from satellite gravity gradients. *J. Geod.* **2002**, *76*, 359–368. [CrossRef]
73. Hansen, P.C. The L-curve and its use in the numerical treatment of inverse problems. In *Computational Inverse Problems in Electrocardiology*; Johnston, P., Ed.; WIT Press: Southampton, UK, 2000; pp. 119–142.
74. Pavlis, N.K.; Holmes, S.A.; Kenyon, S.C.; Factor, J.K. The development and evaluation of the Earth Gravitational Model 2008 (EGM2008). *J. Geophys. Res. Solid Earth* **2012**, *117*. [CrossRef]
75. Pavlis, N.K.; Factor, J.K.; Holmes, S.A. Terrain-related gravimetric quantities computed for the next EGM. In Proceedings of the 1st International Symposium of the International Gravity Field Service (IGFS), Istanbul, Turkey, 28 August–1 September 2006; pp. 318–323.
76. Torge, W.; Müller, J. *Geodesy*; Walter de Gruyter: Berlin, Germany, 2012; ISBN 978-3-11-025000-8.
77. Forsberg, R. *A Study of Terrain Reductions, Density Anomalies and Geophysical Inversion Methods in Gravity Field Modelling*; Technical Report; Department Of Geodetic Science and Surveying, Ohio State University: Columbus, OH, USA, 1984.
78. Kern, M.; Schwarz, K.; Sneeuw, N. A study on the combination of satellite, airborne, and terrestrial gravity data. *J. Geod.* **2003**, *77*, 217–225. [CrossRef]
79. Sjöberg, L.; Eshagh, M. A theory on geoid modelling by spectral combination of data from satellite gravity gradiometry, terrestrial gravity and an Earth gravitational model. *Acta Geod. Geophys. Hung.* **2012**, *47*, 13–28. [CrossRef]
80. Jiang, T.; Wang, Y.M. On the spectral combination of satellite gravity model, terrestrial and airborne gravity data for local gravimetric geoid computation. *J. Geod.* **2016**, *90*, 1405–1418. [CrossRef]
81. Holota, P.; Nesvadba, O. On the Combination of Terrestrial Data and GOCE Based Models in Earth's Gravity Field Studies: Compatibility and Optimization. In Proceedings of the 5th International GOCE User Workshop, Paris, France, 25–28 November 2014; Volume 728.

82. Reuter, R. Über Integralformeln der Einheitssphäre und Harmonische Splinefunktionen. Ph.D. Thesis, RWTH Aachen University, Aachen, Germany, 1982.
83. Sánchez, L.; Ågren, J.; Huang, J.; Wang, Y.; Forsberg, R. Basic Agreements for the Computation of Station Potential Values as IHRS Coordinates, Geoid Undulations and Height Anomalies within the Colorado 1 cm Geoid Experiment. 2018. Available online: https://ihrs.dgfi.tum.de/fileadmin/JWG_2015/Colorado_Experiment_Basic_req_V0.5_Oct30_2018.pdf (accessed on 26 April 2020).
84. Wang, Y.; Sánchez, L.; Ågren, J.; Huang, J.; Forsberg, R. Colorado geoid computation experiment – Overview and Summary. *J. Geod.* **2020**, submitted.



© 2020 by the authors. Licensee MDPI, Basel, Switzerland. This article is an open access article distributed under the terms and conditions of the Creative Commons Attribution (CC BY) license (http://creativecommons.org/licenses/by/4.0/).

A2 Publication II

Reference

Liu, Q., Schmidt, M., Sánchez, L., and Willberg, M. (2020b). **Regional gravity field refinement for (quasi-) geoid determination based on spherical radial basis functions in Colorado**. *Journal of Geodesy*, 94, 99. https://doi.org/10.1007/s00190-020-01431-2

Copyright

This work originally has been published in Journal of Geodesy, with open access. The publication is available under the creative commons license. The copyright remains with the authors.

Declaration of own contribution

The overall own contribution of Qing Liu to P-II is estimated to be 85%, which is a weighted average of the five contribution parts listed in the Table 2.

Table 2: Contribution of Qing Liu to P-II

	Weight	Estimated contribution
Ideas and conceptual design	30%	80%
Realization and computation	10%	85%
Analysis and discussion	30%	85%
Figure compilation	10%	100%
Manuscript writing	20%	85%
Overall		**85%**

Confirmation by the Co-authors

I hereby confirm the correctness of the declaration of own contribution by Qing Liu for the publication
Liu, Q., Schmidt, M., Sánchez, L., and Willberg, M. (2020b) Regional gravity field refinement for (quasi-) geoid determination based on spherical radial basis functions in Colorado. *Journal of Geodesy*, 94, 99. https://doi.org/10.1007/s00190-020-01431-2

Michael Schmidt
Deutsches Geodätisches Forschungsinstitut der Technischen Universität München (DGFI-TUM), Germany

Signature: ..... Date: 24.05.2022

Laura Sánchez
Deutsches Geodätisches Forschungsinstitut der Technischen Universität München (DGFI-TUM), Germany

Signature: ..... Date: 24.05.2022

Martin Willberg
Institute for Astronomical and Physical Geodesy, Technical University of Munich, Germany

Signature: ..... Date: 25.3.2021

Journal of Geodesy (2020) 94:99
https://doi.org/10.1007/s00190-020-01431-2

ORIGINAL ARTICLE

Regional gravity field refinement for (quasi-) geoid determination based on spherical radial basis functions in Colorado

Qing Liu[1] · Michael Schmidt[1] · Laura Sánchez[1] · Martin Willberg[2]

Received: 3 March 2020 / Accepted: 31 August 2020 / Published online: 10 October 2020
© The Author(s) 2020

Abstract
This study presents a solution of the '1 cm Geoid Experiment' (Colorado Experiment) using spherical radial basis functions (SRBFs). As the only group using SRBFs among the fourteen participated institutions from all over the world, we highlight the methodology of SRBFs in this paper. Detailed explanations are given regarding the settings of the four most important factors that influence the performance of SRBFs in gravity field modeling, namely (1) the choosing bandwidth, (2) the locations of the SRBFs, (3) the type of the SRBFs as well as (4) the extensions of the data zone for reducing the edge effect. Two types of basis functions covering the same spectral range are used for the terrestrial and the airborne measurements, respectively. The non-smoothing Shannon function is applied to the terrestrial data to avoid the loss of spectral information. The cubic polynomial (CuP) function which has smoothing features is applied to the airborne data as a low-pass filter for filtering the high-frequency noise. Although the idea of combining different SRBFs for different observations was proven in theory to be possible, it is applied to real data for the first time, in this study. The RMS error of our height anomaly result along the GSVS17 benchmarks w.r.t the validation data (which is the mean results of the other contributions in the 'Colorado Experiment') drops by 5% when combining the Shannon function for the terrestrial data and the CuP function for the airborne data, compared to those obtained by using the Shannon function for both the two data sets. This improvement indicates the validity and benefits of using different SRBFs for different observation types. Global gravity model (GGM), topographic model, the terrestrial gravity data, as well as the airborne gravity data are combined, and the contribution of each data set to the final solution is discussed. By adding the terrestrial data to the GGM and the topographic model, the RMS error of the height anomaly result w.r.t the validation data drops from 4 to 1.8 cm, and it is further reduced to 1 cm by including the airborne data. Comparisons with the mean results of all the contributions show that our height anomaly and geoid height solutions at the GSVS17 benchmarks have an RMS error of 1.0 cm and 1.3 cm, respectively; and our height anomaly results give an RMS value of 1.6 cm in the whole study area, which are all the smallest among the participants.

Keywords '1 cm Geoid Experiment' · Spherical radial basis functions · Regional geoid modeling · Heterogeneous data combination

1 Introduction

The unification of physical height systems is an essential geodetic application of the Earth's gravity field. It is important and urgent to have a globally consistent height system within a few centimeters or better, for both scientific and societal reasons (Plag et al. 2009; Sánchez 2012; Ihde et al. 2017). In 2015, the International Association of Geodesy (IAG) introduced the International Height Reference System (IHRS) as the global standard for the determination of physical heights (see Drewes et al. 2016). The IHRS is defined as a geopotential reference system corotating with the Earth. Station coordinates are given by (1) potential values $W(\boldsymbol{X})$ (and their changes with time $\mathrm{d}W(\boldsymbol{X})/\mathrm{d}t$) defined within the Earth's gravity field and, (2) geocentric Cartesian coordinates $\boldsymbol{X}$ (and their changes with time $\mathrm{d}\boldsymbol{X}/\mathrm{d}t$) referring to the International Terrestrial Reference System (ITRS, Petit and Luzum 2010). For practical purposes, potential values $W(\boldsymbol{X})$

Qing Liu
qingqing.liu@tum.de

[1] Deutsches Geodätisches Forschungsinstitut der Technischen Universität München (DGFI-TUM), Arcisstrasse 21, 80333 Munich, Germany

[2] Institute of Astronomical and Physical Geodesy, Technical University of Munich, Arcisstrasse 21, 80333 Munich, Germany

and geocentric positions $\boldsymbol{X}$ can be transformed to geopotential numbers C_P and ellipsoidal heights h, respectively (Ihde et al. 2017). The determination of potential values as IHRS coordinates may be performed following the strategies applied for the (quasi-) geoid modeling. In the following, we basically determine the disturbing potential $T(\boldsymbol{X})$, and after restoring the reference potential $U(\boldsymbol{X})$, we can obtain $W(\boldsymbol{X}) = U(\boldsymbol{X}) + T(\boldsymbol{X})$. According to Ihde et al. (2017), the target uncertainty of $W(\boldsymbol{X})$ should be at the 10^{-2} m^2/s^2 level (equivalent to around 1 mm for physical heights). However, the reliability of the potential estimation undergoes the same limitations of the precise (quasi-) geoid modeling. Thus, a high-resolution and high-precision (quasi-) geoid model is the key for the realization of the IHRS.

Satellite gravity observation missions such as the Gravity Recovery and Climate Experiment (GRACE, Tapley et al. 2004) and the Gravity Field and Steady-State Ocean Circulation Explorer (GOCE, Rummel et al. 2002) are the main data sources for global geoid modeling. However, the main limitation of satellite gravity models is the spatial resolution, since they lack information about spatial wavelengths below 70–80 km (Pail et al. 2011). This missing high-frequency part of the gravity signal can cause an omission error of 20 to 40 cm in terms of geoid heights (Rummel 2012). This value can be even higher in regions with very rough topography. In contrast, other types of measurements such as airborne, shipborne or terrestrial gravity observations can provide a much higher spatial resolution of a few kilometers. Thus, they can be used in addition to the global models for regional geoid refinement to improve the resolution and accuracy. High-resolution regional gravity modeling is especially inevitable in mountainous areas, since the very short wavelengths are correlated with local topography to a large extent (Bucha et al. 2016).

This study focuses on the computation of height anomalies, geoid heights, and geopotential values (as IHRS coordinates) in Colorado, USA (Fig. 1). These results contribute to the '1 cm Geoid Experiment' (Wang et al. 2020). This study is of great interest and importance for three reasons, namely (1) Colorado is a mountainous area with high elevations and rugged topography, which makes the gravity field modeling challenging, (2) with altogether fourteen contributions worldwide (see Wang et al. 2020 for the list of the participants) involved in this experiment with different methodologies, the comparison of the results should highlight the disparities of each method, (3) we apply an approach based on spherical radial basis functions (SRBFs), which has not been widely studied for modeling the airborne data (Li 2018). According to Sánchez et al. (2020), the calculation of reference stations for the IHRS realization might be distributed worldwide, and the calculation methods have to be verified and documented beforehand. Within the '1 cm Geoid Experiment,' we prove that our SRBF-based (quasi-) geoid model is consistent with thirteen independent results calculated by different methods, and we provide a detailed documentation about our method within this paper.

Wu et al. (2017a) pointed out that it is difficult to combine heterogeneous data using the Stokes/Molodensky integral, since it requires a grid interpolation; and when dealing with large number of point-wise data (which is the case for the 'Colorado Experiment'), the least-squares collocation (LSC) is numerically inefficient (Wittwer 2009). SRBFs are an appropriate tool for regional gravity field modeling, since they fulfill the Laplace equation such as the spherical harmonics (SHs), due to their relations to the Legendre polynomials. Although SRBFs are thus also global functions, they can be used appropriately for regional applications to consider the heterogeneity of different data types, due to their localizing feature. SRBFs are a good compromise between ideal frequency localization (SHs) and ideal spatial localization (Dirac delta functions) (Freeden et al. 1998). The fundamentals of SRBFs are introduced by Freeden et al. (1998), Freeden and Michel (2004), among many others. They have been applied in gravity field modeling during the last two decades, e.g., by Schmidt et al. (2006), Schmidt et al. (2007) and Klees et al. (2008). The SRBFs are placed on point grids, to which the unknown coefficients are associated. These coefficients can be estimated from the observations, and they reflect the energy of the gravity signal (Naeimi et al. 2015). The modeled gravitational functionals are then computed from these estimated coefficients. Four factors of the SRBFs need to be specified, which influence the modeling accuracy. We discuss in detail (see Sect. 4.2) the choice of (1) the choosing bandwidth, (2) the locations of the SRBFs, (3) the type of the SRBFs, and (4) the extensions of the data zone for reducing edge effects.

Two types of high-resolution data sets, the terrestrial and the airborne gravity measurements, are combined in this study. However, the GRAV-D (Gravity for the Redefinition of the American Vertical Datum) airborne gravity data require additional editing or low-pass filtering before being used (see e.g., GRAV-D Science Team 2018). Various low-pass filtering methods exist and have been applied to the airborne gravity data, such as the spatial Gaussian filter, the fast Fourier transform (FFT, Childers et al. 1999), and the Butterworth filter (Forsberg et al. 2001). Lieb et al. (2015) proposed a low-pass filtering in the spectral domain by SRBFs. Li (2018) demonstrated that the SRBFs show certain de-noising or smoothing properties of the high-frequency noise in the airborne data. In this study, we apply the low-pass filter to the airborne gravity data by using the cubic polynomial (CuP) function, and the smoothing features in this type of SRBFs are used for filtering the high-frequency noise in the airborne data. An advantage of using the CuP function for low-pass filtering is that the filtering process is automatically done when establishing the observation equations, i.e., no extra compu-

tation efforts are required. For the terrestrial gravity data, the non-smoothing Shannon function is preferred to avoid the loss of spectral information (Bucha et al. 2016). Schreiner (1999) showed that it is possible to use different types of SRBFs for different types of observations, since the coefficients are independent on the choice of the SRBFs, as long as they cover the same frequency range. Klees et al. (2018) achieved an improvement by applying a truncated SRBF for the terrestrial data but a tapered SRBF for the satellite data, based on simulations. However, to the best of our knowledge, the idea of combining different types of SRBFs for different types of observations has not been applied to real data sets yet. Thus, our results based on real data also indicate the validity of this idea.

We apply the remove–compute–restore (RCR) procedure (e.g., Forsberg and Tscherning 1981; Forsberg 1993), in which a global gravity model (GGM) is usually removed before the computation. In this study, however, not only a GGM, but also a topographic model is removed, due to the high elevation and rugged terrain of the study area. Forsberg and Tscherning (1981) pointed out that the inclusion of the topographic effects is indispensable for regional gravity field modeling in mountainous areas. Hirt (2010) showed that the signal omission error (gravity field components which are omitted by a truncated expansion) can be greatly reduced, and the model accuracy can be significantly improved by including the residual terrain model (RTM) in mountainous areas. After the remove step, the remaining part is then modeled by the combination of the terrestrial and airborne observations. These two types of observations are combined within a parameter estimation procedure (Schmidt et al. 2007). However, the derived least-squares system is in most cases ill-posed or even singular, due to three reasons, namely (1) the number of used basis functions is usually larger as required, (2) the given data gaps as well as (3) the downward continuation of the airborne or satellite measurements to the surface of the Earth. Thus, regularization is necessary to obtain a numerically stable solution. We apply the Tikhonov regularization which can be interpreted as an estimation with prior information (Koch 1990). The relative weight between the two observation types as well as the relative weight between the observations and the prior information, which can be interpreted as the regularization parameter, is determined by the method of variance component estimation (VCE, Koch 1999; Koch and Kusche 2002). Naeimi et al. (2015) demonstrated, however, that VCE does not always give reliable regularization results. Thus, the L-curve method (see e.g., Hansen 1990) or the generalized cross-validation (GCV, see e.g., Golub et al. 1979) could be used instead. We here propose a method which combines VCE for determining the relative weight between the two observation types and the L-curve method for determining the regularization parameter (Liu et al. 2020).

This work is organized as follows: In Sect. 2, we present the study area as well as the available data; also the procedure of data preprocessing is briefly described. Section 3 introduces the fundamental concepts of SRBFs, the spherical convolution, and the parameter estimation procedure. We explain how the observation equations are formulated, how the unknown coefficients are estimated, and how the resulting gravitational functionals are calculated. Section 4 explains the computation procedure: the RCR, the choices of each factors in SRBFs, and the combination of the data sets. Section 5 presents our models as well as the validation of the results. Finally, Sect. 6 provides the conclusions and outlook.

2 Study area and data preprocessing

2.1 Study area and data

This study is conducted between $-110°$ and $-102°$ longitude and between 35° and 40° latitude (Fig. 1a), majorly located in Colorado, USA. It is a mountainous area, with an average elevation of 2017 m. The highest location reaches 4386 m, the lowest 932 m. The eastern part of the study area is more flat than the western and the central part, while it is still higher than 1000 m. The larger the topographic heights are, the worse the accuracy of the geoid becomes (Foroughi et al. 2019). Thus, this is a challenging study area, due to the rugged terrain, high elevation, and varying gravity field.

Two data sets are provided by the National Geodetic Survey (NGS). Figure 1b shows the spatial distribution of these two data sets, projected on the Earth's surface. The terrestrial gravity data (blue points) have full coverage over the whole study area, but they are not evenly distributed. Comparing Fig. 1a, b, it is clear that this data set has a higher density in the area with higher elevation and a lower density in the low elevation area (eastern part). However, the average point distance reaches approximately 3 km for the whole terrestrial data set. The airborne gravity data (green flight tracks) were collected by the GRAV-D project (GRAV-D Science Team 2017) at a mean flight altitude of 6186 m. They cover most of the study area in the southeastern part, generally between $-109°$ and $-102°$ longitude and between 35° and 38.5° latitude. The along-track spatial resolution depends on the aircraft speed, with an average of around 100 m; the cross-track resolution is almost 10 km. We use the data given at their original observation sites, i.e., the observation equations are directly established at the observation points.

We compute two sets of output gravity functionals, and the results will be presented and discussed. The first one is at the Geoid Slope Validation Survey 2017 (GSVS17) benchmarks (red line in Fig. 1b), and the second one is the quasi-geoid and geoid model for the target area from $-109°$ to $-103°$

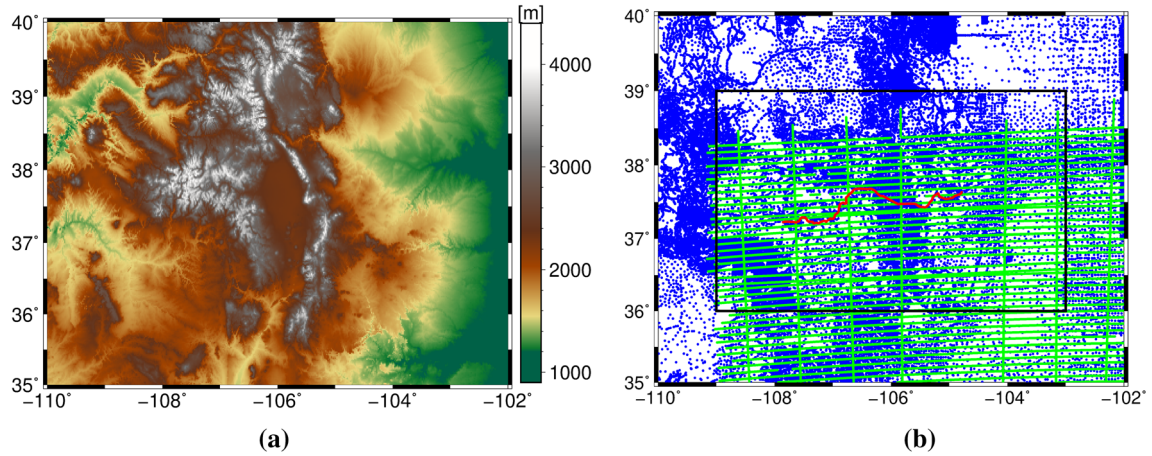


Fig. 1 **a** Terrain map of the study area; **b** given terrestrial (blue points) and airborne (green flight tracks) gravity data, GSVS17 benchmarks (223 points of the red line) as well as the model grid area (black rectangle)

and 36° to 39° (black box in Fig. 1b) with a spatial resolution of $1' \times 1'$.

2.2 Data preprocessing

In the original terrestrial data (with a total amount of 59,303 points), there are cases that several gravity observations locate at the same position, and we then use only the first of these observations (1090 points deleted). However, in case gravity observations at the same position differ with more than 2mGal from each other, we delete both of them (85 points deleted). Since the measurements are provided in orthometric heights H, we transform them to the ellipsoidal heights h using the geoid model 'GEOID 12B,' provided by the National Geodesy Survey (NGS 2012)

$$h = H + N_{\text{Geoid 12B}}. \tag{1}$$

The airborne data have a very dense distribution with a total amount of 283,716 observation points, resulting in a design matrix with a size of 55 GB (see Sect. 3.3). To save computation time and to improve the efficiency, we reduce the sampling interval from 1 to 1/8 Hz, i.e., only one observation of an eight-observation block is kept. Thus, an average spatial resolution of approximately 1 km along-track is obtained. The reason that justifies the 'down sampling' procedure of the airborne data is that consecutive airborne observations are highly correlated.

Then, for both types of observations, the following data preprocessing steps are performed:

1. Transfer the observations in terms of absolute gravity g to gravity disturbance δg by subtracting the normal gravity γ at the ellipsoidal height h of the observations

$$\delta g_{\text{obs}} = g - \gamma. \tag{2}$$

2. Add the atmospheric correction to the observations

$$\delta g = \delta g_{\text{obs}} + \delta g_{\text{ATM}}, \tag{3}$$

the atmospheric correction δg_{ATM} is calculated following Torge (1989) by

$$\delta g_{\text{ATM}} = 0.874 - 9.9 \cdot 10^{-5} h + 3.56 \cdot 10^{-9} h^2. \tag{4}$$

3 Methodology

3.1 Spherical radial basis function

In general, SRBFs are centered at points P_k with position vector $\boldsymbol{x}_k$ on a sphere Ω_R with radius R. A spherical radial basis function $B(\boldsymbol{x}, \boldsymbol{x}_k)$ can be defined between P_k and an observation point P by the Legendre series (Freeden et al. 1998; Schmidt et al. 2007),

$$B(\boldsymbol{x}, \boldsymbol{x}_k) = \sum_{n=0}^{\infty} \frac{2n+1}{4\pi} \left(\frac{R}{r}\right)^{(n+1)} B_n P_n(\boldsymbol{r}^T \boldsymbol{r}_k) \tag{5}$$

wherein $\boldsymbol{x} = r \cdot \boldsymbol{r} = r \cdot [\cos\phi \cos\lambda, \cos\phi \sin\lambda, \sin\phi]^{\text{T}}$ is the position vector of the observation point P, λ is the spherical longitude, ϕ is the spherical latitude, and $r = R + h'$ with h' the spherical height of P above the sphere Ω_R. The position vector of P_k reads $\boldsymbol{x}_k = R \cdot \boldsymbol{r}_k$, P_n is the Legendre polynomial of degree n, and B_n is the Legendre coefficient which contributes to specify the shape of the SRBFs.

A harmonic function $F(\boldsymbol{x})$ can be represented as a series expansion of the SRBFs $B(\boldsymbol{x}, \boldsymbol{x}_k)$

$$F(\boldsymbol{x}) = \sum_{k=1}^{K} d_k B(\boldsymbol{x}, \boldsymbol{x}_k), \tag{6}$$

where K is the number of basis functions, and thus, the number of grid points P_k and unknown coefficients d_k as well.

The general expression (Eq. 5) needs to be adapted for describing different gravitational functionals (Lieb et al. 2016). In this study, the observations are given in terms of gravity disturbances δg, which can be expressed as the gradient of the disturbing potential T. In spherical approximation, the magnitude of the gravity disturbance can be written as (Heiskanen and Moritz 1967).

$$\delta g = -\frac{\partial T}{\partial r}. \tag{7}$$

Thus, if T is modeled as in Eq. (6), the adapted spherical basis function for describing $\delta g(\boldsymbol{x})$ given at an observation site P with position vector $\boldsymbol{x}$ is given as

$$B_r(\boldsymbol{x}, \boldsymbol{x}_k) = \sum_{n=0}^{\infty} \frac{2n+1}{4\pi} \left(\frac{n+1}{r}\right) \left(\frac{R}{r}\right)^{(n+1)} B_n P_n(\boldsymbol{r}^T \boldsymbol{r}_k). \tag{8}$$

A complete list of basis functions adapted to different functionals of the disturbing potential can be found in Koop (1993) or Liu et al. (2020).

3.2 SRBF as a filter

Any SRBF (Eq. 5) can be used as a high-pass, low-pass, or band-pass filter (Schmidt et al. 2007; Lieb 2017), and a harmonic function $F(\boldsymbol{x})$ can be filtered by it through a spherical convolution. The filtered function $G(\boldsymbol{x})$ can then be represented by

$$G(\boldsymbol{x}) = (B * F)(\boldsymbol{x}). \tag{9}$$

In case the SRBF $B(\boldsymbol{x}, \boldsymbol{x}_k)$ in Eq. (6) is chosen as a unique reproducing kernel $Z(\boldsymbol{x}, \boldsymbol{x}_k)$, in which $B_n = 1$ for $n = 0, \ldots, \infty$, i.e.,

$$Z(\boldsymbol{x}, \boldsymbol{x}_k) = \sum_{n=0}^{\infty} \frac{2n+1}{4\pi} \left(\frac{R}{r}\right)^{n+1} P_n(\boldsymbol{r}^T \boldsymbol{r}_k), \tag{10}$$

the filtered function equals the original function

$$F(\boldsymbol{x}) = (Z * F)(\boldsymbol{x}) = \sum_{k=1}^{K} d_k Z(\boldsymbol{x}, \boldsymbol{x}_k). \tag{11}$$

In case of using a band-limited SRBF, which means setting the Legendre coefficient $B_n = 0$ for all degree $n > n_{\max}$, the SRBF acts as a low-pass filter. Schreiner (1999) and Freeden et al. (1998) prove a theorem which shows that the coefficients d_k are independent on the type of SRBFs as soon as they are band-limited to the same degree.

Theorem In a Hilbert space $L^2(\Omega_R)$ of all real square-integrable functions F on Ω_R, let $B(\boldsymbol{x}, \boldsymbol{x}_k)$, Eq. (5), be a band-limited SRBF with

$$B_n = \begin{cases} \neq 0 & \text{for } n = 0, 1, \ldots, n_{\max} \\ = 0 & \text{for } n > n_{\max} \end{cases} \tag{12}$$

the filtered function $G_1(\boldsymbol{x})$ by the spherical convolution reads

$$G_1(\boldsymbol{x}) = (B * F)(\boldsymbol{x}) = \sum_{k=1}^{K} d_k B(\boldsymbol{x}, \boldsymbol{x}_k). \tag{13}$$

If $C(\boldsymbol{x}, \boldsymbol{x}_k) = \sum_{n=0}^{\infty} \frac{2n+1}{4\pi} (\frac{R}{r})^{n+1} C_n P_n(\boldsymbol{r}^T \boldsymbol{r}_k)$ has the band limitation $C_n = 0$ for $n > n_{\max}$, then

$$G_2(\boldsymbol{x}) = (C * F)(\boldsymbol{x}) = \sum_{k=1}^{K} d_k C(\boldsymbol{x}, \boldsymbol{x}_k) \tag{14}$$

holds by using the same coefficients d_k, as in Eq. (13). The only condition is that they are band-limited to the same degree $n_{\max}$. This theorem makes it possible to use different SRBFs for different data sets and to use different SRBFs in the analysis step (in which the unknown coefficients are estimated) and in the synthesis step (in which the estimated coefficients are used to calculate the output gravitational functionals), respectively.

3.3 Estimation model

As discussed in Sect. 3.1, an observation in terms of gravity disturbance can be represented as

$$\delta g(\boldsymbol{x}) + e(\boldsymbol{x}) = \sum_{k=1}^{K} d_k B_r(\boldsymbol{x}, \boldsymbol{x}_k), \tag{15}$$

where $e(\boldsymbol{x})$ is the observation error and B_r is described in Eq. (8). With L observations, we can set up the Gauss–Markov model

$$\boldsymbol{f} + \boldsymbol{e} = \boldsymbol{A}\boldsymbol{d} \quad \text{with} \quad D(\boldsymbol{f}) = \sigma^2 \boldsymbol{P}^{-1} \tag{16}$$

where $\boldsymbol{f}$ is the observation vector, $\boldsymbol{e}$ is the error vector, $\boldsymbol{A}$ is the design matrix which contains the corresponding basis functions, $\boldsymbol{d}$ is the vector of the unknown coefficients, and $D(\boldsymbol{f})$ is the covariance matrix of the observation vector $\boldsymbol{f}$, with σ^2 being the unknown variance factor and $\boldsymbol{P}$ being the given positive definite weight matrix. However, the associated least-squares system is ill-posed or even singular due to

the three reasons mentioned in the Introduction. This problem can be solved by introducing the expectation vector $\boldsymbol{\mu}_d = E(\boldsymbol{d})$ of the coefficient vector $\boldsymbol{d}$ as prior information. Then, the additional linear model can be formulated as

$$\boldsymbol{\mu}_d + \boldsymbol{e}_d = \boldsymbol{d} \quad \text{with} \quad D(\boldsymbol{\mu}_d) = \sigma_d^2 \boldsymbol{P}_d^{-1}, \tag{17}$$

where $\boldsymbol{e}_d$ is the error vector of the prior information. Combining the terrestrial observations $\boldsymbol{f}_1$ and the airborne observations $\boldsymbol{f}_2$, as well as the additional linear model, the extended Gauss–Markov model can be set up (see e.g., Schmidt et al. 2007; Liu et al. 2020 for more details). Applying the least-squares method to the extended Gauss–Markov model, the unknown coefficients are estimated as

$$\begin{aligned}\widehat{\boldsymbol{d}} = &(\boldsymbol{A}_1^T \boldsymbol{P}_1 \boldsymbol{A}_1 + \omega \boldsymbol{A}_2^T \boldsymbol{P}_2 \boldsymbol{A}_2 + \lambda \boldsymbol{P}_d)^{-1} \\ &(\boldsymbol{A}_1^T \boldsymbol{P}_1 \boldsymbol{f}_1 + \omega \boldsymbol{A}_2^T \boldsymbol{P}_2 \boldsymbol{f}_2 + \lambda \boldsymbol{P}_d \boldsymbol{\mu}_d),\end{aligned} \tag{18}$$

with the covariance matrix:

$$D(\widehat{\boldsymbol{d}}) = \sigma_1^2 (\boldsymbol{A}_1^T \boldsymbol{P}_1 \boldsymbol{A}_1 + \omega \boldsymbol{A}_2^T \boldsymbol{P}_2 \boldsymbol{A}_2 + \lambda \boldsymbol{P}_d)^{-1}. \tag{19}$$

$\omega = \sigma_1^2/\sigma_2^2$ is the relative weight between the airborne observations $\boldsymbol{f}_2$ and the terrestrial observations $\boldsymbol{f}_1$, $\lambda = \sigma_1^2/\sigma_d^2$ is the regularization parameter (Koch and Kusche 2002; Schmidt et al. 2007), and the numerical values for the variance factors σ_1^2, σ_2^2, σ_d^2 can be estimated by VCE (see Sect. 4.3). The covariance matrix (19) describes the accuracy of the estimated coefficients. Its main diagonal contains the variances $v(\widehat{d})$, which define the standard deviations of the estimated coefficients as $\widehat{\sigma} = \sqrt{v(\widehat{d})}$.

3.4 Computation of the resulting gravitational functionals

In the synthesis step, the estimated unknown coefficients are used to determine the disturbing potential T at the computation points $\boldsymbol{x}_c$

$$\widehat{\boldsymbol{T}} = \boldsymbol{B}\widehat{\boldsymbol{d}}, \tag{20}$$

where $\widehat{\boldsymbol{T}}$ is the vector of the computed disturbing potential and $\boldsymbol{B}$ is the design matrix, which contains the basis functions between the grid points P_k and the computation points P_c.

Applying the error propagation law to Eq. (20), the covariance matrix

$$D(\widehat{\boldsymbol{T}}) = \boldsymbol{B} D(\widehat{\boldsymbol{d}}) \boldsymbol{B}^T \tag{21}$$

is obtained. The estimated standard deviations of the modeled disturbing potential, $\widehat{\sigma}_T = \sqrt{v(\widehat{T})}$, indicate the accuracy of the resulting gravity model.

The gravity potential values $W(P_c)$ at computation points P_c are then calculated by adding the normal gravity potential $U(P_c)$ to the disturbing potential $T(P_c)$, i.e.,

$$\widehat{W}(P_c) = \widehat{T}(P_c) + U(P_c). \tag{22}$$

From the disturbing potential, the height anomaly (quasi-geoid) ζ at the computation points P_c can be calculated following the Bruns' formula (Heiskanen and Moritz 1967):

$$\widehat{\zeta} = \frac{\widehat{T}}{\gamma} \tag{23}$$

where γ is the normal gravity at the normal height of point P_c. Following Sánchez et al. (2018), we use the ellipsoid GRS80 (Moritz 2000) for the computation of U and γ. According to the error propagation law, the standard deviation of the quasi-geoid vector σ_ζ can be calculated by

$$\widehat{\sigma}_\zeta = \frac{\widehat{\sigma}_T}{\gamma}. \tag{24}$$

The geoid height N can then be calculated from the quasi-geoid ζ following the transformation formula in Heiskanen and Moritz (1967). It is worth mentioning that since the geoid height is obtained from a transformation which includes an approximation, it is expected to be less accurate than the quasi-geoid model. The same transformation formula is also used by most of the other participants in the 'Colorado Experiment,' in order to facilitate the comparison between different contributions.

It is worth mentioning that the zero-degree terms T_0 and ζ_0 (Heiskanen and Moritz 1967) have been added to our final results (see Sánchez et al. 2018), which include the difference between the constant GM values of the GGM (which is the XGM2016 in our case) and the reference ellipsoid GRS80, as well as the difference between the reference potential value W_0 adopted by the IHRS and the potential U_0 on the reference ellipsoid (Sánchez et al. 2016; Sánchez and Sideris 2017),

$$T_0 = \frac{\mathrm{GM_{GGM}} - \mathrm{GM_{GRS80}}}{r_P} \tag{25}$$

$$\zeta_0 = \frac{(\mathrm{GM_{GGM}} - \mathrm{GM_{GRS80}})}{r_P \cdot \gamma_Q} - \frac{\Delta W_0}{\gamma_Q} \tag{26}$$

with $\mathrm{GM_{GGM}} = 3.986004415 \cdot 10^{14}\,\mathrm{m^3/s^2}$, $\mathrm{GM_{GRS80}} = 3.986005 \cdot 10^{14}\,\mathrm{m^3/s^2}$, $\Delta W_0 = -7.45\,\mathrm{m^2/s^2}$, and r_P is the geocentric radial distance of the computation points P_c.

4 Computation configuration

4.1 Remove–compute–restore procedure

We apply the remove–compute–restore (RCR) procedure (e.g., Forsberg 1993). As is described by its name, the RCR procedure means that a part δg_R of the observations (signal) δg is removed before the computation

$$\Delta\delta g = \delta g - \delta g_R. \tag{27}$$

The remaining part $\Delta\delta g$ is then processed using the SRBFs to model the gravitational functional $\Delta\widehat{T}$. Afterward, the removed part is restored in terms of the disturbing potential T_R as

$$T = \Delta\widehat{T} + T_R. \tag{28}$$

The removed part δg_R is usually the long-wavelength component from a GGM, since existing global models approximate this part very accurately (Lieb et al. 2016). The RCR procedure also solves the problem that regional gravimetry cannot estimate the long-wavelength parts (Lieb et al. 2016). Beside the GGM, a further improvement in the modeling results can be achieved by additionally including a residual terrain model (RTM) to δg_R in the remove step (Hirt et al. 2010; Sjöberg 2005). The topographic effect plays a key role especially in mountainous areas, since it smoothens the input observations, and this smoothing step is of utmost importance for obtaining a good least-squares fit (Bucha et al. 2016).

In this study, the long-wavelength component is computed from the global gravity model XGM2016 (Pail et al. 2018) up to maximum degree 719 for both the terrestrial and the airborne data. The topographic model dV_ELL_Earth2014 (Rexer et al. 2016) from degree 720 to degree 2159 and a residual terrain model ERTM2160 (Hirt et al. 2014) from degree 2160 to degree ∼80,000 (equivalent to a spatial resolution of 250 m) are removed from the terrestrial data; the dV_ELL_Earth2014 from degree 720 to degree 5480 is removed from the airborne data. We use two different topographic models above degree 2160 for the terrestrial and airborne data; this is justifiable due to the fact that the two models (dV_ELL_Earth2014 and ERTM2160) are calculated using the same original data and contain the same signal (Hirt et al. 2014; Rexer et al. 2016). For airborne data, the effect of dV_ELL_Earth2104 from degree 2160 to degree 5480 is equal to the ERTM2160, but the ERTM2160 is only available as a grid on the Earth surface, i.e., not as spherical harmonic coefficients with which the gravity values can be computed at any height.

Figure 2 visualizes the remove step. Comparing the last two rows, it is clear that after the GGM reduction, the gravity field is dominated by the topographic effect, which is very large in this study. This implies the importance of including the topographic effect in the RCR, especially in mountainous areas. After subtracting this topographic effect, the gravity field becomes much smoother, especially in regions with varying elevation (mid part of the study area). As shown by the statistics listed in Table 1, the terrestrial observations are smoothed by 42% in terms of the standard deviation (SD) by subtracting the GGM, and by 82% after including the topographic model. The airborne observations are smoothed by 72% by subtracting the GGM and by 89% after including the topographic model. Such significant smoothing effects enable a better least-squares fit. Including the topographic model gives larger smoothing effects for the terrestrial observations than for the airborne observations. This could be explained by the fact that the high-frequency signal of the gravity field decreases with height, and the airborne gravity measurement is less sensitive to the high-frequency part than the terrestrial gravity measurement. Thus, subtracting the topographic effect affects the terrestrial gravity data more than the airborne gravity data.

4.2 Model configuration

4.2.1 Maximum degree of expansion

The maximum degree $n_{\max}$ of expansion is related to the spatial resolution (sr) of the observations (Bucha et al. 2016), and their relation reads (Lieb et al. 2016).

$$n_{\max} \leq \frac{\pi R}{\mathrm{sr}}. \tag{29}$$

Although the observations are distributed unevenly in this study area, the mean spatial resolution counts around 3.5 km for the whole study area. Consequently, $n_{\max} = 5600$ is chosen as the maximum degree of expansion.

4.2.2 Definition of the target, observation, and computation area

In regional gravity modeling, the extension of the target area $\partial\Omega_{\mathrm{T}}$, the observation area $\partial\Omega_{\mathrm{O}}$, and the computation area $\partial\Omega_{\mathrm{C}}$ needs to be defined carefully. In the border of the observation area $\partial\Omega_{\mathrm{O}}$, the unknown coefficients d_k cannot be appropriately estimated, due to the lack of fully surrounding observations. This fact provokes edge effects. The observation area $\partial\Omega_{\mathrm{O}}$, where the observations are given, should be larger than the target area $\partial\Omega_{\mathrm{T}}$, in which the final output gravitational functionals are computed. Furthermore, the computation area $\partial\Omega_{\mathrm{C}}$, where the SRBFs are located, should be larger than the observation area $\partial\Omega_{\mathrm{O}}$. The reason for this extension is due to the oscillation of the SRBFs, especially at the boundaries of the computation area $\partial\Omega_{\mathrm{C}}$, where the

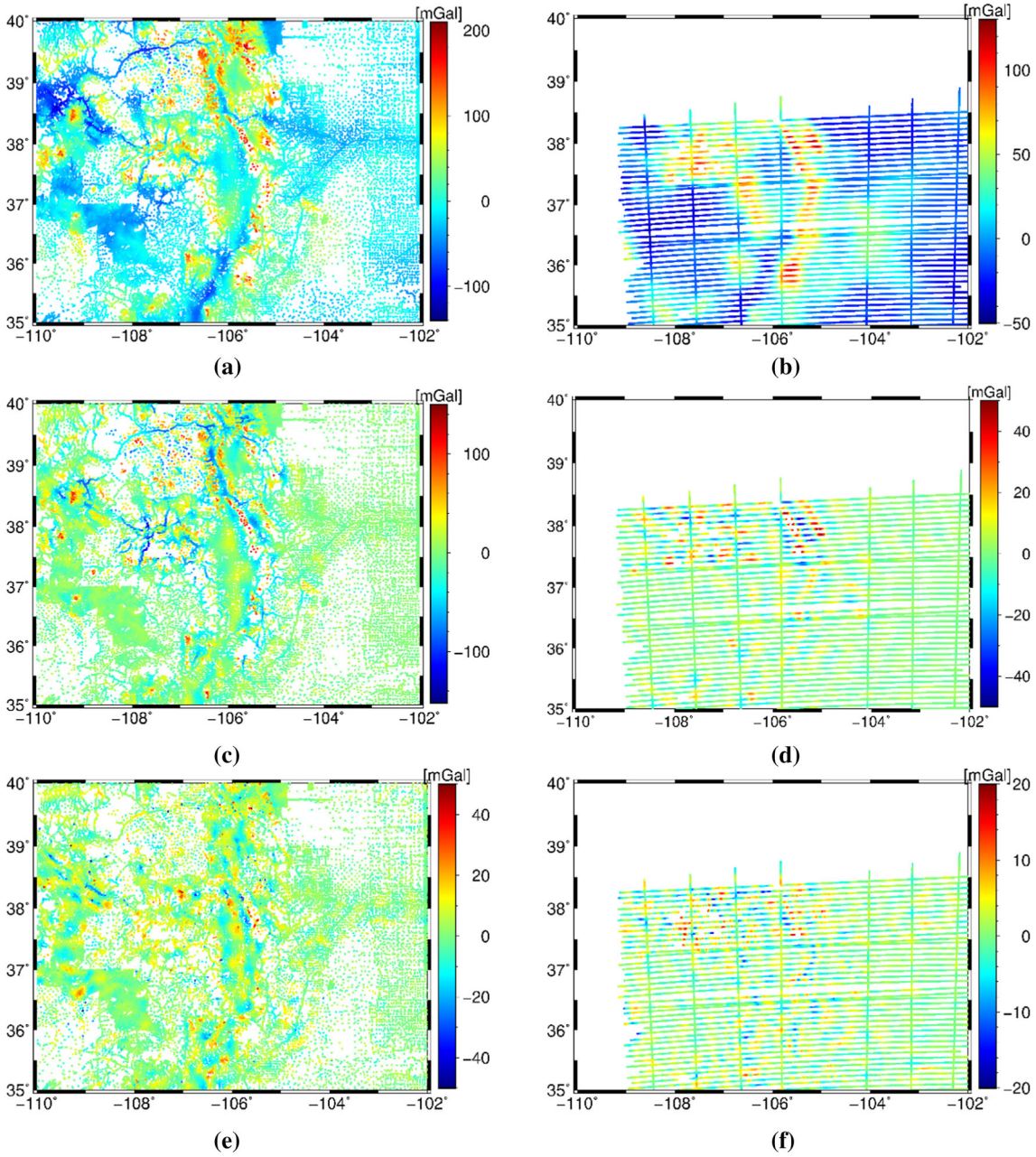


Fig. 2 **a**, **b** The observations (δg); **c**, **d** the remaining gravity disturbance after the GGM reduction (δg-δg_{GGM}); **e**, **f** the remaining parts after both the GGM and topographic reduction (δg-δg_{GGM}-δg_{Topo}) for the terrestrial data (left column) and the airborne data (right column)

Table 1 The statistics of the observations δg, the remaining parts after subtracting the GGM, and the remaining parts after subtracting both GGM and the topographic model

	Min (mGal)	Max (mGal)	Mean (mGal)	SD (mGal)
Terrestrial δg	− 146.37	207.87	0.34	38.71
Terrestrial $\delta g - \delta g_{\mathrm{GGM}}$	− 151.46	137.17	− 5.83	22.39
Terrestrial $\delta g - \delta g_{\mathrm{GGM}} - \delta g_{\mathrm{Topo}}$	− 135.98	75.12	0.57	6.91
Airborne δg	− 43.56	123.87	7.66	29.47
Airborne $\delta g - \delta g_{\mathrm{GGM}}$	− 43.07	68.28	0.26	8.14
Airborne $\delta g - \delta g_{\mathrm{GGM}} - \delta g_{\mathrm{Topo}}$	− 17.82	17.96	0.30	3.19

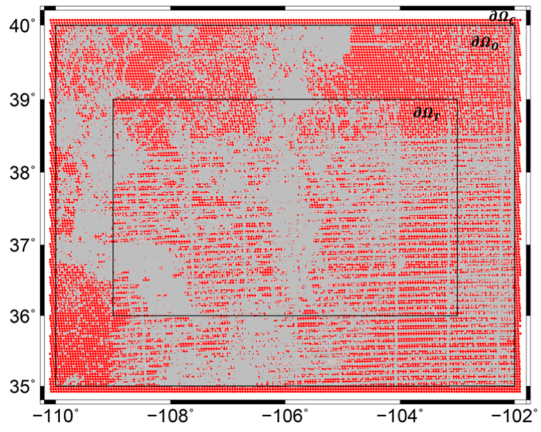


Fig. 3 The different extensions for the areas of computation $\partial\Omega_C$, of observations $\partial\Omega_O$ and of target $\partial\Omega_T$, as well as the location of the observations (grey points) and the location of the grid points (red points)

oscillations cannot overlap and balance with each other (see Naeimi et al. 2015; Lieb et al. 2016 for more details). Thus, $\partial\Omega_T \subset \partial\Omega_O \subset \partial\Omega_C$.

To minimize the edge effects in the computation, margins η need to be defined between the three areas. Usually, the margin size $\eta_{O,T}$ between $\partial\Omega_O$ and $\partial\Omega_T$ and the margin size $\eta_{C,O}$ between $\partial\Omega_C$ and $\partial\Omega_O$ are chosen equally (Bentel et al. 2013a, b). In our case, the target area $\partial\Omega_T$ is given to be between $-109°$ to $-103°$, and $36°$ to $39°$. The observations (grey points in Fig. 3) are mainly located between $-110°$ and $-102°$ and $35°$ and $40°$. So, the margin size $\eta_{O,T}$ between $\partial\Omega_O$ and $\partial\Omega_T$ is fixed to be $1°$. The determination of the margin size $\eta_{C,O}$ between $\partial\Omega_C$ and $\partial\Omega_O$ follows a method described by Lieb et al. (2016), but it is modified to

$$\eta_{C,O} = \frac{360°}{n_{max}\cos(|\phi_{max}|)}, \tag{30}$$

where ϕ_{max} is the maximum latitude value of the target area. The margin size is influenced by the shape of the SRBFs, when the n_{max} is higher, the SRBFs become narrower, and thus, a smaller margin size should be chosen. With $n_{max} = 5600$, the value $\eta_{C,O} \approx 0.1°$ follows. Figure 3 visualizes the target area, the observation area, the computation area, as well as the margins.

4.2.3 The location of the SRBFs

The location of the SRBFs depends on the type and number of the grid points. Eicker (2008) examined four types of grids, and the results indicate that the Reuter grid and the triangle vertex grid are the most suitable choices for space localizing basis functions. According to Bentel et al. (2013a), different grid types do not have a strong impact on the modeling results, especially comparing to the other three factors listed in the Introduction. In this study, the Reuter grid (Reuter 1982) is chosen. The points of the Reuter grid have a homogeneous coverage on the sphere Ω_R. The total number Q of the Reuter grid points on the global sphere is determined following the rule (Lieb et al. 2016),

$$(n_{max}+1)^2 \le Q \le 2 + \frac{4}{\pi}(n_{max}+1)^2, \tag{31}$$

and it amounts to $Q = 31{,}828{,}509$. Then, those Reuter grid points that are distributed in the computation area $\partial\Omega_C$ are used as the locations of the SRBFs (see Fig. 3). In this case, the number of the SRBFs amounts to $K = 26{,}012$.

4.2.4 The type of the SRBFs

Different types of basis functions are introduced and studied in, for example, Schmidt et al. (2007) and Bentel et al. (2013b). Here, the following three types are considered:

1. The Shannon function, and its Legendre coefficients are given by

$$B_n = \begin{cases} 1 & \text{for } n \in [0, n_{max}] \\ 0 & \text{else} \end{cases}. \tag{32}$$

2. The Blackman function, and its Legendre coefficients are given by

$$B_n = \begin{cases} 1 & \text{for } n \in [0, n_1) \\ (A(n))^2 & \text{for } n \in [n_1, n_{max}] \\ 0 & \text{else} \end{cases}, \tag{33}$$

where

$$A(n) = \frac{21}{50} - \frac{1}{2}\cos\left(\frac{2\pi(n-n_{max})}{2(n_{max}-n_1)}\right) + \frac{2}{25}\cos\left(\frac{4\pi(n-n_{max})}{2(n_{max}-n_1)}\right). \tag{34}$$

3. The cubic polynomial (CuP) function, and its Legendre coefficients are given by

$$B_n = \begin{cases} (1-\frac{n}{n_{max}})^2(1+\frac{2n}{n_{max}}) & \text{for } n \in [0, n_{max}] \\ 0 & \text{else} \end{cases}. \tag{35}$$

Figure 4 visualizes the characteristics of these three basis functions in the spatial and the spectral domain, correspondingly. The Shannon function has the highest localization in the spectral domain, but it also gets the strongest oscillations in the spatial domain. In contrast, the CuP function has the least oscillations in the spatial domain but has a smoothing decay and extracts the least spectral information in the spectral domain. The Blackman function is regarded as a

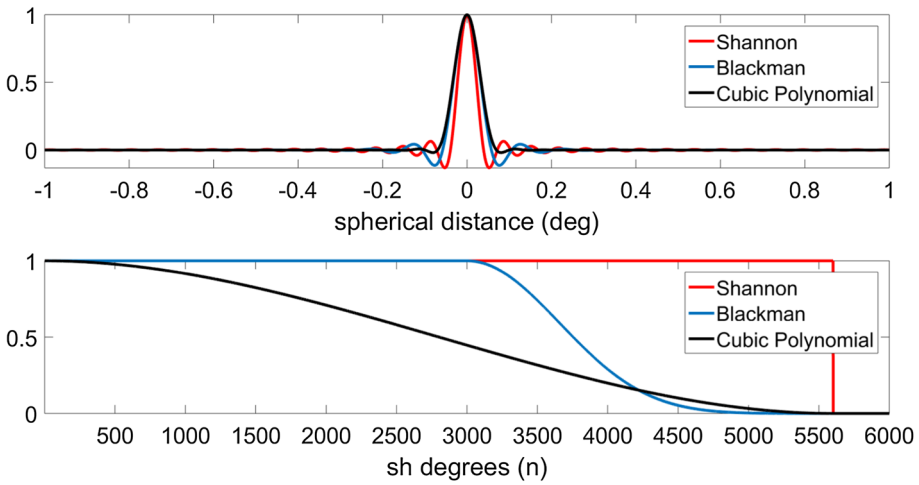


Fig. 4 Different SRBFs in the spatial domain (top, ordinate values are normed to 1) and the spectral domain (bottom) for $n_{\max} = 5600$ ($n_1 = 3000$ is chosen in the Blackman function)

compromise between these two domains. Usually, the Shannon function is used in the analysis step to avoid the loss of spectral information, and the Blackman function or the CuP function is applied in the synthesis step to reduce erroneous systematic effects (Lieb et al. 2016).

In this study, we apply the CuP function in the synthesis step. In the analysis step, we use the Shannon function for the terrestrial observations; the advantages of using the Shannon function for terrestrial data are explained in Bucha et al. (2016). For the airborne observations, however, we choose the CuP function in the analysis step. This is due to the fact that noise in the high frequencies of the airborne data is large; thus, a low-pass filtering is necessary. Forsberg and Olesen (2010) explained why all types of airborne gravity data need filtering; the filtering is a compensation between the resolution and the accuracy. In the low-frequency part of the airborne data, the gravity signal dominates the noise (Childers et al. 1999); thus, low-pass filters are the most commonly used filters. Bucha et al. (2015) showed that the SRBFs could act as a low-pass filter, and Naeimi (2013) demonstrated that both the Blackman function and the CuP function can be used as build-in low-pass filters, due to their smoothing features. We used the Blackman function and the CuP function for low-pass filtering, and the results (presented in Sect. 5.1) show that both of these two functions can low-pass-filter the airborne observations well. We choose the CuP function for the airborne observations in this study, as it gives slightly better results than the Blackman function does (see Table 2 in Sect. 5.1). And as already discussed in Sect. 3.2, different types of SRBFs can be used for different observation types, in case of the same band limitation.

4.3 Combination of the terrestrial and the airborne data

We combine the terrestrial data and the airborne data using the extended Gauss–Markov model (see Sect. 3.3). Since information about the data quality is not available, we assume that the measurements have the same accuracy and are uncorrelated, and thus, $\boldsymbol{P}_p = \boldsymbol{I}$, where $\boldsymbol{I}$ is the identity matrix. The same assumptions are commonly used in existing publications (see e.g., Lieb et al. 2016; Wu et al. 2017b; Slobbe et al. 2019), since it is usually difficult to acquire the realistic full error variance–covariance matrix, and the procedure would become computationally intensive by including it. Moreover, Olesen et al. (2002) showed that for airborne gravity disturbances, noise correlations can be ignored if one aims at a 1-cm quasi-geoid model. Furthermore, we set $\boldsymbol{P}_d = \boldsymbol{I}$ by assuming that the coefficients are not correlated and have the same accuracy. The models subtracted in the remove step of the RCR procedure serve as the prior information; in this case, we can set the expectation vector $\boldsymbol{\mu}_d$ to the zero vector (Schmidt et al. 2007). The solution for the estimated coefficients can be obtained from Eq. (18), where two variables need to be determined; one is the relative weight ω between the two types of observations, and another is the regularization parameter λ.

The relative weight ω is determined by VCE, which is an iterative process to estimate the variance factors $\sigma_1^2, \sigma_2^2, \sigma_d^2$ of different observation types and the prior information. The iteration starts from initial values for $\sigma_1^2, \sigma_2^2, \sigma_d^2$, and it ends when convergence is reached. The variance factors obtained from VCE read $\widehat{\sigma}_1^2 = 6.13 \times 10^{-10}$, $\widehat{\sigma}_2^2 = 1.61 \times 10^{-10}$, and $\widehat{\sigma}_d^2 = 8.17 \times 10^{-14}$. These estimates indicate that the airborne gravity data might have a higher quality than the terrestrial data. It is explainable since the terrestrial observations were gathered during a large time span (since the late 1930s), and thus, their quality may vary regionally. On the other hand, the GRAV-D airborne data were collected in the recent few years. Moreover, the value of $\widehat{\sigma}_1$ (2.48 mGal) coincides with Saleh et al. (2013), who estimated the NGS's terrestrial gravity data to contain error with an RMS of $\sim$ 2.2 mGal. However, it should be noted that the estimated variance factors actually

Table 2 RMS values of the height anomaly results w.r.t the validation data, when using the Shannon function, the Blackman function, and the CuP function for the airborne observations, respectively

Terrestrial + Airborne	Min (cm)	Max (cm)	Mean (cm)	RMS (cm)
Shannon + Shannon	− 3.95	1.78	− 0.28	1.135
Shannon + Blackman	− 3.93	1.57	− 0.34	1.080
Shannon + CuP	− 3.89	1.87	− 0.13	1.075

represent the quality of the least-squares fit rather than the accuracy of the data (Bucha et al. 2016).

From the estimated variance factors, the relative weight between the terrestrial data and the airborne data $\omega = \widehat{\sigma}_1^2/\widehat{\sigma}_2^2$ and the regularization parameter $\lambda_{\mathrm{VCE}} = \widehat{\sigma}_1^2/\widehat{\sigma}_d^2$ can be obtained. However, according to Liu et al. (2020), this regularization parameter is not always reliable, so we apply the L-curve method (see e.g., Hansen and O'Leary 1993; Eriksson 2000) to regenerate the regularization parameter λ, based on the relative weighting ω. In this case, the regenerated regularization parameter is $\lambda = 10{,}000$.

5 Results and discussion

As already mentioned in Sect. 2.1, we compute two sets of output gravity functionals. The first one is at the GSVS17 benchmarks, at which thirteen groups worldwide have provided independent height anomaly results as well as geopotential values, and fourteen groups have provided the geoid height results. A list of all participants, as well as an external validation to the leveling-based physical heights, can be found in Wang et al. (2020). Since we do not have access to the leveling-based validation data, we validate various solutions using the mean value of the other groups. Thus, the term 'validation data' used in Sects. 5.1–5.2 refers to the mean height anomaly results of the other twelve groups along the GSVS17 benchmarks. We do not include our own results in the evaluation of models to keep the comparison independent; however, the validation of our final results to the mean value of all participants (including ours) is also presented in Sect. 5.4. The second one is a model grid from $-109°$ to $-103°$ and $36°$ to $39°$ with a resolution of $1' \times 1'$. Thirteen groups have provided the height anomaly grid models, fourteen groups have provided the geoid height grid model, and the comparison between our models and the mean of all the models are given.

5.1 Evaluation of the low-pass filtering

To test the validity of the low-pass filtering based on the CuP function, we compare this low-pass filtering result to the ones using the Shannon function or the Blackman function for the airborne observations. The height anomaly results at the GSVS17 benchmarks when using these three functions for the airborne data, respectively, are compared with respect to the validation data. (The Shannon function is used for the terrestrial data as already discussed in Sect. 4.2.4.) The statistics are listed in Table 2. The RMS deviations w.r.t the validation data when using the CuP function and the Blackman function for the airborne data are 1.075 cm and 1.080 cm, respectively, which are around 0.5 mm smaller than that when using the Shannon function for both the data sets. It should be noted that when using the Blackman function or the CuP function as low-pass filters, the results improve by 5%, which is not neglectable. These results also indicate the importance of the low-pass filtering for the airborne data. Although the results obtained from the Blackman function and the CuP function are similar, the CuP function still gives a slightly better result (i.e., smaller RMS error) than the Blackman function, and thus, the CuP function is chosen for low-pass filtering the airborne data.

It is worth mentioning that we have also tried to smooth the airborne gravity observations directly by a mean filter, i.e., assign the average value of consecutive observations to the mid observation, and then use the Shannon function. However, the results are worse than those using the CuP function to the original data, which indicates the efficiency of applying the CuP function for smoothing the airborne observations.

5.2 Evaluation of the combined solution comparing to the terrestrial or the airborne-only solution

Shih et al. (2015) demonstrated that the RMS error of their gravity anomaly model drops when an additional data set is incorporated. Jiang and Wang (2016) showed that by adding the GRAV-D airborne data, the agreement to the GPS/leveling data (GSVS11) improves from 1.1 to 0.8 cm in Texas, USA. Forsberg et al. (2012) reported an improvement by the airborne data from 15 to 13 cm in the United Arab Emirates. To assess how much our quasi-geoid model benefits from the regional terrestrial and airborne gravity data, the computation is also conducted to the terrestrial observations and the airborne observations, individually, in the same manner. Each result is compared to the combined solution with respect to the validation data. The differences between our height anomaly results and the validation data when using both data sets, using the terrestrial data only, using the air-

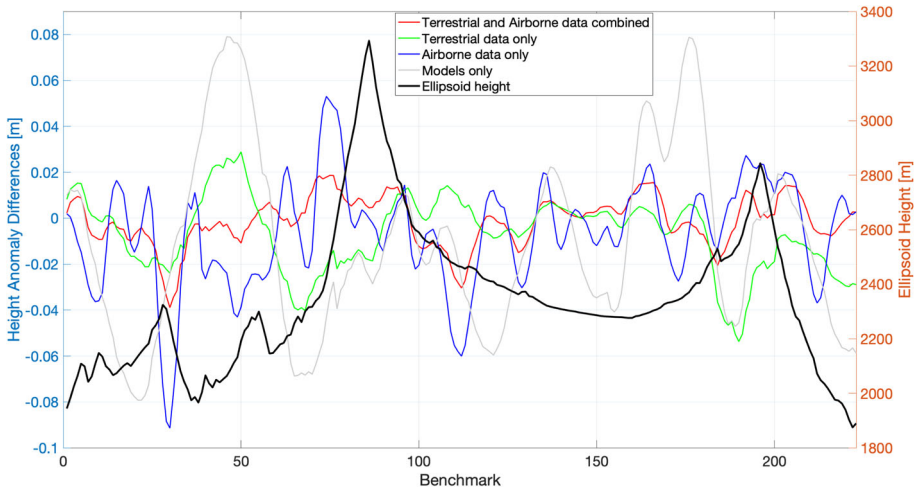


Fig. 5 Differences between our solutions and the mean value of all the other institutions at the GSVS17 benchmarks

Table 3 Comparison between the combined solution and the terrestrial-only, airborne-only, or models-only solution at the GSVS17 benchmarks, w.r.t the validation data

	Min (cm)	Max (cm)	Mean (cm)	RMS (cm)
Combined	− 3.89	1.87	− 0.13	1.08
Terrestrial-only	− 5.37	2.88	− 0.70	1.76
Airborne-only	− 9.14	5.30	− 0.64	2.38
Models-only	− 7.93	7.90	− 1.03	4.04

borne data only, and using no observation data, i.e., only the GGM and the topographic model (models-only solution), are plotted in Fig. 5, respectively. (The ellipsoidal height of the GSVS17 benchmarks is plotted for interpretation reasons.) The statistics are listed in Table 3.

Compared to the validation data, using only the GGM and the topographic model without any observation data gives the worst result, with an RMS error of 4.04 cm; it is improved to 1.76 cm by adding the terrestrial data and further improved to 1.08 cm by including the airborne data. Figure 5 shows that the models-only solution (grey) has the largest variation comparing to the validation data (zero value line), although the models reach a very high harmonic degree. It shows that the topographic models cannot represent the true high-frequency gravity signal accurately, since they usually assume the topographic masses to have constant density (Hirt et al. 2010; Bucha et al. 2016), which is not the case in practice. Thus, regional gravity field refinement with local data is necessary, despite the availability of high-resolution topographic models. From Fig. 5, we can see that the airborne-only solution (blue) has larger oscillations than the terrestrial-only solution (green), and the combined solution (red) benefits from both data sets. The terrestrial-only solution is better than the airborne-only solution, which could be explained by the larger coverage of the terrestrial data as well as the downward continuation of the airborne data. To be more specific, the airborne measurements are collected at an average altitude of 6 km to model the gravity field on the Earth surface, and thus, the modeling results are expected to be less accurate than using the surface gravity data. The improvement in the combined solution is 39% compared to using terrestrial data only and 55% compared to using airborne data only, and it reaches 73% compared to using no gravity observations but only GGM and topographic models. Such significant improvements indicate the validity of our combination model.

A significant outcome from Fig. 5 is that the differences between the terrestrial-only solution and the validation data are highly correlated with the variations of the topography (black) at the GSVS17 benchmarks. To be more specific, when the ellipsoidal heights are constant (between around benchmark Nr. 110–180), the terrestrial solution is almost identical to the combined solution; when there are big changes in the ellipsoidal heights (e.g., between around benchmark Nr. 30–90 as well as after benchmark Nr. 180), larger differences between the terrestrial-only solution and the validation data can be observed. Including the airborne data seems to improve the terrestrial-only solution the most in rugged region, which could give some hints about where to place new airborne measurements in mountainous study areas. According to the findings in this study, airborne observations should be taken place in rugged terrain in order to give the maximum benefits, in addition to the local terrestrial data.

5.3 Significance of the estimated coefficients

The estimated coefficients $\widehat{d}$ and their standard deviation $\widehat{\sigma}$ are plotted in Fig. 6a, b. As we can see, the estimated coefficients inside the observation area $\partial\Omega_O$ (black rectangle)

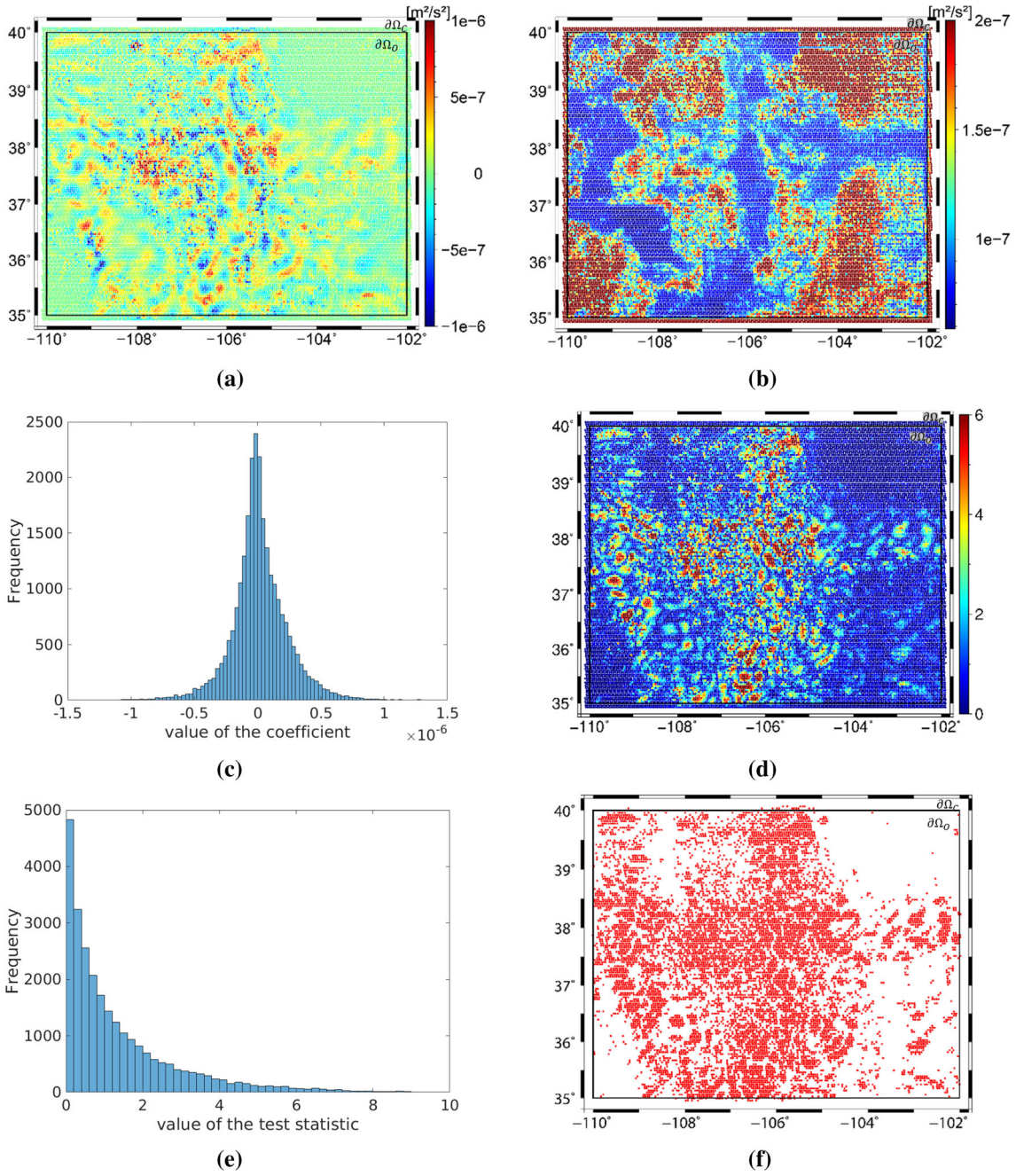


Fig. 6 **a** The estimated coefficients $\widehat{d}$, **b** their standard deviations $\widehat{\sigma}$, **c** the histogram of the estimated coefficients, **d** the test statistic $|\widehat{d}|/\widehat{\sigma}$, **e** the histogram of the test statistic, and **f** the corresponding significant coefficients when $p = 0.9$ is chosen

represent the gravitational structures well, i.e., a correlation between Figs. 2e, f and 6a is visible. Larger values in the estimated coefficients (positive and negative) indicate that additional gravity signals with respect to the background model are captured, which shows the physical meaning of the estimated coefficients (Lieb 2017). Outside the observation area $\partial\Omega_{\mathrm{O}}$ (i.e., in the margin between $\partial\Omega_{\mathrm{O}}$ and $\partial\Omega_{\mathrm{C}}$), the estimated coefficients are close to zero, and their standard deviations are much larger than those inside the observation area. Larger standard deviations also occur in areas with data gaps (referring to Fig. 1b), which is reasonable.

Theoretically, only the coefficients that are significantly different from zero contribute to the obtained signals and, thus, to model the gravitational functionals. The nonsignificant coefficients then must be removed. To test how many coefficients are significant in our study case, we conduct a t test by the test statistic $|\widehat{d}|/\widehat{\sigma}$ (Bentel et al. 2013a). It is worth mentioning that the t test can be applied here because

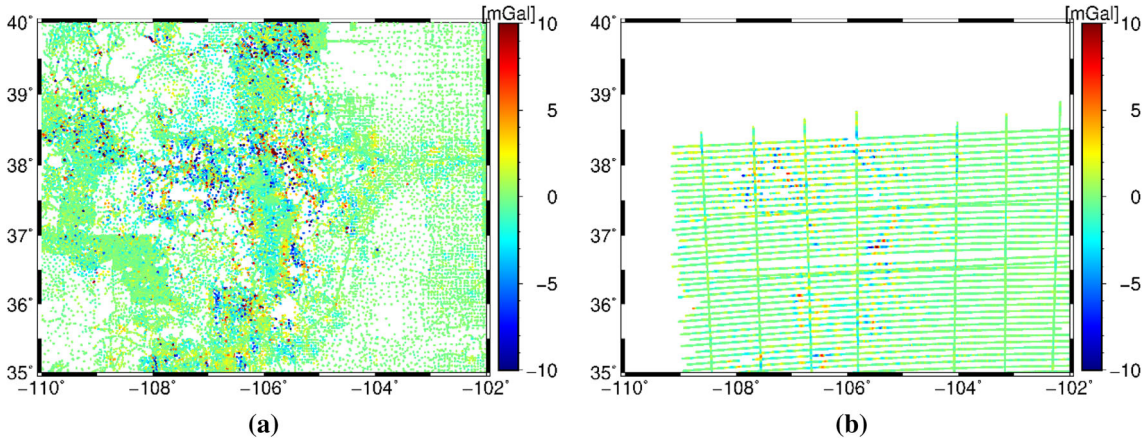


Fig. 7 The least-squares residuals of **a** the terrestrial gravity data, and **b** the airborne gravity data

we assumed that the coefficients are not correlated with each other (see Sect. 4.3). The hypothesis statements to test an individual coefficient d are

$$H_0 : d = 0 \quad \text{vs.} \quad H_1 : d \neq 0 \tag{36}$$

The hypothesis $H_0 : d = 0$ will be rejected if its test statistic $|\widehat{d}|/\widehat{\sigma}$ (Fig. 6d) is larger than a critical value $t_{nu,p}$ for the t test. Figure 6e shows the histogram of the test statistic $|\hat{d}|/\hat{\sigma}$. In our case, the degree of freedom nu is equal to $90{,}236 - 26{,}012 = 64{,}224$, where 90,236 is the number of observations and 26,012 is the number of unknown coefficients. The confidence level $p = 0.9$ is chosen, then $t_{64224,0.9} = 1.282$. It means that if the test statistic $|\widehat{d}|/\widehat{\sigma}$ is larger than 1.282, then this coefficient is significantly different from zero with 90% confidence, and the corresponding coefficients are considered. The corresponding significant coefficients are plotted in Fig. 6f.

5.4 Final results and validation

5.4.1 Least-squares residuals of our estimated model

Figure 7 displays the residuals of the least-squares adjustment for the terrestrial gravity observations (Fig. 7a) and the airborne gravity observations (Fig. 7b). The residuals of the terrestrial observations have a mean value of -0.19 mGal, with a SD of 2.13 mGal, and the residuals of the airborne data have a mean value of -0.15 mGal, with a SD of 1.25 mGal. The functional model fits the airborne data better than the terrestrial data, which could be explained by the fact that the airborne data get a higher weight than the terrestrial data during the VCE procedure. It is also clear from Fig. 7 that the prominent residuals are located in high-elevation areas for both the terrestrial and airborne data, and a clear correlation with Fig. 1a can be observed. This indicates that a further improvement in our model could be achieved by (1) applying a more accurate terrain model that might be available in the near future, or (2) including a better gravity data distribution on the rugged topography areas.

5.4.2 Height anomaly and geoid height results at the GSVS17 benchmarks

Our height anomaly as well as the geoid height results are displayed in Fig. 8, in comparison with the mean value of all participants. It is visible that our results agree very well with other contributions, with differences ranging between -4 and 4 cm. The geoid height (blue) fits worse than the height anomaly (red) with respect to the mean, which is as expected due to the transformation (see Sect. 3.4). According to Wang et al. (2020), the RMS errors of our height anomaly and geoid height compared to the mean value of all groups are 1.0 cm and 1.3 cm, respectively, which are the smallest among all the participants. It is worth mentioning that we have also calculated the geopotential values W, and it has a mean of 0.01 m^2/s^2 with a standard deviation of 0.09 m^2/s^2 comparing to the mean results of all the contributions, which is also the smallest. A detailed comparison of the geopotential values is presented in Sánchez et al. (2020).

The validation with the GPS/leveling data is done by Wang et al. (2020), and the differences of our height anomaly results compared to the GSVS17 GPS/leveling data range between -7.6 and 4.5 cm, with a mean value of 0.81 cm and a SD of 2.89 cm. Considering the not homogeneously distributed observations with obvious data gaps, this result is quite satisfying. However, it has to be mentioned that the quality of these GPS/leveling data is not reported by data providers yet, and thus, the validation with the mean values of all participants is of higher importance.

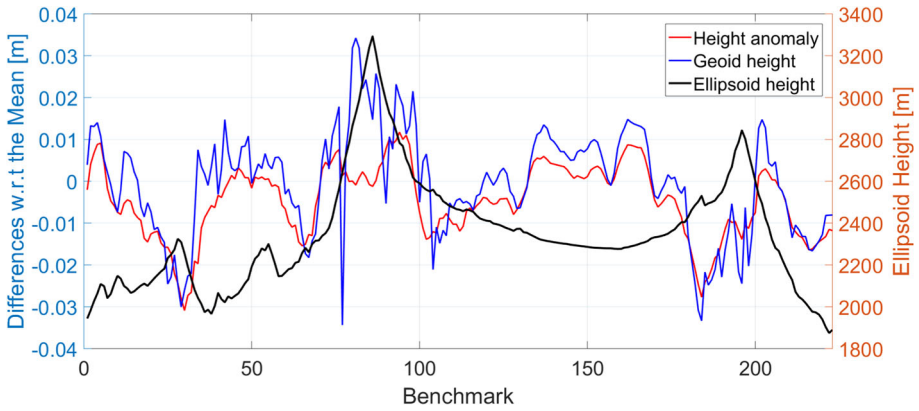


Fig. 8 Results at the GSVS 17 benchmarks

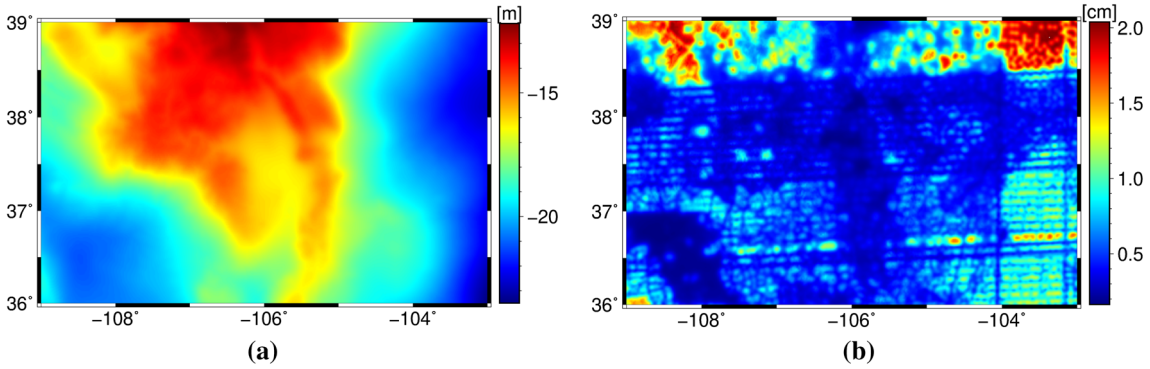


Fig. 9 **a** Height anomaly and **b** its standard deviation

5.4.3 Height anomaly and geoid height results in the whole study area

Figure 9a visualizes the quasi-geoid model for the whole target area $\partial\Omega_T$, with a grid resolution of $1' \times 1'$. The standard deviation map of the modeled height anomaly is plotted in Fig. 9b, which ranges from only few millimeters to around 2 cm. The values are smaller in regions with denser observations. The RMS error of our height anomaly and geoid height grid model comparing to the mean value of all groups are 1.6 cm (which is the smallest among all the participants) and 2.9 cm, respectively (Wang et al. 2020).

Comparisons are also made between our height anomaly model and two widely used global gravity models, namely EGM2008 with d/o 2190 (Pavlis et al. 2012, 2013) and EIGEN6c4 with d/o 2190 (Förste et al. 2014). As shown in Fig. 10a, b, the differences are at the decimeter level. Comparing these differences to the terrain map (Fig. 1a), it is clear that the large differences are mainly observed in areas with high topography. These differences could be coming from the effects above degree 2190, i.e., the GGMs are only modeled till degree 2190, while we model the gravity signals till a much higher degree. To verify the reason for these differences, we also compare our height anomaly model to the XGM2019e with d/o 5540 in Fig. 10c, and their difference does not show a correlation with the topography as strong as in Fig. 10a, b. In Fig. 10d, we add the residual terrain model ERTM2160 to the EIGEN6c4 and compare it with our height anomaly model. The difference is heavily reduced in this case, and the plot becomes much smoother. Due to the consideration of the topographic effect as well as the large amount of observations in the mountainous area, our model improves a lot in this study area comparing to the global gravity model. The poor performance of the GGMs implies that they are not reliable for engineering purposes or geophysical investigation (Wu et al. 2017a), especially in mountainous areas. Moreover, the regional gravity field modeling with locally distributed data improves the fine structures primarily, which demonstrate the importance of regional gravity field refinement.

6 Conclusion and outlook

In this study, we calculate the high-resolution quasi-geoid model and geoid model using spherical radial basis functions in Colorado, USA. The results contribute to the '1 cm Geoid Experiment,' which enables a comparison of our SRBF-based results to thirteen independent solutions calculated within other approaches, such as LSC (Moritz 1980; Tsch-

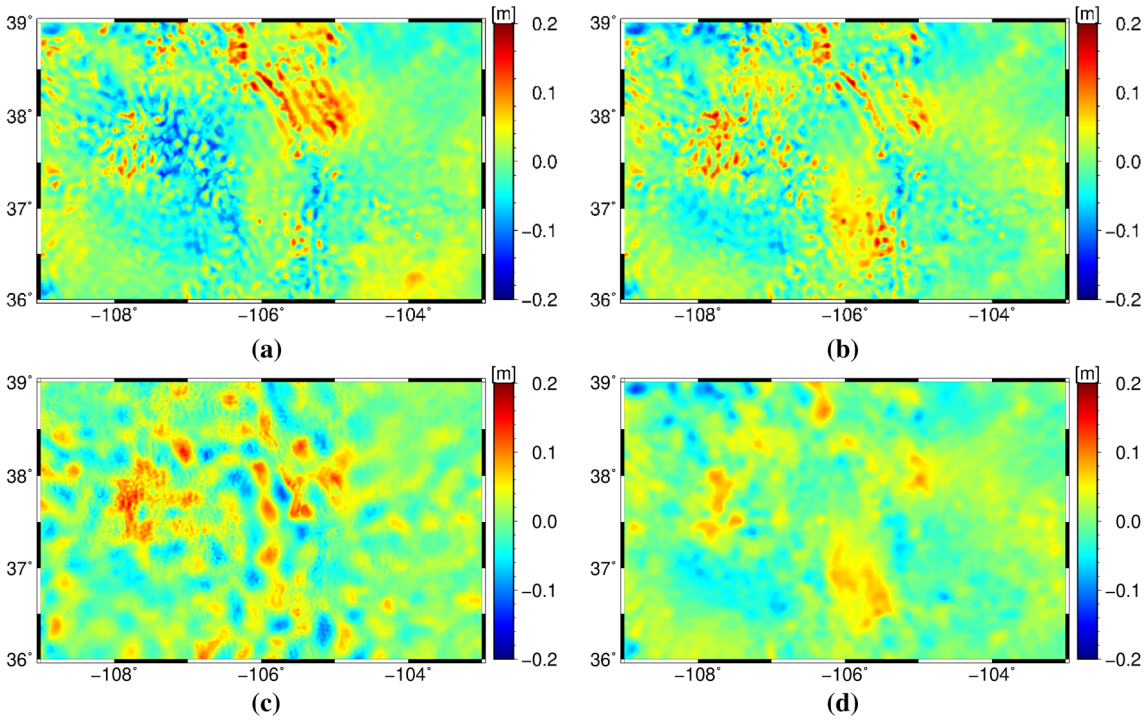


Fig. 10 Height anomaly differences between our model and **a** EGM2008, **b** EIGEN6c4, **c** XGM2019, **d** EIGEN6c4+ERTM2160

erning 2013) and the least-squares modification of Stokes' formula (Sjöberg 2003, 2010). Detailed explanations are given regarding the choice of the SRBFs characteristics: the bandwidth, the location, the type of the SRBFs as well as the extensions of the data zone.

We combine two types of basis functions covering the same spectral domain in the analysis step. The non-smoothing Shannon function is applied to the terrestrial data to avoid the loss of spectral information. The CuP function is applied to the airborne data as a low-pass filter, and the smoothing features of this type of SRBFs are used for filtering the high-frequency noise in the airborne data. The RMS error of our height anomaly result along the GSVS17 benchmarks w.r.t the mean results of the other twelve groups drops by 5% when combining the Shannon function for the terrestrial data and the CuP function for the airborne data, compared to those obtained by using the Shannon function for both the two data sets. We present a theorem which shows that the unknown coefficients are independent of the type of SRBFs as soon as they are band-limited to the same degree, and thus, different types of SRBFs can be used for different types of observations. As no publications based on real data are known to the authors which applied the idea of combining different types of SRBFs for different observations, our results also serve as an application of this idea and further indicate its validity and benefits.

We combine the GGM, topographic model, terrestrial gravity data, and airborne gravity data within the RCR procedure and the parameter estimation procedure. Numerical investigations show that including the topographic model is of great importance in mountainous areas, as it helps to obtain a better least-squares fit. However, the topographic model alone does not guarantee an accurate regional gravity field model, despite their high resolution. Comparing to the mean value of other contributions at the GSVS17 benchmarks, combining the GGM and the topographic model gives an RMS error of 4.04 cm, which is reduced to 1.76 cm after adding the terrestrial observations and further reduced to 1.08 cm after including the airborne data. These results indicate the importance of local data sets in regional gravity field refinement.

Comparisons are made with respect to the mean results of all the contributions, and our height anomaly and geoid height solutions at the GSVS17 benchmarks give an RMS error of 1.0 cm and 1.3 cm, respectively. Our quasi-geoid and geoid grid models for the whole study area deliver an RMS value of 1.6 cm and 2.9 cm, respectively. Both our height anomaly and geoid height results at the GSVS17 benchmarks, as well as the height anomaly result in the whole study area, have the smallest RMS value w.r.t the mean values of all participants, which validates our SRBF-based model. However, there is a disagreement between the RMS error w.r.t the mean solutions and w.r.t the GPS/leveling data. Thus, a major concern for the future work is to understand this disagreement after the release of the GPS/leveling data.

Acknowledgements The authors would like to thank the German Research Foundation (DFG) for funding the project 'Optimally combined regional geoid models for the realization of height systems in developing countries' (grant number: SCHM 2433/11-1). Furthermore, the authors acknowledge the developers of the Generic Mapping Tool (GMT) mainly used for generating the figures in this work. Finally, we thank the three reviewers and two editors for their comments that helped us to significantly improve the manuscript.

Author contributions QL conceptualized and designed the study. QL developed the theoretical formalism, performed the calculations, compiled the figures, and wrote the manuscript with the assistance from MS. MW helped in data preprocessing. LS helped in the comparison with other groups. All authors reviewed and commented on the original manuscript.

Funding Open Access funding provided by Projekt DEAL.

Data Availability Statement The terrestrial gravity data, the airborne gravity data, and the point file of the GSVS17 GPS/leveling data used in this study were provided by the National Geodetic Survey, for the '1 cm Geoid Experiment.' The airborne gravity data are freely available on https://www.ngs.noaa.gov/GRAV-D/data_products.shtml. Geoid and quasi-geoid models will be distributed through the International Service for the Geoid (ISG) Web site.

Compliance with ethical standards

Conflict of interest The authors declare that they have no conflict of interest.

Open Access This article is licensed under a Creative Commons Attribution 4.0 International License, which permits use, sharing, adaptation, distribution and reproduction in any medium or format, as long as you give appropriate credit to the original author(s) and the source, provide a link to the Creative Commons licence, and indicate if changes were made. The images or other third party material in this article are included in the article's Creative Commons licence, unless indicated otherwise in a credit line to the material. If material is not included in the article's Creative Commons licence and your intended use is not permitted by statutory regulation or exceeds the permitted use, you will need to obtain permission directly from the copyright holder. To view a copy of this licence, visit http://creativecommons.org/licenses/by/4.0/.

References

Bentel K, Schmidt M, Denby CR (2013a) Artifacts in regional gravity representations with spherical radial basis functions. J Geod Sci 3:173–187. https://doi.org/10.2478/jogs-2013-0029

Bentel K, Schmidt M, Gerlach C (2013b) Different radial basis functions and their applicability for regional gravity field representation on the sphere. GEM-Int J Geomath 4:67–96. https://doi.org/10.1007/s13137-012-0046-1

Bucha B, Bezděk A, Sebera J, Janák J (2015) Global and regional gravity field determination from GOCE kinematic orbit by means of spherical radial basis functions. Surv Geophys 36(6):773–801. https://doi.org/10.1007/s10712-015-9344-0

Bucha B, Janák J, Papčo J, Bezděk A (2016) High-resolution regional gravity field modelling in a mountainous area from terrestrial gravity data. Geophys J Int 207:949–966. https://doi.org/10.1093/gji/ggw311

Childers VA, Bell RE, Brozena JM (1999) Airborne gravimetry: an investigation of filtering. Geophysics 64:61–69. https://doi.org/10.1190/1.1444530

Drewes H, Kuglitsch F, Ádám J, Rózsa S (2016) The geodesists' handbook 2016. J Geod 90:907–1205. https://doi.org/10.1007/s00190-016-0948-z

Eicker A (2008) Gravity field refinement by radial basis functions from in-situ satellite data. PhD thesis, Universität Bonn

Eriksson P (2000) Analysis and comparison of two linear regularization methods for passive atmospheric observations. J Geophys Res Atmos 105(D14):18157–18167. https://doi.org/10.1029/2000JD900172

Foroughi I, Vaníček P, Kingdon RW, Goli M, Sheng M, Afrasteh Y, Novák P, Santos MC (2019) Sub-centimetre geoid. J Geod 93:849–868. https://doi.org/10.1007/s00190-018-1208-1

Forsberg R (1993) Modelling the fine-structure of the geoid: methods, data requirements and some results. Surv Geophys 14(4–5):403–418. https://doi.org/10.1007/BF00690568

Forsberg R, Olesen AV (2010) Airborne gravity field determination. In: Xu G (ed) Sciences of geodesy-I. Springer, Berlin, pp 83–104. https://doi.org/10.1007/978-3-642-11741-1_3

Forsberg R, Tscherning CC (1981) The use of height data in gravity field approximation by collocation. J Geophys Res Solid Earth 86(B9):7843–7854. https://doi.org/10.1029/JB086iB09p07843

Forsberg R, Olesen A, Keller K (2001) Airborne gravity survey of the North Greenland continental shelf. In: Sideris MG (ed) Gravity, geoid and geodynamics 2000. Springer, Berlin, pp 235–240

Forsberg R, Ses S, Alshamsi A, Din AH (2012) Coastal geoid improvement using airborne gravimetric data in the United Arab Emirates. Int J Phys Sci 7:6012–6023. https://doi.org/10.5897/IJPS12.413

Förste C, Bruinsma S, Abrikosov O, Lemoine JM, Marty JC, Flechtner F, Balmino G, Barthelmes F, Biancale R (2014) EIGEN-6C4-The latest combined global gravity field model including GOCE data up to degree and order 2190 of GFZ Potsdam and GRGS Toulouse. https://doi.org/10.5880/icgem.2015.1

Freeden W, Michel V (2004) Multiscale potential theory: with applications to geoscience. Birkhäuser, Basel

Freeden W, Gervens T, Schreiner M (1998) Constructive approximation on the sphere with applications to geomathematics. Oxford University Press on Demand, New York

Golub GH, Heath M, Wahba G (1979) Generalized cross-validation as a method for choosing a good ridge parameter. Technometrics 21:215–223. https://doi.org/10.2307/1268518

GRAV-D Science Team (2017) GRAV-D airborne gravity data user manual. https://www.ngs.noaa.gov/GRAV-D/data/NGS_GRAV-D_General_Airborne_Gravity_Data_User_Manual_v2.1.pdf

GRAV-D Science Team (2018) Block MS05 (Mountain South 05); GRAV-D airborne gravity data user manual. https://www.ngs.noaa.gov/GRAV-D/data_ms05.shtml

Hansen PC (1990) Truncated singular value decomposition solutions to discrete ill-posed problems with ill-determined numerical rank. SIAM J Sci Stat Comput 11:503–518. https://doi.org/10.1137/0911028

Hansen PC, O'Leary DP (1993) The use of the L-curve in the regularization of discrete ill-posed problems. SIAM J Sci Comput 14(6):1487–1503. https://doi.org/10.1137/0914086

Heiskanen WA, Moritz H (1967) Physical geodesy. W.H. Freeman and Company, San Francisco

Hirt C (2010) Prediction of vertical deflections from high-degree spherical harmonic synthesis and residual terrain model data. J Geod 84:179–190. https://doi.org/10.1007/s00190-009-0354-x

Hirt C, Featherstone W, Marti U (2010) Combining EGM2008 and SRTM/DTM2006.0 residual terrain model data to improve quasi-

geoid computations in mountainous areas devoid of gravity data. J Geod 84:557–567. https://doi.org/10.1007/s00190-010-0395-1
Hirt C, Kuhn M, Claessens S, Pail R, Seitz K, Gruber T (2014) Study of the Earth's short-scale gravity field using the ERTM2160 gravity model. Comput Geosci 73:71–80. https://doi.org/10.1016/j.cageo.2014.09.001
Ihde J, Sánchez L, Barzaghi R, Drewes H, Foerste C, Gruber T, Liebsch G, Marti U, Pail R, Sideris M (2017) Definition and proposed realization of the International Height Reference System (IHRS). Surv Geophys 38:549–570. https://doi.org/10.1007/s10712-017-9409-3
Jiang T, Wang YM (2016) On the spectral combination of satellite gravity model, terrestrial and airborne gravity data for local gravimetric geoid computation. J Geod 90:1405–1418. https://doi.org/10.1007/s00190-016-0932-7
Klees R, Tenzer R, Prutkin I, Wittwer T (2008) A data-driven approach to local gravity field modelling using spherical radial basis functions. J Geod 82:457–471. https://doi.org/10.1007/s00190-007-0196-3
Klees R, Slobbe D, Farahani H (2018) A methodology for least-squares local quasi-geoid modelling using a noisy satellite-only gravity field model. J Geod 92:431–442. https://doi.org/10.1007/s00190-017-1076-0
Koch KR (1990) Bayesian inference with geodetic applications. Springer, Berlin
Koch KR (1999) Parameter estimation and hypothesis testing in linear models. Springer, Berlin
Koch KR, Kusche J (2002) Regularization of geopotential determination from satellite data by variance components. J Geod 76:259–268. https://doi.org/10.1007/s00190-002-0245-x
Koop R (1993) Global gravity field modelling using satellite gravity gradiometry. Nederlandse Commissie voor Geodesie, Delft
Li X (2018) Using radial basis functions in airborne gravimetry for local geoid improvement. J Geod 92(5):471–485. https://doi.org/10.1007/s00190-017-1074-2
Lieb V (2017) Enhanced regional gravity field modeling from the combination of real data via MRR. PhD thesis, Technische Universität München
Lieb V, Bouman J, Dettmering D, Fuchs M, Schmidt M (2015) Combination of GOCE gravity gradients in regional gravity field modelling using radial basis functions. In: Sneeuw N, Novák P, Crespi M, Sansò F (eds) VIII Hotine–Marussi symposium on mathematical geodesy. Springer, Berlin, pp 101–108. https://doi.org/10.1007/1345_2015_71
Lieb V, Schmidt M, Dettmering D, Börger K (2016) Combination of various observation techniques for regional modeling of the gravity field. J Geophys Res Solid Earth 121:3825–3845. https://doi.org/10.1002/2015JB012586
Liu Q, Schmidt M, Pail R, Willberg M (2020) Determination of the regularization parameter to combine heterogeneous observations in regional gravity field modeling. Remote Sens 12(10):1617. https://doi.org/10.3390/rs12101617
Moritz H (1980) Advanced physical geodesy. Herbert Wichmann Verlag, Kalsruhe
Moritz H (2000) Geodetic reference system 1980. J Geod 74:128–133. https://doi.org/10.1007/s001900050278
Naeimi M (2013) Inversion of satellite gravity data using spherical radial base functions. PhD thesis, Leibniz Universität Hannover
Naeimi M, Flury J, Brieden P (2015) On the regularization of regional gravity field solutions in spherical radial base functions. Geophys J Int 202:1041–1053. https://doi.org/10.1093/gji/ggv210
NGS (2012) Technical details for GEOID12/12A/12B. https://www.ngs.noaa.gov/GEOID/GEOID12B/GEOID12B_TD.shtml
Olesen AV, Andersen OB, Tscherning CC (2002) Merging of airborne gravity and gravity derived from satellite altimetry: test cases along the coast of Greenland. Stud Geophys Geod 46(3):387–394. https://doi.org/10.1023/A:1019577232253
Pail R, Bruinsma S, Migliaccio F, Förste C, Goiginger H, Schuh WD, Höck E, Reguzzoni M, Brockmann JM, Abrikosov O et al (2011) First GOCE gravity field models derived by three different approaches. J Geod 85:819. https://doi.org/10.1007/s00190-011-0467-x
Pail R, Fecher T, Barnes D, Factor J, Holmes S, Gruber T, Zingerle P (2018) Short note: the experimental geopotential model XGM2016. J Geod 92:443–451. https://doi.org/10.1007/s00190-017-1070-6
Pavlis N, Holmes S, Kenyon S, Factor J (2013) Correction to "the development and evaluation of the Earth Gravitational Model 2008 (EGM2008)". J Geophys Res Solid Earth 118:2633–2633. https://doi.org/10.1002/jgrb.50167
Pavlis NK, Holmes SA, Kenyon SC, Factor JK (2012) The development and evaluation of the earth gravitational model 2008 (EGM2008). J Geophys Res Solid Earth. https://doi.org/10.1029/2011JB008916
Petit G, Luzum B (2010) IERS conventions (2010). Tech. rep., Verlag des Bundesamts für Kartographie und Geodäsie, Frankfurt am Main. https://www.iers.org/IERS/EN/Publications/TechnicalNotes/tn36.html
Plag HP, Rothacher M, Pearlman M, Neilan R, Ma C (2009) The global geodetic observing system. In: Satake K (ed) Advances in geosciences: solid earth (SE), vol 13. World Scientific, Singapore, pp 105–127. https://doi.org/10.1142/9789812836182_2008
Reuter R (1982) Über Integralformeln der Einheitssphäre und harmonische Splinefunktionen. PhD thesis, RWTH Aachen University
Rexer M, Hirt C, Claessens S, Tenzer R (2016) Layer-based modelling of the Earth's gravitational potential up to 10-km scale in spherical harmonics in spherical and ellipsoidal approximation. Surv Geophys 37:1035–1074. https://doi.org/10.1007/s10712-016-9382-2
Rummel R (2012) Height unification using GOCE. J Geod Sci 2:355–362. https://doi.org/10.2478/v10156-011-0047-2
Rummel R, Balmino G, Johannessen J, Visser P, Woodworth P (2002) Dedicated gravity field missions-principles and aims. J Geodyn 33:3–20. https://doi.org/10.1016/S0264-3707(01)00050-3
Saleh J, Li X, Wang Y, Roman D, Smith D (2013) Error analysis of the NGS' surface gravity database. J Geod 87:203–221. https://doi.org/10.1007/s00190-012-0589-9
Sánchez L (2012) Towards a vertical datum standardisation under the umbrella of global geodetic observing system. J Geod Sci 2:325–342. https://doi.org/10.2478/v10156-012-0002-x
Sánchez L, Sideris MG (2017) Vertical datum unification for the International Height Reference System (IHRS). Geophys J Int 209:570–586. https://doi.org/10.1093/gji/ggx025
Sánchez L, Cunderlík R, Dayoub N, Mikula K, Minarechová Z, Šíma Z, Vatrt V, Vojtíšková M (2016) A conventional value for the geoid reference potential W_0. J Geod 90:815–835. https://doi.org/10.1007/s00190-016-0913-x
Sánchez L, Agren J, Huang J, Wang Y, Forsberg R (2018) Basic agreements for the computation of station potential values as IHRS coordinates, geoid undulations and height anomalies within the Colorado 1 cm geoid experiment. https://ihrs.dgfi.tum.de/fileadmin/JWG_2015/Colorado_Experiment_Basic_req_V0.5_Oct30_2018.pdf
Sánchez L, Ågren J, Huang J, Wang Y, Mäkinen J, Pail R, Barzaghi R, Vergos G, Ahlgren K, Liu Q (2020) Strategy for the realisation of the International Height Reference System (IHRS). J Geod (under review)
Schmidt M, Han SC, Kusche J, Sanchez L, Shum C (2006) Regional high-resolution spatiotemporal gravity modeling from GRACE data using spherical wavelets. Geophys Res Lett. https://doi.org/10.1029/2005GL025509
Schmidt M, Fengler M, Mayer-Gürr T, Eicker A, Kusche J, Sánchez L, Han SC (2007) Regional gravity modeling in terms of spherical

base functions. J Geod 81:17–38. https://doi.org/10.1007/s00190-006-0101-5

Schreiner M (1999) A pyramid scheme for spherical wavelets. Tech. rep., Technische Universität Kaiserslautern. https://kluedo.ub.uni-kl.de/frontdoor/index/index/docId/605

Shih HC, Hwang C, Barriot JP, Mouyen M, Corréia P, Lequeux D, Sichoix L (2015) High-resolution gravity and geoid models in Tahiti obtained from new airborne and land gravity observations: data fusion by spectral combination. Earth Planets Space 67:124. https://doi.org/10.1186/s40623-015-0297-9

Sjöberg L (2005) A discussion on the approximations made in the practical implementation of the remove-compute-restore technique in regional geoid modelling. J Geod 78:645–653. https://doi.org/10.1007/s00190-004-0430-1

Sjöberg LE (2003) A computational scheme to model the geoid by the modified Stokes formula without gravity reductions. J Geod 77(7–8):423–432. https://doi.org/10.1007/s00190-003-0338-1

Sjöberg LE (2010) A strict formula for geoid-to-quasigeoid separation. J Geod 84:699–702. https://doi.org/10.1007/s00190-010-0407-1

Slobbe C, Klees R, Farahani HH, Huisman L, Alberts B, Voet P, Doncker FD (2019) The impact of noise in a GRACE/GOCE global gravity model on a local quasi-geoid. J Geophys Res Solid Earth 124(3):3219–3237. https://doi.org/10.1029/2018JB016470

Tapley BD, Bettadpur S, Watkins M, Reigber C (2004) The gravity recovery and climate experiment: mission overview and early results. Geophys Res Lett. https://doi.org/10.1029/2004GL019920

Torge W (1989) Gravimetry. Walter de Gruyter, Berlin

Tscherning CC (2013) Geoid determination by 3D least-squares collocation. In: Sansò F, Sideris M (eds) Geoid determination. Lecture notes in earth system sciences. Springer, Berlin, pp 311–336. https://doi.org/10.1007/978-3-540-74700-0_7

Wang Y, Sánchez L, Ågren J, Huang J, Forsberg R, Abd-Elmotaal H, Barzaghi R, Bašić T, Carrion D, Claessens S, Erol B, Erol S, Filmer M, Grigoriadis V, Isik M, Jiang T, Koç Ö, Li X, Ahlgren K, Krcmaric J, Liu Q, Matsuo K, Natsiopoulos D, Novák P, Pail R, Pitonák M, Schmidt M, Varga M, Vergos G, Véronneau M, Willberg M, Zingerle P (2020) Colorado geoid computation experiment - overview and summary. J Geod (under review)

Wittwer T (2009) Regional gravity field modelling with radial basis functions. PhD thesis, Netherlands Geodetic Commission

Wu Y, Luo Z, Chen W, Chen Y (2017a) High-resolution regional gravity field recovery from Poisson wavelets using heterogeneous observational techniques. Earth Planets Space 69:34. https://doi.org/10.1186/s40623-017-0618-2

Wu Y, Zhou H, Zhong B, Luo Z (2017b) Regional gravity field recovery using the GOCE gravity gradient tensor and heterogeneous gravimetry and altimetry data. J Geophys Res Solid Earth 122(8):6928–6952. https://doi.org/10.1002/2017JB014196

A3 Publication III

Reference

Liu, Q., Schmidt, M., and Sánchez, L. (2022). **Combination of different observation types through a multi-resolution representation of the regional gravity field using the pyramid algorithm and parameter estimation**. *Journal of Geodesy*, 96, 80. https://doi.org/10.1007/s00190-022-01670-5

Copyright

This work has been published in Journal of Geodesy, with open access. The publication is available under the creative commons license. The copyright remains with the authors.

Declaration of own contribution

The overall own contribution of Qing Liu to P-III is estimated to be 84%, which is a weighted average of the five contribution parts listed in the Table 3.

Table 3: Contribution of Qing Liu to P-III

	Weight	Estimated contribution
Ideas and conceptual design	30%	80%
Realization and computation	10%	90%
Analysis and discussion	30%	80%
Figure compilation	10%	95%
Manuscript writing	20%	85%
Overall		**84%**

Confirmation by the Co-authors

I hereby confirm the correctness of the declaration of own contribution by Qing Liu for the publication

Liu, Q., Schmidt, M., Sánchez, L. (2022) Combination of different observation types through a multi-resolution representation of the regional gravity field using the pyramid algorithm and parameter estimation. *Journal of Geodesy*, in review

Michael Schmidt

Deutsches Geodätisches Forschungsinstitut der Technischen Universität München (DGFI-TUM), Germany

Signature: ..... Date: 24.05.2022

Laura Sánchez

Deutsches Geodätisches Forschungsinstitut der Technischen Universität München (DGFI-TUM), Germany

Signature: ..... Date: 24.05.2022

Journal of Geodesy (2022) 96:80
https://doi.org/10.1007/s00190-022-01670-5

ORIGINAL ARTICLE

Combination of different observation types through a multi-resolution representation of the regional gravity field using the pyramid algorithm and parameter estimation

Qing Liu[1] · Michael Schmidt[1] · Laura Sánchez[1]

Received: 17 May 2021 / Accepted: 24 September 2022 / Published online: 18 October 2022
© The Author(s) 2022

Abstract
The optimal combination of different types of gravity observations is the key to obtaining a high-resolution and high-precision regional gravity model. Current studies based on spherical radial basis functions (SRBFs) majorly consider a single-level approach for data combination. Despite the promising results reported in numerous publications, it has been suspected that the single-level model might be biased towards high-resolution measurements. Instead, a multi-resolution representation (MRR) can be applied to further take into consideration the varying spectral sensitivities of different observation techniques. In this study, we develop a new MRR scheme based on the pyramid algorithm and sequential parameter estimation. We propose strategies to solve the challenges in the practical application of the pyramid algorithm, and this study represents its first successful realization in regional gravity field modeling. The modeling results based on both simulated and real gravity data show that either the single-level approach or the MRR without pyramid algorithm is able to capture gravity information from lower resolution measurements as sufficient as our newly developed MRR algorithm. In the simulated case, the RMS error w.r.t. the validation data obtained by the MRR based on the pyramid algorithm decreases by 50% and 35%, in comparison to that of the single-level model and the MRR without pyramid algorithm, respectively. In the real case, the improvement achieved by the MRR based on the pyramid algorithm is 35% and 23% in the onshore area, and it reaches 63% and 57% in the offshore area, compared to the single-level approach and the MRR without pyramid algorithm, respectively.

Keywords Heterogeneous data combination · Multi-resolution representation · Pyramid algorithm · Regional gravity filed modeling · Spherical radial basis functions

1 Introduction

Regional gravity field modeling is an important topic in geodesy; it plays an essential role for applications in geophysics and physical height system realization. A high-resolution and high-precision geoid model derived from regional gravity field modeling is the key to the realization of the International Height Reference System (IHRS, Sánchez et al. 2021). In the last decades, spherical radial basis functions (SRBFs, see e.g., Freeden et al. 1998; Freeden and Michel 2004; Schmidt et al. 2007) have been widely used for regional gravity field modeling. Thanks to their localizing features in both the spectral and the spatial domain, SRBFs are an appropriate approach to consider the heterogeneity of different gravity data types with varying spectral and spatial resolutions.

In regional gravity field modeling, local high-resolution gravity measurements (e.g., terrestrial, airborne, and ship-borne gravity data) are usually combined with medium-resolution data (e.g., inferred from satellite altimetry missions) and low-resolution global data provided by dedicated satellite gravity missions, such as the Gravity Recovery and Climate Experiment (GRACE, Tapley et al. 2004) and the Gravity Field and Steady-State Ocean Circulation Explorer (GOCE, Rummel et al. 2002). Each observation technique has different spectral sensitivities and varying data distribution. Thus, a data combination method that extracts the maximum gravity information from different measurements is required to ensure the best possible high-precision regional gravity model. Typically, the data combination based on

Qing Liu
qingqing.liu@tum.de

[1] Deutsches Geodätisches Forschungsinstitut der Technischen Universität München (DGFI-TUM), Arcisstrasse 21, 80333 Munich, Germany

SRBFs is implemented using a single-level approach (see, e.g., Bentel et al. 2013a, b; Lieb et al. 2016; Bucha et al. 2016; Wu et al. 2017a, b; Liu et al. 2020a, b). In this approach, different observation techniques are combined at the maximum degree of expansion, and their contributions to the final gravity model are determined by the relative weighting between each data set. This approach is straightforward, and promising modeling results have been reported in the aforementioned publications. However, the contribution of measurements with medium to low resolution (e.g., altimetry data, satellite gravity data) could be understated, since they are not sensitive at high spectral degrees. For instance, Klees et al. (2018) demonstrate that the single-scale model lacks the flexibility to deal with data sets of significantly different bandwidths, while Wu et al. (2018) state that the single-level approach may fail to extract the full information contained in the gravity data.

To take the spectral sensitivity of different observation techniques into consideration and to combine heterogeneous data by spectral weights, a spectral combination can be applied (see, e.g., Sjöberg 1981; Kern et al. 2003; Denker 2013). The spectral combination based on SRBFs can be realized through a multi-resolution representation (MRR). The MRR of the gravity field was initially proposed by Freeden et al. (1998), Freeden (1999), and Haagmans et al. (2002), and its realization has been investigated in the last two decades. The MRR is often associated with wavelet functions. Kusche et al. (1998) conclude that the spherical wavelet functions show outstanding properties in the medium frequency band, and they are thus recommended for modeling the medium wavelength part of the gravity field. Beylkin and Cramer (2002) present several multi-resolution gravity models and show their performance results. Fengler et al. (2007) set up an MRR approach based on GRACE data using the cubic polynomial (CuP) wavelets and show that they are an appropriate tool to investigate regional and temporal variations of the Earth's gravity field. Panet et al. (2011) introduce the iterative domain decomposition by extending the Poisson wavelet modeling approach (Holschneider et al. 2003) to combine the surface (land, marine and altimetry) gravity data with satellite gravity data. Bolkas et al. (2016) state that wavelet decomposition is a useful tool for fusing terrestrial gravity data with satellite and airborne data and show that the multiscale fused model is able to fill data gaps.

Schmidt et al. (2005, 2006, 2007) develop an MRR approach where the representation is decomposed into an expansion in terms of spherical harmonics for the long-wavelength part, and a number of frequency-dependent detail signals in terms of wavelets for the medium and high frequency parts. This MRR was applied for regional gravity field modeling by Lieb (2017) and Wu et al. (2018), where the coefficients for calculating the detail signals are estimated simultaneously at each resolution level, using all or selected data groups. However, if all observation types are used at each level, the corresponding detail signals are strongly correlated (Lieb 2017). If only specific data sets are used, large data gaps may occur, and the prior information is insufficient for filling these data gaps at higher resolution levels. This leads to large erroneous effects in the output signals. Consequently, Lieb (2017) recommends for future work the implementation of the pyramid algorithm (Freeden et al. 1998) to consider all available information by connecting the different levels. Klees et al. (2018) show that a two-scale (or multi-scale) model needs to be applied in combination with a sequential estimation of the scale-dependent coefficients. The sequential estimation can be realized by applying the pyramid algorithm, which determines the coefficients of the lower resolution levels sequentially from the coefficients of the higher level, by successive low-pass filtering.

Although the pyramid algorithm was proposed nearly two decades ago, its practical application based on parameter estimation has never been realized in regional gravity field modeling, until this study. This is due to the challenges of applying the pyramid algorithm in the regional case, as stated by Lieb (2017): (1) it is difficult to set up a proper low-pass filter matrix in the regional case, and (2) the margin size has to be adapted appropriately at each level to minimize edge effects. We come up with methods in this study to solve these difficulties: (1) a low-pass filter is newly introduced in case of using the Reuter grid; (2) the choice of the margin size and the setting up of the estimation model at each resolution level are characterized; (3) strategies for reducing edge effects in the calculated detail signals are proposed.

A new MRR scheme based on the pyramid algorithm is developed, as visualized in Fig. 1, the text in blue highlights the novelty of this work. One main innovation is the realization of the sequential parameter estimation in the MRR scheme. The coefficients are firstly estimated at the highest chosen resolution level I using only the high-resolution data set(s) 1, and they are used to compute the detail signal $\boldsymbol{G}_I$ by wavelet functions. Then, these estimated coefficients are transformed to the next lower level $I-1$ by applying a low-pass filtering, i.e., the pyramid algorithm using the proposed low-pass filter matrix $\boldsymbol{L}_{I-1}$. At the lower level $I-1$, the coefficient vector is updated by the lower-resolution data set(s) 2 introduced at this level. This updated coefficient vector is then used in combination with wavelet functions to calculate the detail signal $\boldsymbol{G}_{I-1}$. Continuing this process until the lowest level i' of the MRR, all data sets are introduced into the scheme at different resolution levels and the coefficient vectors as well as the detail signals are obtained. At each lower resolution level, the coefficients from the pyramid algorithm are combined directly with the new data set(s), through the parameter estimation procedure. In the two-scale model presented by Klees et al. (2018), the coefficients from the high-resolution level are used to generate a new pseudo

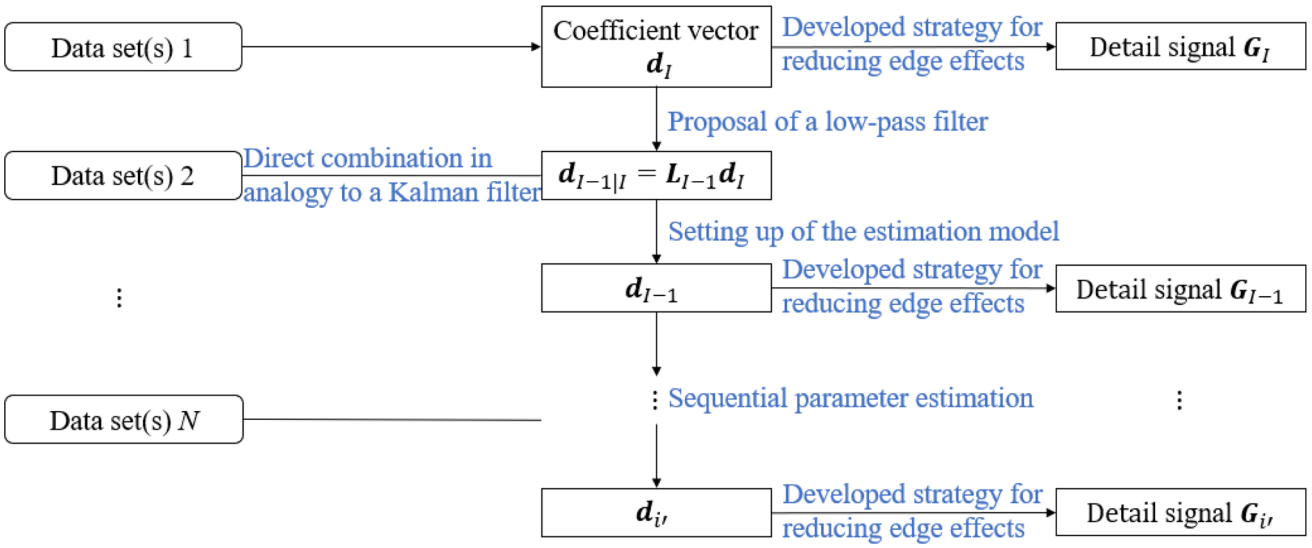


Fig. 1 The developed MRR scheme based on the pyramid algorithm. The text in blue highlights the novelty of this work

data set (with the same resolution as the low-resolution data set), which is then combined with the low-resolution data set to estimate the coefficients of the lower level. However, the authors point out that the high-resolution data set is required to have a larger area coverage than the low-resolution data set (due to edge effects), which frequently cannot be fulfilled when dealing with real data. In this study, we solve this limitation by the direct combination of the coefficient vector and the new data set(s), in analogy to a Kalman filter.

In this research, we additionally demonstrate that: (1) different observation types can be introduced into the evaluation model at the spectral level of their highest sensitivities, which makes it possible to benefit from the individual strengths of each data set optimally; (2) since all computations within the pyramid algorithm are based on linear equation systems (Schmidt et al. 2015), all covariance information can easily be calculated following the law of error propagation from the higher levels and serve as input for the lower levels; (3) as the number of required SRBFs decreases from the highest level to the lower levels, the design matrices of the lower-resolution data sets are now calculated with a smaller number of grid points, which reduces the computational effort significantly. We test the MRR based on the pyramid algorithm by using simulated data and then apply it to real data in different study areas. The modeling results are directly compared to those obtained from the single-level approach and the MRR without using the pyramid algorithm (where the coefficients are estimated independently at each level using all types of observations) in order to highlight the benefits of the MRR based on the pyramid algorithm.

This work is organized as follows: In Sect. 2, we introduce the fundamental concepts of the MRR based on SRBFs, the wavelet functions, and the pyramid algorithm. Section 3 explains the newly developed MRR procedure based on the sequential parameter estimation, and shows how the coefficient vector from the pyramid algorithm is updated by including new observations at the lower levels. Sections 4 and 5 present the performance of our approach based on simulated and real data, respectively. The model configuration is explained, and the developed strategy for reducing edge effects is demonstrated. The results are evaluated and discussed, and comparisons are made with both the single-level approach and the MRR without pyramid algorithm. Finally, Sect. 6 provides conclusions and outlook.

2 Multi-resolution representation

2.1 Spherical radial basis functions

In general, SRBFs are isotropic localizing functions centered at grid points P_k on a sphere Ω_R with radius R (Freeden et al. 1998; Schmidt et al. 2007), and can be defined by the Legendre series

$$B(\boldsymbol{x}, \boldsymbol{x}_k) = \sum_{n=0}^{n_{\max}} \frac{2n+1}{4\pi R^2} \left(\frac{R}{r}\right)^{n+1} B_n P_n(\boldsymbol{r}^T \boldsymbol{r}_k), \tag{1}$$

wherein $\boldsymbol{x} = r \cdot \boldsymbol{r}$ is the position vector of an arbitrary point $P(\varphi, \lambda, r)$, with latitude φ, longitude λ, and radial distance $r = |\boldsymbol{x}| = R + h'$; h' is the height of P over the sphere Ω_R; $\boldsymbol{r} = [\cos\varphi \cos\lambda, \cos\varphi \sin\lambda, \sin\varphi]^T$ is the corresponding unit vector. $\boldsymbol{x}_k = R \cdot \boldsymbol{r}_k$ is the position vector of a grid point P_k. P_n is the Legendre polynomial of degree n, which is a function of the spherical distance between the point P and the grid point P_k. $n_{\max}$ is the maximum degree of the

i	1	2	3	4	5	6	7	8	9	10	11	…
$n_i = 2^i - 1$	1	3	7	15	31	63	127	255	511	1023	2047	…
$\rho_i = \frac{\pi R}{n_i}$ [km]	20000	6667	2857	1333	645	317	157	78	39	20	10	…
			satellite gravimetry									
			satellite altimetry									
								terrestrial, air-/shipborne				

Fig. 2 Spectral degree n_i and spatial resolution ρ_i of each resolution level i in the MRR

expansion. B_n is the Legendre coefficients, which specify the shape of the SRBFs. In case of $B_n = 1$ for all degree values $n = 0, 1, \ldots, n_{\max}$, the SRBF is defined as the reproducing kernel $K_{\text{rep}}(\boldsymbol{x}, \boldsymbol{x}_k)$, which has the ability of the unique reproduction of a harmonic function. To be more specific, the convolution of a harmonic function $F(\boldsymbol{x})$ (band-limited with $n = 0, 1, \ldots, n' \leq n_{\max}$) with the reproducing kernel K_{rep} is equal to the original function (Schmidt et al. 2007), i.e.,

$$F(\boldsymbol{x}) = (K_{\text{rep}} * F)(\boldsymbol{x}). \tag{2}$$

Any gravity observation $y(\boldsymbol{x})$ can be represented as a series expansion in terms of the SRBFs, i.e.,

$$y(\boldsymbol{x}) - e(\boldsymbol{x}) = \sum_{k=1}^{K} d_k B(\boldsymbol{x}, \boldsymbol{x}_k) + s(\boldsymbol{x}), \tag{3}$$

where K and d_k are the number of grid points and the corresponding series coefficients, respectively. $s(\boldsymbol{x})$ is the truncation error, and $e(\boldsymbol{x})$ is the observation error. It is worth mentioning that the general expression (1) of the basis functions $B(\boldsymbol{x}, \boldsymbol{x}_k)$ needs to be adapted for describing different gravitational functionals (e.g., the gravity disturbance δg or the gravity anomaly Δg). A list of basis functions adapted to different functionals can be found in Koop (1993) and Liu et al. (2020a).

2.2 Multi-resolution representation

The fundamental idea of the MRR is to split a given input signal into a smoothed version and a number of detail signals by successive low-pass filtering (Schmidt et al. 2007). Following Schmidt et al. (2006), the MRR of the gravity functional $F(\boldsymbol{x})$ can be expressed as

$$F(\boldsymbol{x}) = \bar{F}(\boldsymbol{x}) + \sum_{i=i'}^{I} G_i(\boldsymbol{x}) + s(\boldsymbol{x}) \tag{4}$$

where $\bar{F}(\boldsymbol{x})$ is a reference model, i.e., usually the long-wavelength component from a global gravity model (GGM), and it is used as the background model within the remove-compute-restore (RCR, e.g., Forsberg 1993) procedure. $G_i(\boldsymbol{x})$ is the detail signal of resolution level i, and $s(\boldsymbol{x})$ is the truncation error.

To set up the resolution level i, the frequency domain needs to be discretized. Each resolution level defines a frequency band, and thus, includes a certain number of degree values. In this study, the upper boundary (maximum degree value) n_i of each level is defined as

$$n_i = 2^i - 1. \tag{5}$$

It is worth mentioning that the resolution levels can also be adapted differently, i.e., the base 2 in Eq. (5), which specifies the range of the frequency bands, can be chosen as a different number (see Schmidt et al. 2007 for more details). Figure 2 (cf. Lieb et al. 2016) visualizes the discretization of the frequency domain, and the relation between the resolution level i and its corresponding spectral degree n_i as well as spatial resolution ρ_i. The corresponding maximum spatial resolution of level i is $\rho_i = \pi R/n_i$, with R the Earth's radius. Gravity data obtained from different observation techniques can then be classified according to their spectral resolution. Terrestrial, airborne, and shipborne observations are high-resolution regional data, thus, they cannot be used to estimate the low-frequency part. Therefore, they should be combined with the medium-resolution satellite altimetry measurements, and the low-resolution satellite gravimetry data, such as GRACE and GOCE.

2.3 Wavelet functions

SRBFs (1) can act as high-pass, low-pass or band-pass filters, depending on the chosen Legendre coefficients B_n, and a harmonic function $F(\boldsymbol{x})$ can be filtered by it through a spherical convolution (Schmidt et al. 2007; Liu et al. 2020b). In case of using a band-limited SRBF, e.g., a spherical scaling function $B(\boldsymbol{x}, \boldsymbol{x}_k) =: \Phi_i(\boldsymbol{x}, \boldsymbol{x}_{k,i})$, which means the Legendre coefficient $B_n =: \phi_{n,i} > 0$ for degree $n = 0, 1, \ldots, n_{\max} =: 2^i - 1$ and $\phi_{n,i} = 0$ for degree $n > 2^i - 1$, the SRBF acts as a low-

pass filter. Based on the scaling function, a spherical wavelet function $\Psi_i(\boldsymbol{x}, \boldsymbol{x}_{k,i})$, which can be interpreted as a band-pass filter, is defined as

$$\begin{aligned}\Psi_i(\boldsymbol{x}, \boldsymbol{x}_{k,i}) &= \Phi_i(\boldsymbol{x}, \boldsymbol{x}_{k,i}) - \Phi_{i-1}(\boldsymbol{x}, \boldsymbol{x}_{k,i}) \\ &= \sum_{n=0}^{2^i-1} \frac{2n+1}{4\pi R^2} \left(\frac{R}{r}\right)^{n+1} \psi_{n,i} P_n(\boldsymbol{r}^T \boldsymbol{r}_{k,i})\end{aligned} \tag{6}$$

where $\boldsymbol{x}_{k,i}$ is the position vector of the grid point $P_{k,i}$ at resolution level i, and the Legendre coefficients $\psi_{n,i}$ are computed as

$$\psi_{n,i} = \phi_{n,i} - \phi_{n,i-1}. \tag{7}$$

The detail signal $G_i(\boldsymbol{x})$ of level i in Eq. (4) can then be defined in terms of the spherical wavelet function as

$$G_i(\boldsymbol{x}) = \sum_{k=1}^{K_i} d_{k,i} \Psi_i(\boldsymbol{x}, \boldsymbol{x}_{k,i}), \tag{8}$$

where K_i and $d_{k,i}$ are the number of grid points and the corresponding series coefficients, respectively, at the level i. As explained in Liu et al. (2020b), the coefficients $d_{k,i}$ do not depend on the choice of the SRBFs, as soon as the SRBFs are band-limited up to the same degree, i.e., their Legendre coefficients are equal to 0 for all degree values $n > 2^i - 1$. Thus, the same set of unknown coefficients $d_{k,i}$ at level i can be used with both the spherical scaling function and the spherical wavelet function of the same level. Also, it is possible to use different types of SRBFs in the analysis step (in which the unknown coefficients are estimated) and in the synthesis step (in which the estimated coefficients are used to calculate the output gravity models), respectively.

In this study, we use the following spherical scaling functions (see Schmidt et al. 2007; Lieb et al. 2016):

1. The Shannon function, which could be interpreted as the reproducing kernel (see Sect. 2.1), its Legendre coefficients are given by

$$\phi_{n,i}^{Sha} = \begin{cases} 1 & \text{for } n \in [0, 2^i - 1] \\ 0 & \text{else} \end{cases}. \tag{9}$$

2. The Blackman function, its Legendre coefficients are given by

$$\phi_{n,i}^{Bla} = \begin{cases} 1 & \text{for } n \in [0, 2^{i-1} - 1] \\ (A(n))^2 & \text{for } n \in [2^{i-1}, 2^i - 1] \\ 0 & \text{else} \end{cases}, \tag{10}$$

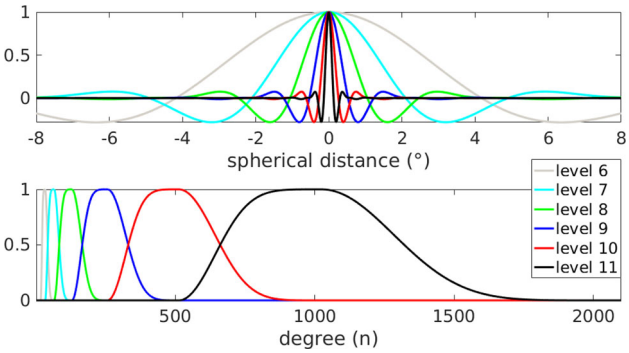


Fig. 3 The Blackman wavelet function at different resolution levels, in the spatial domain (upper, ordinate values are normed to 1), and in the spectral domain (bottom)

where

$$A(n) = \frac{21}{50} - \frac{1}{2}\cos\left(\frac{2\pi n}{2^i}\right) + \frac{2}{25}\cos\left(\frac{4\pi n}{2^i}\right). \tag{11}$$

The Shannon scaling function is used in the analysis step to estimate the unknown coefficients, and the Blackman wavelet function (with Legendre coefficients $\psi_{n,i}^{Bla} = \phi_{n,i}^{Bla} - \phi_{n,i-1}^{Bla}$) is applied in the synthesis step to calculate the detail signals at each level. The reason for using the Shannon function in the analysis step is to avoid the loss of spectral information. An SRBF with smoothing features, such as the Blackman function, is used in the synthesis step to reduce erroneous effects (Lieb et al. 2016; Liu et al. 2020b). Figure 3 visualizes the characteristics of the Blackman wavelet function in the spatial (upper plot) and the spectral domain (bottom plot) for different resolution levels. As we can see, the Blackman wavelet function has smoothing features. At the same time, it has strict band-pass features, i.e., only the Legendre coefficients within the spectral band $[2^{i-2}, 2^i)$ are not zero. The spectral weight, which is defined by the Legendre coefficients, increases from degree 2^{i-2} to 2^{i-1} and decreases from degree 2^{i-1} to 2^i. In the spectral domain, the corresponding frequency band becomes wider at higher resolution levels. In the spatial domain, with increasing resolution level i, the peak becomes sharper.

2.4 The pyramid algorithm

Freeden (1999) shows that the coefficients of neighboring resolution levels depend on each other linearly, and thus, can be computed successively. Therefore, the pyramid algorithm can be set up to determine the coefficients of the lower resolution levels from the coefficients of the higher level by a low-pass filtering. This procedure is based on a down sampling strategy, as the number of coefficients decreases at each level. With the pyramid algorithm, the coefficients at level i

$(i = i', i'+1, \ldots, I-2, I-1)$ can be expressed as

$$\boldsymbol{d}_{i|i+1} = \boldsymbol{L}_i \boldsymbol{d}_{i+1} \tag{12}$$

$$\boldsymbol{\Sigma}_{d_{i|i+1}} = \boldsymbol{L}_i \boldsymbol{\Sigma}_{d_{i+1}} \boldsymbol{L}_i^T \tag{13}$$

where $\boldsymbol{L}_i$ is a $K_i \times K_{i+1}$ low-pass filter matrix, transforming the $K_{i+1} \times 1$ coefficient vector $\boldsymbol{d}_{i+1}$ of the higher level $i+1$ to the $K_i \times 1$ coefficient vector $\boldsymbol{d}_{i|i+1}$ of the lower level i. $\boldsymbol{\Sigma}_{d_{i|i+1}}$ is the covariance matrix of $\boldsymbol{d}_{i|i+1}$ obtained from the covariance matrix $\boldsymbol{\Sigma}_{d_{i+1}}$ following the law of error propagation.

According to Schmidt et al. (2007), the low-pass filter matrix $\boldsymbol{L}_i$ can be decomposed as

$$\boldsymbol{L}_i = \boldsymbol{W}_i \boldsymbol{H}_i \tag{14}$$

where $\boldsymbol{H}_i$ is a $K_i \times K_{i+1}$ matrix containing the reproducing kernel $K_{\text{rep}}(\boldsymbol{x}_{k,i}, \boldsymbol{x}_{k,i+1})$ between the grid points $P_{k,i+1}$ $(k = 1, 2, \ldots, K_{i+1})$ of level $i+1$ and the grid points $P_{k,i}$ $(k = 1, 2, \ldots, K_i)$ of level i. $\boldsymbol{W}_i$ is the $K_i \times K_i$ diagonal matrix of the integration weights associated with the grid points $P_{k,i}$ of level i, and it depends on the implemented type of grid. Although the Reuter grid (Reuter 1982) is one of the most commonly used grids in regional gravity field modeling, there are no previous studies about how to define $\boldsymbol{W}_i$ for this type of grid. In this study, we develop a strategy to set up the corresponding integration weights, which read

$$w_i = \frac{4\pi R^2}{Z_i} \tag{15}$$

where Z_i is the total number of the Reuter grid points on the sphere at level i. Reuter grids are regarded as equidistributed point systems on the sphere (Fengler et al. 2004; Eicker 2008), and the corresponding integration weights are constant for each grid point.

3 Parameter estimation

In this paper, a new MRR scheme is developed based on the pyramid algorithm using sequential parameter estimation. The initial step of the MRR procedure is to estimate the unknown coefficient vector $\boldsymbol{d}_I = [d_{1,I}, d_{2,I}, \ldots, d_{K_I,I}]^T$ at the highest resolution level I using parameter estimation (Koch 1999; Schmidt et al. 2007). Assuming that P groups of observations are used at level I, the estimated coefficient vector $\widehat{\boldsymbol{d}}_I$ and the corresponding covariance matrix $D(\widehat{\boldsymbol{d}}_I) = \widehat{\boldsymbol{\Sigma}}_{d_I}$ can be obtained as (Liu et al. 2020a, b)

$$\widehat{\boldsymbol{d}}_I = \left(\sum_{p=1}^{P} \left(\frac{1}{\sigma_{p,I}^2} \boldsymbol{A}_{p,I}^T \boldsymbol{P}_{p,I} \boldsymbol{A}_{p,I} \right) + \frac{1}{\sigma_\mu^2} \boldsymbol{P}_\mu \right)^{-1} \left(\sum_{p=1}^{P} \left(\frac{1}{\sigma_{p,I}^2} \boldsymbol{A}_{p,I}^T \boldsymbol{P}_{p,I} \boldsymbol{y}_{p,I} \right) + \frac{1}{\sigma_\mu^2} \boldsymbol{P}_\mu \boldsymbol{\mu} \right) \tag{16}$$

$$\widehat{\boldsymbol{\Sigma}}_{d_I} = \left(\sum_{p=1}^{P} \left(\frac{1}{\sigma_{p,I}^2} \boldsymbol{A}_{p,I}^T \boldsymbol{P}_{p,I} \boldsymbol{A}_{p,I} \right) + \frac{1}{\sigma_\mu^2} \boldsymbol{P}_\mu \right)^{-1} \tag{17}$$

$\boldsymbol{y}_{p,I}$ is the observation vector of the p^{th} gravity data set used at level I, $\boldsymbol{P}_{p,I}$ is its positive definite weight matrix, and $\boldsymbol{A}_{p,I}$ is the design matrix, which contains the corresponding (adapted) scaling functions. $\boldsymbol{\mu}$ is the expectation vector of the coefficient vector $\boldsymbol{d}_I$, and $\boldsymbol{P}_\mu$ is its given positive definite weight matrix. $\sigma_{p,I}^2$ and σ_μ^2 are the corresponding variance factors for the observations $\boldsymbol{y}_{p,I}$ and the prior information $\boldsymbol{\mu}$, respectively.

After estimating the scaling coefficient vector and its covariance matrix, they are used to calculate the scaling coefficient vector $\boldsymbol{d}_{I-1|I}$ and the corresponding covariance matrix $\boldsymbol{\Sigma}_{d_{I-1|I}}$ of the next lower level, by applying the pyramid algorithm according to Eqs. (12) and (13). Then, instead of transforming the coefficient vector $\boldsymbol{d}_{I-1|I}$ directly to the next lower level $I-2$, which is the usual procedure in previous studies about the pyramid algorithm, it is updated by the gravity observations introduced at this level $I-1$. The updated coefficient vector $\boldsymbol{d}_{I-1}$ is then transformed to the level $I-2$ following Eqs. (12) and (13). Assuming that Q groups of observations $\boldsymbol{y}_{q,I-1}$ are introduced at level $I-1$, the combination of $\boldsymbol{y}_{q,I-1}$ and $\boldsymbol{d}_{I-1|I}$ is realized through the parameter estimation:

$$\begin{bmatrix} \boldsymbol{y}_{1,I-1} \\ \boldsymbol{y}_{2,I-1} \\ \vdots \\ \boldsymbol{y}_{Q,I-1} \\ \boldsymbol{d}_{I-1|I} \end{bmatrix} - \begin{bmatrix} \boldsymbol{e}_{1,I-1} \\ \boldsymbol{e}_{2,I-1} \\ \vdots \\ \boldsymbol{e}_{Q,I-1} \\ \boldsymbol{e}_d \end{bmatrix} = \begin{bmatrix} \boldsymbol{A}_{1,I-1} \\ \boldsymbol{A}_{2,I-1} \\ \vdots \\ \boldsymbol{A}_{Q,I-1} \\ \boldsymbol{I} \end{bmatrix} \cdot \boldsymbol{d}_{I-1} \quad \text{with}$$

$$D\left(\begin{bmatrix} \boldsymbol{y}_{1,I-1} \\ \boldsymbol{y}_{2,I-1} \\ \vdots \\ \boldsymbol{y}_{Q,I-1} \\ \boldsymbol{d}_{I-1|I} \end{bmatrix} \right) = \begin{bmatrix} \sigma_{1,I-1}^2 \boldsymbol{P}_{1,I-1}^{-1} & \boldsymbol{0} & \boldsymbol{0} & \cdots & \boldsymbol{0} \\ \boldsymbol{0} & \sigma_{2,I-1}^2 \boldsymbol{P}_{2,I-1}^{-1} & \vdots & \vdots & \vdots \\ \vdots & \boldsymbol{0} & \ddots & \vdots & \vdots \\ \vdots & \vdots & \vdots & \sigma_{Q,I-1}^2 \boldsymbol{P}_{Q,I-1}^{-1} & \boldsymbol{0} \\ \boldsymbol{0} & \boldsymbol{0} & \cdots & \boldsymbol{0} & \boldsymbol{\Sigma}_{d_{I-1|I}} \end{bmatrix} \tag{18}$$

The updated coefficient vector of level $I-1$ is estimated as

$$\widehat{\boldsymbol{d}}_{I-1} = \left(\sum_{q=1}^{Q} \left(\frac{1}{\sigma_{q,I-1}^2} \boldsymbol{A}_{q,I-1}^T \boldsymbol{P}_{q,I-1} \boldsymbol{A}_{q,I-1} \right) + \boldsymbol{\Sigma}_{d_{I-1|I}}^{-1} \right)^{-1} \left(\sum_{q=1}^{Q} \left(\frac{1}{\sigma_{q,I-1}^2} \boldsymbol{A}_{q,I-1}^T \boldsymbol{P}_{q,I-1} \boldsymbol{y}_{q,I-1} \right) + \boldsymbol{\Sigma}_{d_{I-1|I}}^{-1} \boldsymbol{d}_{I-1|I} \right) \tag{19}$$

with the covariance matrix

$$\widehat{\boldsymbol{\Sigma}}_{d_{I-1}} = \left(\sum_{q=1}^{Q} \left(\frac{1}{\sigma_{q,I-1}^2} \boldsymbol{A}_{q,I-1}^T \boldsymbol{P}_{q,I-1} \boldsymbol{A}_{q,I-1} \right) + \boldsymbol{\Sigma}_{d_{I-1|I}}^{-1} \right)^{-1} \tag{20}$$

The variance factors $\sigma_{1,I-1}^2, \sigma_{2,I-1}^2, \ldots, \sigma_{Q,I-1}^2$ of the data sets $\boldsymbol{y}_{1,I-1}, \boldsymbol{y}_{2,I-1}, \ldots, \boldsymbol{y}_{Q,I-1}$ are estimated by the variance component estimation (VCE, Koch and Kusche 2002).

The combination of $\boldsymbol{y}_{I-1} = [\boldsymbol{y}_{1,I-1}^T, \boldsymbol{y}_{2,I-1}^T, \ldots, \boldsymbol{y}_{Q,I-1}^T]^T$ and $\boldsymbol{d}_{I-1|I}$ can also be solved in analogy to the Kalman filter (Kalman 1960), where $\boldsymbol{d}_{I-1|I}$ and $\boldsymbol{\Sigma}_{d_{I-1|I}}$ can be regarded as the predicted state vector and the related predicted covariance matrix, respectively. Then the corrected state vector $\boldsymbol{d}_{I-1}$ as well as its covariance matrix $\boldsymbol{\Sigma}_{d_{I-1}}$ are computed by incorporating the involved measurements $\boldsymbol{y}_{I-1}$ at level $I-1$

$$\widehat{\boldsymbol{d}}_{I-1} = \boldsymbol{d}_{I-1|I} + \boldsymbol{K}_{I-1} \left(\boldsymbol{y}_{I-1} - \boldsymbol{A}_{I-1} \boldsymbol{d}_{I-1|I} \right) \tag{21}$$

$$\widehat{\boldsymbol{\Sigma}}_{d_{I-1}} = \left(\boldsymbol{I} - \boldsymbol{K}_{I-1} \boldsymbol{A}_{I-1} \right) \boldsymbol{\Sigma}_{d_{I-1|I}} \tag{22}$$

where $\boldsymbol{K}_{I-1}$ is the gain matrix

$$\boldsymbol{K}_{I-1} = \boldsymbol{\Sigma}_{d_{I-1|I}} \boldsymbol{A}_{I-1}^T \left(\boldsymbol{A}_{I-1} \boldsymbol{\Sigma}_{d_{I-1|I}} \boldsymbol{A}_{I-1}^T + \boldsymbol{\Sigma}_{y_{I-1}} \right)^{-1} \tag{23}$$

with $\boldsymbol{A}_{I-1} = [\boldsymbol{A}_{1,I-1}^T, \boldsymbol{A}_{2,I-1}^T, \ldots, \boldsymbol{A}_{Q,I-1}^T]^T$, and $\boldsymbol{\Sigma}_{y_{I-1}}$ being the covariance matrix of the observation vector $\boldsymbol{y}_{I-1}$. After taking into account the matrix identities, the solution delivered by Eqs. (21) and (22) ends up identical to Eqs. (19) and (20). We refer to Koch (1999) and Erdogan et al. (2020) for the details of the matrix identities.

In the synthesis step, the estimated coefficient vector $\widehat{\boldsymbol{d}}_{I-1}$ and its covariance matrix $\widehat{\boldsymbol{\Sigma}}_{d_{I-1}}$ are used to calculate the estimated detail signal $\widehat{\boldsymbol{G}}_{I-1}$ as well as its covariance matrix $\widehat{\boldsymbol{\Sigma}}_{G_{I-1}}$

$$\widehat{\boldsymbol{G}}_{I-1} = \boldsymbol{B}_{I-1} \widehat{\boldsymbol{d}}_{I-1} \tag{24}$$

$$\widehat{\boldsymbol{\Sigma}}_{G_{I-1}} = \boldsymbol{B}_{I-1} \widehat{\boldsymbol{\Sigma}}_{d_{I-1}} \boldsymbol{B}_{I-1}^T, \tag{25}$$

where $\widehat{\boldsymbol{G}}_{I-1} = [\widehat{G}_{I-1}(\boldsymbol{x}_1), \widehat{G}_{I-1}(\boldsymbol{x}_2), \ldots, \widehat{G}_{I-1}(\boldsymbol{x}_C)]^T$ is the vector of the estimated detail signal values at the computation points $\boldsymbol{x}_1, \boldsymbol{x}_2, \ldots, \boldsymbol{x}_C$ of the output gravity model. $\boldsymbol{B}_{I-1}$ is the design matrix, which contains the Blackman wavelet functions $\Psi_{I-1}(\boldsymbol{x}_c, \boldsymbol{x}_{k,I-1})$, as defined in Eq. (6), between the computation points of the gravity model and the grid points of level $I-1$.

The developed MRR procedure is summarized in Fig. 4: after determining the estimated coefficient vector $\widehat{\boldsymbol{d}}_I$ at the highest level I, it can be used to compute the detail signal $\widehat{\boldsymbol{G}}_I$ and to start the pyramid algorithm, i.e., to calculate the coefficient vector $\boldsymbol{d}_{I-1|I}$ of the next lower level. Then, this coefficient vector $\boldsymbol{d}_{I-1|I}$ is updated by introducing the observations at level $I-1$. Continuing this process until the lowest level of the MRR, the scaling coefficients and the detail signals of each level can be obtained, and thus, the final gravity functional is obtained according to Eq. (4). In this process, the input gravity data obtained from different observation techniques can be introduced into the estimation model at the resolution level of their highest sensitivities. Hence, they are able to contribute to the final model with maximum gravity information. Typically, the terrestrial data are used at the highest level. Then the shipborne or airborne data can be introduced at a level lower, followed by the altimetry data and the satellite gravity data, if applicable (see Fig. 2). Another advantage of including data by levels is that the high frequencies of the airborne data, which have large noise (Childers et al. 1999), could be excluded to guarantee a stable solution (Jiang and Wang 2016). Moreover, since the data are now introduced at the lower levels which require less grid points, the size of the design matrices, and consequently, the computation time is significantly reduced.

4 Validation with simulated data

4.1 Data

In the following, the MRR based on the pyramid algorithm is first realized and evaluated using simulated data to benefit from the availability of an accurate validation data set serving as the "truth". The study area is between 10° and 20° longitude and between 39° and 45° latitude (Fig. 5), covering parts of South Europe, the Adriatic Sea, and the Tyrrhenian Sea. Five types of gravity observations are used, namely terrestrial, airborne, and altimetry data, as well as satellite data from GOCE and GRACE. These data are simulated from the global gravity model GECO (Gilardoni et al. 2016), with the position of the observations provided by the IAG-ICCT (International Association of Geodesy - Inter Commission Committee on Theory) Joint Study Group (JSG) 0.3 ("Comparison of current methodologies in regional gravity field modeling"), running from 2011 to 2015. All observations

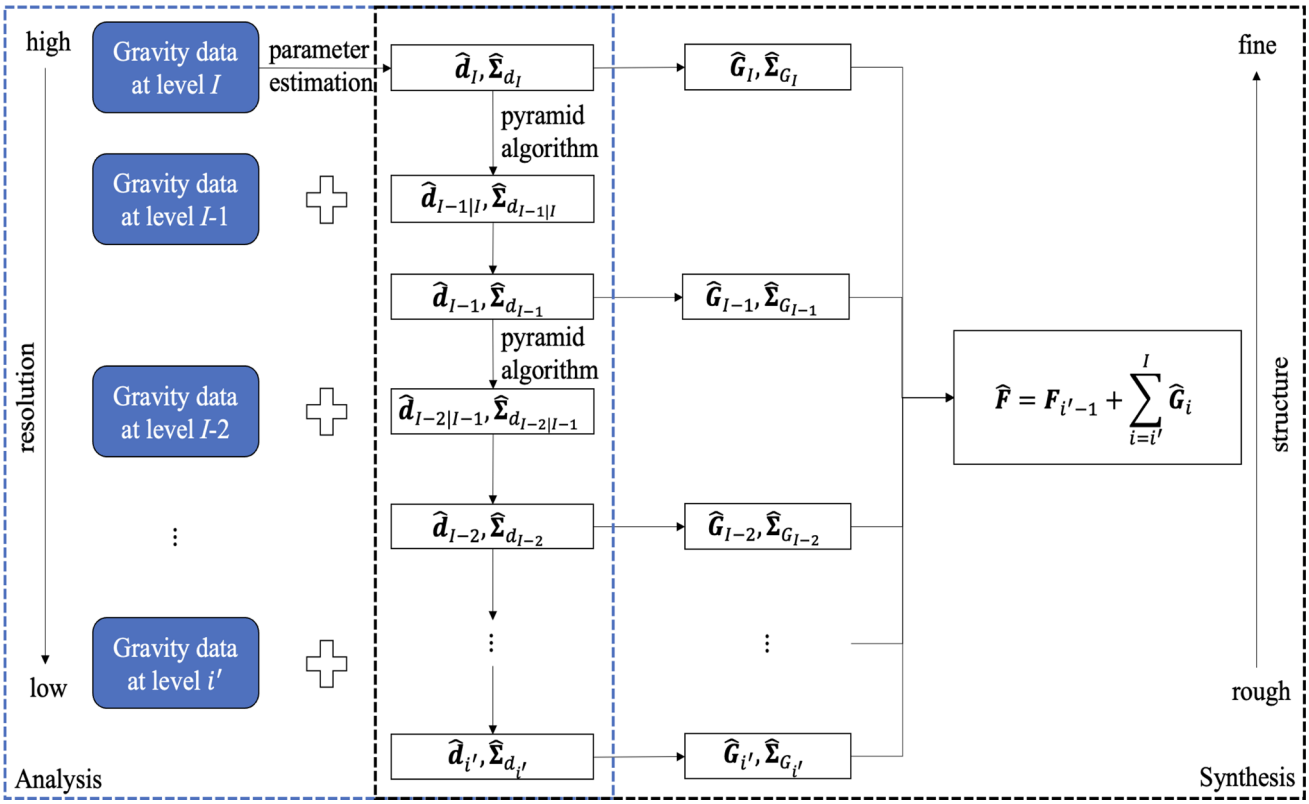


Fig. 4 The multi-resolution representation (MRR) based on the pyramid algorithm

are simulated in the sense of disturbing gravity field quantities, i.e., functionals of the disturbing potential. A detailed data description can be found in Liu et al. (2020a). The terrestrial observations (yellow dots in Fig. 5) are generated on a regular grid at the surface of the topography (DTM2006.0, Pavlis et al. 2006) with a grid spacing of $5'$ (which corresponds to a spatial resolution of 10 km). They are simulated up to spherical harmonic (SH) degree and order (d/o) 2190, in terms of the first order radial derivatives of the disturbing potential. The airborne data (red dots in Fig. 5) are located over the Adriatic Sea along synthetic flight tracks with an altitude of 2.5 km, generated in terms of the first order radial derivatives of the disturbing potential up to SH d/o 1600. The altimetry data (green dots in Fig. 5) are simulated up to SH d/o 1000 in terms of geoid height N, based on the real ground track of the altimetry mission Envisat (Extended Mission). The GOCE (grey dots in Fig. 5) and GRACE (blue dots in Fig. 5) data are simulated up to SH d/o 250, based on real satellite orbits with a time span of 61 days and one month, respectively. They are used in terms of the second-order radial derivatives of the disturbing potential for GOCE and the disturbing potential differences between the two satellites for GRACE. Observation noise is also generated and added to the gravity data, while the noise level is chosen according to the assumptions of the JSG 0.3. White noise with standard

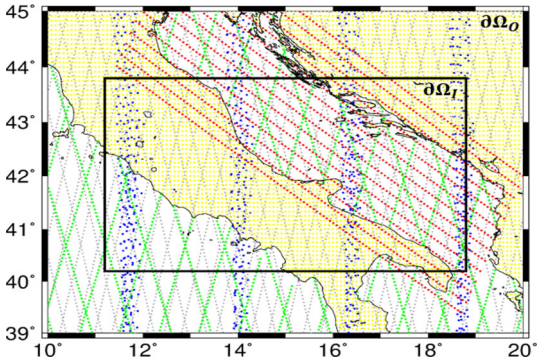


Fig. 5 The study area (observation area $\partial\Omega_O$) and simulated gravity data, including terrestrial (yellow dots), airborne (red dots), altimetry (green dots), GOCE (grey dots), and GRACE (blue dots) data. The black rectangle represents the investigation area $\partial\Omega_I$, where the final gravity model is calculated

deviations of 0.01 mGal, 1 mGal, and 0.03 m is added to the terrestrial, airborne, and altimetry data, respectively. Colored noise (Austen and Grafarend 2004; Naeimi 2013) is added to the satellite data of GOCE and GRACE, with standard deviations of 10 mE and $8 \cdot 10^{-4}$ m^2/s^2, respectively. Validation data are disturbing potential values simulated from GECO with a spatial resolution of $5' \times 5'$ and a maximum degree of 2190.

Table 1 The data sets involved at each resolution level i

i	1	2	3	4	5	6	7	8	9	10	11
data sets	GGM						GRACE	GOCE	altimetry	airborne	terrestrial

4.2 Model configuration

In this study case, the highest resolution level of MRR is chosen as $I = 11$, considering the spatial resolution of the data (see Fig. 2). The terrestrial data are used at the highest level to calculate the unknown coefficients of this level following Eq. (16), with the expectation vector $\boldsymbol{\mu}$ set to the zero vector and the weight matrix $\boldsymbol{P}_{p,I}$ and $\boldsymbol{P}_{\mu}$ set to be the identity matrix $\boldsymbol{I}$ (Lieb et al. 2016; Liu et al. 2020a, b). As listed in Table 1, the airborne data are included at level 10, the altimetry data are then added at level 9, followed by the GOCE observations at level 8 and GRACE observations at level 7. The long-wavelength component (up to level 6) is modeled by the GGM within the RCR procedure, i.e., the background model GECO up to spherical harmonic degree $n_6 = 2^6 - 1 = 63$ is removed from each observation, and then restored to the estimated model in the synthesis step. The single-level model and the MRR without the pyramid algorithm (see Sect. 1) are also calculated to serve as comparison scenarios. For the single-level model, all observations are combined at level 11, with the long-wavelength component (up to degree 63) modeled by GECO. For the MRR without pyramid algorithm, the unknown coefficients are estimated at each resolution level by combining all types of observations, and these coefficients are used to calculate the detail signals of each level. Wu et al. (2018) point out that the existing publications lack comparisons between the MRR and the single-level approach. Thus, the direct comparison of the single-level approach, the MRR without pyramid algorithm, and the MRR based on the pyramid algorithm, presented in this study fills this gap in current literature.

The Reuter grid is used, which generates a homogeneous coverage of equidistributed grid points on the sphere. The total number Z of Reuter grid points on the sphere is decided by a control parameter γ, and $\gamma + 1$ denotes the number of points along the meridian (Eicker 2008). In this study, we choose the parameter γ to be equal to the maximum spectral degree n_i of the expansion at each resolution level i (Wittwer 2009; Bentel et al. 2013b). In regional gravity field modeling, the computation area $\partial\Omega_C$, where the SRBFs are located, needs to be chosen larger than the observation area $\partial\Omega_O$, where the observations are given (Fig. 5), and $\partial\Omega_O$ needs to be larger than the investigation area $\partial\Omega_I$, where the final gravity models are computed, i.e., $\partial\Omega_C \supset \partial\Omega_O \supset \partial\Omega_I$. This hierarchy is necessary to mitigate edge effects. The margin size $\eta_{C,O}$ between the computation area $\partial\Omega_C$ and the observation area $\partial\Omega_O$ is determined following (Lieb et al. 2016), with

$$\eta_{C,O} = \frac{360^\circ}{n_i \cos(|\varphi_{\max}|)} \tag{26}$$

where $\varphi_{\max}$ is the maximum latitude value. The margin size is influenced by the shape of the SRBFs; they become wider at the lower resolution levels (i.e., when $n_{\max}$ is smaller, see Fig. 3), and thus, a larger margin size has to be chosen to reduce edge effects (Liu et al. 2020b). In this case, the $\eta_{C,O}$ is chosen as 0.3°, 0.6°, 1.2°, 2.4°, 4.8° for the levels 11, 10, 9, 8, 7, correspondingly (as shown in Fig. 6). Consequently, the number of unknown coefficients is decided by the generated Reuter grid points that are located inside the computation area $\partial\Omega_C$ of each resolution level (which amounts to $K_{11} = 7759$, $K_{10} = 2238$, $K_9 = 856$, $K_8 = 326$, and $K_7 = 157$). In the single-level approach, the margin size $\eta_{O,I}$ between the observation area $\partial\Omega_O$ and the investigation area $\partial\Omega_I$ is usually chosen the same as $\eta_{C,O}$. For the MRR, multiple values of $\eta_{C,O}$ are chosen for the different resolution levels. Numerical investigations in this work show that it is sufficient to choose the margin size $\eta_{O,I}$ as the median of the applied $\eta_{C,O}$ of each level, i.e., $\eta_{O,I} = 1.2^\circ$. Figure 5 (black rectangle) presents the corresponding investigation area $\partial\Omega_I$.

In case of the MRR based on the pyramid algorithm, only specific observation groups are used at the higher resolution levels, which means the involved observations do not have full coverage over the observation area $\partial\Omega_O$. This will cause strong edge effects at the border of the high-resolution observations in the calculated detail signals, and further contaminate the final gravity model. For example, at level 11, the terrestrial data are available only in the onshore area. Strong edge effects in $\boldsymbol{G}_{11}$ thus show up at the border of the terrestrial data coverage, i.e., near the coastal lines (as will be shown in Sect. 4.3). As pointed out by Lieb (2017), it is a challenging task to handle the edge effects properly in case of MRR, and it is one of the major difficulties in the practical realization of the pyramid algorithm. To address this issue, we develop a strategy in this study to reduce the edge effects in the calculated detail signals of each level. Besides the observation area $\partial\Omega_O$ (Fig. 5) and the investigation area $\partial\Omega_I$ (black rectangle in Fig. 5) for the whole study area, we also define $\partial\Omega_{O_i}$ and $\partial\Omega_{I_i}$ for each resolution level i when calculating the detail signals. To be more specific, $\partial\Omega_{O_i}$ depends on the data coverage of the observation groups involved at this level, and $\partial\Omega_{I_i}$ is adapted to $\partial\Omega_{I_i} = \partial\Omega_{O_i} \cap \partial\Omega_I$. As an example, $\partial\Omega_{O_{11}}$ is defined as the onshore areas in Fig. 5 since only terrestrial observations are involved at level 11. Consequently, $\partial\Omega_{I_{11}}$ (see Fig. 7) is adapted to the onshore areas within the investigation area $\partial\Omega_I$. The detail signals $\boldsymbol{G}_i$ of level i are then calculated within $\partial\Omega_{I_i}$.

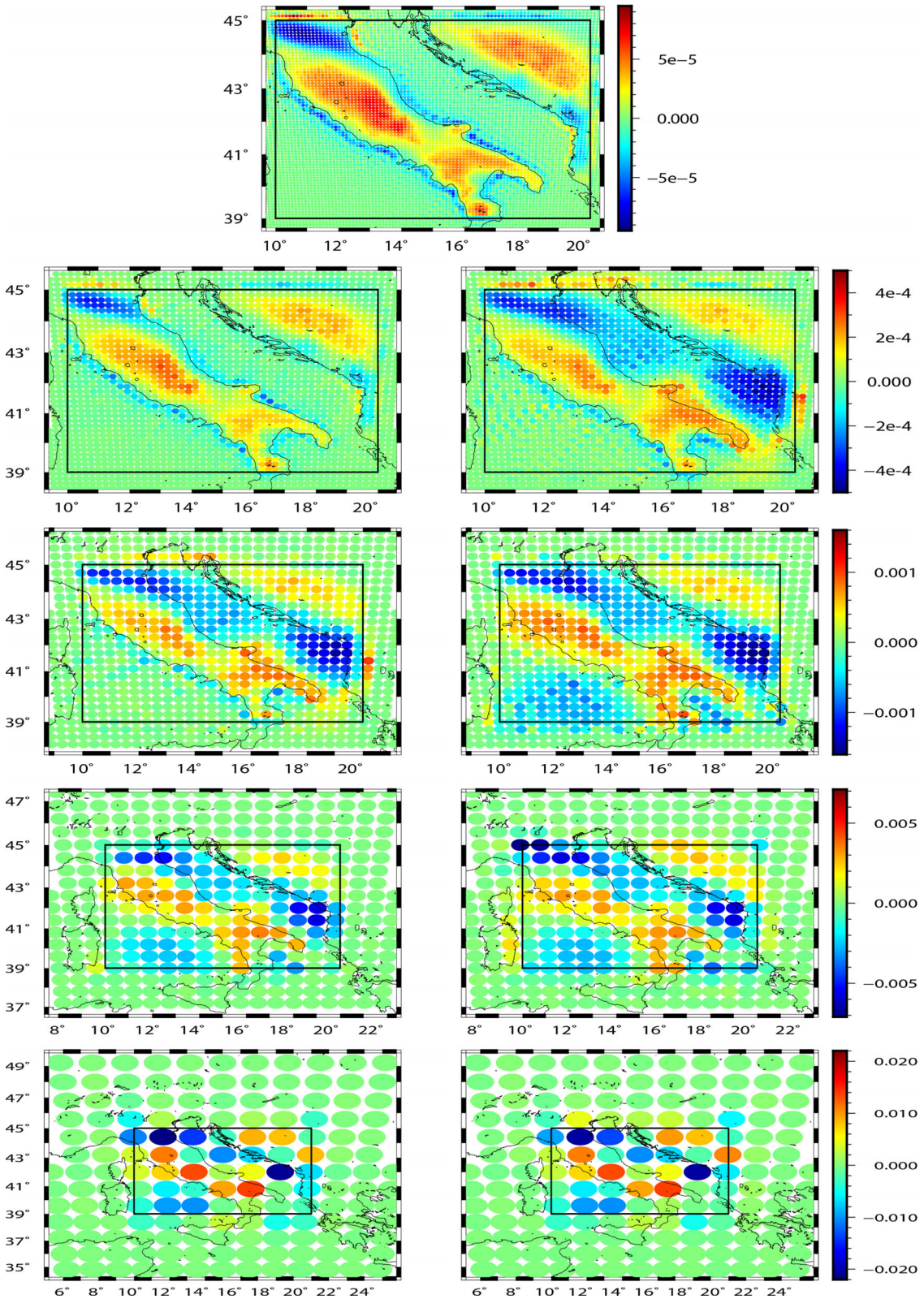


Fig. 6 The estimated scaling coefficients at level 11 (first row), and levels 10, 9, 8, 7 (second to fifth row). From the second to the fifth row, the left column represents the coefficients $\boldsymbol{d}_{i|i+1}$ estimated directly from the pyramid algorithm, and the right column represents the updated coefficients $\boldsymbol{d}_i$ after including the new data at this level (following the procedure explained in Sect. 3). The black rectangle inside each plot shows the observation area $\partial\Omega_O$

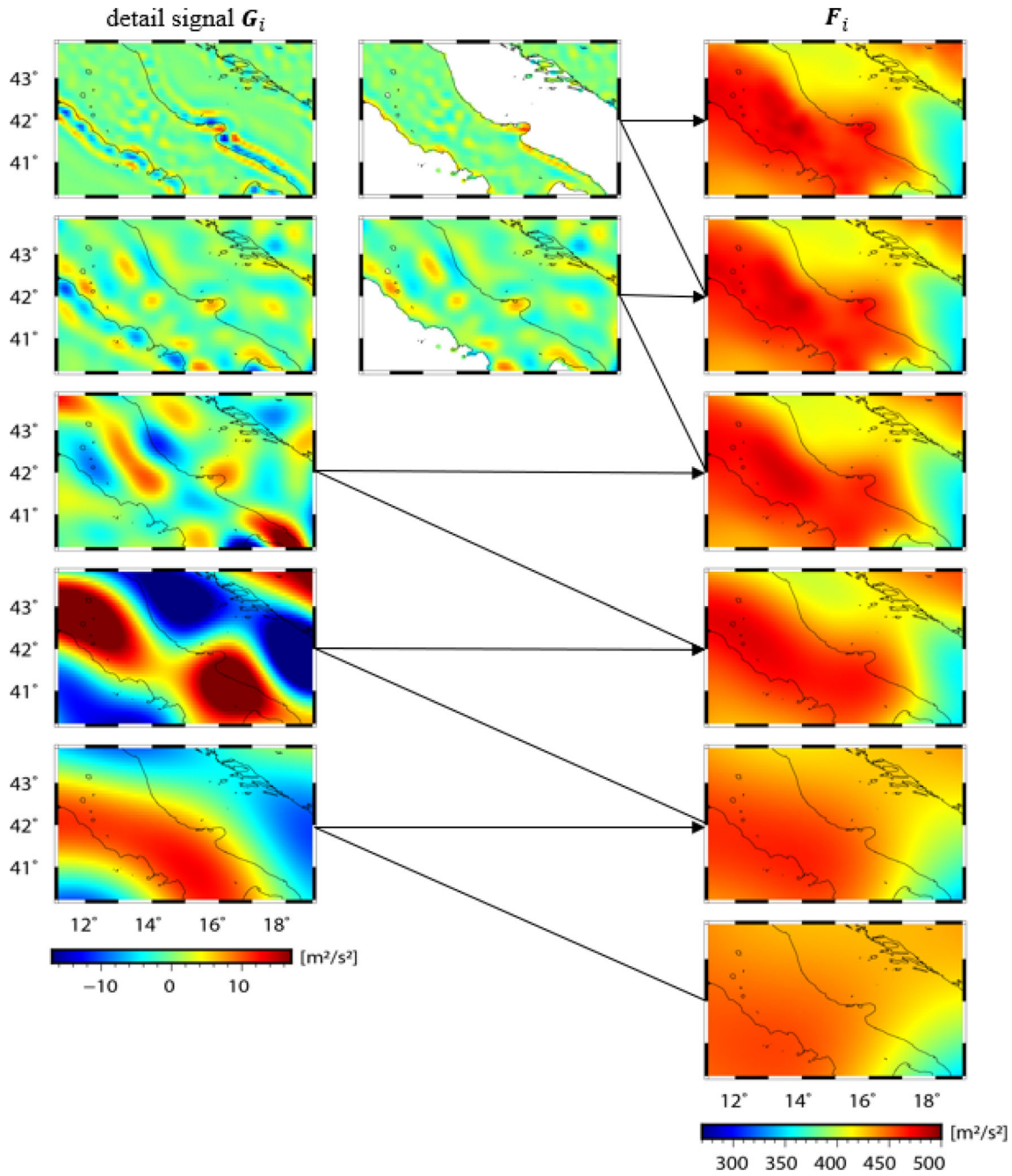


Fig. 7 The detail signal $\boldsymbol{G}_i$ of the MRR based on the pyramid algorithm before (left column) and after (mid column) adapting the investigation area $\partial\Omega_{I_i}$, as well as the modeled gravity signal (in terms of disturbing potential) $\boldsymbol{F}_{I'} = \bar{\boldsymbol{F}} + \sum_{i=7}^{I'} \boldsymbol{G}_i$ (right column) from level 11 (first row) to level 7 (fifth row), with $\bar{\boldsymbol{F}}$ (right column, last row) modeled from GECO

4.3 Modeling results and discussions

The estimated coefficients at each level are plotted in Fig. 6, and the black rectangle inside each plot represents the observation area $\partial\Omega_O$ (Fig. 5). From the first row (level 11) to the fifth row (level 7), the margin size $\eta_{C,O}$ increases and the number of unknown coefficients decreases. The top row shows the scaling coefficients $\boldsymbol{d}_{11}$ at level 11, which are estimated from the terrestrial observations only. Comparing the plot of $\boldsymbol{d}_{11}$ to Fig. 5, it is clear that the values of the coefficients are almost zero in the area where no terrestrial data exist, and larger absolute values are observed where these data are available. This shows that additional gravity information with respect to the background model is only captured

at the locations with terrestrial data coverage, which is reasonable (Liu et al. 2020b). The left plot at the second row shows the scaling coefficients $\boldsymbol{d}_{10|11}$ calculated directly from the pyramid algorithm, and the right one displays the updated coefficients $\boldsymbol{d}_{10}$ after including the airborne data at level 10. Comparing the two plots at level 10, we can see that the airborne observations insert additional gravity information in the region where they are located. They fill parts of the data gaps from the terrestrial data, and the gravity signals captured from the previous level (level 11) are preserved at the same time. At level 9 (third row), the same behavior as at level 10 can be observed, i.e., the altimetry data fill data gaps at the left bottom corner of the observation area, and meanwhile, the gravity signals from level 10 are kept. At level 8 (fourth row) and level 7 (fifth row), the satellite data which have even distributions are used. It can be observed that the right plots show darker colors (larger values) than the left ones inside the observation area $\partial\Omega_O$, which indicate the contribution of the GOCE and GRACE data at level 8 and level 7, respectively.

Figure 7 (left column) visualizes the detail signals $\boldsymbol{G}_i$ of the MRR based on the pyramid algorithm at each level, which show the spectral information contained in the corresponding frequency ranges (see Fig. 2). At level 11, the detail signal $\boldsymbol{G}_{11}$ captures gravity information only in onshore area where the terrestrial data are located. However, at the border of the terrestrial data, strong edge effects show up. The same is valid in the detail signal $\boldsymbol{G}_{10}$ of level 10, large edge effects occur at the border of the data coverage, i.e., in the coastal area of the Tyrrhenian Sea. We thus apply the strategy explained in Sect. 4.2 to reduce these edge effects by defining $\partial\Omega_{I_i}$, i.e., by setting $\partial\Omega_{I_{11}} = \partial\Omega_{O_{11}} \cap \partial\Omega_I$ and $\partial\Omega_{I_{10}} = \partial\Omega_{O_{10}} \cap \partial\Omega_I$. After level 9, the involved observations have full coverage over the observation area $\partial\Omega_O$ (i.e., $\partial\Omega_{I_i} = \partial\Omega_I$), and no edge effects are visible within $\partial\Omega_I$. Correspondingly, the new detail signals of level 11 and 10 after adapting $\partial\Omega_{I_i}$ are presented in Fig. 7 (mid column), and the edge effects are significantly reduced. Figure 7 (right column) shows the gravity signal $\boldsymbol{F}_{I'} = \bar{\boldsymbol{F}} + \sum_{i=7}^{I'} \boldsymbol{G}_i$ of each level. The gravity signal (in terms of disturbing potential) of level 6 ($\bar{\boldsymbol{F}}$, right column, last row) is the long wavelength component from the global gravity model GECO, which only contains very smooth information. When the resolution level increases from level 7 (fifth row) to level 11 (first row), more and more fine structures show up in both the detail signals and the gravity signals.

The final modeling result (Fig. 7 right column, first row) is evaluated by the validation data, and their difference is visualized in Fig. 8d. For comparison, the single-level model, the MRR without pyramid algorithm, and the MRR based on pyramid algorithm before adapting the $\partial\Omega_{I_i}$ are also computed, and their differences to the validation data are shown in Fig. 8a, b, and c, respectively. The corresponding statistics are listed in Table 2. As shown in Fig. 8a, the single-level model delivers small differences compared to the validation data in onshore regions, where the terrestrial data are available. However, in offshore regions with no terrestrial data coverage, the differences are quite large. This result demonstrates that the single-level approach majorly recovers gravity information from the terrestrial observations, and the contribution of other measurements which are sensitive to lower spectral bands is not captured sufficiently. It indicates that the single-level model is not able to benefit from all the observation types, as mentioned in the Introduction, and the MRR is necessary, especially in cases where the terrestrial data do not have large coverage over the study area. After applying the MRR, the differences w.r.t. the validation data in offshore regions decrease (see Fig. 8b), which indicates that the gravity information in lower-resolution observations are better extracted. The MRR without pyramid algorithm delivers an RMS error of 4.21 m^2/s^2, which is 23% smaller than the one given by the single-level approach. However, Fig. 8b still shows the same pattern as the single-level model, i.e., larger differences show up in the offshore regions compared to the onshore regions. Although the MRR (without pyramid algorithm) already gives better results than the single-level approach, it is not optimal. Indeed, Lieb (2017) points out that the detail signals of different levels become correlated when all the observation groups are used at each level and recommends the implementation of the pyramid algorithm as further development of the MRR approach.

In case of the MRR based on the pyramid algorithm, as shown in Fig. 8d, the differences between the calculated gravity model and the validation data do not show dependency on the distribution of certain types of observations, i.e., the offshore area does not show larger differences than the area with terrestrial data. It suggests that each observation type makes a contribution to the final result, and the MRR benefits from all the measurements. This statement is supported by the fact that the RMS value delivered by the MRR based on the pyramid algorithm decreases by 50% w.r.t. the one delivered by the single-level approach, and 35% w.r.t. that of the MRR without pyramid algorithm. The comparison between Fig. 8d and Fig. 8c shows the benefit of applying the proposed strategy for reducing edge effects, i.e., by adapting the investigation area $\partial\Omega_{I_i}$ at each level. The edge effects at the border (outside the coverage) of the terrestrial data are significantly reduced in Fig. 8d. The improvement achieved by applying this strategy is 21% in terms of RMS, w.r.t. the validation data. However, at the border (inside the coverage) of the terrestrial observations, the edge effects remain the same after adapting $\partial\Omega_{I_i}$, as also shown in the calculated detail signals at level 11 and level 10 (Fig. 7, mid column). Thus, a main challenge to be faced in future studies regarding the MRR based on the pyramid algorithm is to further reduce these edge effects.

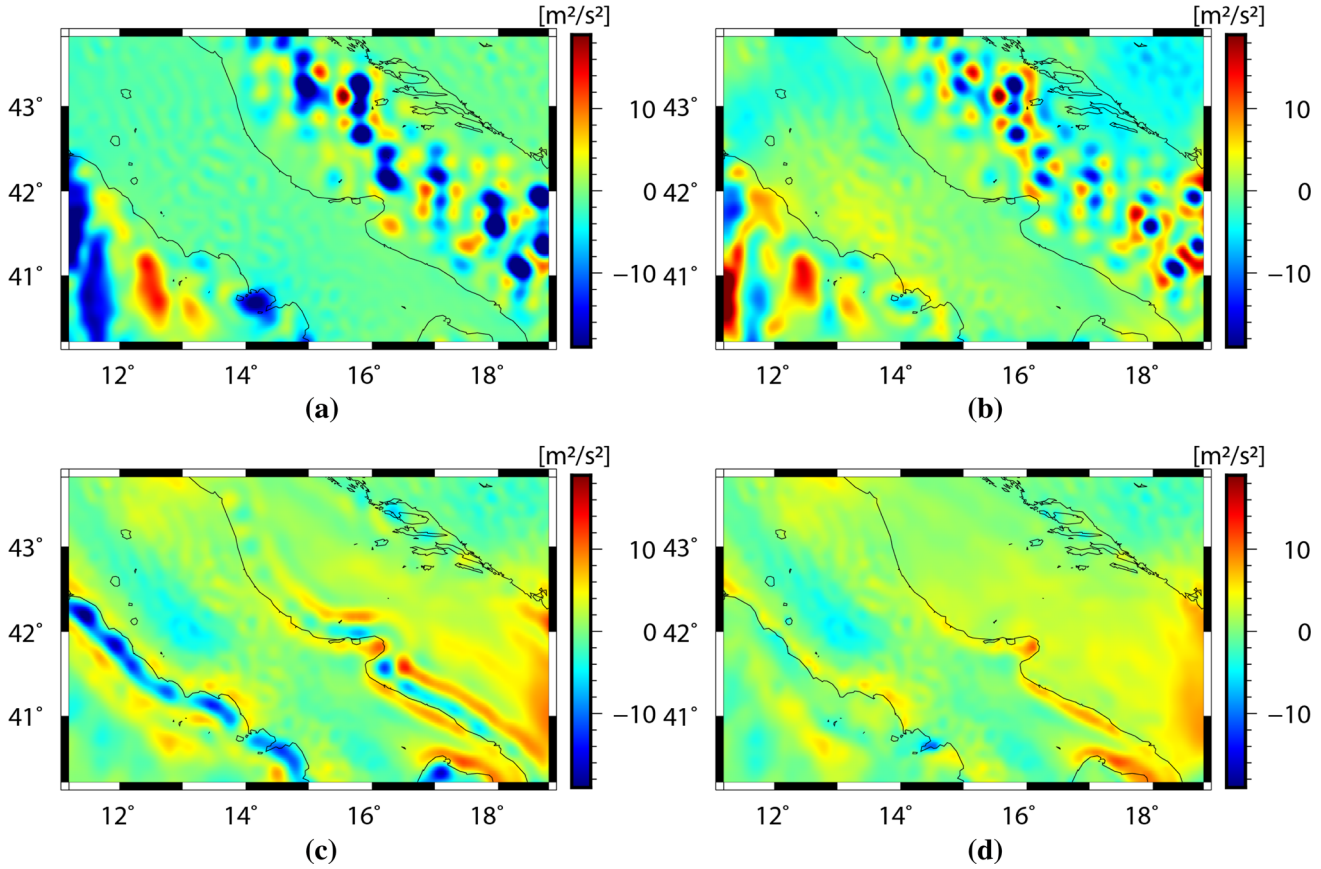


Fig. 8 Differences between the modeled disturbing potential results and the validation data, delivered by **a** the single-level approach, **b** the MRR without pyramid algorithm, **c** the MRR based on the pyramid algorithm before adapting the investigation area $\partial\Omega_{I_i}$, and **d** the MRR based on pyramid algorithm after adapting $\partial\Omega_{I_i}$ to reduce edge effects

Table 2 Comparison between the single-level model, the MRR without pyramid algorithm, and the MRR based on the pyramid algorithm, with respect to the validation data in terms of disturbing potential values (unit $[m^2/s^2]$)

	Min	Max	RMS
Single-level model (Fig. 8a)	−38.22	21.64	5.48
MRR without pyramid algorithm (Fig. 8b)	−27.13	27.64	4.21
MRR based on pyramid algorithm (before adapting $\partial\Omega_{I_i}$, Fig. 8c)	−20.98	12.82	3.44
MRR based on pyramid algorithm (after adapting $\partial\Omega_{I_i}$ to reduce edge effects, Fig. 8d)	−11.63	11.41	2.72

5 Validation with real data

5.1 Data and model configuration

After testing the performance of the MRR based on the pyramid algorithm with simulated data successfully, we apply this method to real data sets. Figure 9 shows the study area, located between 5.9° and 14.3° longitude and between 53.2° and 55.3° latitude, covering Northern Germany, parts of the North Sea and the Baltic Sea, and a small part of the Netherlands and Denmark. The gravity observations are taken from Lieb et al. (2016), where a detailed data description can be found. The terrestrial data (yellow dots in Fig. 9) are provided by the Federal States Schleswig-Holstein, Mecklenburg West-Pomerania, and Lower Saxony, with 23,465 observations covering Northern Germany. This high-resolution data set is given in terms of absolute gravity g and used in terms of gravity anomalies Δg. Two airborne data sets (orange flight tracks in Fig. 9) are provided by the Federal Agency of Cartography and Geodesy (BKG), one over the North Sea, and another one over the Baltic Sea, collected in 2007/2008 and 2006, respectively. They have been preprocessed and are provided in terms of gravity disturbance δg; the data accuracy is estimated by BKG to be 2 to 3 mGal.

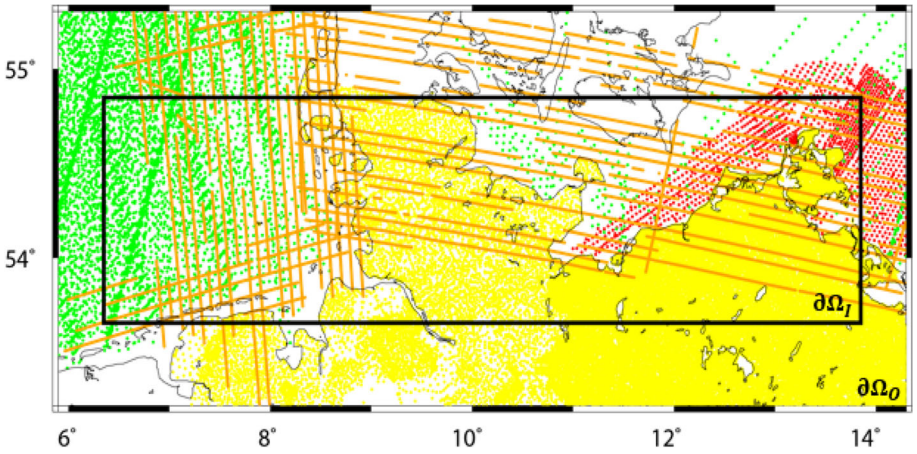


Fig. 9 The observation area $\partial\Omega_O$ and the distribution of real gravity data, including terrestrial (yellow dots), shipborne (red dots), airborne (orange dots), and altimetry (green dots) data. The black rectangle represents the investigation area $\partial\Omega_I$, where the final gravity model is calculated

The flight campaign over the North Sea contains 5,651 observations, with an average flight altitude of 592 m; the flight campaign over the Baltic Sea contains 6,508 observations, with an average flight altitude of 832 m. The 1,183 shipborne measurements (red dots in Fig. 9) in the Baltic Sea are preprocessed and provided by the Federal State Mecklenburg West-Pomerania in terms of gravity anomalies Δg. Satellite altimetry data (green dots in Fig. 9) are provided by the DGFI-TUM altimetry group in terms of geoid height N, which is derived from the measured sea surface heights (SSH) and the instantaneous dynamic ocean topography (iDOT) (Bosch et al. 2013). The altimetry data include measurements from multiple altimetry missions, namely the ERS-1e/f (Geodetic Mission phase, 1994–1995, cycles Nr. 139-143), Envisat (Extended Mission phase, 2010–2012, cycles Nr. 096-113), Jason-1 (Geodetic Mission phase, 2012–2013, cycles Nr. 500-537), and Cryosat (2010-2013, cycles Nr. 011-035), with an average spatial resolution of 10 km in the North Sea. In the Baltic Sea, we use a sparse altimetry data distribution deliberately in order to test our approach also in areas with poor data coverage. For each altimetry measurement, corrections derived from a multi-mission cross-calibration (Bosch et al. 2014) have been applied. The satellite data from GOCE and GRACE are included in this study case as the satellite-only global gravity model (GGM), instead of direct observations. Lieb et al. (2016) point out that the study area is too small (especially in the north–south direction) in comparison with the spatial resolution of the satellite data, and thus, does not allow resolving reliable long-wavelength information. In this way, we present the performance of the MRR based on the pyramid algorithm in two different scenarios of using the satellite data, i.e., as direct observations and as a satellite-only GGM, in the simulated (Sect. 4) and real case, respectively.

The highest resolution level of the MRR is chosen as $I = 12$ according to the spatial resolution of the data, and only the terrestrial data are used at the highest level to calculate the unknown coefficients of this level and to start the pyramid algorithm. The shipborne and the airborne data are included at level 11 and level 10, respectively, and the altimetry data are added at level 9. The long-wavelength component up to level 8 (degree 255) is modeled by using the RCR procedure with GOCO06s (Kvas et al. 2021), which enhances an optimal combination of the GOCE and GRACE data. Same as in the simulated case (see Sect. 4), we also calculate the single-level model and the MRR without the pyramid algorithm for comparison. The number of Reuter grid points at each level is determined in the same manner as for the simulated study case, and the margin size $\eta_{C,O}$ between the computation area $\partial\Omega_C$ and the observation area $\partial\Omega_O$ is determined following Eq. (26). In this study case, the $\eta_{C,O}$ is chosen as 0.15°, 0.3°, 0.6°, 1.2° for levels 12, 11, 10, 9, correspondingly. Consequently, the number of unknown coefficients amounts to $K_{12} = 6638$, $K_{11} = 2111$, $K_{10} = 684$, and $K_9 = 315$ at each resolution level. The margin size $\eta_{O,I}$ between the observation area $\partial\Omega_O$ and the investigation area $\partial\Omega_I$ (black rectangle in Fig. 9) is chosen as the median of the applied $\eta_{C,O}$, i.e., $\eta_{O,I} = 0.45°$. As discussed in Sect. 4.2, strong edge effects show up in the calculated detail signals of the high resolution levels, due to the fact that the involved observations at these levels do not have full coverage over $\partial\Omega_O$. Again, we apply the strategy proposed in Sect. 4.2, and define $\partial\Omega_{I_i} = \partial\Omega_{O_i} \cap \partial\Omega_I$ for calculating the detail signals at each level. In the following, we always refer the MRR based on the pyramid algorithm to the one after adapting $\partial\Omega_{I_i}$.

5.2 Modeling results and discussions

The elements of the estimated coefficient vectors $\widehat{\boldsymbol{d}}_i$ and their standard deviations at each level i are plotted in Fig. 10; the black rectangle inside each plot represents the observation area $\partial\Omega_O$. As we can see, the estimated coefficients at level 12 only contain additional gravity information from the terrestrial data. Consequently, their standard deviations are much larger in regions without terrestrial observations, which is reasonable. At level 11, level 10, and level 9, the shipborne,

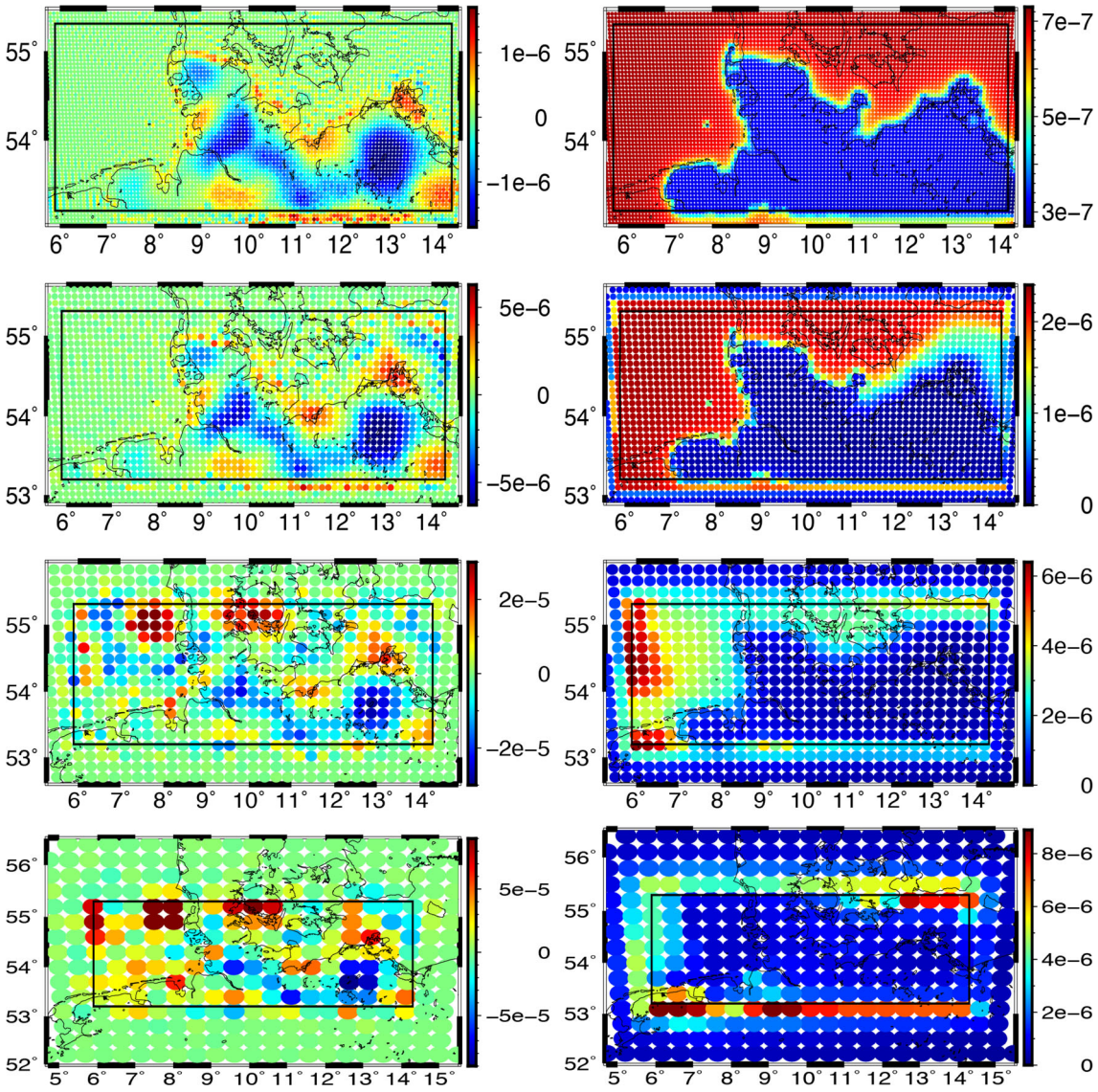


Fig. 10 The estimated scaling coefficients (left column) and their standard deviations (right column) from level 12 (first row) to level 9 (fourth row). The black rectangle inside each plot represents the observation area $\partial\Omega_O$

airborne, and altimetry data insert additional information, respectively. The new observations introduced at the lower levels fill the data gaps from the terrestrial observations, and the features from the highest level are preserved at the same time. The behavior of the standard deviations coincides with the coefficients, i.e., from level 12 to level 10, the standard deviations at the locations with shipborne and airborne data decrease, and from level 10 to level 9, those within the altimetry data coverage decrease.

The computed regional quasi-geoid models from the single-level approach, the MRR without pyramid algorithm, and the MRR based on the pyramid algorithm (after adapting $\partial\Omega_{I_i}$) are firstly validated using GPS/leveling data in Northern Germany (Gruber et al. 2011). 53 data points are available within the investigation area $\partial\Omega_I$ (black rectangle in Fig. 9), which are derived from GPS-based ellipsoidal heights and leveling-based normal heights. The differences between the computed height anomaly results and those from GPS/leveling are shown in Fig. 11, and the corresponding statistics are listed in Table 3. The mean value of the difference between the gravimetrically determined height anomalies and those from GPS/leveling amounts to around 33 cm. It is consistent with the value reported in Gruber et al. (2011)), and is caused by differences in the height system definition, i.e., the local normal heights in Germany refer to the vertical datum of the European Vertical Network (EUVN), which is defined as the equipotential surface of the Earth's gravity field passing through the "Normaal Amsterdams Peil" (NAP; fundamental tide gauge in Amsterdam, the Netherlands). Figure 11 shows clearly that the MRR based on

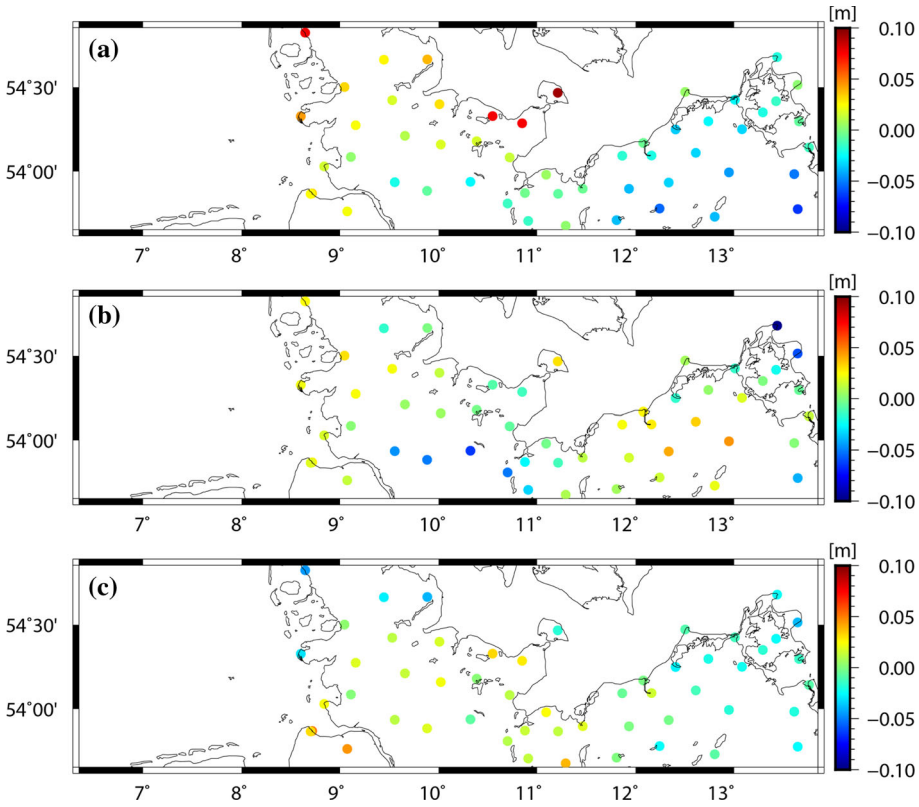


Fig. 11 Differences between the calculated quasi-geoid model and the GPS/leveling data, delivered by **a** the single-level approach, **b** the MRR without pyramid algorithm, and **c** the MRR based on the pyramid algorithm. Note that the mean values of the differences are removed

Table 3 Comparison between the single-level approach, the MRR without pyramid algorithm, and the MRR based on the pyramid algorithm w.r.t. GPS/leveling data (in terms of quasi-geoid, note that the mean differences are removed) and w.r.t. the DTU17 grid (in terms of gravity anomaly)

	w.r.t. GPS/leveling data (unit [cm])			w.r.t. the DTU17 grid (unit [mGal])		
	Min	Max	RMS	Min	Max	RMS
Single-level	−6.48	9.36	3.43	−53.24	60.46	7.22
MRR without pyramid algorithm	−9.70	4.57	2.88	−44.17	39.63	6.25
MRR based on pyramid algorithm	−4.50	5.15	2.23	−7.98	8.70	2.67

the pyramid algorithm delivers the smallest difference w.r.t. the GPS/leveling data, with an RMS error of 2.23 cm, which is 23% smaller than the one given by the MRR without pyramid algorithm, and 35% smaller than that of the single-level model. Such large improvements demonstrate the benefits of applying the MRR based on the pyramid algorithm. Figure 11a (single-level approach) and Fig. 11b (MRR without pyramid algorithm) show much larger differences w.r.t. the GPS/leveling data in comparison to Fig. 11c (MRR based on the pyramid algorithm), even in regions with very dense terrestrial data (between 11° and 13.85° longitude).

In the offshore area where no GPS/leveling data are available, the computed gravity models are validated with the $2' \times 2'$ altimetric gravity anomaly grid DTU17 (Andersen and Knudsen 2019). The differences between the computed gravity anomaly results and the DTU17 are shown in Fig. 12, and the corresponding statistics are listed in Table 3. Again, the largest differences are delivered by the single-level approach (Fig. 12a), with an RMS error of 7.22 mGal. In the single-level model, much smaller differences show up in regions with shipborne data coverage (see Fig. 9), which suggests that it majorly recovers gravity information from the high-resolution shipborne data, and information from other measurement types are not captured sufficiently. This result agrees with the conclusion drawn from the simulated study case (see Sect. 4.3). In comparison to the single-level model, applying the MRR (without pyramid algorithm) improves the modeling results by 13%. Comparing Fig. 12b with Fig. 12a reveals significant improvements in regions where the altimetry data are located (between 6.35° and 7° longitude). This indicates that the MRR extracts gravity information from the lower resolution altimetry data better than the single-level approach. However, it can still be seen from Fig. 12b that larger differences occur in regions without shipborne data

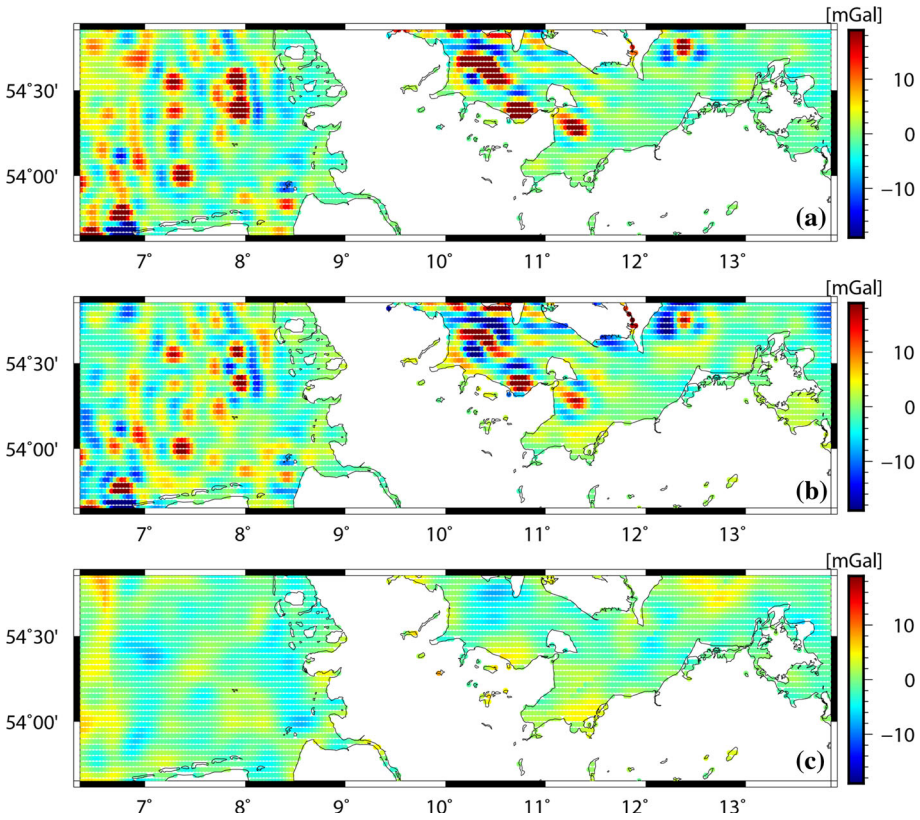


Fig. 12 Differences between the calculated gravity anomaly results and the DTU17 grid in the offshore area, delivered by **a** the single-level approach, **b** the MRR without pyramid algorithm, and **c** the MRR based on the pyramid algorithm

coverage. The differences w.r.t. the DTU17 are significantly reduced when the MRR based on the pyramid algorithm is applied, giving an RMS of 2.67 mGal, which is 57% smaller than the one delivered by the MRR without pyramid algorithm, and 63% smaller than that of the single-level approach. The improvement achieved by applying the MRR based on the pyramid algorithm is larger in the offshore area than in the onshore area, where high-resolution terrestrial data are available. It demonstrates that the single-level approach cannot represent the lower-resolution data in an optimal way, and the MRR based on the pyramid algorithm is beneficial, especially in regions where high-resolution gravity data are not available. In the MRR based on the pyramid algorithm (Fig. 12c), larger differences again occur at the border of the higher-resolution gravity data (shipborne and airborne), which is caused by edge effects, as discussed in Sect. 4.3.

It is worth mentioning that validation in the offshore area was also made w.r.t. the NKG2015 gravimetric quasi-geoid model (Ågren et al. 2016) to rule out possible conflicts when validating our results with external models also based on satellite altimetry data as the DTU17. The differences between the calculated quasi-geoid results and the NKG2015 model show the same pattern as those w.r.t. the DTU17, i.e., Fig. 12. Thus, this comparison is not shown in detail here due to the length of the manuscript. In comparison to the NKG2015, the improvement achieved by applying the developed MRR scheme based on the pyramid algorithm is 39% w.r.t. the MRR without pyramid algorithm, and it reaches 55% w.r.t. the single-level approach, in terms of RMS value.

6 Conclusion and outlook

This study focuses on the spectral combination of different types of gravity observations through the MRR based on the pyramid algorithm, which is realized successfully for the first time in connection with sequential parameter estimation, in regional gravity field modeling. We address in this paper the challenges regarding the practical realization of the pyramid algorithm. Firstly, a successive low-pass filtering for transforming the estimated coefficients of the highest resolution level to lower resolution levels is proposed. Furthermore, we develop an innovative MRR scheme where the coefficients for calculating the detail signals at each lower resolution level are not only determined from the pyramid algorithm but also updated by a direct combination with observation groups included according to their spectral resolution. The main contribution of our approach is that the final gravity model is able to benefit from the individual strengths of each observation type. The settings of the MRR are characterized, including the type of the SRBFs, the location of the SRBFs, and the margin size applied at each level. When the MRR based on the pyramid algorithm is applied, only specific data sets are used at the higher resolution levels, resulting

in strong edge effects at the border of the high-resolution observations. Therefore, we additionally develop a suitable strategy to adapt the investigation area $\partial\Omega_{I_i}$ at each level i according to the coverage of involved observations. This is also a remarkable innovation of our approach as it reduces edge effects in the calculated detail signals (and therefore, the final gravity model) significantly.

The performance of the MRR based on the pyramid algorithm is evaluated in comparison to the conventional single-level approach and the MRR without pyramid algorithm using both simulated and real gravity data. In the simulated study case, the RMS obtained by the MRR based on the pyramid algorithm is 50% smaller than the one delivered by the single-level approach, and 35% smaller than the one given by the MRR without pyramid algorithm, comparing to the validation data. Moreover, the single-level model shows very large differences to the validation data in offshore regions, which indicates that the contribution of other types of observations is not captured as sufficiently as the terrestrial observations. This shows that the single-level approach is biased towards the terrestrial measurements, and the gravity information from measurements with medium to low resolution is not extracted sufficiently. Applying the MRR (without pyramid algorithm) improves the modeling results in offshore regions. However, it still shows larger differences w.r.t. the validation data in the offshore area in comparison to the onshore area. Thus, it is important and beneficial to apply the MRR based on the pyramid algorithm, especially when the high-resolution terrestrial data do not have full coverage over the study area.

In the real data case, the MRR based on the pyramid algorithm is applied for regional gravity field modeling in Northern Germany. The terrestrial, shipborne, airborne, and altimetry observations are used at the resolution levels 12, 11, 10, and 9, respectively. At the lower levels, the gravity information obtained from the highest level is preserved, and at the same time, the new observations introduced at this specific level contribute with additional information and fill data gaps. Such features in the estimated coefficients are observed in both the simulated and real data cases. The computed gravity models are validated in terms of quasi-geoid and gravity anomaly with GPS/leveling data in land and the DTU17 in offshore area, respectively. In comparison to the single-level approach, the improvement achieved by the MRR based on the pyramid algorithm is 35% and 63% in terms of RMS value, w.r.t. the GPS/leveling data and DTU17, respectively. Compared with the MRR without pyramid algorithm, the RMS error obtained by the MRR based on the pyramid algorithm decreases by 23% and 57% w.r.t. the GPS/leveling data and DTU17, respectively. Such significant improvements further demonstrate the benefits of the MRR based on the pyramid algorithm. Results in the real case again show that both the single-level approach and the MRR without pyramid algorithm cannot recover gravity information from the lower-resolution observations as sufficient as the MRR based on the pyramid algorithm.

In both the simulated and the real cases, larger differences w.r.t. the validation data in the MRR based on the pyramid algorithm occur at the border of the high-resolution data, due to edge effects. Thus, a major concern for future work is to develop strategies for further reducing the edge effects in the calculated detail signals. We also plan to include the full variance-covariance matrix of the GGM. In current studies, the weight matrix of the prior information (used at the highest level) is defined as the identity matrix, which is computationally easy. However, better and more realistic modeling results might be obtained by considering the full covariance matrix of the GGM instead of a simple identity matrix. In addition, it is also planned for future work to use real GOCE gravity gradients and K-band range-rate (KBRR) data from GRACE as direct observations in our developed MRR scheme.

Acknowledgements The authors would like to thank the German Research Foundation (DFG) for funding the project "Optimally combined regional geoid models for the realization of height systems in developing countries" (grant number: SCHM 2433/11-1). We thank the Federal Angency of Cartography and Geodesy (BKG) and the federal states Schleswig-Holstein, Mecklenburg West-Pomerania, and Lower Saxony for providing us the terrestrial, airborne, and shipborne data sets. We thank Dr. Thomas Gruber from IAPG-TUM for kindly providing the GPS/leveling data in North Germany. Furthermore, the authors acknowledge the developers of the Generic Mapping Tool (GMT) mainly used for generating the figures in this work. Finally, we thank the reviewers and editors for their comments that helped us to significantly improve the manuscript.

Author Contributions The concept of the paper was proposed by QL. QL designed the study, performed the calculations, compiled the figures, and wrote the manuscript with the assistance from MS. All authors edited, reviewed, and commented on the original manuscript.

Funding Open Access funding enabled and organized by Projekt DEAL. This research was funded by the German Research Foundation (DFG) under grant number SCHM 2433/11-1 (project ORG4Heights).

Data Availability The terrestrial, airborne, and shipborne gravity data in North Germany were provided by the Federal Angency of Cartography and Geodesy (BKG) and the federal states Schleswig-Holstein, Mecklenburg West-Pomerania, and Lower Saxony. The altimetry data were generated by DGFI-TUM and are freely available through https://openadb.dgfi.tum.de/. The global gravity models can be publicly accessed from http://icgem.gfz-potsdam.de/. The DTU17 grid is downloaded from https://ftp.space.dtu.dk/pub/DTU17/, and the NKG2015 gravimetric quasi-geoid model is freely accessible through the International Service for the Geoid https://www.isgeoid.polimi.it/.

Declarations

Conflict of interest The authors declare that they have no conflict of interest.

Open Access This article is licensed under a Creative Commons Attribution 4.0 International License, which permits use, sharing, adaptation, distribution and reproduction in any medium or format, as long as you give appropriate credit to the original author(s) and the source, provide a link to the Creative Commons licence, and indicate if changes were made. The images or other third party material in this article are included in the article's Creative Commons licence, unless indicated otherwise in a credit line to the material. If material is not included in the article's Creative Commons licence and your intended use is not permitted by statutory regulation or exceeds the permitted use, you will need to obtain permission directly from the copyright holder. To view a copy of this licence, visit http://creativecommons.org/licenses/by/4.0/.

References

Ågren J, Strykowski G, Bilker-Koivula M, Omang O, Märdla S, Forsberg R, Ellmann A, Oja T, Liepins I, Parseliunas E, Kaminskis J, Sjöberg L, Valsson G (2016) The NKG2015 gravimetric geoid model for the Nordic-Baltic region. In: 1st Joint Commission 2 and IGFS Meeting International Symposium on Gravity, Geoid and Height Systems, pp 19–23, https://doi.org/10.13140/RG.2.2.20765.20969

Andersen O, Knudsen P (2019) The DTU17 global marine gravity field: First validation results. In: Fiducial reference measurements for altimetry. Springer, pp 83–87, https://doi.org/10.1007/1345_2019_65

Austen G, Grafarend E (2004) Gravitational field recovery from GRACE data of type high-low and low-low SST. In: Proceedings of the Joint CHAMP/GRACE science meeting

Bentel K, Schmidt M, Denby CR (2013a) Artifacts in regional gravity representations with spherical radial basis functions. J Geod Sci 3:173–187. https://doi.org/10.2478/jogs-2013-0029

Bentel K, Schmidt M, Gerlach C (2013b) Different radial basis functions and their applicability for regional gravity field representation on the sphere. Int J Geomath 4:67–96. https://doi.org/10.1007/s13137-012-0046-1

Beylkin G, Cramer R (2002) Toward multiresolution estimation and efficient representation of gravitational fields. Celest Mech Dyn Astron 84(1):87–104. https://doi.org/10.1023/A:1019941111529

Bolkas D, Fotopoulos G, Braun A (2016) Comparison and fusion of satellite, airborne, and terrestrial gravity field data using wavelet decomposition. J Surv Eng 142(2):04015010. https://doi.org/10.1061/(ASCE)SU.1943-5428.0000162

Bosch W, Dettmering D, Schwatke C (2014) Multi-mission cross-calibration of satellite altimeters: constructing a long-term data record for global and regional sea level change studies. Remote Sens 6(3):2255–2281. https://doi.org/10.3390/rs6032255

Bosch W, Savcenko R, Dettmering D, Schwatke C (2013) A two-decade time series of eddy-resolving dynamic ocean topography (iDOT). In: Ouwehand L (ed) Proceedings of "20 Years of Progress in Radar Altimetry", Sept. 2012, Venice, Italy, ESA SP-710 (CD-ROM), ESA/ESTEC. ISBN 978-92-9221-274-2

Bucha B, Janák J, Papčo J, Bezděk A (2016) High-resolution regional gravity field modelling in a mountainous area from terrestrial gravity data. Geophys J Int 207:949–966. https://doi.org/10.1093/gji/ggw311

Childers VA, Bell RE, Brozena JM (1999) Airborne gravimetry: an investigation of filtering. Geophysics 64:61–69. https://doi.org/10.1190/1.1444530

Denker H (2013) Regional gravity field modeling: theory and practical results. In: Sciences of geodesy-II. Springer, pp 185–291, https://doi.org/10.1007/978-3-642-28000-9_5

Eicker A (2008) Gravity field refinement by radial basis functions from in-situ satellite data. PhD thesis, Universität Bonn

Erdogan E, Schmidt M, Goss A, Görres B, Seitz F (2020) Adaptive modeling of the global ionosphere vertical total electron content. Remote Sens 12(11):1822. https://doi.org/10.3390/rs12111822

Fengler M, Freeden W, Kohlhaas A, Michel V, Peters T (2007) Wavelet modeling of regional and temporal variations of the Earth's gravitational potential observed by GRACE. J Geodesy 81(1):5–15. https://doi.org/10.1007/s00190-006-0040-1

Fengler M, Freeden W, Michel V (2004) The Kaiserslautern multiscale geopotential model SWITCH-03 from orbit perturbations of the satellite CHAMP and its comparison to the models EGM96, UCPH2002_02_0.5, EIGEN-1s and EIGEN-2. Geophys J Int 157(2):499–514. https://doi.org/10.1111/j.1365-246X.2004.02209.x

Forsberg R (1993) Modelling the fine-structure of the geoid: methods, data requirements and some results. Surv Geophys 14(4–5):403–418. https://doi.org/10.1007/BF00690568

Freeden W (1999) Multiscale modelling of spaceborne geodata. Teubner, Stuttgart

Freeden W, Michel V (2004) Multiscale potential theory: with applications to geoscience. Birkhäuser, Basel

Freeden W, Gervens T, Schreiner M (1998) Constructive approximation on the sphere with applications to geomathematics. Oxford University Press on Demand, New York

Gilardoni M, Reguzzoni M, Sampietro D (2016) GECO: a global gravity model by locally combining GOCE data and EGM2008. Stud Geophys Geod 60(2):228–247. https://doi.org/10.1007/s11200-015-1114-4

Gruber T, Visser P, Ackermann C, Hosse M (2011) Validation of goce gravity field models by means of orbit residuals and geoid comparisons. J Geodesy 85(11):845–860. https://doi.org/10.1007/s00190-011-0486-7

Haagmans R, Prijatna K, Omang O (2002) An alternative concept for validation of GOCE gradiometry results based on regional gravity. In: Tziavos N (ed) Proceedings of the 3rd meeting of the international gravity and geoid commission, Ziti Editions, pp 281–286

Holschneider M, Chambodut A, Mandea M (2003) From global to regional analysis of the magnetic field on the sphere using wavelet frames. Phys Earth Planet Inter 135(2–3):107–124. https://doi.org/10.1016/S0031-9201(02)00210-8

Jiang T, Wang YM (2016) On the spectral combination of satellite gravity model, terrestrial and airborne gravity data for local gravimetric geoid computation. J Geodesy 90:1405–1418. https://doi.org/10.1007/s00190-016-0932-7

Kalman RE (1960) A new approach to linear filtering and prediction problems. J Basic Eng 82(1):35–45. https://doi.org/10.1115/1.3662552

Kern M, Schwarz K, Sneeuw N (2003) A study on the combination of satellite, airborne, and terrestrial gravity data. J Geodesy 77(3–4):217–225. https://doi.org/10.1007/s00190-003-0313-x

Klees R, Slobbe D, Farahani H (2018) A methodology for least-squares local quasi-geoid modelling using a noisy satellite-only gravity field model. J Geodesy 92:431–442. https://doi.org/10.1007/s00190-017-1076-0

Koch KR (1999) Parameter estimation and hypothesis testing in linear models. Springer Berlin Heidelberg, Berlin

Koch KR, Kusche J (2002) Regularization of geopotential determination from satellite data by variance components. J Geodesy 76:259–268. https://doi.org/10.1007/s00190-002-0245-x

Koop R (1993) Global gravity field modelling using satellite gravity gradiometry. Nederlandse Commissie voor Geodesie, Delft

Kusche J, Ilk K, Rudolph S, Thalhammer M (1998) Application of spherical wavelets for regional gravity field recovery - a comparative study. In: Geodesy on the Move, Springer, pp 213–218, https://doi.org/10.1007/978-3-642-72245-5_30

Kvas A, Brockmann JM, Krauss S, Schubert T, Gruber T, Meyer U, Mayer-Gürr T, Schuh WD, Jäggi A, Pail R (2021) GOCO06s—a satellite-only global gravity field model. Earth Syst Sci Data 13(1):99–118. https://doi.org/10.5194/essd-13-99-2021

Lieb V (2017) Enhanced regional gravity field modeling from the combination of real data via MRR. PhD thesis, Technische Universität München

Lieb V, Schmidt M, Dettmering D, Börger K (2016) Combination of various observation techniques for regional modeling of the gravity field. J Geophys Res Solid Earth 121:3825–3845. https://doi.org/10.1002/2015JB012586

Liu Q, Schmidt M, Pail R, Willberg M (2020a) Determination of the regularization parameter to combine heterogeneous observations in regional gravity field modeling. Remote Sens 12(10):1617. https://doi.org/10.3390/rs12101617

Liu Q, Schmidt M, Sánchez L, Willberg M (2020b) Regional gravity field refinement for (quasi-) geoid determination based on spherical radial basis functions in Colorado. J Geodesy 94(10):1–19. https://doi.org/10.1007/s00190-020-01431-2

Naeimi M (2013) Inversion of satellite gravity data using spherical radial base functions. PhD thesis, Leibniz Universität Hannover

Panet I, Kuroishi Y, Holschneider M (2011) Wavelet modelling of the gravity field by domain decomposition methods: an example over Japan. Geophys J Int 184(1):203–219. https://doi.org/10.1111/j.1365-246X.2010.04840.x

Pavlis NK, Factor JK, Holmes SA (2006) Terrain-related gravimetric quantities computed for the next EGM. In: Proceedings of the 1st International Symposium of the International Gravity Field Service (IGFS), Istanbul, pp 318–323

Reuter R (1982) Über Integralformeln der Einheitssphäre und harmonische Splinefunktionen. PhD thesis, RWTH Aachen University

Rummel R, Balmino G, Johannessen J, Visser P, Woodworth P (2002) Dedicated gravity field missions - principles and aims. J Geodyn 33:3–20. https://doi.org/10.1016/S0264-3707(01)00050-3

Sánchez L, Ågren J, Huang J, Wang YM, Mäkinen J, Pail R, Barzaghi R, Vergos GS, Ahlgren K, Liu Q (2021) Strategy for the realisation of the International Height Reference System (IHRS). J Geodesy 95(3):1–33. https://doi.org/10.1007/s00190-021-01481-0

Schmidt M, Fabert O, Shum C (2005) On the estimation of a multi-resolution representation of the gravity field based on spherical harmonics and wavelets. J Geodyn 39(5):512–526. https://doi.org/10.1016/j.jog.2005.04.007

Schmidt M, Han SC, Kusche J, Sanchez L, Shum C (2006) Regional high-resolution spatiotemporal gravity modeling from GRACE data using spherical wavelets. Geophys Res Lett. https://doi.org/10.1029/2005GL025509

Schmidt M, Fengler M, Mayer-Gürr T, Eicker A, Kusche J, Sánchez L, Han SC (2007) Regional gravity modeling in terms of spherical base functions. J Geodesy 81:17–38. https://doi.org/10.1007/s00190-006-0101-5

Schmidt M, Göttl F, Heinkelmann R (2015) Towards the combination of data sets from various observation techniques. In: Kutterer H, Seitz F, Alkhatib H, Schmidt M (eds) The 1st International Workshop on the Quality of Geodetic Observation and Monitoring Systems (QuGOMS'11), Springer, pp 35–43, https://doi.org/10.1007/978-3-319-10828-5_6

Sjöberg L (1981) Least-squares combination of satellite and terrestrial data in physical geodesy. Ann Geophys 37:25–30

Tapley BD, Bettadpur S, Watkins M, Reigber C (2004) The gravity recovery and climate experiment: mission overview and early results. Geophys Res Lett. https://doi.org/10.1029/2004GL019920

Wittwer T (2009) Regional gravity field modelling with radial basis functions. PhD thesis, Netherlands Geodetic Commission

Wu Y, Luo Z, Chen W, Chen Y (2017a) High-resolution regional gravity field recovery from Poisson wavelets using heterogeneous observational techniques. Earth Planets Space 69:34. https://doi.org/10.1186/s40623-017-0618-2

Wu Y, Zhou H, Zhong B, Luo Z (2017b) Regional gravity field recovery using the GOCE gravity gradient tensor and heterogeneous gravimetry and altimetry data. J Geophys Res Solid Earth 122(8):6928–6952. https://doi.org/10.1002/2017JB014196

Wu Y, Luo Z, Zhong B, Xu C (2018) A multilayer approach and its application to model a local gravimetric quasi-geoid model over the North Sea: QGNSea V1.0. Geosci Model Dev 11(12):4797–4815. https://doi.org/10.5194/gmd-11-4797-2018

A4 Co-author publications

CP-I

Sánchez, L., Ågren, J., Huang, J., Wang, Y., Mäkinen, J., Pail, R., Barzaghi, R., Vergos, G., Ahlgren, K., and Liu, Q. (2021). **Strategy for the realisation of the International height Reference System (IHRS)**. *Journal of Geodesy*, 95, 33. https://doi.org/10.1007/s00190-021-01481-0

This publication discusses the strategy for the realization of the IHRS, i.e., the implementation of the IHRF. Three methods for the IHRF physical coordinates determination are evaluated, namely (1) using high-resolution GGMs, (2) precise regional gravity field modeling, and (3) local height systems unification. Experimental results show that the second method, i.e., regional gravity field modeling is recommended for the determination of potential values, except for regionals without (or with very few) surface gravity data. Based on the analysis and discussion regarding these three options, a strategy for the IHRF establishment is defined, including the data requirement, standards and conventions for the determination of IHRF physical coordinates (e.g., the zero-degree correction, mass center convention, and the treatment of the permanent tide), a first IHRF reference network configuration, and the usability and sustainability of the IHRF. One highlight of this publication is the evaluation of the potential values calculated using different regional gravity field modeling methods by the fourteen participating groups in the "1 cm geoid experiment". Compared with the mean value, the individual solutions agree within ± 0.09 and ± 0.23 m^2/s^2 in terms of STD.

The contribution of Q. Liu to CP-I is mainly the calculation of potential values from the different high-resolution GGMs.

CP-II

Wang, Y., Sánchez, L., Ågren, J., Huang, J., Forsberg, R., Abd-Elmotaal, H., Barzaghi, R., Bašić, T., Carrion, D., Claessens, S., Erol, B., Erol, S., Filmer, M., Grigoriadis, V., Isik, M., Jiang, T., Koç, Ö., Li, X., Ahlgren, K., Krcmaric, J., Liu, Q., Matsuo, K., Natsiopoulos, D., Novák, P., Pail, R., Pitoňák, M., Schmidt, M., Varga, M., Vergos, G., Véronneau, M., Willberg, M., Zingerle, P. (2021). **Colorado geoid computation experiment – Overview and Summary**. *Journal of Geodesy*, 95, 127. https://doi.org/10.1007/s00190-021-01567-9

This publication gives a detailed overview of the "1 cm geoid experiment", summarizes the methods and procedures applied by different participating groups, and evaluates the delivered (quasi-) geoid results. The gravity data, digital elevation model, as well as the GNSS/leveling data, that are available within this experiment are described. The computation methodologies, as well as the data processing strategies implemented by the fourteen participating groups, are listed, including the key characteristics considering three main computation stages, namely (1) the handling of topographic effects on gravity, (2) the preparation of surface gravity data, and (3) the solution of the Geodetic Boundary Value Problem (GBVP). The (quasi-) geoid results calculated by each group are evaluated in three aspects: (1) quasi-geoid validation w.r.t. the mean value in the whole target area (see Fig. 3.3a), and the RMS value of the individual solutions ranges from 1.6 to 5.3 cm; (2) quasi-geoid validation w.r.t. the GNSS/leveling data at the GSVS17 benchmarks; the STD of the individual solutions ranges from 1.7 to 3.6 cm; (3) GSVS17 differential quasi-geoid (slope) comparison, which shows that the RMS values increase w.r.t. the baseline length. Finally, recommendations to improve the model precision towards the 1-cm level are also provided in this publication.

The main contribution of Q. Liu to CP-II is the computation of the solution "DGFI" by the method of SRBFs, and the review of the paper in different versions.